

Astronomy Unit
School of Physics and Astronomy
Queen Mary, University of London

Relativistic effects in the galaxy bispectrum

Eline Maaike de Weerd

Supervised by Dr Chris Clarkson

Submitted in partial fulfillment of the requirements of the Degree of
Doctor of Philosophy

Declaration

I, Eline Maaike de Weerd, confirm that the research included within this thesis is my own work or that where it has been carried out in collaboration with, or supported by others, that this is duly acknowledged below and my contribution indicated. Previously published material is also acknowledged below.

I attest that I have exercised reasonable care to ensure that the work is original, and does not to the best of my knowledge break any UK law, infringe any third party's copyright or other Intellectual Property Right, or contain any confidential material.

I accept that the College has the right to use plagiarism detection software to check the electronic version of the thesis.

I confirm that this thesis has not been previously submitted for the award of a degree by this or any other university. The copyright of this thesis rests with the author and no quotation from it or information derived from it may be published without the prior written consent of the author.

Details of collaboration and publications: Part of this work has been done in collaboration with Stefano Camera, Chris Clarkson, Sheean Jolicoeur, Roy Maartens, and Obinna Umeh. It is based on the following publications, all of which I have contributed to:

- The dipole of the galaxy bispectrum
C. Clarkson, E.M. De Weerd, S. Jolicoeur, R. Maartens, O. Umeh
Published: *MNRAS Letters* 486 (2019) L101, arXiv: 1812.09512 [astro-ph.CO]
- Detecting the relativistic galaxy bispectrum
R. Maartens, S. Jolicoeur, O. Umeh, E.M. De Weerd, C. Clarkson, S. Camera
Published: *JCAP*03(2020)065, arXiv: 1911.02398 [astro-ph.CO]

- Multipoles of the relativistic galaxy bispectrum
E.M. De Weerd, C. Clarkson, S. Jolicoeur, R. Maartens, O. Umeh
Published: *JCAP05(2020)018*, arXiv: 1912.11016 [astro-ph.CO]
- Detecting the relativistic bispectrum in 21cm intensity maps
S. Jolicoeur, R. Maartens, E.M. De Weerd, O. Umeh, C. Clarkson, S. Camera
Published: *JCAP06(2021)039*, arXiv: 2009.06197 [astro-ph.CO]
- Local primordial non-Gaussianity in the relativistic galaxy bispectrum
R. Maartens, S. Jolicoeur, O. Umeh, E.M. De Weerd, C. Clarkson
Published: *JCAP04(2021)013*, arXiv: 2011.13660 [astro-ph.CO]

This work was supported by an STFC PhD studentship.

Signature:

Date: 17.12.2021

Abstract

Next-generation large scale galaxy surveys will provide us with a wealth of high-precision cosmological data. To be able to use this information in an as unbiased manner as possible, theoretical accuracy must match the experimental precision. On these scales, a variety of relativistic effects come into play once the galaxy number-count fluctuation is projected onto the past lightcone. It is important for these effects to be taken into account in our theoretical treatment, as they will contaminate the primordial non-Gaussian signal and bias measurements. These effects have been well-studied for the power spectrum or two-point function. The bispectrum is the first of the higher-order statistics beyond the power spectrum, and contains information both complementary and additional to what is contained in the power spectrum. On large scales, the galaxy bispectrum will be a key probe for measuring primordial non-Gaussianity, improving constraints on cosmological parameters, and help discriminate between various models of inflation and other theories of the early universe.

In this thesis, we examine in detail how the relativistic projection effects in the galaxy bispectrum, and how these effects contribute to the invariant multipoles of the galaxy bispectrum about the observer's line of sight. The Fourier-space bispectrum is complex, with an imaginary part arising from the relativistic effects only, which generates odd multipoles. This means that detection of this imaginary part is a smoking gun signal of the relativistic contributions, and we show that such a signal is in principle detectable in future surveys, although with a higher signal-to-noise ratio for spectroscopic surveys compared to 21cm intensity mapping surveys. Finally, we include local primordial non-Gaussianity in the theoretical description of the relativistic galaxy bispectrum. This allows for more precise separation of the relativistic corrections from the primordial signal.

Abbreviations and Conventions

Abbreviations

Notation	Description
BAO	Baryon Acoustic Oscillations
CDM	Cold Dark Matter
CMB	Cosmic Microwave Background
GR	General Relativity (Relativistic)
IM	Intensity Mapping
ISW	Integrated Sachs-Wolfe
LIMD	Local-in-mass-density
LSS	Large scale structure
N	Newtonian
PNG	Primordial non-Gaussianity
RSD	Redshift-space distortion
SKA	Square Kilometre Array
SNR	Signal-to-noise ratio
SN	Supernova(e)

Conventions

We assume a flat Λ CDM model, based on GR and perturbed up to second order.

For numerical forecasts for future surveys, we use the Planck 2018 best-fit parameters.

Our second-order perturbed metric is,

$$a^{-2} ds^2 = - [1 + 2\Psi^{(1)} + \Phi^{(2)}] d\eta^2 + [1 - 2\Psi^{(1)} - \Psi^{(2)}] dx^2.$$

(In Λ CDM, $\Phi^{(1)} = \Psi^{(1)}$.)

We expand perturbed quantities as,

$$X = X^{(1)} + \frac{1}{2}X^{(2)}.$$

Our Fourier convention is,

$$\begin{aligned} f(\mathbf{x}) &= \int \frac{d^3k}{(2\pi)^3} e^{i\mathbf{k}\cdot\mathbf{x}} f(\mathbf{k}), \\ f(\mathbf{k}) &= \int d^3x e^{-i\mathbf{k}\cdot\mathbf{x}} f(\mathbf{x}) = \int \frac{d^3k'}{(2\pi)^3} (2\pi)^3 \delta^D(\mathbf{k} - \mathbf{k}') f(\mathbf{k}'). \end{aligned}$$

And the Fourier transform of a product $h(\mathbf{x}) = f(\mathbf{x})g(\mathbf{x})$ is a convolution,

$$h(\mathbf{k}) = f(\mathbf{k}) \circledast g(\mathbf{k}) = \int \frac{d^3k_1}{(2\pi)^3} \frac{d^3k_2}{(2\pi)^3} f(\mathbf{k}_1)g(\mathbf{k}_2)(2\pi)^3 \delta^D(\mathbf{k}_1 + \mathbf{k}_2 - \mathbf{k}).$$

We use standard orthonormal spherical harmonics,

$$Y_{\ell m}(\theta, \varphi) = \sqrt{\frac{2\ell+1}{4\pi}} \sqrt{\frac{(\ell-m)!}{(\ell+m)!}} P_{\ell m}(\cos \theta) e^{im\varphi}.$$

We often use shorthand cp or c.p. to denote cyclic permutations of $(1, 2, 3)$. Since we work with quantities that are symmetric on the first two indices, this means $(1, 2, 3) + (1, 3, 2) + (2, 3, 1)$.

Contents

Abstract	4
Abbreviations and Conventions	5
1. Introduction	10
1.1. The standard cosmological model	11
1.2. Observing large scale structure	15
1.3. Statistics of galaxy clustering	18
1.3.1. The two-point function	19
1.3.2. The three-point function	21
1.4. Primordial non-Gaussianity	24
1.5. Galaxy bias	27
1.5.1. Local model of galaxy bias	28
1.5.2. Scale-dependent bias in the presence of PNG	30
1.6. Thesis outline	30
2. The dipole of the galaxy bispectrum	33
2.1. The dipole of the power spectrum	33
2.2. Leading order relativistic contributions to the bispectrum	35
2.3. Extracting the dipole	38
2.4. Squeezed, equilateral and flattened limits	39
2.5. The dipole in intensity mapping and galaxy surveys	41
2.6. Conclusions	43
3. Detectability in next-generation galaxy surveys	44
3.1. Detecting the leading-order relativistic signature	44
3.2. Signal-to-Noise	49
3.2.1. Relativistic contributions to the variance	50
3.2.2. Nonlinear effects	50
3.2.3. Summations over triangles	51
3.3. Next-generation galaxy surveys	52
3.3.1. Evolution bias and magnification bias	54
3.3.2. Relativistic signal-to-noise ratio	58
3.3.3. Inclusion of cosmological parameters	64
3.3.4. SNR using the 2019 luminosity function model	65
3.3.5. Recap of detectability in spectroscopic surveys	67
3.4. 21cm intensity mapping surveys	70
3.4.1. Relativistic effects in the 21cm IM bispectrum	70

Contents

3.4.2. Effects of foregrounds	76
3.4.3. Maximum and minimum scales probed	78
3.4.4. Instrumental noise	79
3.4.5. Future 21cm IM surveys	80
3.4.6. Forecasts for the relativistic signal-to-noise ratio	83
3.5. Conclusions	88
4. Higher order relativistic effects in the bispectrum	91
4.1. Lightcone projection effects in the galaxy number density	92
4.1.1. Observed galaxy number density contrast	93
4.1.2. The galaxy number density contrast in Fourier space	98
4.2. Construction of the galaxy bispectrum	103
4.3. Contributions from second-order vector and tensor modes	106
5. Multipoles of the bispectrum	112
5.1. The relativistic bispectrum	112
5.2. Extracting the multipoles	118
5.3. Analysis of the multipoles	130
5.3.1. Co-linear, squeezed and equilateral limits	130
5.3.2. Numerical analysis for next-generation surveys	133
5.4. Conclusion	142
6. Local primordial non-Gaussianity in the bispectrum	144
6.1. Galaxy clustering statistics and primordial non-Gaussianity	145
6.2. Local primordial non-Gaussianity in the galaxy bias	150
6.2.1. First-order bias	150
6.2.2. Second-order bias: Newtonian approximation	152
6.2.3. Second-order bias: relativistic corrections	154
6.2.4. Second-order metric and velocity potentials	156
6.3. Local primordial non-Gaussianity in the relativistic bispectrum	158
6.3.1. Matter bispectrum	158
6.3.2. Observed number density	158
6.3.3. Galaxy bispectrum	161
6.3.4. Numerical examples	164
6.4. Conclusions	168
7. Conclusions and Outlook	171
A. Beta coefficients	175
B. Beta coefficient tables	178
C. Upsilon coefficients	186
D. Presentation of kernel coefficients	188
E. Squeezed limit of multipoles	196

Contents

Bibliography	198
List of Figures	218
List of Tables	225

1. Introduction

Recent years have seen enormous advances in the field of cosmology. Thanks to technological advancements, wide-field galaxy surveys have helped mapping the universe, and in particular have provided high-precision data on the distribution of galaxies. From the earliest realisations that these observed galaxies can be used to trace the underlying matter density fields, the field of large-scale structure research has been transformed into a data-driven science.

Next-generation surveys will be able to observe the large scale structure of galaxies at unprecedented precision. To make the most of this wealth of high-precision cosmological data, our theoretical description must match experimental precision. The work in this thesis was undertaken as an effort to extend the theoretical description of the galaxy bispectrum, which will be a key probe in future large scale surveys. On equality scales and above, a variety of relativistic effects come into play once the observed number-count fluctuation is projected onto the past lightcone. These effects need to be accounted for properly in order for them to not bias measurements of primordial non-Gaussianity and other cosmological parameters.

To start, in this chapter we will introduce the standard cosmological model, Λ CDM, and briefly discuss the observational evidence supporting the standard model of cosmology. We also discuss structure formation in the universe, and introduce galaxy statistics, which has been the crucial tool for studying the clustering of galaxies in the universe. Up to now, the two-point correlation function, or power spectrum in Fourier space, has been a cosmologist's most reliable statistic describing the LSS and constraining cosmological parameters. We will give a brief overview of the power spectrum, and introduce the galaxy bispectrum as the first of the higher-order correlation functions. Finally, we finish off our introduction with a short discussion of the role that primordial non-Gaussianity and galaxy bias play.

1.1. The standard cosmological model

Over the past several decades, a consensus model for describing the evolution of the universe has emerged. Evidence for this model is provided by a variety of observations, made possible due to technological advancements, such as the measurements of the cosmic microwave background (CMB), distance measurements using Type 1a Supernovae (SNe) and the BAO, and large-scale structure surveys.

This standard model for the evolution of the universe predicts that approximately 13.8 billion years ago, the universe was in a hot and dense ‘Big Bang’ state, from which it has continued to expand since. From Type 1a SNe measurements, it has been inferred that the late-time expansion of the universe is accelerating due to an energy component referred to as ‘dark energy’, the physical origin of which has not yet been understood, but described by the cosmological constant, Λ . Approximately 70% of the universe’s energy budget at the present day is comprised of this dark energy. The remaining amount primarily consists of ‘cold dark matter’ (CDM), a collisionless component which makes up about 25% of the universe’s energy content. The small remaining amount is comprised of roughly 4% of the more familiar baryonic matter, which interacts electromagnetically, and a small relativistic radiation component (photons and neutrinos). See Figure 1.1 for an illustration of the energy components of the universe at present day. It is from these dominant energy components that the colloquial name of the standard cosmological model is derived– it is referred to as Λ CDM.

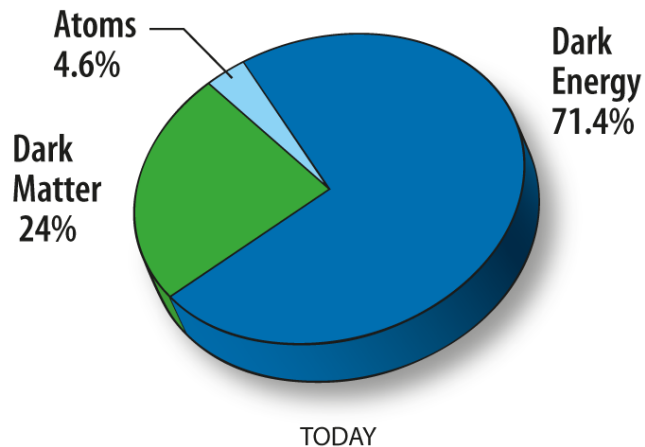


Figure 1.1.: An illustration of the modern-day dominant energy components in the universe, taken from [1].

1. Introduction

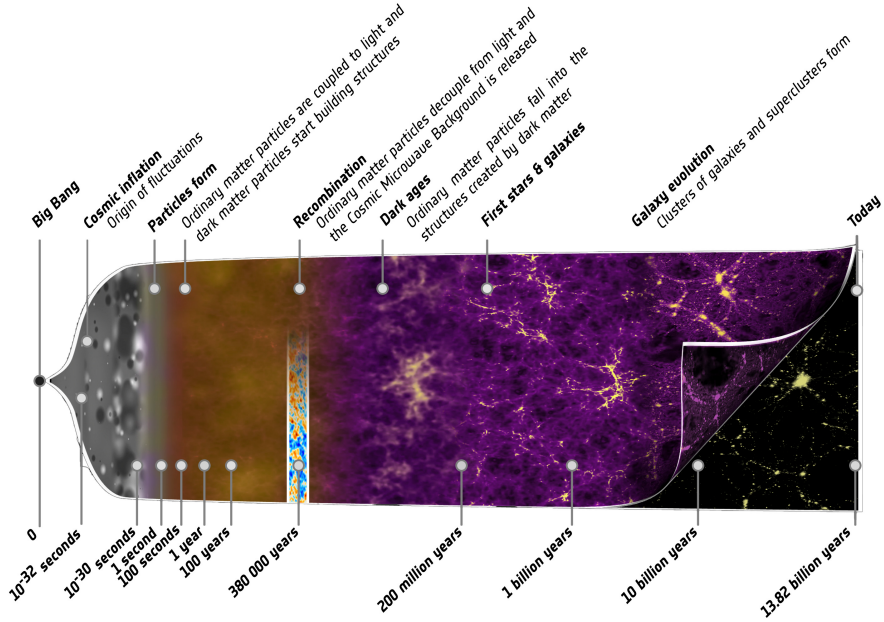


Figure 1.2.: Illustration of the timeline of the universe, starting from the Big Bang (*left side*) and including inflation, matter formation, recombination, and the formation of stars, galaxies, and larger structures observed today (*right side*). Taken from [2].

In the 1980's, the theory of inflation was proposed [3–5], which has since become the prevailing theory for the early universe and its initial conditions. As a theory, it aims to solve the horizon, flatness, homogeneity and isotropy problems. During inflation, the universe is expanding exponentially, rapidly increasing its scale by a factor of at least $\sim 10^{27}$. During this period of exponential expansion, quantum fluctuations are stretched to macroscopic level. These are the seeds of the cosmic structure we observe today. It is worth noting that while the properties of the universe (near homogeneous, isotropic, and spatially flat) as predicted by inflation have been confirmed observationally, but as of yet there is no conclusive observational evidence for the inflationary model itself.

After inflation ends, the universe cools down, and keeps expanding though at a much slower rate than it did before. The thermal evolution of the universe is defined by the ‘competition’ between the interaction rates of the particles and the expansion rate of the universe itself. The baryonic mass of the universe consists of approximately 75% hydrogen ions and 25% helium ions, plus small amounts of deuterium and lithium, all of which are created through Big Bang nucleosynthesis. Electrons and neutrinos are

1. Introduction

also present, and the charged baryonic matter is tightly coupled by electromagnetic interaction. Furthermore, the free electrons are tightly coupled also, to the photons, via Thompson scattering. All of this results in the so-called photon-baryon fluid. The pressure of this fluid prevents the fluctuations from gravitationally collapsing, which leads instead to the generation of acoustic waves. These are known as the Baryon Acoustic Oscillations (BAO), propagating until the protons and baryons decouple. This occurs around the time of ‘recombination’ around 400,000 years after the Big Bang. At recombination, the universe has cooled down sufficiently for neutral hydrogen to form, and the now decoupled photons can free stream from the ‘surface of last scattering’ through the universe. This background radiation, the ‘first light’ of the universe, can be observed today and has a temperature of about 2.7 K – it is known as the Cosmic Microwave Background (CMB), and primordial fluctuation patterns are imprinted on the temperature fluctuations of the CMB.

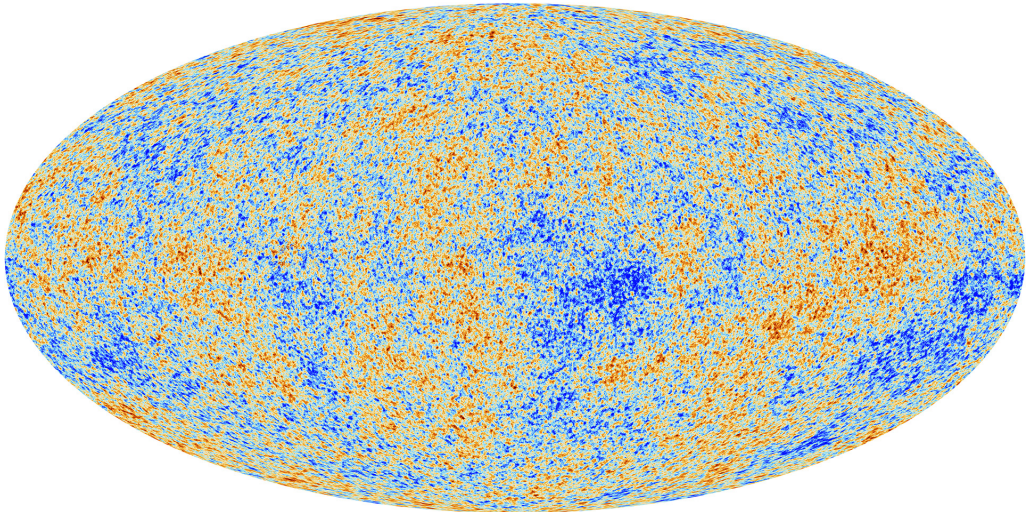


Figure 1.3.: Mollweide projection of the CMB map as observed by the Planck satellite. The colours show tiny (order μK) fluctuations in temperature, which correspond to regions of slightly different density and are the seeds of the structure we observe today. Figure is taken from [6].

Around 50,000 years after the Big Bang, and after a period of radiation domination, the universe becomes dominated by its matter content. This matter dominated era lasts for about 10 billion years. Under matter domination, the primordial density fluctuations grow due to gravitational instability. This gravitational collapse eventually leads to the formation of the cosmic web, which is a non-linear structure formed by haloes, voids, and filaments, dominated by CDM. See Figure 1.4 for a snapshot from simulations of the cosmic web.

1. Introduction

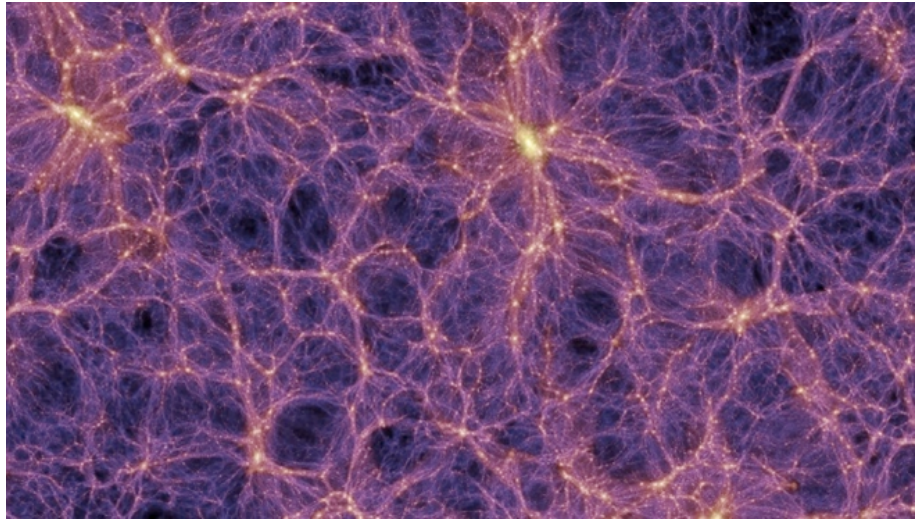


Figure 1.4.: Snapshot of Millennium simulations [7] showing non-linear LSS. There are dense filaments (lighter) surrounded by milder underdensities (darker).

Baryonic matter inside these dark matter haloes cools down, collapses, and goes on to form stars and galaxies. The resulting evolution of structure can be well-described by a linear description of perturbations on large scales (of about 150Mpc), but the small-scale nonlinearities of the fluctuations pose serious theoretical challenges.

In the standard Λ CDM model, the universe is assumed to be spatially flat, and its evolution is described by six parameters— the present-day baryon and cold dark matter densities, the angular size of the sound horizon, the optical depth due to reionisation, the scalar power spectrum index, and the amplitude of the primordial curvature perturbations. The current best constraints on these parameters are given in Table 1.1, taken from [8]. These are the parameters used for forecasts in this thesis. The current tightest constraints on non-linear parameter f_{NL} also come from CMB constraints provided by Planck [9]. For local shapes, $f_{\text{NL}} = -0.9 \pm 5.1$. In our analysis in Chapter 6 of this work, we explore a larger range of possible values outside of the confidence interval as found by the Planck collaboration, to explore the sensitivity of the bispectrum amplitude across a range of values for the non-linear parameter.

Support for the Λ CDM model comes from a variety of observational probes. The anisotropies of the CMB as measured by the WMAP [10] and Planck [8] satellites, and the ground-based telescopes Atacama Cosmology Telescope [11] and South Pole Telescope [12] have all supplied strong constraints on matter and radiation densities, the angular diameter distance to the surface of last scattering, and the shape and the

1. Introduction

Parameter	Value
$\Omega_b h^2$	0.02242 ± 0.00014
$\Omega_c h^2$	0.11933 ± 0.00091
$100\theta_*$	1.04101 ± 0.00029
τ	0.0561 ± 0.0071
n_s	0.9665 ± 0.0038
$\ln(10^{10} A_s)$	3.047 ± 0.014

Table 1.1.: Planck 2018 best-fit parameters in the standard, spatially flat, Λ CDM model [8]. The tabulated parameters are from top to bottom the baryon density ($\Omega_b h^2$), the CDM density ($\Omega_c h^2$), the angular size of the sound horizon ($100\theta_*$), the optical depth due to reionisation (τ), the scalar power spectrum index (n_s), and the amplitude of primordial curvature perturbations ($\ln(10^{10} A_s)$).

amplitude of the primordial power spectrum. The BAO features have been measured successfully by galaxy redshift surveys on scales of about 150 Mpc. This BAO feature is the imprint of the acoustic waves in the baryon-photon fluid onto the clustering of density field tracers. Measurements of the BAO have provided constraints on the expansion rate of the universe across a wide range of different redshifts [13–18]. Furthermore, Type 1a SNe have yielded the first evidence for dark energy [19, 20], as well as complementary constraints on the expansion rate of the universe and the value of the present-day Hubble parameter H_0 [21–24]. Further constraints on the growth of structure are obtained from weak gravitational lensing [25, 26] and RSD analyses of anisotropic clustering measurements [27, 28]. All these observations considered together provide compelling evidence for the Λ CDM model.

1.2. Observing large scale structure

As described previously, the most natural explanation for the formation of the large scale structure of the universe as observed in galaxy surveys is for them to be the result of an amplification of the primordial fluctuations due to gravitational interaction of cold dark matter. Already before the detailed observations of the CMB anisotropies that reveal the imprint of the stretched-out primordial fluctuations, it was known that the galaxies in our universe are not randomly distributed. The first detections of this structure on larger scales was through a variety of galaxy surveys that aimed to observe and map the distribution of galaxies in the local universe. This all started off with Hubble’s first detections of inhomogeneities in the

1. Introduction

early 20th century, at the time incorrectly thought to be ‘spiral nebulae’ [29, 30]. Following this, advancements in cosmology have been primarily held back by lack of sufficient technological progress to carry out precision surveys at large scales, until the publication of larger galaxy catalogues in the 1960’s [31, 32]. Around the same time, theoretical modelling advanced with the realisation that galaxies could be used as biased tracers of the underlying dark matter density field. A series of important papers followed, from systematic analysis of galaxy catalogues [33] to the first cosmological inferences from LSS data [34–41].

Technological advancements, allowing for larger and more precise datasets, made further theoretical progress possible. Interpretations of clustering results gave rise to a new field of study known as galaxy bias, studying the relationship between the galaxies and the underlying dark matter [42–45]—a brief overview of the relevant local model of galaxy bias for the purpose of this thesis is given in Section 1.5. Peculiar velocities of galaxies were found to influence observations of clustering, which lead to several important publications on redshift-space distortions [37, 46, 47]. These in turn were significant for the early redshift surveys [48–50]. The early analyses also provided some of the earliest evidence for the Λ CDM model, by showing that the then-prevailing theory of a flat, matter-dominated universe did not explain the observed clustering data.

Accurate redshift measurements made possible by the rise of new multi-fibre spectrograph technology allowed for redshift-space mapping of hundreds of thousands of objects. Pioneering surveys in this field are the Two-degree Field Galaxy Redshift Survey (2dFGRS) [52] and the Sloan Digital Sky Survey [53]—see Figure 1.5 for an example of the large scale structure as measured by these redshift surveys.

Measurements of the BAO in galaxy clustering surveys can help optimise constraints on the expansion rate and on properties of dark energy. The Baryon Acoustic Oscillation Survey (BOSS) [54] has yielded a dataset with redshift measurements for more than 1.5 million galaxies, with redshifts ranging from $0.2 < z < 0.75$, which has resulted in percent-level constraints on the expansion rate in this redshift range [13]. These constraints are complemented at lower redshift by results from the 6dF Redshift Survey [17] and at higher redshift by the WiggleZ survey [55, 56].

There remains a number of unanswered questions in cosmology and LSS, for example finding out more about the origin of cosmic acceleration, and studying the physics of the early universe, which includes detection of primordial non-Gaussianity. Such a detection could help discriminate between various theories of inflation and other

1. Introduction

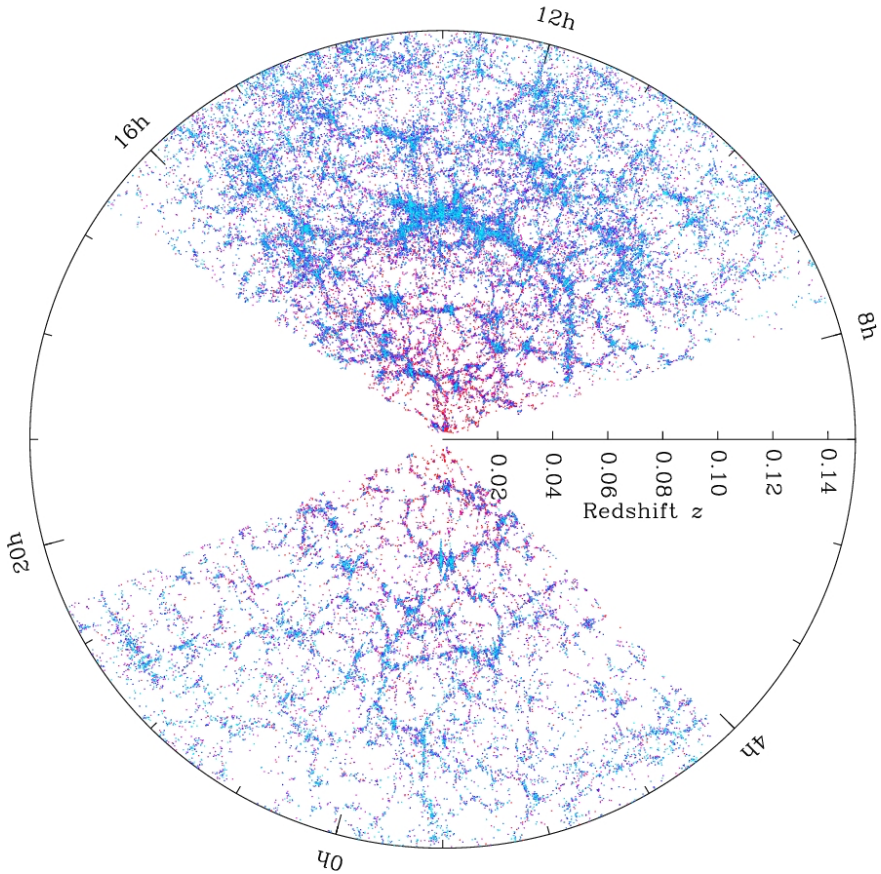


Figure 1.5.: Example sky map of a redshift survey, with the cosmic web at increasing redshift. This figure is adapted from the SDSS Science Results [51].

models of the early universe. The current state-of-the-art surveys are the so-called Stage III surveys, and they include eBOSS [57], the Dark Energy Survey (DES) [58], and the Hobby-Eberly Telescope Dark Energy Experiment (HETDEX) [59]. The next-generation surveys, which will provide us with a wealth of high precision cosmological information, are known as Stage IV surveys. These include e.g. the Dark Energy Spectroscopic Instrument (DESI¹), the Subaru Prime Focus Spectrograph (PFS²), 4MOST³, LSST on the Vera Rubin Telescope⁴, the space-based instruments Nancy Grace Roman Space Telescope⁵ (formerly WFIRST) and Euclid⁶, and 21cm

¹<https://www.desi.lbl.gov>

²<https://pfs.ipmu.jp>

³<https://www.4most.eu/cms/>

⁴<https://www.lsst.org>

⁵<https://roman.gsfc.nasa.gov>

⁶<https://www.euclid-ec.org>

1. Introduction

intensity mapping surveys MeerKAT⁷, the SKA⁸, and HIRAX⁹.

In this thesis, we treat two surveys with specific interest. The first is a Stage IV spectroscopic galaxy survey similar to what will be carried out by the Euclid satellite. Secondly, we consider in more detail the use of intensity mapping of 21cm emission as a tracer of the galaxy distribution in cosmology, such as the SKA, HIRAX, and PUMA (the latter of which is still in proposal stage). These surveys are discussed in more detail in Chapter 3.

1.3. Statistics of galaxy clustering

A goal of theoretical cosmology is to make statistical predictions which depend on the statistical properties of primordial perturbations, which in turn lead to the formation of large scale structures in the universe. In these models, the observable universe is modelled simply as a stochastic realisation of a statistical ensemble of possibilities. The most widely considered models are based on the inflationary paradigm, and the simplest (single-field slow-roll) models generally give rise to adiabatic Gaussian initial fluctuations. In this case, the origin of stochasticity lies in quantum fluctuations that were generated in the early universe.

In a LSS galaxy survey, the fluctuations in the number of galaxies are measured and mapped across the sky. Such a galaxy map can be pixelised in bins in solid angle and redshift. If we observe in some observed direction \mathbf{n} and at some redshift z , we count the number of galaxies in a bin of size dz and solid angle $d\Omega$ centered at this (\mathbf{n}, z) , which gives the observed angular number density of galaxies $N(\mathbf{n}, z)$. The mean angular number density at each redshift, $\bar{N}(z)$, can be obtained by averaging over all observed directions \mathbf{n} . Then, the observed galaxy number count fluctuation is defined simply by,

$$\Delta_g(\mathbf{n}, z) = \frac{N(\mathbf{n}, z) - \bar{N}(z)}{\bar{N}(z)}. \quad (1.1)$$

We will briefly review some of the results that have been obtained from studying the two-point correlation function of the intrinsic galaxy density fluctuation $\delta_g(\mathbf{n}, z)$. A purely Gaussian field would be fully described by the two-point correlation, which is

⁷www.sarao.ac.za/science/meerkat/

⁸www.skatelescope.org/

⁹hirax.ukzn.ac.za/

1. Introduction

the joint ensemble average of the density fluctuation at two different points. However, one of the primary goals of next-generation surveys is to detect primordial non-Gaussianity, and for this to be possible, theoretical accuracy must match experimental precision. This gives rise to the need for analysis of higher-order correlators, which will contain information that is both complementary and additional to what is contained in the power spectrum. The first of these higher-order correlation functions is the three-point function or bispectrum. The bispectrum will be crucial for helping improve constraints in future surveys, and the remainder of this thesis is concerned with improving the theoretical description of the bispectrum of galaxies, as well as exploring the feasibility of detecting such a signal in upcoming surveys.

1.3.1. The two-point function

A purely Gaussian field $\delta(\mathbf{x})$ is fully described by the two-point correlation function or power spectrum. The two-point correlation function is defined as the joint ensemble average of the density at two different points \mathbf{x} and $\mathbf{x} + \mathbf{r}$, i.e.

$$\xi(r) = \langle \delta(\mathbf{x})\delta(\mathbf{x} + \mathbf{r}) \rangle, \quad (1.2)$$

which is dependent on the distance r between the two points only, due to statistical homogeneity and isotropy which are assumed throughout. Usually, the density contrast δ is expressed in terms of its Fourier space components. Since the density contrast is real, this means that we have

$$\delta(\mathbf{k}) = \delta^*(-\mathbf{k}). \quad (1.3)$$

Similarly, the correlators can also be computed in Fourier space, as follows,

$$\langle \delta(\mathbf{k})\delta(\mathbf{k}') \rangle = \int d^3x d^3r \langle \delta(\mathbf{x})\delta(\mathbf{x} + \mathbf{r}) \rangle e^{-i(\mathbf{k}+\mathbf{k}') \cdot \mathbf{x} - i\mathbf{k}' \cdot \mathbf{r}}. \quad (1.4)$$

This can be rewritten using the definition of the two-point correlation function as

$$\langle \delta(\mathbf{k})\delta(\mathbf{k}') \rangle = \int d^3x d^3r \xi(r) e^{-i(\mathbf{k}+\mathbf{k}') \cdot \mathbf{x} - i\mathbf{k}' \cdot \mathbf{r}}, \quad (1.5)$$

and, performing the integrals over x ,

$$\langle \delta(\mathbf{k})\delta(\mathbf{k}') \rangle = (2\pi)^3 \delta^D(\mathbf{k} + \mathbf{k}') \int d^3r \xi(r) e^{i\mathbf{k} \cdot \mathbf{r}} \quad (1.6)$$

1. Introduction

$$\equiv (2\pi)^3 \delta^D(\mathbf{k} + \mathbf{k}') P(k), \quad (1.7)$$

where $P(k)$ is by definition the (density) power spectrum. There are several cosmology codes available for simulating the evolution of linear perturbations in the universe and computing LSS observables—most well known are Class (Cosmic Linear Anisotropy Solving System, [60]) and CAMB (Code for Anisotropies in the Microwave Background, [61]), both of which are used to generate power spectra and other quantities used in numerical results in this thesis. An example of a power spectrum generated with CAMB is given in Figure 1.6.

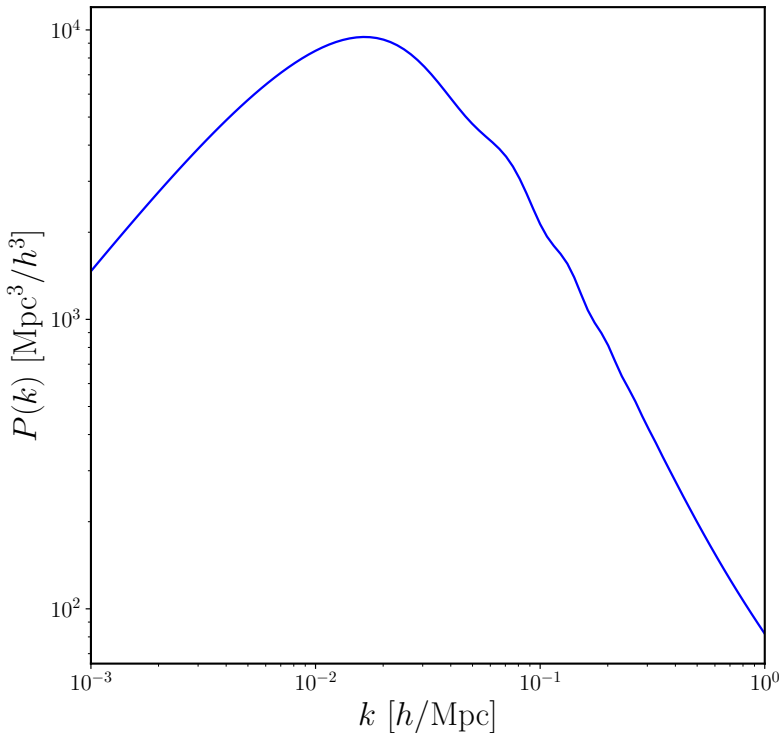


Figure 1.6.: Example of a linear matter power spectrum as generated by CAMB, at redshift $z = 1$.

The galaxy power spectrum has been used extensively to extract cosmological information from large scale surveys. However, the observed distribution of galaxies has several more complex features, such as e.g. non-linearity and baryon feedback. These features are captured to some extent by two-point statistics, but since the field is non-Gaussian, two-point statistics do not fully describe the field statistics. This means that especially when more precise measurements are carried out, such as will be the case for the next generation of surveys, information would be lost. This gives rise to the need for higher-order statistics and their Fourier transforms.

1. Introduction

1.3.2. The three-point function

Construction of higher-order correlators

Higher-order correlation functions are defined as the connected part of the joint ensemble average of the density in an arbitrary number of locations. In principle, it is possible to define any order of correlation function like this, but they will rapidly become more computationally complex and expensive. In the case of a purely Gaussian field, the only non-vanishing connected part is the two-point correlation function. This is a direct consequence of Wick's theorem for Gaussian fields, and has a number of important consequences. Firstly it means that a purely Gaussian, statistically homogeneous and isotropic field is fully described by its power spectrum, and secondly it means that the statistical properties of any field, which is not necessarily linear, can be written in terms of combinations of two-point correlation functions – as long as the field is built from a Gaussian field δ . In a generic form, Wick's theorem can be expressed as

$$\begin{aligned} \langle \delta(\mathbf{k}_1) \dots \delta(\mathbf{k}_{2p+1}) \rangle &= 0 \\ \langle \delta(\mathbf{k}_1) \dots \delta(\mathbf{k}_{2p}) \rangle &= \sum_{[\text{all distinct pairs}]} \prod_{[p \text{ pairs } (i,j)]} \langle \delta(\mathbf{k}_i) \delta(\mathbf{k}_j) \rangle. \end{aligned} \quad (1.8)$$

More concretely, this means that for a purely Gaussian field, $\langle \delta(\mathbf{k}_1) \delta(\mathbf{k}_2) \delta(\mathbf{k}_3) \rangle = 0$. However, this changes in the presence of any sources of non-linearity. An important consequence of non-linear evolution of structure is that the statistics of odd-number density fields are no longer vanishing.

The Fourier-space bispectrum

The leading odd-number statistic which will be non-zero in the case of non-linear evolution is the three-point correlation function, or the bispectrum in Fourier space. The dark matter bispectrum is,

$$\langle \delta(\mathbf{k}_1) \delta(\mathbf{k}_2) \delta(\mathbf{k}_3) \rangle = (2\pi)^3 \delta^D(\mathbf{k}_1 + \mathbf{k}_2 + \mathbf{k}_3) [2F_2(\mathbf{k}_1, \mathbf{k}_2) P(\mathbf{k}_1) P(\mathbf{k}_2) + \text{2 c.p.}] \quad (1.9)$$

where F_2 is the Fourier space density evolution kernel which is defined through,

$$\delta^{(2)}(\mathbf{k}) = \int \frac{d^3 k_1}{(2\pi)^3} \frac{d^3 k_2}{(2\pi)^3} \delta^{(1)}(\mathbf{k}_1) \delta^{(1)}(\mathbf{k}_2) F_2(\mathbf{k}_1, \mathbf{k}_2) (2\pi)^3 \delta^D(\mathbf{k}_1 + \mathbf{k}_2 - \mathbf{k}), \quad (1.10)$$

1. Introduction

determined by the Fourier transform of the equation of motion of the density field [62]. The kernel F_2 is constructed according to a recursion relation (see [63, 64] for derivations) and is given by,

$$F_2(\mathbf{k}_1, \mathbf{k}_2) = 1 + \frac{F}{D^2} + \left(\frac{k_1}{k_2} + \frac{k_2}{k_1} \right) \mathbf{k}_1 \cdot \mathbf{k}_2 + \left(1 - \frac{F}{D^2} \right) (\mathbf{k}_1 \cdot \mathbf{k}_2)^2 , \quad (1.11)$$

where $F \equiv F(a)$ is the second-order growth factor, and the Einstein-de Sitter relation $F/D^2 = 3/7$ is a very good approximation for Λ CDM. Further, P is the linear power spectrum from the previous discussion, and redshift dependence is suppressed for brevity. More generally, we can write,

$$\langle \delta(\mathbf{k}_1)\delta(\mathbf{k}_2)\delta(\mathbf{k}_3) \rangle = (2\pi)^3 \delta^D(\mathbf{k}_1 + \mathbf{k}_2 + \mathbf{k}_3) B_g(\mathbf{k}_1, \mathbf{k}_2, \mathbf{k}_3) , \quad (1.12)$$

where redshift dependence is suppressed once again, and B_g is the galaxy bispectrum, dependent on direction and moduli of the three wavevectors, and roughly proportional to $P(k)^2$ in amplitude.

The bispectrum is a non-Gaussian statistic, and as such is especially sensitive to any forms of non-linearity in the universe. It is an essential probe for e.g. primordial non-Gaussianity in next-generation surveys. There are other sources of non-Gaussianity in the universe, for example gravitational instability on small scales. Primordial non-Gaussianity, which is often parametrised by the non-linear parameter f_{NL} , is predicted by different types of inflation and other theories of the early universe. This means that improvement of constraints on f_{NL} could help discriminate between these theories and help shed light on the very early universe and the seeds of structure formation.

The bispectrum in Fourier space forms a closed triangle correlating three different wavevectors and, unlike the power spectrum, is able to correlate different scales. The matter bispectrum is distinct from the well-studied CMB bispectrum in that it is able to form a three-dimensional map of the universe, whereas the cosmic microwave background provides a two-dimensional snapshot of the first light only. It is therefore essential to try and improve the theoretical description of the matter bispectrum if we are to utilise the wealth of information from next-generation high-precision galaxy surveys in as good and as unbiased a manner as possible.

Similar to how the power spectrum is a measure of probability of finding pairs of galaxies at a given separation from each other, the bispectrum analogously maps this to a probability in a three-dimensional equivalent. That is, it can correspond

1. Introduction

directly to the filamentary structure formed by matter and voids which we know as the cosmic web. The bispectrum has degrees of freedom in both moduli of the wavevectors, i.e. scales of correlation, as well as the shape of the triangle itself. See Figure 1.7 for an example of how a given triangle shape in Fourier space translates to a real-space structure of overdensities and voids.

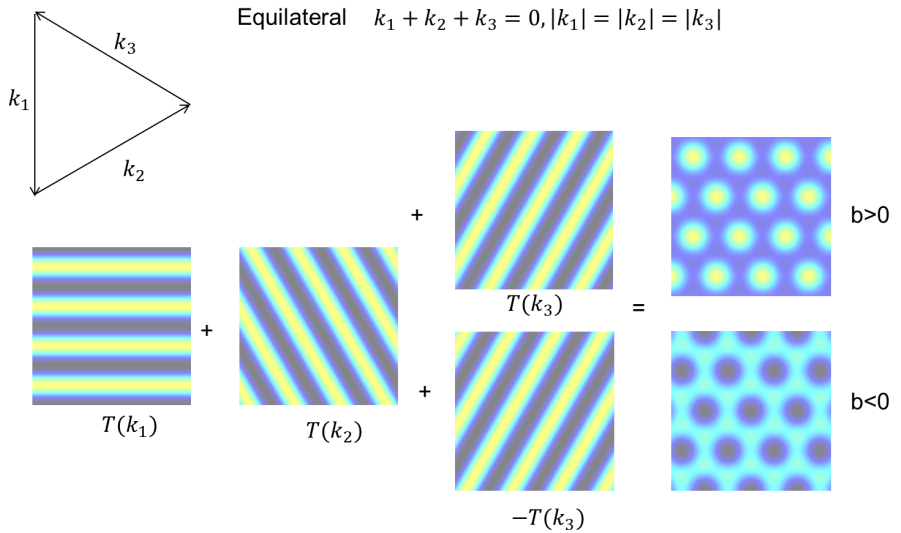


Figure 1.7.: An illustration of a Fourier-space triangle shape and the corresponding real space signature— in this case the equilateral bispectrum. The field (denoted T here) can be decomposed into plane waves, and the three components that form an equilateral triangle can have different signs relative to each other. This gives an overall sign to bispectrum b , to be interpreted as an average probability of which sign is more likely. A positive sign corresponds to the combination of wavevectors being more likely to produce concentrated overdensities surrounded by areas of milder underdensity. For a negative equilateral bispectrum, this is the other way round, and one would expect to see on average more concentrated underdensities surrounded by areas with mild overdensity. Please note that these are slices of 3D figures, which extend into the page— meaning that a positive sign on the bispectrum corresponds to filaments of overdensities surrounded by areas of mild underdensity. Note also that this concerns a statistical quantity only, so while on average one would expect to see more of one type of signature, the observed distribution does not uniformly look like a given real space structure. Figure taken from [65].

1. Introduction

Measurements of the bispectrum

Most measurements of higher-order correlation functions so far are rather noisy and imprecise, and there is a lack of dedicated analysis tools (e.g. theoretical predictions, estimators, likelihood models) for higher-order statistics compared to the analysis toolkit available for two-point statistics. Forecasts for constraints using the galaxy bispectrum usually assume that the main cosmological parameters are known exactly, and determine expected uncertainty on the bias and/or non-Gaussianity parameters [66–71], which recently got extended to theories of modified gravity [72]. Bispectrum measurements of LSS have already been obtained [73–78]. See Figure 1.8 for an example of a measurement of the bispectrum in the BOSS DR12 galaxy sample.

Fisher forecasts using joint galaxy clustering data and CMB data are presented in [79]. Other related work has focussed on developing optimal compression algorithms for three-point statistics [80, 81], and on detecting PNG due to massive spinning particles during the inflationary era [82]. Forecasts combining measurements of the galaxy power spectrum and bispectrum to constrain the standard cosmological parameters was done in [83], which uses the standard Newtonian contributions to the galaxy bispectrum only for signal-to-noise ratio calculations as well as Fisher forecasts. See Figure 1.9 for an example of a forecast for the SNR using the bispectrum.

1.4. Primordial non-Gaussianity

Every model of inflation is characterised by specific predictions for the primordial curvature perturbations. Studies of the bispectrum often involve constraining a single amplitude parameter f_{NL} , the non-Gaussian parameter. In linear theory, the leading, linearly-extrapolated non-Gaussian contribution to the matter bispectrum is,

$$B(k_1, k_2, k_3, z) = \mathcal{M}(k_1, z)\mathcal{M}(k_2, z)\mathcal{M}(k_3, z)B_\varphi(k_1, k_2, k_3), \quad (1.13)$$

where B_φ is the primordial gravitational potential bispectrum predicted by inflationary theories, and \mathcal{M} is a scale-dependent function relating the late-time matter density contrast to the primordial potential, which will be defined later on in Chapter 6.

1. Introduction

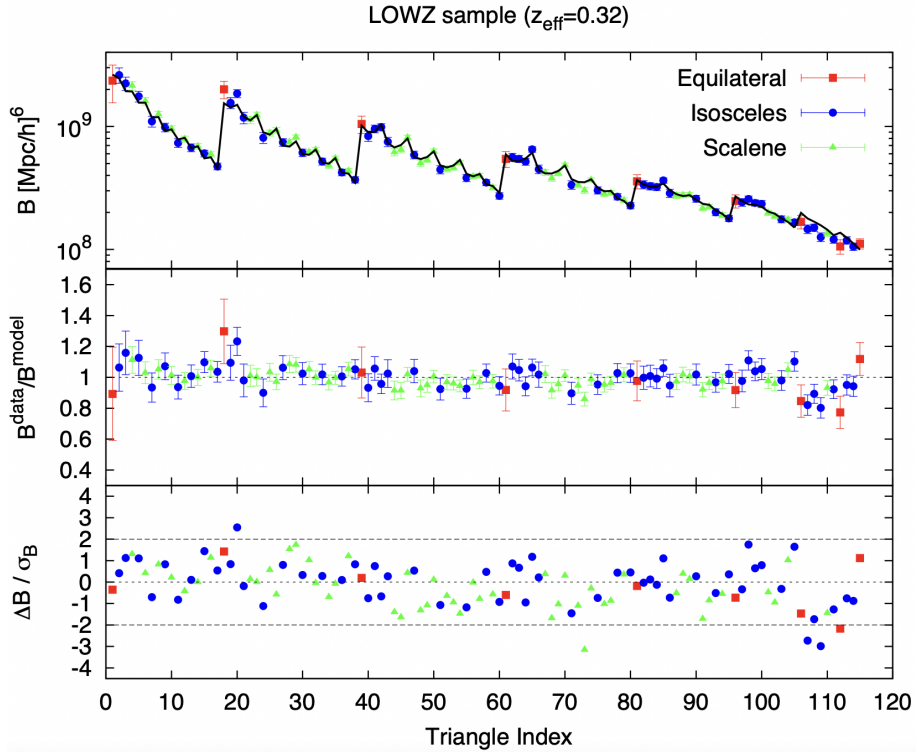


Figure 1.8.: Bispectrum monopole measurements in the LOWZ galaxy sample of BOSS DR12. The sample contains 361,762 galaxies with an effective redshift of $z = 0.32$. The wavevectors of the triangles are contained by $0.03 \text{ } h\text{Mpc}^{-1} \leq k \leq 0.18 \text{ } h\text{Mpc}^{-1}$, in 160 bins. The colours represent different triangle shapes as indicated—equilateral (red), isosceles (blue), and scalene (green) triangles. The black solid line represents the best-fit model, and the middle and bottom panel show the deviation of the model from the data. The binned bispectrum is plotted such that the first value plotted is an equilateral triangle with sides $N_0\Delta k$, where Δk is the bin size used and N_0 is an integer corresponding to the first bin size used—the ‘triangle index’. The plotting then loops sequentially through all possible values of k_1, k_2, k_3 up to a truncation value set by the scale constraints. Taken from [77]—see the reference for a detailed discussion.

Inflationary predictions for both amplitude f_{NL} and the shape of the bispectrum are strongly model-dependent. Note subscript ‘NL’ on the non-Gaussian parameter, to mean ‘non-linear’, since a common phenomenological model for the non-Gaussianity of the initial conditions of the universe can be expressed simply as a non-linear transformation of a Gaussian field. In a more general sense, non-Gaussianity in the universe is associated with non-linearities, such as non-trivial dynamics during inflation or non-linear post-inflationary evolution. There are three types of shapes that are generally studied; these are the three limits, the squeezed shape (with one

1. Introduction

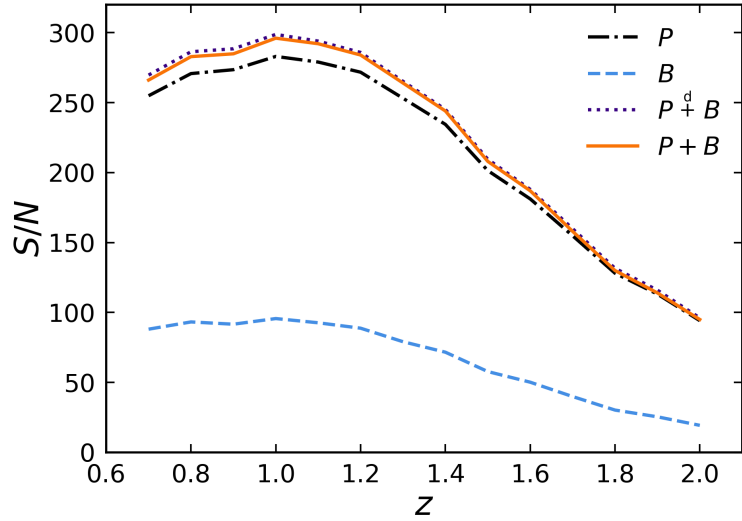


Figure 1.9.: Signal-to-noise ratio for measurements of the galaxy power spectrum and bispectrum in a Euclid-like galaxy survey as a function of redshift z , as computed by [83]. Displayed are the SNR for the power spectrum (dot-dashed), bispectrum (dashed). Solid line is the combined SNR, and the SNR computed by neglecting the cross-covariance between the power spectrum and bispectrum is denoted by a dotted line.

side $k_3 \ll k_1, k_2$), equilateral shapes (where $k_1 = k_2 = k_3$), and the co-linear or flattened shape ($k_1 = k_2 \approx \frac{1}{2}k_3$), see Figure 1.10 for an illustration of the triangle shapes. Often, the bispectrum dependence on the non-Gaussian parameter and the triangle shape is expressed as,

$$B_\varphi \sim f_{\text{NL}} F(k_1, k_2, k_3), \quad (1.14)$$

where $F(k_1, k_2, k_3)$ is the shape function, which encodes the functional dependence of the bispectrum on the specific triangular configuration.

The current tightest constraints on f_{NL} come from CMB constraints provided by Planck [9]. Constraints on f_{NL} using LSS measurements in principle have huge potential for improvement over CMB constraints (at least for specific triangle shapes). This is because LSS provides us with a 3D map, covering a large volume and range of scales, giving access to a much larger amount of modes than the 2D CMB maps. In this section we will briefly discuss PNG of the local type, which is the most-studied primordial model, and the one that is relevant to the work presented in this thesis. We follow discussions in [84, 85].

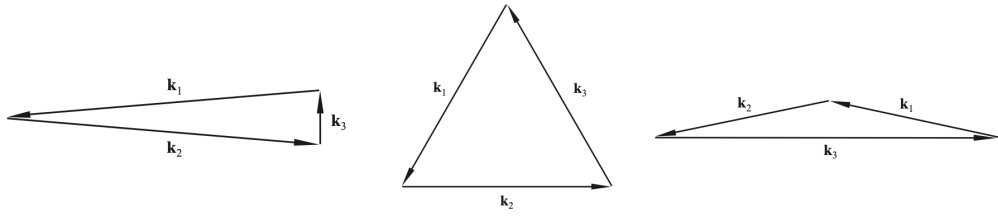


Figure 1.10.: The three triangular configurations generally discussed in literature on the bispectrum and primordial non-Gaussianity. *Left*: squeezed shapes, where one side $k_3 \ll k_1, k_2$, *middle*: equilateral shapes, where $k_1 = k_2 = k_3$, and *right*: co-linear shapes, where $k_1 = k_2 \approx k_3/2$. Figure taken from [84].

There exists a wide range of inflationary models in which the non-Gaussianity is produced by local interactions. In the local model, the contributions from the squeezed triangles are dominant. This model is well-motivated physically, since it encompasses superhorizon effects during inflation, when a large-scale mode (k_3 , shortest wavevector corresponding to largest scale), which has exited the Hubble radius, exerts a non-linear influence on smaller scale modes k_1 and k_2 . This effect is small in single-field slow-roll models, but can be much larger in multi-field models of inflation [84]. The squeezed/local bispectrum shapes are defined as,

$$B_\varphi^{\text{loc}}(k_1, k_2, k_3) = 2f_{\text{NL}}^{\text{loc}} [P_\varphi(k_1)P_\varphi(k_2) + 2 \text{ c.p.}] . \quad (1.15)$$

Single-field slow-roll inflation is dominated by the local type. Large local-type PNG can also be produced in multi-field scenarios.

1.5. Galaxy bias

Galaxy bias is the statistical relation between the observed distribution of galaxies and the underlying matter distribution. On scales where the cosmic density fields are quasi-linear, the clustering of galaxies can be described by a perturbative bias expansion. In this formalism, the complicated physics concerning formation of galaxies can be absorbed by a finite set of expansion coefficients known as the bias parameters. In this section we will briefly review the origin of the field and set out the relevant bias models for this thesis. We will refrain from giving full expressions for bias models and parameters, as they are more technical than appropriate at an introductory stage, and they will be introduced in full in the relevant chapters. For

1. Introduction

the majority of this thesis, that is, up to Chapter 5, we use a simple local Gaussian model of galaxy bias. Primordial non-Gaussianity, which we include in Chapter 6, introduces a scale-dependence in galaxy bias and hence requires separate treatment. It is worth noting that we consider only PNG of the local type. For a full review of galaxy bias, see [86].

All sorts of galaxy surveys and the resulting statistical studies of the distribution of galaxies critically rely on a robust description of the relation between the galaxies and the underlying dark matter. Of course galaxies are not the only tracers of this dark matter distribution, but the term galaxy bias is often used as a convenient term to encompass the biasing of all such tracers. Other examples include, but are not limited to, halo bias, the Lyman- α forest, and HI intensity mapping— the latter of which is considered in this thesis along with the more traditional spectroscopic galaxy surveys.

Roughly speaking, LSS can be divided into two regimes, small non-linear scales, which cannot be described with perturbation theory, and large quasi-linear scales (of approximately $k \geq 0.1 h\text{Mpc}^{-1}$), which can adequately be described by perturbation theory, provided if it is carried out to sufficiently high order. Here we will consider only quasi-linear scales, so that perturbation theory will not break down. On these scales, the complex process of galaxy formation, which is itself far from being understood in detail, can at each order in perturbations and at fixed time, be absorbed into a finite set of parameters called the bias parameters. This is a remarkable result, and relies on the fact that on large scales the formation of structure is almost entirely determined by gravity.

1.5.1. Local model of galaxy bias

The simplest example of a local model of galaxy bias is the local-in-mass-density (LIMD) model of galaxy bias. In this model, we assume that dark matter haloes form on top of regions of overdensity (i.e. regions above some threshold density δ_{cr}). These regions collapse to form haloes, in which galaxies are formed. See Figure 1.11 for an illustration.

A generic bias expansion in this simplest case can then be understood as just the coefficients of the expansion operators $O(\mathbf{x}, \eta)$ in an expansion of the galaxy number

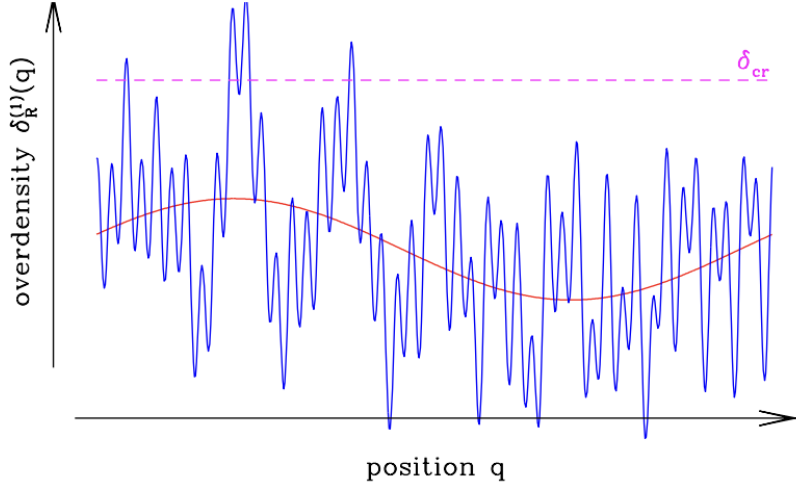


Figure 1.11.: Illustration of the LIMD model of galaxy bias. The red line indicates a long wavelength perturbation, and the blue line denotes the density field δ_R . The dashed horizontal magenta line shows the critical density δ_{cr} . Regions of overdensity δ_R that get pushed above this critical density threshold collapse to form haloes in which galaxies are formed.

density,

$$\delta_g(\mathbf{x}, \eta) = \sum_O b_O(\eta) O(\mathbf{x}, \eta). \quad (1.16)$$

In the simplest LIMD model of galaxy bias, we expand in density only, leading to,

$$\delta_g(\mathbf{x}) = b_1 \delta + \frac{b_2}{2} \delta^2 + \dots \quad (1.17)$$

A general perturbative bias expansion however would contain all operators that are relevant at a given order in perturbation theory. For our purpose, we must make sure that the general definition of galaxy bias is gauge-independent and consistent on very large scales. The LIMD model of galaxy bias itself does not include tidal bias. Gravitational evolution generates a term which quadratic in the tidal tensor K_{ij} [87]. This term is present in the Eulerian (local) density field, even if it is absent in the Lagrangian space (the initial conditions). As a result, the tidal operator is part of the leading order gravitational observables of long-wavelength spacetime perturbations [86]. Hence, we need to include it in our local model of galaxy bias, as a term of the form,

$$b_{\text{tidal}} [K_{ij}]^2, \quad (1.18)$$

1. Introduction

with a tidal bias coefficient b_{tidal} and tidal operator K_{ij} .

1.5.2. Scale-dependent bias in the presence of PNG

Scale-dependent bias in literature can refer to any non-trivial (i.e. k -dependent) Fourier-space relation between galaxy overdensity and the underlying dark matter density. Primordial non-Gaussianity generates such a leading non-local term in the bias relation. In this thesis we only consider PNG of the local type. This is defined as a simple form of non-linearity in the primordial curvature perturbation, which is local in configuration space. Usually, these perturbations are expressed in terms of the Bardeen potential φ . This in turn is directly related to the curvature perturbation in comoving gauge. At first order, the galaxy number density contrast bias relation can be expressed as,

$$\delta_{gC} = b_{10}\delta_C + b_{01}\varphi_p , \quad (1.19)$$

where φ_p is the linear primordial potential (which is related to the late-time matter density contrast via the Poisson equation), and subscript C denotes the comoving gauge. The bias coefficients b_{10} and b_{01} are the Gaussian and non-Gaussian bias coefficients respectively, where $b_{10} \equiv b_1$ from the previous section on the local model of galaxy bias, and b_{01} is the non-Gaussian coefficient, which is proportional to f_{NL} ,

$$b_{01} \propto f_{\text{NL}} \frac{\mathcal{H}^2}{k^2} . \quad (1.20)$$

Note how the scale dependence of the non-Gaussian bias is at the same order as the relativistic corrections to the power spectrum of a single tracer (Equation 2.5 in Chapter 2). The leading-order scale dependence of the bispectrum is less suppressed—see Chapter 2.

At second order, the bias relation gets more complex, and is given in Chapter 6.

1.6. Thesis outline

So far, we have introduced the standard cosmological model ΛCDM , as well as the primary statistical tools used to study the LSS of the universe—the power spectrum and bispectrum. Detecting primordial non-Gaussianity is a key goal of the next-generation LSS surveys. When observing LSS, there is a variety of relativistic effects

1. Introduction

that come into play once the number-count fluctuation is projected onto our past lightcone. These are for example the well-studied Kaiser redshift space distortions— the apparent ‘squashing’ and distortion of the spatial distribution of galaxies when their positions are considered as a function of redshift rather than a function of distance. Other examples are e.g. distortions due to lensing convergence, Doppler, Sachs-Wolfe, Integrated Sachs-Wolfe, and time delay effects. Contributing to the bispectrum also are couplings between these effects, which appear once one goes up to non-linear order in perturbation theory.

The relativistic effects have a scale dependence starting at $\mathcal{O}(\mathcal{H}/k)$. On large scales, this means that the relativistic effects can mimic the scale dependence of PNG, which starts at $\mathcal{O}(\mathcal{H}^2/k^2)$. To avoid biasing future measurements of PNG, accurate theoretical modelling of relativistic effects is crucial. This motivates the work presented in this thesis— an extension to the theoretical description of the bispectrum including relativistic corrections.

The rest of this thesis is organised as follows. In Chapter 2, we introduce the lowest order (i.e. least suppressed) relativistic corrections to the bispectrum and consider how they affect the amplitude of the bispectrum. These leading-order relativistic corrections give rise to a local dipole with respect to the observer’s line-of-sight, which is absent in the purely Newtonian picture. The amplitude of this dipole, which if detected would be a smoking-gun signal for relativistic corrections, is even on equality scales about 10% of that of the monopole (at redshift $z = 1$). This implies that the dipole of the bispectrum is a unique signature of GR on cosmological scales. In Chapter 3, we make an estimate for the detectability of such a relativistic signal in next-generation spectroscopic and intensity mapping surveys. For a Stage IV spectroscopic survey similar to *Euclid*, we find that the signal-to-noise ratio for these leading order effects is ~ 17 , while the 21cm intensity mapping surveys suffer from foreground and beam effects— we forecast a marginally detectable SNR of ~ 6 for SKA1 and ~ 5 for HIRAX. Then, Chapter 4 summarises past work on adding local relativistic corrections at all orders of \mathcal{H}/k to the bispectrum, and a fully analytic multipole expansion with relevant numerical analyses for future surveys is presented in Chapter 5. The relativistic bispectrum generates non-zero multipoles for both even and odd multipole number ℓ , where the odd multipoles are induced by relativistic effects only. Finally, we expand the theoretical description of the Fourier-space galaxy bispectrum by adding local primordial non-Gaussianity in Chapter 6. This allows for better separation of the relativistic signature and biasing due to the presence of PNG— we find that the bias from using a Newtonian analysis of the

1. Introduction

squeezed bispectrum could be as large as $\Delta f_{\text{NL}} \sim 5$ for a Stage IV H α survey.

2. The dipole of the galaxy bispectrum

When carrying out large scale galaxy surveys, there is a variety of effects which distort the observed galaxy number counts, and for studies of galaxy clustering it is crucial for this to be accounted for properly. These effects arise from the fact that we observe on the past lightcone— the galaxies’ redshifts and the directions of the incoming photons all are distorted by inhomogeneities in our universe. In this chapter we examine the leading relativistic contributions in the galaxy bispectrum, which arise predominantly from RSD and other Doppler-type observational effects. These give rise to corrections at $\mathcal{O}(\mathcal{H}/k)$ in the galaxy bispectrum. Higher order \mathcal{H}/k contributions are, while being subdominant, still present in the galaxy bispectrum; and a full treatment of the bispectrum at all orders in $\mathcal{O}(\mathcal{H}/k)$ can be found from Chapter 4 onwards. The content from this Chapter is taken from [88]. It is structured as follows. First, the leading-order relativistic effects are introduced, after which the analytic extraction of the dipole of the bispectrum is presented. A numerical analysis of the dipole for Stage IV surveys is presented, before summarising our findings in the conclusions.

2.1. The dipole of the power spectrum

The dominant RSD effect on galaxy number counts at first order is given by,

$$\delta_g(z, \mathbf{k}) = (b_1(z) + f(z)\mu^2)\delta(z, \mathbf{k}), \quad (2.1)$$

where $\mu = \mathbf{n} \cdot \hat{\mathbf{k}}$, with \mathbf{n} the line-of-sight direction, f the growth rate, and b_1 is the linear bias. Henceforth the redshift dependence will be dropped for brevity as we are working at fixed redshift. At leading order, there is a Doppler type correction to

2. The dipole of the galaxy bispectrum

this effect [46, 89, 90] (see also [91–93]) proportional to $\mathbf{v} \cdot \mathbf{n}$, where \mathbf{v} is the peculiar velocity:¹

$$\delta_g(\mathbf{x}) = b_1 \delta(\mathbf{x}) - \frac{1}{\mathcal{H}} \partial_r (\mathbf{v} \cdot \mathbf{n}) + A \mathbf{v} \cdot \mathbf{n} \rightarrow \quad (2.2)$$

$$\delta_g(\mathbf{k}) = \left(b_1 + f\mu^2 + iA f\mu \frac{\mathcal{H}}{k} \right) \delta(\mathbf{k}), \quad (2.3)$$

where

$$A = b_e + 3\Omega_m/2 - 3 + (2 - 5s)(1 - 1/r\mathcal{H}). \quad (2.4)$$

Here $b_e = \partial(a^3 \bar{n}_g)/\partial \ln a$ is the evolution of comoving galaxy number density, $s = -(2/5)\partial \ln \bar{n}_g/\partial \ln L$ is the magnification bias (L is at the threshold luminosity), r is the comoving radial distance ($\partial_r = \mathbf{n} \cdot \nabla$) and we have assumed a Λ CDM background ($\mathcal{H}'/\mathcal{H}^2 = 1 - 3\Omega_m/2$, where \mathcal{H} is the conformal Hubble rate, a prime is differentiation with respect to conformal time, Ω_m is the evolving matter density parameter). In the Fourier space expression (2.3) we can read off the relative contribution of each term by how they scale with k : terms like \mathcal{H}/k are suppressed on small scales when $\mathcal{H}/k \ll 1$ but become important around and above the equality scale.

Although the galaxy density contrast (2.3) is complex, the power spectrum of a single tracer is real:

$$\langle \delta_g(\mathbf{k}) \delta_g(-\mathbf{k}) \rangle = \left[(b_1 + f\mu^2)^2 + \left(A f\mu \frac{\mathcal{H}}{k} \right)^2 \right] \langle \delta(\mathbf{k}) \delta(-\mathbf{k}) \rangle, \quad (2.5)$$

since $\mu_{-\mathbf{k}} = -\mu_{\mathbf{k}}$ enforces a cancellation of the imaginary part, and the RSD contribution is separate from the Doppler term. However, if we consider the cross-power spectrum for *two* matter tracers, this cancellation breaks down, and there is an imaginary part in the cross-power [89, 94],

$$\begin{aligned} P_{g\tilde{g}}(k) = & \left\{ \left[(b_1 + f\mu^2)(\tilde{b}_1 + f\mu^2) + A\tilde{A}f^2\mu^2 \frac{\mathcal{H}^2}{k^2} \right] \right. \\ & \left. + i f\mu \left[(\tilde{b}_1 + f\mu^2)A - (b_1 + f\mu^2)\tilde{A} \right] \frac{\mathcal{H}}{k} \right\} P(k). \end{aligned} \quad (2.6)$$

While the Doppler contribution to P_g is $\mathcal{O}((\mathcal{H}/k)^2)$, the Doppler contribution to $P_{g\tilde{g}}$ mixes with the density and RSD to give an additional less suppressed part, i.e. $\mathcal{O}(\mathcal{H}/k)$. The nonzero multipoles of P_g are $\ell = 0, 2, 4$, whereas $P_{g\tilde{g}}$ has a nonzero dipole (as well as a smaller octupole). There are also further relativistic corrections to this dipole part of the cross power spectrum [95].

¹[90] provides the relativistic correction to the coefficient of $\mathbf{v} \cdot \mathbf{n}$ given in [46, 89].

2.2. Leading order relativistic contributions to the bispectrum

A natural question is: what about the galaxy bispectrum? In the standard ‘Newtonian’ approximation, with only RSD, the galaxy bispectrum for a single tracer at fixed redshift has no dipole, and only has even multipoles [96, 97]. But with a lightcone corrected galaxy density contrast, the 3-point correlator, even for a *single* tracer, will no longer be an even function of $\mathbf{k}_a \cdot \mathbf{n}$ ($a = 1, 2, 3$). In order to compute the consequent contribution to the galaxy bispectrum, (2.2) is not sufficient: we need its second-order generalisation, $\delta_g \rightarrow \delta_g + \delta_g^{(2)}/2$.

At second order, the Doppler correction in (2.2) generalises to $A \mathbf{v}^{(2)} \cdot \mathbf{n}$, but there are also quadratic coupling terms. The couplings involve not only the Doppler effect, but also radial gradients of the potential (‘gravitational redshift’), volume distortion effects, and second-order corrections to the density contrast. Most of these contributions are small, but those that scale as $(\mathcal{H}/k)\delta^2$ are not, even on equality scales. Except on super-equality scales we can often neglect any terms $\mathcal{O}((\mathcal{H}/k)^2)$ and higher, which makes the calculation considerably simpler. The treatment of higher-order terms is left to chapter 5.

The leading correction can be extracted from the general expressions that include all relativistic corrections to the Newtonian approximation, as given in [98] (see also [95, 99–102]),

$$\begin{aligned} \delta_{gD}^{(2)} &= A \mathbf{v}^{(2)} \cdot \mathbf{n} + 2C(\mathbf{v} \cdot \mathbf{n})\delta + 2\frac{E}{\mathcal{H}}(\mathbf{v} \cdot \mathbf{n})\partial_r(\mathbf{v} \cdot \mathbf{n}) \\ &\quad + 2\frac{b_1}{\mathcal{H}}\phi\partial_r\delta + \frac{2}{\mathcal{H}^2}[\mathbf{v} \cdot \mathbf{n}\partial_r^2\phi - \phi\partial_r^2(\mathbf{v} \cdot \mathbf{n})] - \frac{2}{\mathcal{H}}\partial_r(\mathbf{v} \cdot \mathbf{v}), \end{aligned} \quad (2.7)$$

where ϕ is the gravitational potential, and the coefficients C and E are,

$$C = b_1(A + f) + b'_1/\mathcal{H} + 2(1 - 1/r\mathcal{H})\partial b_1/\partial \ln L, \quad (2.8)$$

and

$$E = 4 - 2A - \frac{3}{2}\Omega_m. \quad (2.9)$$

This is in agreement with the independent re-derivation of the leading correction given in [95]. We have corrected a typo in the last bracket of line 1 of Eq. (2.15): $-f_{\text{evo}} \rightarrow -2f_{\text{evo}} \equiv -2b_e$. Note that our \mathbf{n} is minus theirs, and they use the convention $\delta_g + \delta_g^{(2)}$. All but one of the contributions to this leading term contain Doppler

2. The dipole of the galaxy bispectrum

contributions, so we label these terms with a D subscript. In this sense, they can be thought of as the relativistic correction to redshift space distortions, but their origin is considerably more subtle than in the Newtonian picture [95, 99]. These relativistic corrections all arise as projections along the line-of-sight \mathbf{n} . It is this projection that is responsible for the dipole in the observed bispectrum. Beyond these leading terms in (2.7) there are a host of local coupled terms which appear on larger scales.

We follow most work on the Fourier bispectrum and neglect the effect of lensing magnification. This is reasonable for correlations at the same redshift and when using very thin redshift bins allowed by spectroscopic surveys [103]. We also use the standard plane-parallel approximation, which is reasonable at high redshift. However, we note that wide-angle effects in the power spectrum can be of the same order of magnitude as the Doppler-type effects in certain circumstances [104], and these should be incorporated in a more complete treatment.

The galaxy bispectrum is defined in Fourier space by,

$$B_g(\mathbf{k}_1, \mathbf{k}_2, \mathbf{k}_3) = \mathcal{K}(\mathbf{k}_1)\mathcal{K}(\mathbf{k}_2)\mathcal{K}^{(2)}(\mathbf{k}_1, \mathbf{k}_2, \mathbf{k}_3)P(k_1)P(k_2) + 2 \text{ cyclic permutations}. \quad (2.10)$$

The first-order kernel $\mathcal{K} = \mathcal{K}_{\text{N}} + \mathcal{K}_{\text{D}}$ is given by the term in brackets in (2.3). At second order, $\mathcal{K}^{(2)} = \mathcal{K}_{\text{N}}^{(2)} + \mathcal{K}_{\text{D}}^{(2)}$, where the Newtonian kernel is [105]

$$\mathcal{K}_{\text{N}}^{(2)}(\mathbf{k}_1, \mathbf{k}_2, \mathbf{k}_3) = b_2 + b_1 F_2(\mathbf{k}_1, \mathbf{k}_2) + b_s S_2(\mathbf{k}_1, \mathbf{k}_2) + f \mu_3^2 G_2(\mathbf{k}_1, \mathbf{k}_2) + \mathcal{Z}_2(\mathbf{k}_1, \mathbf{k}_2). \quad (2.11)$$

Here $F_2(\mathbf{k}_1, \mathbf{k}_2)$ is the standard Newtonian mode-coupling kernel for ΛCDM [106],

$$F_2(a, \mathbf{k}_1, \mathbf{k}_2) = 1 + \frac{F(a)}{D(a)^2} + \left(\frac{k_1}{k_2} + \frac{k_2}{k_1} \right) \hat{\mathbf{k}}_1 \cdot \hat{\mathbf{k}}_2 + \left[1 - \frac{F(a)}{D(a)^2} \right] \left(\hat{\mathbf{k}}_1 \cdot \hat{\mathbf{k}}_2 \right)^2, \quad (2.12)$$

where F is the second-order growth factor. For ΛCDM , the Einstein-De Sitter relation $F/D^2 = 3/7$ is a very good approximation. Using this approximation, F_2 is essentially time-independent. $G_2(\mathbf{k}_1, \mathbf{k}_2)$ is the second-order velocity kernel,

$$G_2(a, \mathbf{k}_1, \mathbf{k}_2) = \frac{F'(a)}{D(a)D'(a)} + \left(\frac{k_1}{k_2} + \frac{k_2}{k_1} \right) \hat{\mathbf{k}}_1 \cdot \hat{\mathbf{k}}_2 + \left(2 - \frac{F'(a)}{D(a)D'(a)} \right) \left(\hat{\mathbf{k}}_1 \cdot \hat{\mathbf{k}}_2 \right)^2, \quad (2.13)$$

where, since we use the Einstein-De Sitter approximation $F/D^2 = 3/7$ in F_2 , we

2. The dipole of the galaxy bispectrum

have $F'/(DD') = 6/7$ in G_2 . We use a local bias model [86], which includes tidal bias kernel

$$S_2(\mathbf{k}_1, \mathbf{k}_2) = (\hat{\mathbf{k}}_1 \cdot \hat{\mathbf{k}}_2)^2 - \frac{1}{3}, \quad (2.14)$$

with tidal bias b_s . Finally, the kernel $\mathcal{Z}_2(\mathbf{k}_1, \mathbf{k}_2)$ incorporates the non-linear Kaiser RSD contribution [96, 105],

$$\mathcal{Z}_2(\mathbf{k}_1, \mathbf{k}_2) = b_1 f(\mu_1 k_1 + \mu_2 k_2) \left(\frac{\mu_1}{k_1} + \frac{\mu_2}{k_2} \right) + f^2 \frac{\mu_1 \mu_2}{k_1 k_2} (\mu_1 k_1 + \mu_2 k_2)^2. \quad (2.15)$$

The Doppler correction to (2.11) in Fourier space follows from (2.7) [107],

$$\begin{aligned} \mathcal{K}_{\text{D}}^{(2)}(\mathbf{k}_1, \mathbf{k}_2, \mathbf{k}_3) = & i \mathcal{H} \left[-\frac{3}{2} \left(\mu_1 \frac{k_1}{k_2^2} + \mu_2 \frac{k_2}{k_1^2} \right) \Omega_m b_1 + 2\mu_{12} \left(\frac{\mu_1}{k_2} + \frac{\mu_2}{k_1} \right) f^2 \right. \\ & \left(\frac{\mu_1}{k_1} + \frac{\mu_2}{k_2} \right) Cf - \frac{3}{2} \left(\mu_1^3 \frac{k_1}{k_2^2} + \mu_2^3 \frac{k_2}{k_1^2} \right) \Omega_m f \\ & \left. + \mu_1 \mu_2 \left(\frac{\mu_1}{k_2} + \frac{\mu_2}{k_1} \right) \left(\frac{3}{2} \Omega_m - Ef \right) f + \frac{\mu_3}{k_3} G_2(\mathbf{k}_1, \mathbf{k}_2, \mathbf{k}_3) Af \right], \end{aligned} \quad (2.16)$$

where $\mu_{ab} = \hat{\mathbf{k}}_a \cdot \hat{\mathbf{k}}_b$ and $\mu_a = \hat{\mathbf{k}}_a \cdot \mathbf{n}$. The Newtonian kernel (2.11) scales as $(\mathcal{H}/k)^0$, while the Doppler kernel (2.16) scales as (\mathcal{H}/k) . Using (2.11) and (2.16) in (2.10), and dropping terms that scale as $(\mathcal{H}/k)^2$ and $(\mathcal{H}/k)^3$, we find that,

$$\begin{aligned} B_{gN}(\mathbf{k}_1, \mathbf{k}_2, \mathbf{k}_3) = & \mathcal{K}_N(\mathbf{k}_1) \mathcal{K}_N(\mathbf{k}_2) \mathcal{K}_N^{(2)}(\mathbf{k}_1, \mathbf{k}_2, \mathbf{k}_3) P(k_1) P(k_2) \\ & + 2 \text{ cyclic permutations}, \end{aligned} \quad (2.17)$$

$$\begin{aligned} B_{gD}(\mathbf{k}_1, \mathbf{k}_2, \mathbf{k}_3) = & \left\{ \mathcal{K}_N(\mathbf{k}_1) \mathcal{K}_N(\mathbf{k}_2) \mathcal{K}_D^{(2)}(\mathbf{k}_1, \mathbf{k}_2, \mathbf{k}_3) \right. \\ & \left. + [\mathcal{K}_N(\mathbf{k}_1) \mathcal{K}_D(\mathbf{k}_2) + \mathcal{K}_D(\mathbf{k}_1) \mathcal{K}_N(\mathbf{k}_2)] \mathcal{K}_N^{(2)}(\mathbf{k}_1, \mathbf{k}_2, \mathbf{k}_3) \right\} P(k_1) P(k_2) \\ & + 2 \text{ cyclic permutations}. \end{aligned} \quad (2.18)$$

Since (2.16) scales as \mathcal{H}/k it is purely imaginary, as all these contributions have at least one \mathbf{k} projected along the line-of-sight – i.e., they contain odd powers of μ_a 's. This means that *the leading relativistic correction in the observed galaxy Fourier bispectrum of a single tracer is a purely imaginary addition to the Newtonian approximation*. On larger scales, terms $\mathcal{O}((\mathcal{H}/k)^2)$ and higher appear in both the real and imaginary parts, with the kernels given in [102, 107–109]. We include the higher-order terms in our plots below, and a full treatment can be found in Chapter 5.

2.3. Extracting the dipole

The bispectrum can be considered as a function of $k_1, k_2, k_3, \mu_1, \mu_2, \mu_3$ and φ , which is the azimuthal angle giving the orientation of the triangle relative to \mathbf{n} . In order to extract the dipole it is easiest to write $\mu_3 = -(k_1\mu_1 + k_2\mu_2)/k_3$, so that we can write $B_g = \sum_{i,j} \mathcal{B}_{ij} (i\mu_1)^i (i\mu_2)^j$, where $i, j = 0 \dots 6$ which factors out the angular dependence multiplying real coefficients \mathcal{B}_{ij} with no angular dependence. Then, use the identity $\mu_2 = \mu_1 \cos \theta + \sqrt{1 - \mu_1^2} \sin \theta \cos \varphi$, where $\theta = \theta_{12}$ (and we define $\mu = \cos \theta$ – note that θ is the angle outside the triangle as the \mathbf{k}_a 's are head-to-tail). We use standard orthonormal spherical harmonics with the triangle lying in the $y-z$ plane, with \mathbf{k}_1 aligned along the z -axis [97], see Figure 2.1 for a schematic overview of the relevant angles and vectors of our decomposition. Then we have $Y_{\ell m}(\mu_1, \varphi)$,

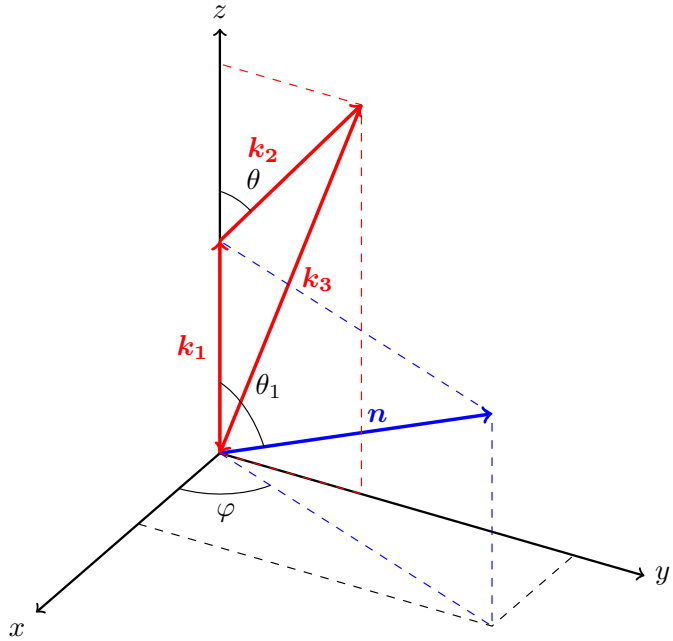


Figure 2.1.: Overview of the relevant vectors and angles for the Fourier-space bispectrum.

so that we can write $B_g = \sum_{\ell m} B_{\ell m} Y_{\ell m}(\mu_1, \varphi)$. The leading relativistic terms we consider here generate odd-power multipoles up to $\ell = 7$, and the full expression generates even and odd multipoles up to $\ell = 8$ – see Chapter 5. Different powers of

2. The dipole of the galaxy bispectrum

$(i\mu_1)$ and $(i\mu_2)$ contribute to the dipole as follows,

$$\int d\Omega (i\mu_1)^a (i\mu_2)^b Y_{1m}^* = \delta_{m,0} \frac{i\sqrt{3\pi}}{15} \begin{bmatrix} 0 & 10\mu & 0 & -6\mu \\ 10 & 0 & -4\mu^2 - 2 & 0 \\ 0 & -6\mu & 0 & \frac{12\mu^3 + 18\mu}{7} \\ -6 & 0 & \frac{24\mu^2 + 6}{7} & 0 \\ \vdots & & & \ddots \end{bmatrix} + \delta_{m,\pm 1} \frac{\sqrt{6\pi}}{15} \begin{bmatrix} 0 & -5 & 0 & 3 \\ 0 & 0 & 2\mu & 0 \\ 0 & 1 & 0 & -\frac{6\mu^2 + 3}{7} \\ 0 & 0 & -\frac{6}{7}\mu & 0 \\ \vdots & & & \ddots \end{bmatrix} \sin \theta, \quad (2.19)$$

where each matrix element corresponds to a particular combination of a, b , where the matrix indices run over the values $a = 0 \dots 6, b = 0 \dots 6$, with powers above 3 not written above; these are polynomials in μ up to order 6. From this we can read off the terms from \mathcal{K}_D contribute to differing $m = 0, \pm 1$. In particular, if $i + j$ is even – i.e., the real part of the bispectrum – there is no contribution: only the imaginary terms, corresponding to $i + j$ odd, contribute. For the monopole, only $i + j$ even contribute. Therefore, at $\mathcal{O}(\mathcal{H}/k)$, *the monopole of the bispectrum is the Newtonian part, while the dipole is purely from the relativistic corrections. The presence of the dipole is therefore a ‘smoking gun’ signal for the leading relativistic correction to the bispectrum.* At order $\mathcal{O}((\mathcal{H}/k)^2)$, relativistic terms appear in the monopole, which were considered in [102, 107–109].

2.4. Squeezed, equilateral and flattened limits

It is relatively straightforward to understand the type of dipole generated in different triangular configurations in our conventions. In particular, for the $\mathcal{O}(\mathcal{H}/k)$ relativistic dipole:

- The squeezed case is zero for $m = 0$, and is non-zero for $m = \pm 1$. We see this directly from (2.19): with $\mu = -1$ the $m = 0$ contribution is anti-symmetric in i, j while \mathcal{B}_{ij} is symmetric in this limit.
- In the equilateral case, the dipole is zero (this is the case for all orders in \mathcal{H}/k).

2. The dipole of the galaxy bispectrum

- The flattened case ($k_1 = k_2 = k_3/2, \theta = 0$) is zero for $m = \pm 1$ (for all orders in \mathcal{H}/k), but is non-zero for $m = 0$. This can be seen directly from (2.19) with $\theta = 0$.

To show the equilateral case is zero is a lengthy calculation involving many cancellations. Let us illustrate instead the squeezed case. We write $k_1 = k_2 = \sqrt{1 + \varepsilon^2}k_S, k_3 = 2\varepsilon k_S$. In this case the triangle has small angle 2ε and equal angles $\pi/2 - \varepsilon$, where the squeezed limit is $\varepsilon \rightarrow 0$. It is convenient to replace $(1, 2, 3)$ by $(S, -S, L)$. Then to $O(\varepsilon)$, $k_{-S} = k_S, k_L = 2\varepsilon k_S, \mu_{-S} = -\mu_S - 2\varepsilon \mu_L, \mu_L = -\sqrt{1 - \mu_S^2} \cos \varphi - \varepsilon \mu_S$. In this limit, the permutations of the relativistic kernels become

$$\begin{aligned} \mathcal{K}_D^{(2)}(\mathbf{k}_L, \mathbf{k}_S, \mathbf{k}_{-S}) &= i\mathcal{H} \left[-\frac{3}{2}\Omega_m b_1 \mu_S \frac{k_S}{k_L^2} + Cf \frac{\mu_L}{k_L} \right. \\ &\quad \left. - \frac{3}{2}\Omega_m f \mu_S^3 \frac{k_S}{k_L^2} + \left(\frac{3}{2}\Omega_m - Ef\right) f \mu_S^2 \frac{\mu_L}{k_L} \right] \end{aligned} \quad (2.20)$$

and $\mathcal{K}_D^{(2)}(\mathbf{k}_{-S}, \mathbf{k}_L, \mathbf{k}_S) = \mathcal{K}_D^{(2)}(\mathbf{k}_L, \mathbf{k}_S, \mathbf{k}_{-S})|_{\mu_S \rightarrow \mu_{-S}}$ while $\mathcal{K}_D^{(2)}(\mathbf{k}_S, \mathbf{k}_{-S}, \mathbf{k}_L) = 0$. In the squeezed limit of the cyclic sum (2.10), the terms $\mathcal{K}^{(2)}(\mathbf{k}_L, \mathbf{k}_S, \mathbf{k}_{-S})$ and $\mathcal{K}^{(2)}(\mathbf{k}_{-S}, \mathbf{k}_L, \mathbf{k}_S)$ appear only in the form $\mathcal{K}^{(2)}(\mathbf{k}_L, \mathbf{k}_S, \mathbf{k}_{-S}) + \mathcal{K}^{(2)}(\mathbf{k}_{-S}, \mathbf{k}_L, \mathbf{k}_S)$. This sum regularises the divergent $k_S/k_L = (2\varepsilon)^{-1}$ and $k_S/k_L^2 = (2\varepsilon k_L)^{-1}$ terms. We obtain the bispectrum in the squeezed limit,

$$\begin{aligned} B_g^{\text{sq}} &= b_{1S} b_{1L} b_{SL} P_L P_S + i b_{1S} \left\{ b_{SL} f A + \frac{3}{2} \Omega_m b_{1S} b_{1L} \right. \\ &\quad \left. + 2b_{1L} f C + b_{1L} \mu_S^2 \left[\frac{3}{2} \Omega_m - Ef \right] \right\} P_L P_S \mu_L \frac{\mathcal{H}}{k_L}, \end{aligned} \quad (2.21)$$

where $P_{S,L} = P(k_{S,L})$, $b_{1S,L} \equiv b_1 + f \mu_{S,L}^2$ and

$$b_{SL} \equiv 2b_2 + \frac{43}{21}b_1 - \frac{4}{21} + \left(2b_1 + \frac{5}{7}\right) f \mu_S^2 + f \mu_L^2 b_{1S}. \quad (2.22)$$

Note that only the first term in the squeezed bispectrum comes from the Newtonian limit.

The type of dipole extracted from this term is seen as follows. To this order we can write $\mu_S^2 = \mu_S \mu_{-S}$. Then, since $\mu_L = -2(\mu_S + \mu_{-S})/\varepsilon$, we see that the $m = 0$ term is zero because B_g^{sq} is symmetric in $\mu_S^i \mu_{-S}^j$ under $i \leftrightarrow j$, while the $m = 0$ term is antisymmetric in (2.19). This leaves just the $m = \pm 1$ contribution in (2.19).

2. The dipole of the galaxy bispectrum

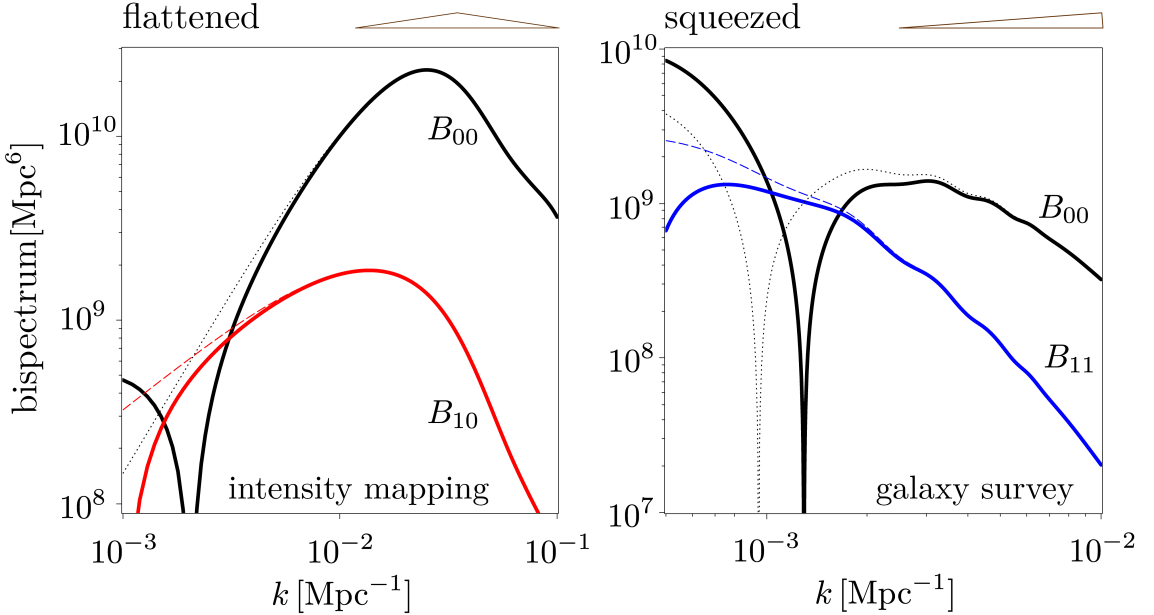


Figure 2.2.: The absolute value of the bispectrum dipole at $z = 1$ as a function of triangle size, in the flattened (Left, $\theta = 2^\circ$, for intensity mapping bias) and squeezed (Right, $\theta = 178^\circ$, for *Euclid*-like bias) configurations, with k_3 as the horizontal axis. Red is the $m = 0$ part and blue is $m = \pm 1$. Dashed (and dotted) lines show up to the $\mathcal{O}(\mathcal{H}/k)$ terms considered analytically here, while solid lines indicate larger-scale contributions. For reference the monopole is in black, with the dotted line the Newtonian part. (The zero-crossing in the monopole for the squeezed case is a result of the tidal bias.)

2.5. The dipole in intensity mapping and galaxy surveys

We now consider the amplitude of the dipole relevant for upcoming galaxy surveys, which have different bias parameters. We consider two different types of survey: an SKA intensity mapping of 21 cm radio emission, as well as a *Euclid*-like optical/infrared spectroscopic survey. An intensity map of the 21cm emission of neutral hydrogen (HI) in the post-reionisation Universe records the total emission in galaxies containing HI, without detecting individual galaxies. There is an equivalence between the brightness temperature contrast and number count contrast [110]. For IM we use the bias parameters at $z = 1$, $b_1 = 0.856, b_2 = -0.321, b'_1 = -0.5 \cdot 10^{-4}, b_e = -0.5, b'_e = 0, s = 2/5$ [110, 111] while for the spectroscopic survey we use $b_1 = 1.3, b_2 = -0.74, b'_1 = -1.6 \cdot 10^{-4}, b_e = -4, b'_e = 0, s = -0.95$ [83, 112].

2. The dipole of the galaxy bispectrum

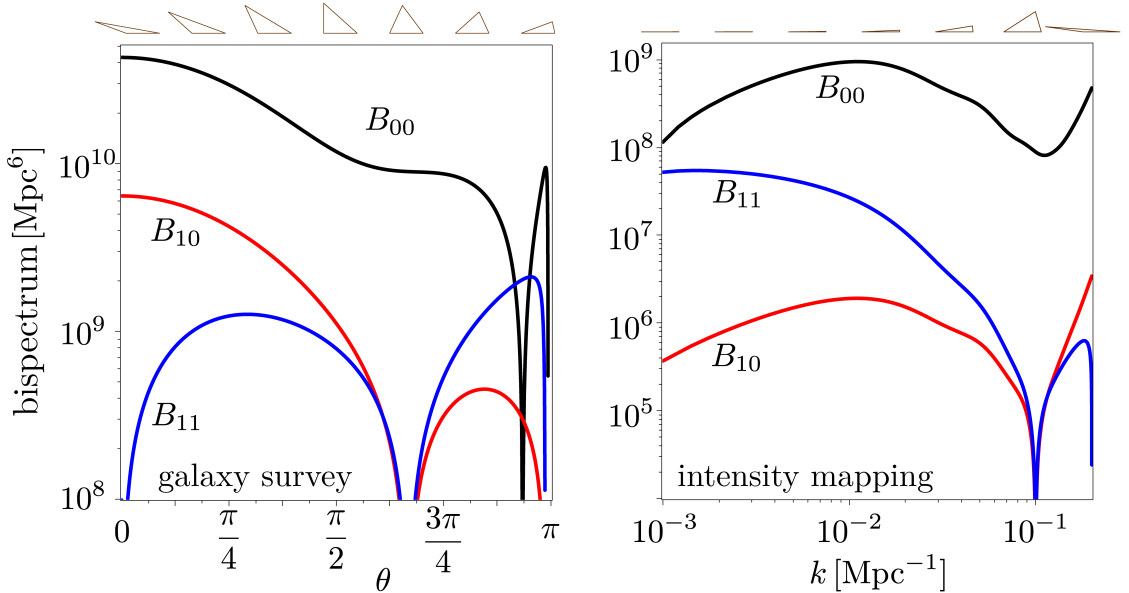


Figure 2.3.: (*Left*) We show the dipoles as a function of θ with a bias appropriate for a *Euclid*-like survey, for $k_1 = k_2 = 0.01 \text{ Mpc}^{-1}$. The left of the plot corresponds to the flattened case where the $m = 0$ (red) dipole reaches 10% of the monopole. (*Right*) We show the IM signal with $k_1 = k_2 = 0.1 \text{ Mpc}^{-1}$ versus the long mode k_3 . Except for very long modes $\theta \approx \pi$, our $\mathcal{O}(\mathcal{H}/k)$ truncation is a very good approximation in these examples.

For intensity mapping, $\partial b_1 / \partial \ln L = 0$ and we assume it is zero for simplicity for the spectroscopic survey. We use a ΛCDM model with standard parameters $\Omega_m = 0.314, h = 0.67, f_{\text{baryon}} = 0.157, n_s = 0.968$. Plots are presented using linear power spectra generated using CAMB [61].

In Figure 2.2, we show how changing the scale of a fixed triangle changes the amplitude of the dipole, with reference to the monopole. In the flattened case with $m = 0$ we see the signal peaks for triangles below the equality scale, while for squeezed shapes, with $m = \pm 1$, the signal is smaller, and peaks when the long mode approaches the Hubble scale. In Figure 2.3, we change the shape with fixed $k_1 = k_2$ for both galaxy and IM surveys. We confirm our analytical results that the equilateral limit is zero, as well as the other limits. For triangles between right-angle and flattened the dipole is more than 10% of the monopole, and the signal is largest in the flattened case – except in the extreme squeezed limit (not shown).

2. The dipole of the galaxy bispectrum

2.6. Conclusions

We have shown for the first time that the relativistic galaxy bispectrum has a leading correction which is a local dipole with respect to the observer’s line-of-sight. In contrast to the power spectrum, this dipole exists even for a single tracer. We have shown analytically how the dipole is generated for the leading terms, and numerically we have included all local contributions, which show up above the equality scale. We have neglected integrated terms which will also contribute to the dipole, but their inclusion in a Fourier space bispectrum is non-trivial. Local relativistic corrections will induce all multipoles up to $\ell = 8$ at every m , in contrast to the Newtonian case which only induces even $\ell = 0, 2, 4$. We will investigate these new multipoles in a forthcoming publication.

We have shown that this dipole is large with respect to the monopole in both the flattened and squeezed limits, which excite different orders of the dipole orientation m . We have shown that even on equality scales it is about 10% of the monopole at $z = 1$ for flattened shapes which have the largest amplitude. In more squeezed cases where the short mode is ~ 10 Mpc the dipole can also be a large part of the IM signal. Furthermore, although we have only considered Gaussian initial conditions here, the dipole will be unaffected by non-Gaussianity at leading order because these corrections start at $\mathcal{O}((\mathcal{H}/k)^2)$, making our predictions relatively robust to this. This implies that the dipole of the bispectrum is a unique signature of general relativity on cosmological scales, and therefore offers a new observational window onto modifications of general relativity.

3. Detectability in next-generation galaxy surveys

In this Chapter, we investigate whether the next generation of high-precision cosmological surveys will be able to make such a detection. First, we consider a Stage IV spectroscopic H α survey similar to *Euclid*, and we find that the cumulative signal to noise of this relativistic signature is $\mathcal{O}(10)$. Secondly, we look at some future 21cm intensity mapping surveys; MeerKAT, SKA, PUMA, and HIRAX. Due to foreground and telescope beam effects, the signal-to-noise ratio for intensity mapping surveys is typically lower than for spectroscopic H α surveys, though also still detectable. This chapter is taken from [113] and [114]. As such, this chapter can roughly be divided into two parts. First, the leading-order relativistic bispectrum is introduced. Following that, we discuss how we estimate the SNR, and account for any nonlinear effects and introduce numerical details of our calculations. We then introduce a Stage IV H α spectroscopic survey similar to *Euclid*, and present the corresponding numerical results. This is followed by a short recap of this calculation before moving on to the next survey type: 21cm intensity mapping surveys. After discussing modifications to the SNR calculation for 21cm IM, we present our findings, and finish off with our conclusions.

3.1. Detecting the leading-order relativistic signature

Here we highlight a feature of the tree-level Fourier galaxy bispectrum which follows from the leading-order relativistic contribution – due to Doppler, gravitational redshift and related line-of-sight effects – that is omitted in the standard Newtonian analysis. These effects generate an imaginary part of the galaxy bispectrum, which can be understood as follows (see also [88, 89, 115] for a more general discussion).

3. Detectability in next-generation galaxy surveys

The Doppler-type contributions to the galaxy density contrast involve one or three derivatives of scalars along the fixed line of sight \mathbf{n} [see (3.6), (3.7) below]. In Fourier space, with the plane-parallel approximation, we have $\mathbf{n} \cdot \nabla \rightarrow i \mathbf{n} \cdot \mathbf{k}$, and this leads to imaginary corrections to the galaxy density contrast, which do not cancel in the bispectrum, unlike in the power spectrum. At first order, we have $\delta_g = \delta_{gN} + \delta_{gD}$, where the Newtonian part δ_{gN} is real and scales as the linear matter density contrast δ . The relativistic Doppler-type part δ_{gD} scales as $i(\mathcal{H}/k)\delta$ (see [88, 89, 93, 116] and below). At second order, the relativistic contribution $\delta_{gD}^{(2)}$ scales as $i(\mathcal{H}/k)(\delta)^2$ (see [88] and below).

In the case of the galaxy auto-power spectrum, $P_g \sim \langle |\delta_g|^2 \rangle$, the relativistic part is real and scales as $(\mathcal{H}/k)^2 P$: therefore we can neglect P_{gD} at leading order. By contrast, for the galaxy bispectrum, $B_g \sim \langle \delta_g \delta_g \delta_g^{(2)} \rangle$, a coupling of relativistic contributions to short-scale Newtonian terms (which is absent in P_g) produces a B_{gD} that is imaginary and scales as $i(\mathcal{H}/k)P^2$. We therefore expect these relativistic effects to be more accessible in the bispectrum than in the power spectrum, for the case of a single tracer of the matter distribution.

Although the galaxy bispectrum is statistically isotropic, the plane-parallel approximation in redshift space breaks 3-dimensional isotropy, since a preferred direction is imposed by the observer's fixed line of sight.

Let us introduce a more explicit analysis, as follows.

At tree-level, the Fourier galaxy bispectrum at a redshift z is given by

$$\langle \delta_g(z, \mathbf{k}_1) \delta_g(z, \mathbf{k}_2) \delta_g^{(2)}(z, \mathbf{k}_3) \rangle + 2 \text{ cp} = 2(2\pi)^3 B_g(z, \mathbf{k}_1, \mathbf{k}_2, \mathbf{k}_3) \delta^{\text{Dirac}}(\mathbf{k}_1 + \mathbf{k}_2 + \mathbf{k}_3), \quad (3.1)$$

where cp denotes cyclic permutation and the factor 2 on the right arises from the convention that the total number density contrast is $\delta_g + \delta_g^{(2)}/2$. In terms of the first- and second-order kernels, we have

$$B_g(z, \mathbf{k}_1, \mathbf{k}_2, \mathbf{k}_3) = \mathcal{K}^{(1)}(z, \mathbf{k}_1) \mathcal{K}^{(1)}(z, \mathbf{k}_2) \mathcal{K}^{(2)}(z, \mathbf{k}_1, \mathbf{k}_2, \mathbf{k}_3) P(z, k_1) P(z, k_2) + 2 \text{ cp}, \quad (3.2)$$

where P is the linear matter power spectrum. The $9 - 3 = 6$ degrees of freedom in the triangle condition $\mathbf{k}_1 + \mathbf{k}_2 + \mathbf{k}_3 = \mathbf{0}$ at each z are reduced to 5 by the fixed observer's line of sight direction \mathbf{n} . The bispectrum can be chosen at each z to be a function of the 3 magnitudes $k_a = (k_1, k_2, k_3)$ and 2 angles that define the

3. Detectability in next-generation galaxy surveys

orientation of the triangle (see Figure 2.1):

$$B_g(z, \mathbf{k}_a) = B_g(z, k_a, \mu_1, \varphi). \quad (3.3)$$

Here $\mu_a = \hat{\mathbf{k}}_a \cdot \mathbf{n} = \cos \theta_a$, and φ is the angle between the triangle plane and the $(\mathbf{n}, \mathbf{k}_1)$ -plane. The three angles $\theta_{ab} = \cos^{-1}(\hat{\mathbf{k}}_a \cdot \hat{\mathbf{k}}_b)$, are determined by k_a ; then $\mu_2 = \mu_1 \cos \theta_{12} + \sin \theta_1 \sin \theta_{12} \cos \varphi$ is determined when φ is given, and $\mu_3 = -(\mu_1 k_1 + \mu_2 k_2)/k_3$.

In the standard Newtonian approximation, $B_g = B_{gN}$, the kernels in (3.2) contain the galaxy bias and the redshift-space distortions (RSD) at first and second order [62, 71],

$$\mathcal{K}_N^{(1)}(\mathbf{k}_1) = b_1 + f\mu_1^2, \quad (3.4)$$

$$\mathcal{K}_N^{(2)}(\mathbf{k}_1, \mathbf{k}_2, \mathbf{k}_3) = b_1 F_2(\mathbf{k}_1, \mathbf{k}_2) + b_2 + f\mu_3^2 G_2(\mathbf{k}_1, \mathbf{k}_2) + f\mathcal{Z}_2(\mathbf{k}_1, \mathbf{k}_2) + b_{s^2} S_2(\mathbf{k}_1, \mathbf{k}_2), \quad (3.5)$$

where we dropped the z -dependence for brevity. Here f is the linear matter growth rate, b_1, b_2 are the linear and second-order clustering biases, and b_{s^2} is the tidal bias. The kernel F_2 is for second-order density, G_2 , \mathcal{Z}_2 are for RSD, and S_2 is the kernel for tidal bias.

The Doppler-type relativistic corrections to the Newtonian number count contrast in redshift space are given at first order by [117],

$$\delta_{gD} = A \mathbf{v} \cdot \mathbf{n}, \quad (3.6)$$

where $A(z)$ is given below in (3.12) and the momentum conservation equation has been used to eliminate the gravitational redshift: $\mathbf{n} \cdot \nabla \Phi \equiv \partial_r \Phi = -\mathbf{v}' \cdot \mathbf{n} - \mathcal{H} \mathbf{v} \cdot \mathbf{n}$. Here Φ is the gravitational potential, \mathbf{v} is the peculiar velocity, \mathcal{H} is the comoving Hubble parameter, and r is the line-of-sight comoving distance. Note that $\mathbf{v} \cdot \mathbf{n} = \partial_r V$, where V is the velocity potential ($v_i = \partial_i V$). At second order, and neglecting vector and tensor modes, it is shown in [88] that (see also [95]),

$$\begin{aligned} \delta_{gD}^{(2)} = & A \mathbf{v}^{(2)} \cdot \mathbf{n} + 2C(\mathbf{v} \cdot \mathbf{n}) \delta + 2\frac{E}{\mathcal{H}}(\mathbf{v} \cdot \mathbf{n}) \partial_r(\mathbf{v} \cdot \mathbf{n}) + \frac{2}{\mathcal{H}^2} [(\mathbf{v} \cdot \mathbf{n}) \partial_r^2 \Phi - \Phi \partial_r^2(\mathbf{v} \cdot \mathbf{n})] \\ & - \frac{2}{\mathcal{H}} \partial_r(\mathbf{v} \cdot \mathbf{v}) + 2\frac{b_1}{\mathcal{H}} \Phi \partial_r \delta. \end{aligned} \quad (3.7)$$

The redshift-dependent coefficients C, E are given below in (3.13), (3.14).

3. Detectability in next-generation galaxy surveys

In Fourier space, neglecting sub-leading $\mathcal{O}(\mathcal{H}^2/k^2)$ terms, we find from (3.2) that,

$$B_{gD}(\mathbf{k}_1, \mathbf{k}_2, \mathbf{k}_3) = \left\{ \left[\mathcal{K}_{\text{N}}^{(1)}(\mathbf{k}_1) \mathcal{K}_{\text{D}}^{(1)}(\mathbf{k}_2) + \mathcal{K}_{\text{D}}^{(1)}(\mathbf{k}_1) \mathcal{K}_{\text{N}}^{(1)}(\mathbf{k}_2) \right] \mathcal{K}_{\text{N}}^{(2)}(\mathbf{k}_1, \mathbf{k}_2, \mathbf{k}_3) + \mathcal{K}_{\text{N}}^{(1)}(\mathbf{k}_1) \mathcal{K}_{\text{N}}^{(1)}(\mathbf{k}_2) \mathcal{K}_{\text{D}}^{(2)}(\mathbf{k}_1, \mathbf{k}_2, \mathbf{k}_3) \right\} P(k_1) P(k_2) + 2 \text{ cp.} \quad (3.8)$$

The relativistic kernels follow from (3.6) and (3.7); they are given in [88] as,

$$\mathcal{K}_{\text{D}}^{(1)}(\mathbf{k}_1) = i \mathcal{H} f A \frac{\mu_1}{k_1}, \quad (3.9)$$

$$\begin{aligned} \mathcal{K}_{\text{D}}^{(2)}(\mathbf{k}_1, \mathbf{k}_2, \mathbf{k}_3) = & i \mathcal{H} f \left[A \frac{\mu_3}{k_3} G_2(\mathbf{k}_1, \mathbf{k}_2) + C \left(\frac{\mu_1}{k_1} + \frac{\mu_2}{k_2} \right) \right. \\ & + \left(\frac{3}{2} \Omega_m - f E \right) \mu_1 \mu_2 \left(\frac{\mu_1}{k_2} + \frac{\mu_2}{k_1} \right) - \frac{3}{2} \Omega_m \left(\mu_1^3 \frac{k_1}{k_2^2} + \mu_2^3 \frac{k_2}{k_1^2} \right) \\ & \left. + 2f \hat{\mathbf{k}}_1 \cdot \hat{\mathbf{k}}_2 \left(\frac{\mu_1}{k_1} + \frac{\mu_2}{k_2} \right) - \frac{3\Omega_m b_1}{2f} \left(\mu_1 \frac{k_1}{k_2^2} + \mu_2 \frac{k_2}{k_1^2} \right) \right]. \end{aligned} \quad (3.10)$$

It is clear from (3.8)–(3.10) and from the general expressions given in [102, 108], that Doppler-type relativistic effects generate an imaginary correction to the Newtonian bispectrum:

$$\text{Re } B_g = B_{gN} + \mathcal{O}(\mathcal{H}^2/k^2), \quad i \text{ Im } B_g = B_{gD} + \mathcal{O}(\mathcal{H}^3/k^3). \quad (3.11)$$

The coefficients in (3.9) and (3.10) are [88],

$$A = b_e - 2\mathcal{Q} + \frac{2(\mathcal{Q} - 1)}{r\mathcal{H}} - \frac{\mathcal{H}'}{\mathcal{H}^2}, \quad (3.12)$$

$$C = b_1 \left(A + f \right) + \frac{b'_1}{\mathcal{H}} + 2 \left(1 - \frac{1}{r\mathcal{H}} \right) \frac{\partial b_1}{\partial \ln L} \Big|_{\text{c}}, \quad (3.13)$$

$$E = 4 - 2A - \frac{3}{2}\Omega_m, \quad (3.14)$$

where a prime is a conformal time derivative, $\Omega_m = \Omega_{m0}(1+z)H_0^2/\mathcal{H}^2$, L is the luminosity, and $|_{\text{c}}$ denotes evaluation at the flux cut.

In addition to the clustering bias b_1 , the relativistic bispectrum is sensitive to the evolution bias and magnification bias, which are defined as [118],

$$b_e = -\frac{\partial \ln n_g}{\partial \ln(1+z)}, \quad \mathcal{Q} = -\frac{\partial \ln n_g}{\partial \ln L} \Big|_{\text{c}}. \quad (3.15)$$

Here and below, n_g is the *comoving* galaxy number density. (Note that the alterna-

3. Detectability in next-generation galaxy surveys

tive magnification bias parameter $s = 2\mathcal{Q}/5$ is often used.)

It is interesting to note that the magnification bias \mathcal{Q} enters the relativistic bispectrum, even though we have not included the effect of the integrated lensing magnification κ . The reason for this apparent inconsistency is that there is a (non-integrated) Doppler correction to κ at leading order [119, 120].

The effect of magnification, which is included through \mathcal{Q} in the bispectrum, on the galaxy number density in the presence of a flux cut can be understood intuitively. Magnification can cause both increase and decrease of the observed number density of galaxies, which is dependent on the specifics of the situation. Of course, magnification can ‘magnify’ less luminous objects, bumping them up to above the flux cut, when without magnification they would be too faint to be included. As a result, the observed number density would increase. However, a direct consequence of massive objects that cause magnification between source and observer is also that the paths of the light rays are affected (bent) by this. This causes a discrepancy between the observed and real-space positions of the objects, i.e. objects appear as coming from outside of the observed patch of space due to this distortion. This effect will cause a decrease in the observed galaxy number density.

The evolution bias in the expression for the bispectrum accounts for the evolution of the source population through time, i.e. any evolution that takes place between the emission of light at the sources at redshift $z = z$ and the observation by the observer at redshift $z = 0$.

In the discussion that follows here, which is taken directly from [114], the evolution and magnification bias parameters as derived in Model 1 in [121]. These bias parameters are, as obvious in equation (3.15), defined as derivatives of the number density of galaxies. They are hence very sensitive to the form of the luminosity function. The impact of differently modelled luminosity functions on magnification and evolution bias is discussed in detail in [122].

Model 1 in [121] is based on the pre-2019 luminosity function. An updated luminosity function is given by Model 3 in [121], which, unlike Models 1 and 2, is based on observational data. The SNR computed using galaxy number density and bias parameters derived from this model is not presented in [114], but we present it in this thesis in Section 3.3.4.

3.2. Signal-to-Noise

The signal-to-noise ratio (SNR) for the bispectrum at some redshift z is in the Gaussian approximation of uncorrelated triangles given by [66],

$$\left[\frac{S}{N}(z) \right]^2 = \sum_{k_a, \mu_1, \varphi} \frac{1}{\text{Var}[B_g(z, k_a, \mu_1, \varphi)]} B_g(z, k_a, \mu_1, \varphi) B_g^*(z, k_a, \mu_1, \varphi), \quad (3.16)$$

where we have introduced the complex conjugate B_g^* as the galaxy bispectrum has an imaginary correction. Here $\text{Var}[B_g]$ is the variance of the bispectrum estimator [123],

$$\hat{B}_g(z, \mathbf{k}_a) = \frac{k_f^3}{V_{123}} \int_{\mathbf{k}_a} d^3\mathbf{q}_1 d^3\mathbf{q}_2 d^3\mathbf{q}_3 \delta^{\text{Dirac}}(\mathbf{q}_1 + \mathbf{q}_2 + \mathbf{q}_3) \delta_g(z, \mathbf{q}_1) \delta_g(z, \mathbf{q}_2) \delta_g(z, \mathbf{q}_3), \quad (3.17)$$

where integration is over the shells $k_a - \Delta k/2 \leq q_a \leq k_a + \Delta k/2$ and the shell volume is $V_{123} = \int_{\mathbf{k}_a} d^3\mathbf{q}_1 d^3\mathbf{q}_2 d^3\mathbf{q}_3 \delta^{\text{Dirac}}(\mathbf{q}_1 + \mathbf{q}_2 + \mathbf{q}_3)$.

In the Newtonian approximation, the Gaussian variance can be given as [66, 71],

$$\text{Var}[B_g(z, k_a, \mu_1, \varphi)] = s_B \frac{\pi k_f(z)^3}{k_1 k_2 k_3 (\Delta k)^3} \frac{N_{\mu_1} N_{\varphi}}{\Delta \mu_1 \Delta \varphi} \tilde{P}_{gN}(z, k_1, \mu_1) \tilde{P}_{gN}(z, k_2, \mu_2) \tilde{P}_{gN}(z, k_3, \mu_3), \quad (3.18)$$

where,

$$\tilde{P}_{gN}(z, k_a, \mu_a) = P_{gN}(z, k_a, \mu_a) + \frac{1}{n_g(z)}, \quad (3.19)$$

and $P_{gN} = (b_1 + f\mu_a^2)^2 P$ is the linear galaxy power spectrum. In (3.18), s_B is 6, 2, 1 respectively for equilateral, isosceles and non-isosceles triangles, and N_{μ_1}, N_{φ} are the ranges for μ_1, φ (which are sometimes reduced from their full values of 2 and 2π using symmetry arguments). The fundamental mode is determined by the comoving survey volume of the redshift bin centred at z , i.e.,

$$k_f(z) = 2\pi V(z)^{-1/3}, \quad (3.20)$$

where $V(z) = 4\pi f_{\text{sky}}[r(z + \Delta z/2)^3 - r(z - \Delta z/2)^3]$.

For a survey with redshift bin centres ranging from z_{\min} to z_{\max} , the cumulative SNR is

$$\frac{S}{N}(\leq z) = \left\{ \sum_{z'=\min}^z \left[\frac{S}{N}(z') \right]^2 \right\}^{1/2}, \quad (3.21)$$

3. Detectability in next-generation galaxy surveys

and then the total SNR is $S/N(\leq z_{\max})$.

3.2.1. Relativistic contributions to the variance

For the full bispectrum, including the relativistic part, (3.17) leads to a variance of the form

$$\text{Var}[B_g(z, \mathbf{k}_a)] \propto \tilde{P}_g(z, k_1, \mu_1) \tilde{P}_g(z, k_2, \mu_2) \tilde{P}_g(z, k_3, \mu_3). \quad (3.22)$$

In the Newtonian approximation, this gives (3.18). By (3.9), the galaxy number density contrast has an imaginary relativistic correction, $\delta_g = \delta_{gN} + \delta_{gD}$. However, since $P_g \sim \langle \delta_g(\mathbf{k}) \delta_g(-\mathbf{k}) \rangle = \langle |\delta_g(\mathbf{k})|^2 \rangle$, the galaxy power spectrum is given by [88, 89, 93],

$$P_g = P_{gN} + P_{gD} = P_{gN} + \mathcal{O}(\mathcal{H}^2/k^2). \quad (3.23)$$

It follows from (3.22) and (3.23) that at leading order, the relativistic contribution to the variance can be neglected,

$$\text{Var}[B_g] = \text{Var}[B_{gN}] + \mathcal{O}(\mathcal{H}^2/k^2). \quad (3.24)$$

Therefore the SNR for the Newtonian and relativistic parts of the bispectrum are,

$$\left(\frac{S}{N} \right)_N^2 = \sum_{k_a, \mu_1, \varphi} \frac{B_{gN} B_{gN}}{\text{Var}[B_{gN}]}, \quad (3.25)$$

$$\left(\frac{S}{N} \right)_D^2 = \sum_{k_a, \mu_1, \varphi} \frac{B_{gD} B_{gD}^*}{\text{Var}[B_{gN}]}. \quad (3.26)$$

3.2.2. Nonlinear effects

In order to avoid nonlinear effects of matter clustering, the maximum k is chosen as a scale where perturbation theory for the matter density contrast begins to break down. It is known that the matter bispectrum is more sensitive to nonlinearity than the matter power spectrum: at $z \sim 0$ nonlinearity sets in at $k \sim 0.1h/\text{Mpc}$ for the matter bispectrum, as opposed to $k \sim 0.2h/\text{Mpc}$ for the matter power spectrum. To account for the growth of k_{\max} with redshift, we use the redshift-dependence proposed in [124] for the power spectrum, but with half the amplitude at $z = 0$,

$$k_{\max}(z) = 0.1h (1+z)^{2/(2+n_s)}. \quad (3.27)$$

3. Detectability in next-generation galaxy surveys

The cut-off $k \leq k_{\max}(z)$ avoids a breakdown of perturbative accuracy in the matter correlations, but nonlinearities in the galaxy correlations due to RSD can affect longer wavelength modes. The effect of RSD on these scales is to damp the power – the ‘FoG’ effect. In order to take account of this, we follow the conventions in [71, 83] and use the simple model of FoG damping,

$$P_g \rightarrow D_P P_g, \quad D_P(z, \mathbf{k}) = \exp \left\{ -\frac{1}{2} [k \mu \sigma(z)]^2 \right\}, \quad (3.28)$$

$$B_g \rightarrow D_B B_g, \quad D_B(z, \mathbf{k}_1, \mathbf{k}_2, \mathbf{k}_3) = \exp \left\{ -\frac{1}{2} [k_1^2 \mu_1^2 + k_2^2 \mu_2^2 + k_3^2 \mu_3^2] \sigma(z)^2 \right\}, \quad (3.29)$$

where σ is the linear velocity dispersion.

On sufficiently large scales the non-Gaussian contribution to the bispectrum covariance can be approximated by including corrections to the power spectra appearing in the bispectrum variance (B.5). This is shown by [123] (see also [71]), using the approximation,

$$\text{Var}[B_g] \rightarrow \text{Var}[B_g] + \delta \text{Var}[B_g], \quad (3.30)$$

$$\delta \text{Var}[B_g] = \frac{s_B \pi k_f^3 N_{\mu_1} N_{\varphi}}{k_1 k_2 k_3 (\Delta k)^3 \Delta \mu_1 \Delta \varphi} \left\{ \tilde{P}_{gN}(1) \tilde{P}_{gN}(2) [\tilde{P}_{gN}^{\text{NL}}(3) - \tilde{P}_{gN}(3)] + 2 \text{cp} \right\}. \quad (3.31)$$

Here $\tilde{P}_{gN}(a) \equiv \tilde{P}_{gN}(z, k_a, \mu_a)$ and $\tilde{P}_{gN}^{\text{NL}}(a) = (b + f \mu_a^2)^2 P^{\text{NL}} + n_g^{-1}$, where P^{NL} is the nonlinear matter power spectrum, computed with a modified Halofit emulator.

3.2.3. Summations over triangles

The counting of triangles $\mathbf{k}_1 + \mathbf{k}_2 + \mathbf{k}_3 = \mathbf{0}$ that contribute to the signal-to-noise involves a sum in k_a -space and a sum over orientations.

The triangle sides are chosen so that $k_1 \geq k_2 \geq k_3$, and must satisfy $k_1 - k_2 - k_3 \leq 0$. For the summation in k_a we choose the minimum and the step-length as

$$k_{\min}(z) = k_f(z) \quad \text{and} \quad \Delta k(z) = k_f(z), \quad (3.32)$$

as in [71, 83]. Then the k_a sum is defined as [84, 125]

$$\sum_{k_a} = \sum_{k_1=k_{\min}}^{k_{\max}} \sum_{k_2=k_{\min}}^{k_1} \sum_{k_3=k_{\min}}^{k_2}. \quad (3.33)$$

3. Detectability in next-generation galaxy surveys

The coordinates ($\mu_1 = \cos \theta_1, \varphi$) describe all possible orientations of the triangle. We follow [71] and choose the ranges $N_{\mu_1} = 2, N_\varphi = 2\pi$. For a given μ_1 , a complete rotation in φ about \mathbf{k}_1 double counts the triangle falling onto the fixed $(\mathbf{n}, \mathbf{k}_1)$ -plane at $\varphi = 0$ and $\varphi = 2\pi$ (see 2.1). Similarly, for a given φ , the end-points $\theta_1 = 0$ and $\theta_1 = \pi$ correspond to equivalent triangles, with $\mathbf{k}_a \rightarrow -\mathbf{k}_a$. This double-counting can be avoided by imposing suitable upper limits: $-1 \leq \mu_1 < 1$ and $0 \leq \varphi < 2\pi$. The signal to noise is quite sensitive to the step-lengths $\Delta\mu_1, \Delta\varphi$. Figure 3.1 shows the effect on the relativistic total SNR of changing the number of orientation bins, $n_{\mu_1} = N_{\mu_1}/\Delta\mu_1 = 2/\Delta\mu_1$ and $n_\varphi = N_\varphi/\Delta\varphi = 2\pi/\Delta\varphi$. It is apparent that reducing the number of bins increases the cumulative SNR. This might seem counterintuitive, since coarser binning cannot add information, so one would not generally expect the cumulative SNR to increase with a lower number of bins in μ_1 and φ . The reason for this apparent inconsistency is due to the approximations taken in our calculation for the SNR. We use the Gaussian approximation of uncorrelated triangles, with simple Gaussian variance. In this case, the signal B_g is held constant across a given bin, and the variance decreases as the bin widths $\Delta\mu_1$ and $\Delta\varphi$ are increased. Combined, these approximations cause an apparent higher cumulative SNR in the case of coarser binning. To find appropriate bin widths that do not appear to increase the SNR as binning gets coarser, we choose our binning at the point where the SNR has converged to a constant minimum value. The cumulative SNR converges towards a minimum for $n_{\mu_1}, n_\varphi > 40$. Following this, we find that a suitable choice for convergence is

$$\Delta\mu_1 = 0.04, \quad \Delta\varphi = \pi/25, \quad (3.34)$$

or $n_{\mu_1} = n_\varphi = 50$.

3.3. Next-generation galaxy surveys

We consider a Stage IV H α spectroscopic survey, with clustering bias, comoving volume, comoving number density and RSD damping parameter given by Table 1 in [83], over the redshift range $0.65 \leq z \leq 2.05$, with $\Delta z = 0.1$ bins. Fitting formulas for these quantities are,

$$b_1(z) = 0.9 + 0.4z, \quad b_2(z) = -0.741 - 0.125z + 0.123z^2 + 0.00637z^3, \quad (3.35)$$

$$b_{s^2}(z) = 0.0409 - 0.199z - 0.0166z^2 + 0.00268z^3, \quad (3.36)$$

$$V(z) = 8.85z^{1.65} \exp(-0.777z) h^{-3} \text{Gpc}^3, \quad (3.37)$$

3. Detectability in next-generation galaxy surveys

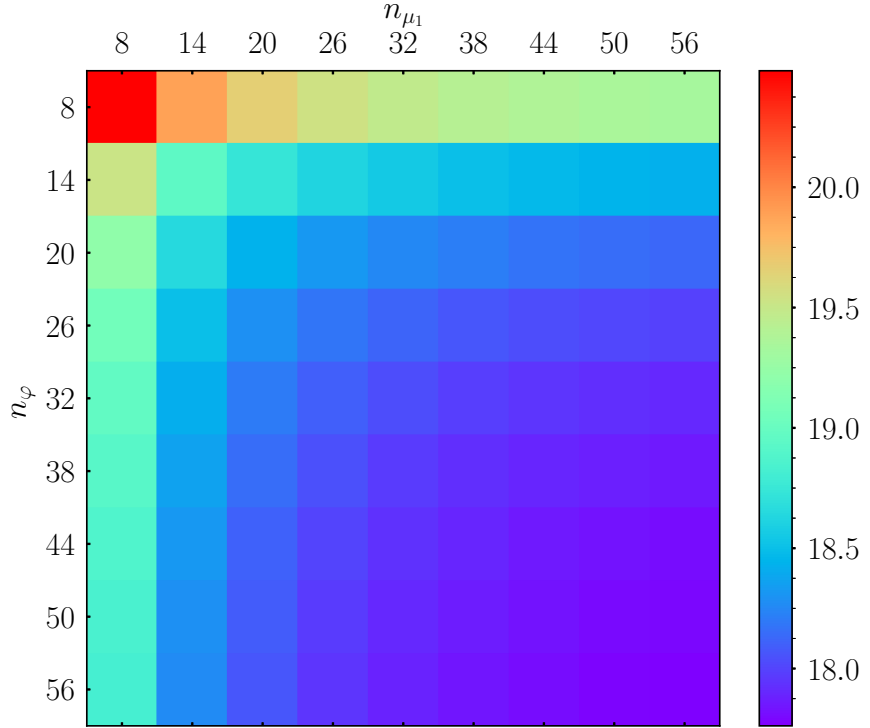


Figure 3.1.: Effect on total relativistic SNR of changing number of φ and μ_1 bins.

$$n_g(z) = 0.0193 z^{-0.0282} \exp(-2.81 z) h^3 \text{Mpc}^{-3}, \quad (3.38)$$

$$\sigma(z) = (5.29 - 0.249 z - 0.720 z^2 + 0.187 z^3) h^{-1} \text{Mpc}. \quad (3.39)$$

Figure 3.2 shows the values given in [83] together with the fitting curves. For the cosmological parameters, we use Planck 2018 [8], $h = 0.6766$, $\Omega_{m0} = 0.3111$, $\Omega_{b0}h^2 = 0.02242$, $\Omega_{c0}h^2 = 0.11933$, $n_s = 0.9665$, $\sigma_8 = 0.8102$, $\gamma = 0.545$, $\Omega_{K0} = 0 = \Omega_{\nu0}$.

We checked that the SNR for the Newtonian bispectrum is consistent with Figure 4 of [83], when we use their redshift-independent $k_{\max} = 0.15h \text{ Mpc}^{-1}$, and when we remove the flattened triangle shapes that are excluded by [83]. When we include the flattened shapes, we checked that we recover the total number of triangles given in Table 1 of [125].

3. Detectability in next-generation galaxy surveys

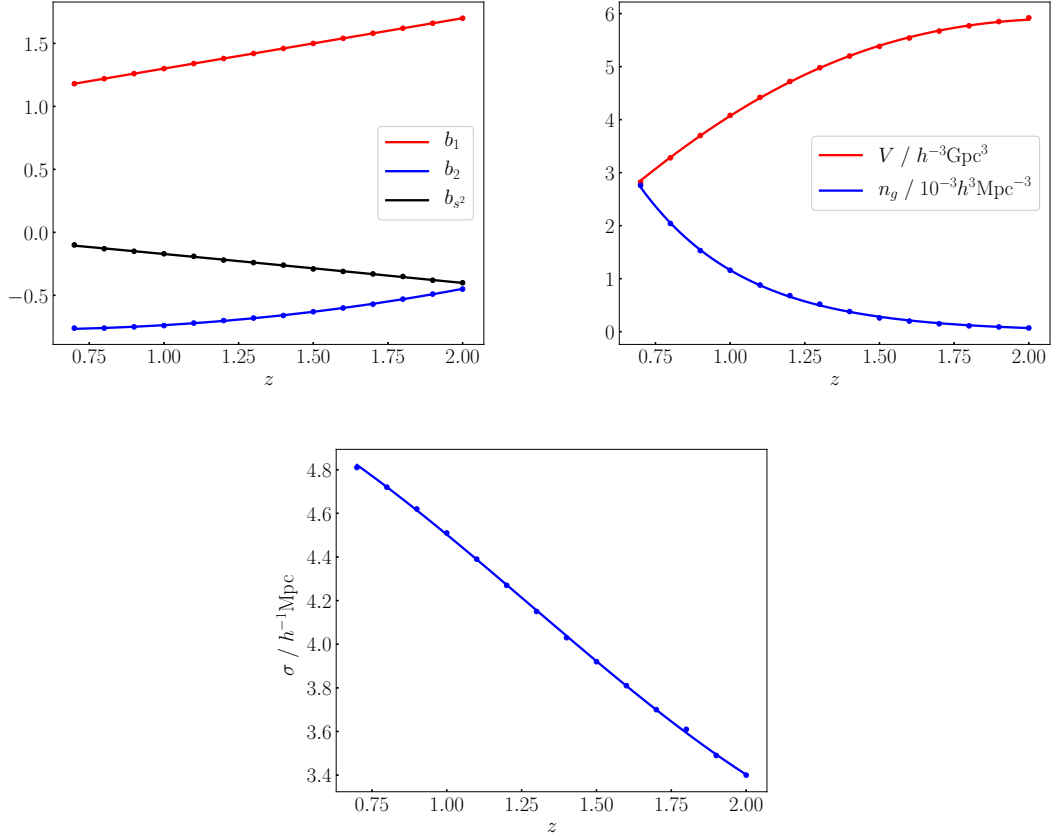


Figure 3.2.: Clustering bias parameters (*left*), comoving volume and number density (*middle*) and RSD damping parameter (*right*). Points are the data from Table 1 in [83].

3.3.1. Evolution bias and magnification bias

The relativistic bispectrum depends also on b_e and \mathcal{Q} , as shown in (3.10)–(3.14). These parameters do *not* appear in the Newtonian approximation, but they are crucial for the relativistic correction, and we need to evaluate them in a physically consistent way. We compute these parameters from the same luminosity function that is used to generate the number density shown in Figure 3.2, i.e., Model 1 in [121]:

$$\Phi(z, y) = \Phi_*(z) y^\alpha e^{-y}, \quad y \equiv \frac{L}{L_*}. \quad (3.40)$$

We have written Φ in terms of the redshift z and the normalised dimensionless luminosity y , where $L_* = L_{*0}(1+z)^\delta$ and L_{*0} is a characteristic luminosity. Here α is the faint-end slope, and Φ_* is a characteristic comoving density of H α emitters,

3. Detectability in next-generation galaxy surveys

modelled as

$$\frac{\Phi_*}{\Phi_{*0}} = \begin{cases} (1+z)^\epsilon & z \leq z_b, \\ (1+z_b)^{2\epsilon}(1+z)^{-\epsilon} & z > z_b. \end{cases} \quad (3.41)$$

The best-fit parameters for Model 1 are given by [121] as

$$\alpha = -1.35, \quad \delta = 2, \quad L_{*0} = 10^{41.5} \text{ erg s}^{-1}, \quad \Phi_{*0} = 10^{-2.8} \text{ Mpc}^{-3}, \quad \epsilon = 1, \quad z_b = 1.3. \quad (3.42)$$

The flux cut F_c translates to a luminosity cut:

$$L_c(z) = 4\pi F_c d_L(z)^2, \quad F_c = 3 \cdot 10^{-16} \text{ erg cm}^{-2} \text{ s}^{-1}, \quad (3.43)$$

where d_L is the background luminosity distance and the choice of F_c follows [83].

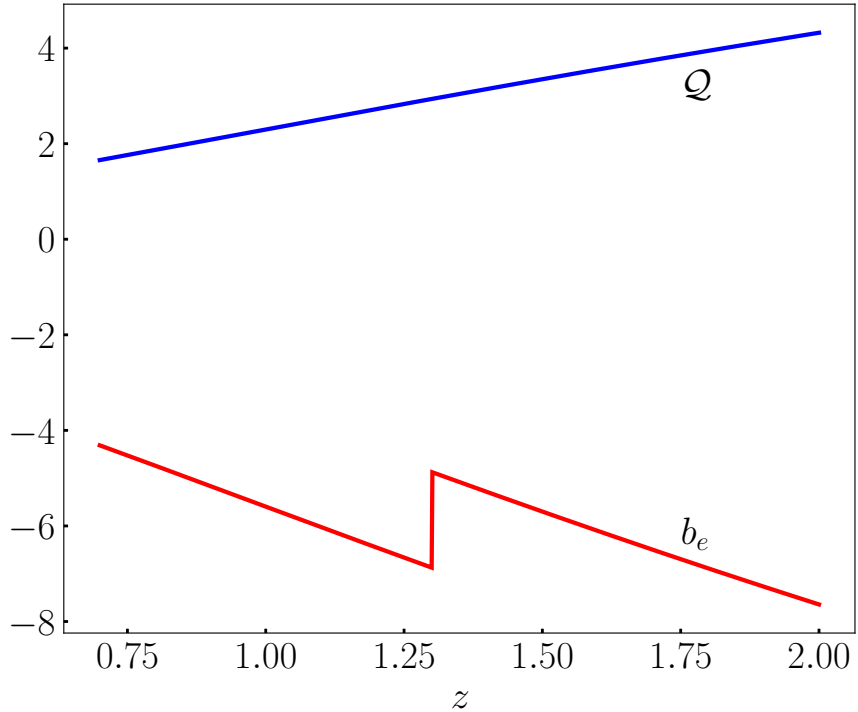


Figure 3.3.: Magnification and evolution bias (3.46), (3.47). The sharp discontinuity in evolution bias at redshift $z = 1.3$ is due to the discontinuity in modelling of the comoving density of H α emitters as in equation 3.41.

3. Detectability in next-generation galaxy surveys

In order to compute b_e and \mathcal{Q} , we require the comoving number density

$$n_g(z) = \int_{y_c(z)}^{\infty} dy \Phi(z, y) = \Phi_*(z) \Gamma(\alpha + 1, y_c(z)), \quad (3.44)$$

where Γ is the upper incomplete Gamma function and

$$y_c(z) = \frac{4\pi F_c}{L_{*0}} r(z)^2 = \left[\frac{r(z)}{2.97 h \cdot 10^3 (\text{Mpc}/h)} \right]^2. \quad (3.45)$$

Using (3.45) and (3.40)–(3.43), we confirm that the analytical form (3.44) for n_g recovers the points from Table 1 in [83].

By (3.15), the magnification bias follows as

$$\mathcal{Q}(z) = \left(y \frac{\Phi}{n_g} \right)_c = \frac{y_c(z)^{\alpha+1} \exp[-y_c(z)]}{\Gamma(\alpha + 1, y_c(z))}, \quad (3.46)$$

since $\partial/\partial \ln L = \partial/\partial \ln y$, and the evolution bias is

$$b_e(z) = -\frac{d \ln \Phi_*(z)}{d \ln(1+z)} - \frac{d \ln L_*(z)}{d \ln(1+z)} \mathcal{Q}(z). \quad (3.47)$$

Figure 3.3 shows the analytical forms (3.46) and (3.47) for b_e and \mathcal{Q} . There is a sharp discontinuity present in the evolution bias b_e at redshift $z = z_b = 1.3$. The origin of this discontinuity is not physical, but instead it is present because of the way the density H α emitters is modelled in Model 1 in [121]. There is a discontinuity in this density at z_b , as the behaviour of the comoving density of H α emitters is modelled to be different below and above the redshift break z_b . Table 3.1 collects the information in Figures 3.2 and 3.3 to provide an extension of Table 1 in [83]. Finally, we need to deal with the luminosity derivative of the bias in (3.13). Simulations by [126] indicate that the clustering bias of H α galaxies does not vary appreciably with luminosity near the fiducial luminosity L_{*0} in (3.42) and for $z \lesssim 2$ (see their Figure 8). We therefore take,

$$\left. \frac{\partial b_1}{\partial \ln L} \right|_c = 0, \quad (3.48)$$

in (3.13).

Table 3.1.: Stage IV H α spectroscopic survey parameters.

z	b_1	b_2	b_{s^2}	b_e	\mathcal{Q}	$10^{-3}h^3\text{Mpc}^{-3}$	n_g	V	σ
						$h^{-3}\text{Gpc}^3$	$h^{-3}\text{Mpc}^{-3}$	$h^{-1}\text{Mpc}$	
0.7	1.18	-0.766	-0.105	-4.31	1.66	2.76	2.82	4.81	
0.8	1.22	-0.759	-0.127	-4.74	1.87	2.04	3.38	4.72	
0.9	1.26	-0.749	-0.149	-5.17	2.08	1.53	3.70	4.62	
1.0	1.30	-0.737	-0.172	-5.60	2.30	1.16	4.08	4.51	
1.1	1.34	-0.721	-0.194	-6.02	2.51	0.880	4.42	4.39	
1.2	1.38	-0.703	-0.217	-6.45	2.72	0.680	4.72	4.27	
1.3	1.42	-0.682	-0.240	-6.76	2.94	0.520	4.98	4.15	
1.4	1.46	-0.658	-0.262	-5.29	3.14	0.380	5.20	4.03	
1.5	1.50	-0.631	-0.285	-5.70	3.35	0.260	5.38	3.92	
1.6	1.54	-0.600	-0.308	-6.10	3.55	0.200	5.54	3.81	
1.7	1.58	-0.567	-0.332	-6.50	3.75	0.150	5.67	3.70	
1.8	1.62	-0.531	-0.355	-6.89	3.94	0.110	5.77	3.61	
1.9	1.66	-0.491	-0.378	-7.27	4.13	0.0900	5.85	3.49	
2.0	1.70	-0.449	-0.401	-7.64	4.32	0.0700	6.92	3.40	

3.3.2. Relativistic signal-to-noise ratio

We can now evaluate the Doppler-type relativistic part of the bispectrum, (3.8)–(3.14), using (3.46)–(3.48). Then the SNR is computed using (3.21) and (3.26) together with (3.31). The results, for SNR in each z -bin, $S/N(z)$, and for the cumulative SNR, $S/N(\leq z)$, are shown in Figure 3.4. Our forecasts indicate that the total SNR, $S/N(\leq z_{\max})$, for a Stage IV H α survey could be $\mathcal{O}(10)$, which is high enough for a detection in principle.

The relativistic SNR is sensitive in particular to two factors:

- Changes in the nonperturbative scale $k_{\max}(z)$: this sensitivity is due to the coupling of long-wavelength relativistic terms to short-wavelength Newtonian terms. We use a conservative and redshift-dependent k_{\max} , given in (3.27). In Figure 3.5 we show the comparison of SNR using (3.27) and using the redshift-independent $k_{\max} = 0.15h/\text{Mpc}$. The redshift-independent model does not incorporate the increase in the nonperturbative scale with growing z , and therefore produces a lower SNR; however, the difference is not large.
- Changes in $b_e(z)$, $\mathcal{Q}(z)$: The effect on the relativistic SNR of changes in magnification bias and in evolution bias is illustrated in Figure 3.6. In Figure 3.6 we illustrate the significant impact on cumulative SNR of changing b_e , \mathcal{Q} . We use a range of constant choices for b_e , \mathcal{Q} – which are not physically motivated. This shows the importance of modelling b_e , \mathcal{Q} self-consistently from the same luminosity function that produces the number density, as we have done.

The sensitivity of the relativistic SNR to k_{\max} reflects the importance of the coupling of the relativistic signal to Newtonian terms on short scales. How sensitive is the SNR to the signal on the largest scales? We can answer this by increasing k_{\min} from its fiducial value k_f , which is the maximal observable scale. The result is that there is only a small reduction when k_{\min}/k_f is increased by a factor up to 5, as shown in Figure 3.7. Even with $k_{\min} = 10k_f$, the total SNR is ~ 10 . This means that the relativistic SNR does not depend critically on accessing the largest possible scales.

It is also interesting to investigate how important for the SNR is the second-order relativistic contribution in the bispectrum, i.e. from terms of the form

$$\mathcal{K}_N^{(1)}(\mathbf{k}_1)\mathcal{K}_N^{(1)}(\mathbf{k}_2)\mathcal{K}_D^{(2)}(\mathbf{k}_1, \mathbf{k}_2, \mathbf{k}_3), \quad (3.49)$$

3. Detectability in next-generation galaxy surveys

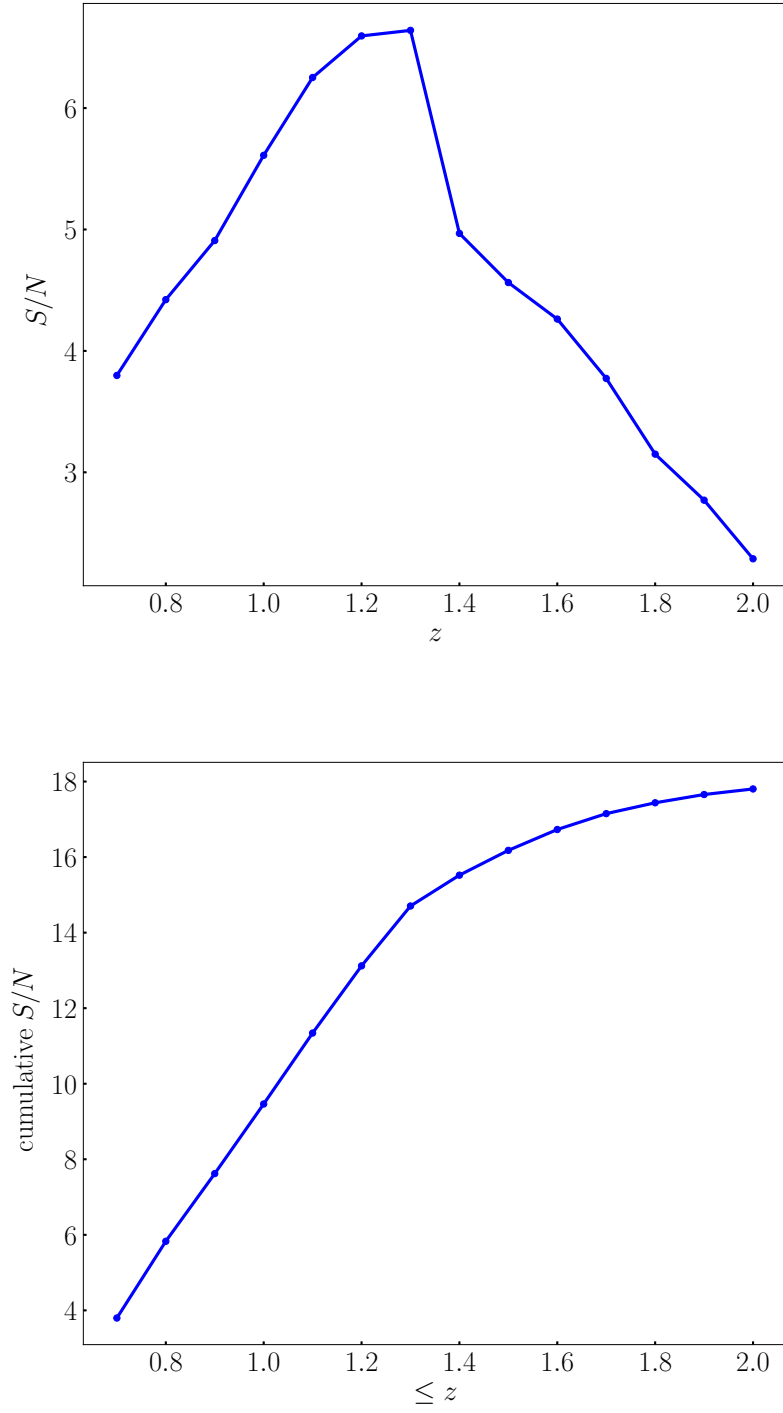


Figure 3.4.: Relativistic SNR per z -bin (*top*) and cumulative (*bottom*) for a Stage IV H α survey.

in (3.8), compared to the first-order contribution, i.e. from terms of the form

$$\left[\mathcal{K}_{\text{N}}^{(1)}(\mathbf{k}_1) \mathcal{K}_{\text{D}}^{(1)}(\mathbf{k}_2) + \mathcal{K}_{\text{D}}^{(1)}(\mathbf{k}_1) \mathcal{K}_{\text{N}}^{(1)}(\mathbf{k}_2) \right] \mathcal{K}_{\text{N}}^{(2)}(\mathbf{k}_1, \mathbf{k}_2, \mathbf{k}_3). \quad (3.50)$$

3. Detectability in next-generation galaxy surveys

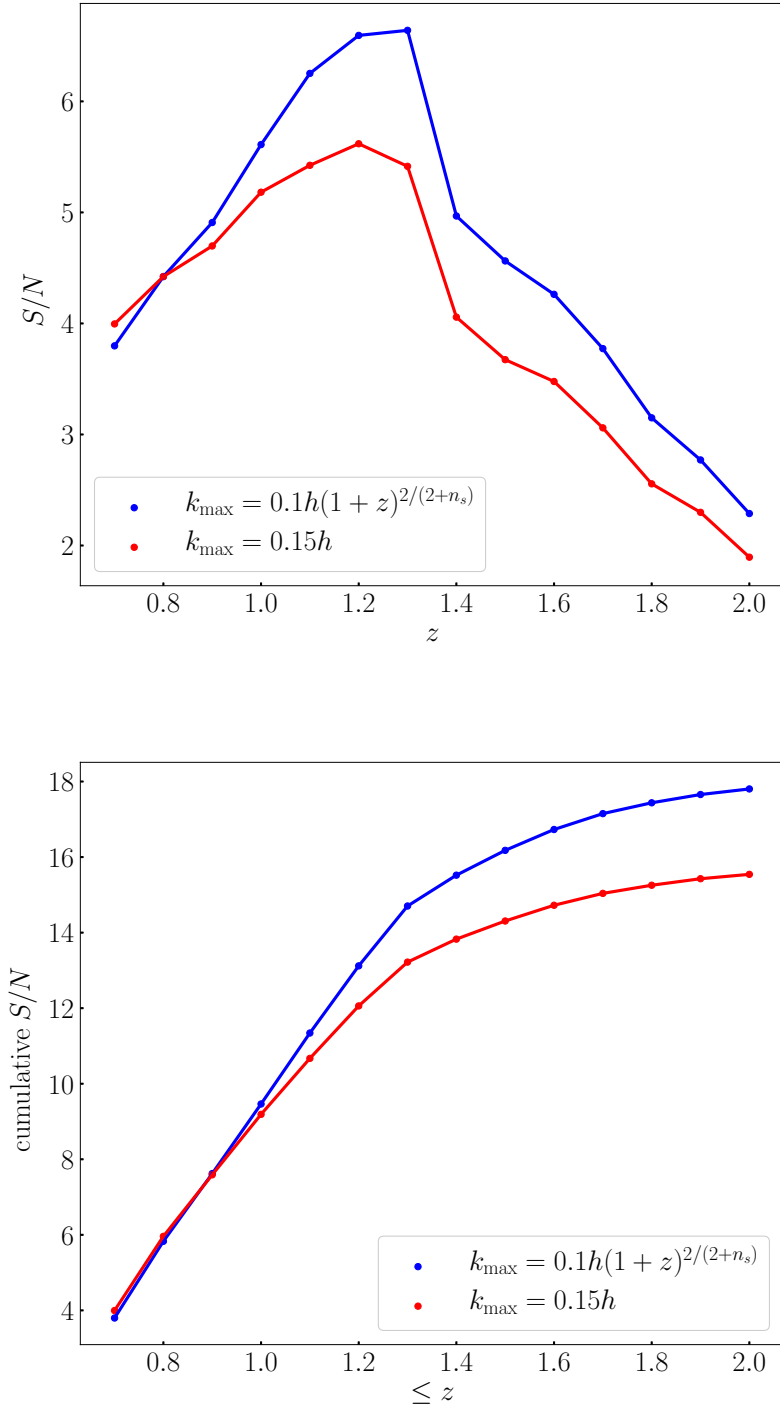


Figure 3.5.: Effect of changing k_{\max} on SNR per bin (*top*) and cumulative SNR (*bottom*).

It is conceivable that the first-order Doppler-type contribution in (3.50) to B_g , which couples to first- and second-order Newtonian terms, dominates the SNR. How-

3. Detectability in next-generation galaxy surveys

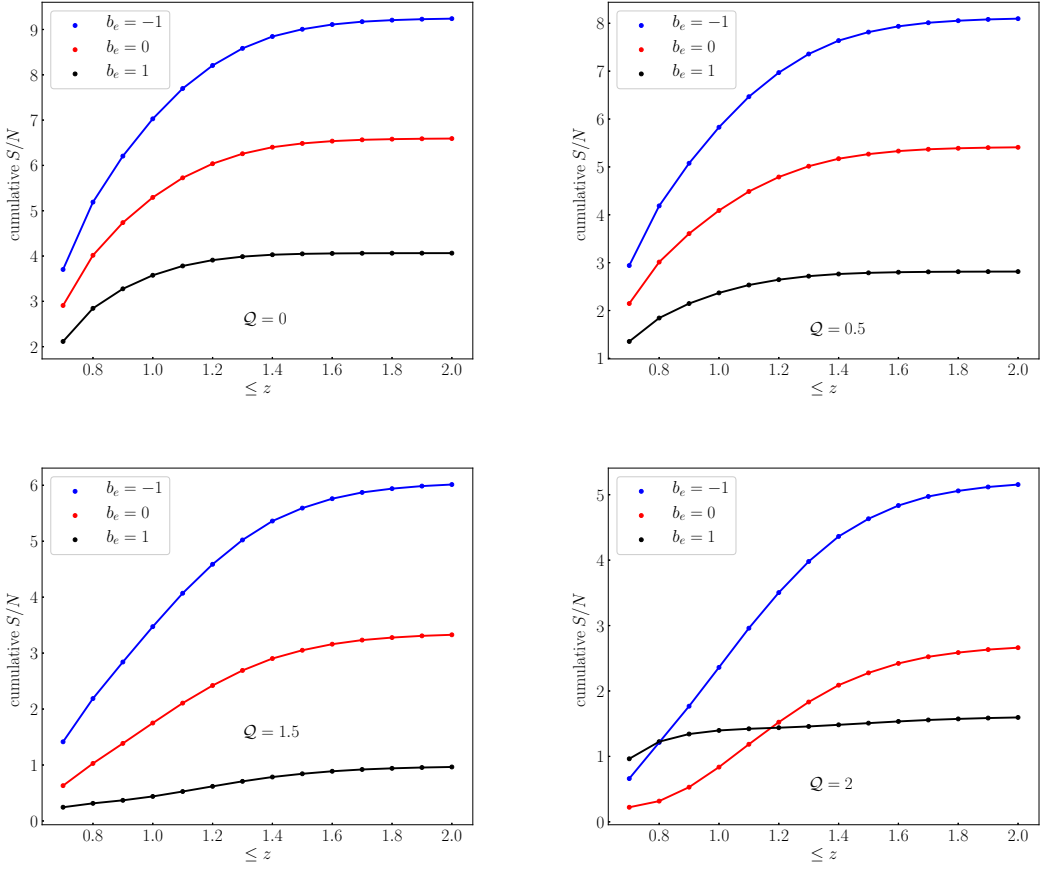


Figure 3.6.: Effect of changing Q and b_e on relativistic cumulative SNR.

ever, we find that the first- and second-order relativistic parts of the bispectrum make comparable contributions to the SNR – see Figure 3.8. We deduce that the second-order relativistic contribution in (3.49) cannot be neglected. Furthermore, this means that it must be accurately modelled, as we have done.

Recently [115] estimated the SNR for the leading relativistic part of the bispectrum. There are significant differences in their analysis compared to ours. In particular, they neglect most of the terms in $\delta_{gD}^{(2)}$ [see our (2.7)] which defines $\mathcal{K}_D^{(2)}$. In [115], a significant number of terms is neglected in the relativistic second-order galaxy number count contrast, $\delta_{gD}^{(2)}$, given by our (2.7). (Note that our (2.7), derived in [88], was independently confirmed by [95]). They have the first term, $A \mathbf{v}^{(2)} \cdot \mathbf{n}$, on the right of (2.7). In the second term, $2C(\mathbf{v} \cdot \mathbf{n})\delta$, they do not have the correct form of the coefficient C – they include only the first part, $b_1 A$, of C [see the right-hand side of eq 26?]. All terms after the second term in (2.7) are omitted by [115]. Note that none of the omitted terms is suppressed by a higher power of k^{-1} ; they all have

3. Detectability in next-generation galaxy surveys

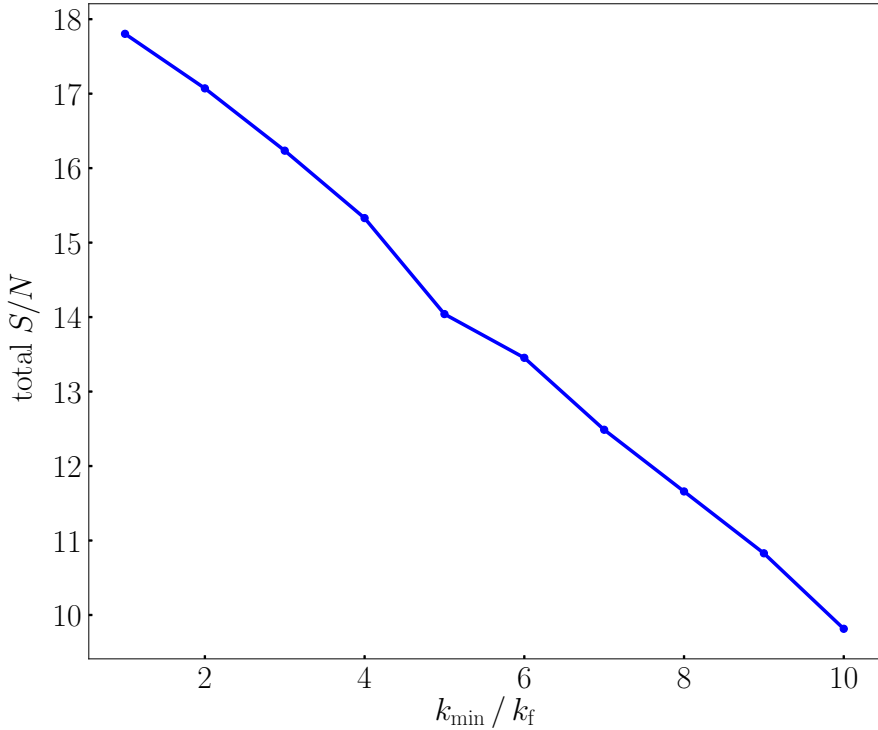


Figure 3.7.: Effect of changing k_{\min} on total relativistic SNR.

the same scaling, i.e., $\propto (\mathcal{H}/k) (\delta)^2$. In detail, they omit the following terms:

$$\begin{aligned} \delta_{gD}^{(2)}(\text{us}) - \delta_{gD}^{(2)}([115]) = & 2 \left[b_1 f + \frac{b'_1}{\mathcal{H}} + 2 \left(1 - \frac{1}{r\mathcal{H}} \right) \frac{\partial b_1}{\partial \ln L} \Big|_c \right] (\mathbf{v} \cdot \mathbf{n}) \delta \\ & + \frac{2}{\mathcal{H}} \left(4 - 2A - \frac{3}{2} \Omega_m \right) (\mathbf{v} \cdot \mathbf{n}) \partial_r (\mathbf{v} \cdot \mathbf{n}) \\ & + \frac{2}{\mathcal{H}^2} [(\mathbf{v} \cdot \mathbf{n}) \partial_r^2 \Phi - \Phi \partial_r^2 (\mathbf{v} \cdot \mathbf{n})] - \frac{2}{\mathcal{H}} \partial_r (\mathbf{v} \cdot \mathbf{v}) + 2 \frac{b_1}{\mathcal{H}} \Phi \partial_r \delta. \end{aligned} \quad (3.51)$$

In addition they do not use self-consistent models for b_e and \mathcal{Q} . These two differences could account for their conclusion that the relativistic signal is not detectable, in contrast to our result.

An interesting feature of the relativistic signal is that there is a significant contribution to the SNR from flattened triangle shapes. This is consistent with the results of [88] for the dipole that is generated by the imaginary part of the bispectrum.

3. Detectability in next-generation galaxy surveys

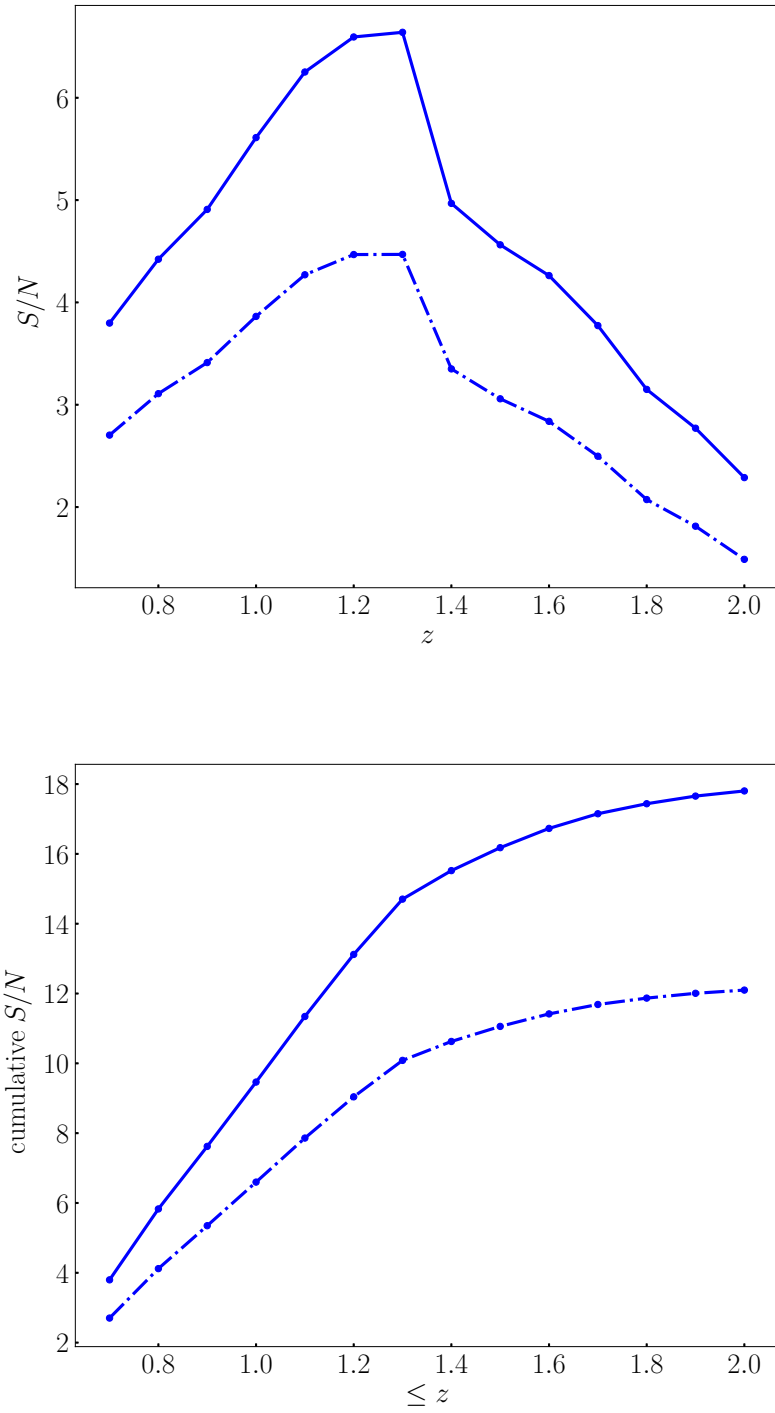


Figure 3.8.: As in Figure 3.4, but showing the effect of omitting the second-order relativistic contribution (3.49) to the bispectrum (dot-dashed curves).

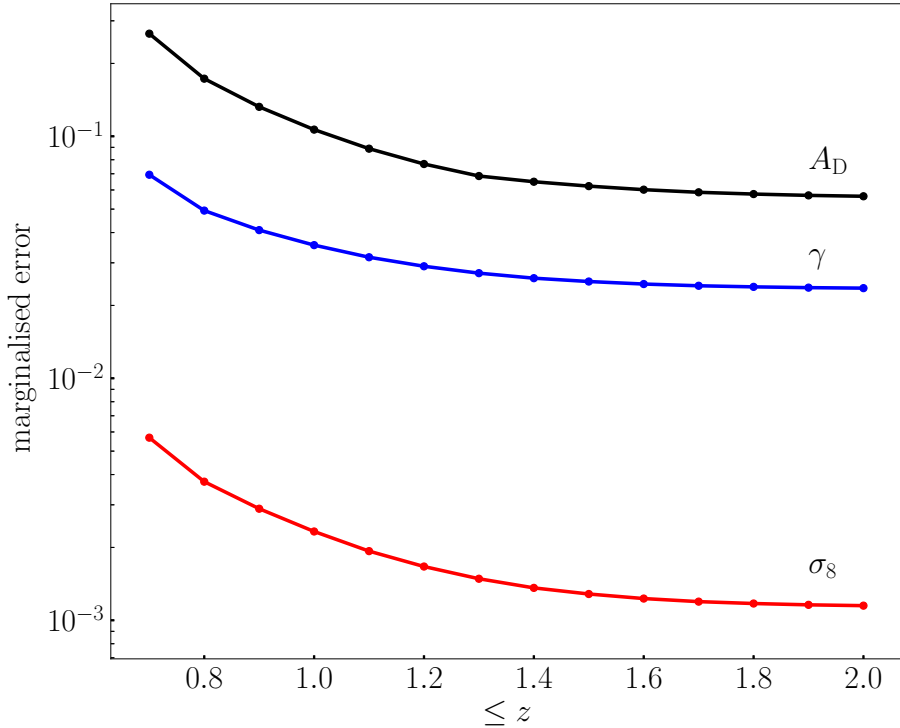


Figure 3.9.: Marginal errors (cumulative) on the relativistic contribution, growth index and clustering amplitude, using the full bispectrum. Bias parameters are held fixed at their theoretical values. Parameter A_D corresponds to the relativistic part of the bispectrum. The fact that $\sigma_{A_D} \lesssim 0.1$ indicates that the relativistic effects remain detectable when the two other parameters are marginalised over.

3.3.3. Inclusion of cosmological parameters

A full treatment of cosmological constraints would marginalise over the standard cosmological parameters, together with the Alcock-Paczynski parameters and the clustering bias parameters. The constraints obtained would depend almost entirely on the Newtonian galaxy power spectrum and bispectrum (as analysed in [83]), given that the relativistic contribution to the power spectrum is below leading order, while in the bispectrum the relativistic SNR is an order of magnitude smaller than the Newtonian SNR.

Our focus here is instead on the detectability of the relativistic signal in the bispectrum, assuming that P_{gN} and B_{gN} have been used to constrain the standard parameters. We now investigate the effect on this detectability when we include the param-

3. Detectability in next-generation galaxy surveys

eters directly related to redshift-space effects, i.e., the growth index $\gamma = \ln f / \ln \Omega_m$ (with fiducial value 0.545), and the clustering amplitude σ_8 (with Planck 2018 fiducial). For forecasts we use the theoretical values of b_e, \mathcal{Q} . In a galaxy survey, they would be measured directly from the observed luminosity function, and their measurement uncertainties would need to be marginalised over.

For the relativistic part of the bispectrum, we introduce a parameter A_D , with fiducial value 1:

$$B_g = B_{gN} + A_D B_{gD}. \quad (3.52)$$

Then the Fisher matrix for the parameters $\vartheta_\alpha = (A_D, \gamma, \sigma_8)$ is

$$F_{\alpha\beta} = \sum_{z, k_a, \mu_1, \varphi} \frac{1}{\text{Var}[B_g]} \frac{\partial B_g}{\partial \vartheta_{(\alpha}}} \frac{\partial B_g^*}{\partial \vartheta_{(\beta)}}, \quad (3.53)$$

where the round brackets denote symmetrisation. The cumulative marginal errors $\sigma_\alpha = [(F^{-1})_{\alpha\alpha}]^{1/2}$ are shown in Figure 3.9. The fact that $\sigma_{A_D} \lesssim 0.1$ means that the relativistic effects remain detectable when the two additional cosmological parameters are marginalised over. It is important to note that in this estimate, as mentioned before, we use theoretical fixed values for the bias parameters and other cosmological parameters. In a more realistic scenario, one would marginalise over the full set of cosmological parameters. Once the bias parameters are allowed to vary, the picture presented in Figure 3.9 is likely to be subject to substantial change— in particular, the error on σ_8 is expected to grow. A fully consistent analysis is left for future work.

3.3.4. SNR using the 2019 luminosity function model

Analytical models of luminosity functions are typically separable in both redshift and luminosity as,

$$\Phi(z, y) = \Phi_*(z)g(y), \quad (3.54)$$

see for example equation (3.40) for the relation for Model 1.

Model 3, as presented in [121], has a luminosity function which is based on observational data— unlike Model 1 (presented in the previous sections) and Model 2 (not discussed here). The updated luminosity function has a reduced redshift range of $0.9 \leq z \leq 1.8$. This luminosity function is separable, and the best-fit is given by a

3. Detectability in next-generation galaxy surveys

broken power law,

$$g(y) = \frac{y^\alpha}{1 + (e - 1)y^\nu}, \quad (3.55)$$

where the factor $e - 1$ is chosen such that L_* is the luminosity at which Φ falls to $1/e$ of the faint-end power law (as in the luminosity function of the Schechter type, which is used for Model 1). The number density, magnification bias, and evolution bias are respectively given by,

$$n_g(z, y_c) = \Phi_*(z)G(y_c), \quad \text{where } G(y_c) = \int_{y_c}^{\infty} dy g(y), \quad (3.56)$$

$$\mathcal{Q}(z, y_c) = y_c \frac{g(y_c)}{G(y_c)}, \quad (3.57)$$

$$b_e(z, y_c) = -\frac{d \ln \Phi_*(z)}{d \ln(1+z)} - \frac{d \ln L_*(z)}{d \ln(1+z)} \mathcal{Q}(z, y_c), \quad (3.58)$$

where $G(y_c)$ needs to be evaluated numerically, $\Phi_*(z) = \Phi_{*0} = 10^{-2.92} \text{ Mpc}^{-3}$, and $L_*(z)$ is defined through,

$$\log L_*(z) = \log L_{*\infty} + \left[\frac{1.5}{(1+z)} \right]^\beta \log \left[\frac{L_*(0.5)}{L_{*\infty}} \right]. \quad (3.59)$$

Here,

$$\begin{aligned} \alpha &= -1.587, & \beta &= 1.615, & \nu &= 2.288, & L_*(0.5) &= 10^{41.733} \text{ erg s}^{-1}, \\ L_{*\infty} &= 10^{42.956} \text{ erg s}^{-1}. \end{aligned} \quad (3.60)$$

Fitting functions for the number density and evolution and magnification biases are given by,

$$n_g(z) = 0.00363 z^{-0.910} e^{0.402z} - 0.00414 h^3 \text{Mpc}^{-3}, \quad (3.61)$$

$$\mathcal{Q}(z) = 0.583 + 2.02z - 0.568z^2 + 0.0411z^3, \quad (3.62)$$

$$b_e(z) = -7.29 + 0.470z + 1.17z^2 - 0.290z^3, \quad (3.63)$$

and Figure 3.10 shows the dependence of the number density and the evolution and magnification biases on redshift z .

We already established earlier on that the value of the SNR is very sensitive to the magnification and evolution biases— highlighting the importance of modelling these self-consistently from the same luminosity function. The SNR is also dependent on the value of the flux cut— we follow [127] with a flux cut of $F_c = 2 \cdot 10^{-16} \text{ erg cm}^{-2} \text{ s}^{-1}$.

3. Detectability in next-generation galaxy surveys

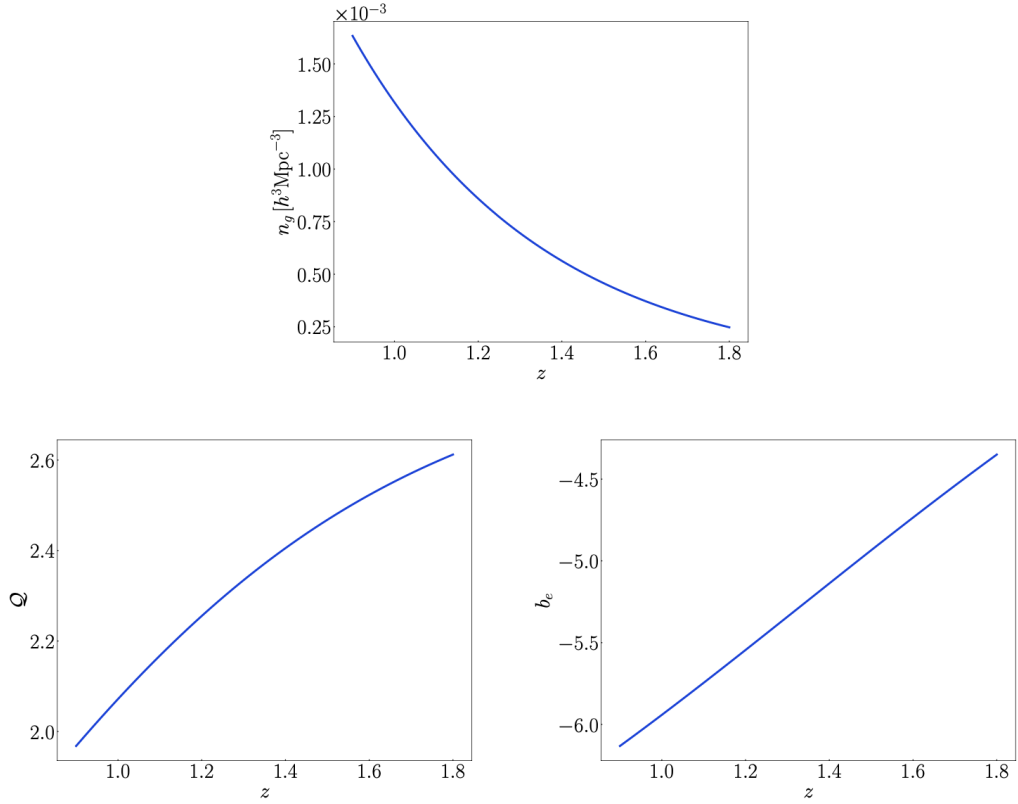


Figure 3.10.: The number density (*top*), magnification bias (*bottom left*), and evolution bias (*bottom right*) for a Euclid-like survey with the Model 3 luminosity function and flux cut $F_c = 2 \cdot 10^{-16} \text{ erg cm}^{-2} \text{s}^{-1}$. Figure taken from [122].

Then resulting SNR for a Euclid-like survey with the Model 3 luminosity function is shown in 3.11. We still obtain a value of ~ 18 for the cumulative signal-to-noise ratio, which still points towards potential detectability despite the reduced redshift range.

3.3.5. Recap of detectability in spectroscopic surveys

Before we move on to discuss detectability of the relativistic bispectrum in 21cm IM surveys, let us recap what we have found in the case of Stage IV H α spectroscopic surveys similar to *Euclid*.

As shown by [88], the tree-level galaxy bispectrum in Fourier space has an imaginary part which is a unique signal of the leading-order relativistic corrections in redshift space. These corrections arise from Doppler and other line-of-sight effects on the past lightcone [see (3.6), (2.7)]. In the galaxy bispectrum, the corrections scale

3. Detectability in next-generation galaxy surveys

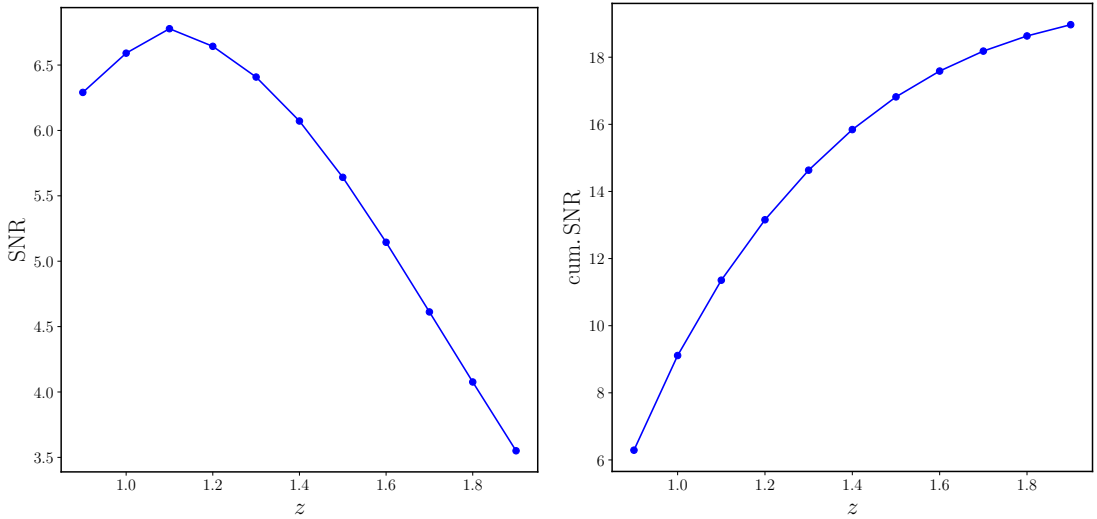


Figure 3.11.: SNR per z -bin (*left*) and cumulative SNR (*right*) for a Euclid-like survey with a Model 3 luminosity function. We obtain a cumulative SNR of ~ 18 , which points towards potential detectability.

as $i(\mathcal{H}/k)P^2$, where P is the linear matter power spectrum [see (3.8)–(3.10)]. By contrast, at leading order in the galaxy power spectrum, the relativistic correction is real and scales as $(\mathcal{H}/k)^2 P$ – i.e., it is suppressed by a further factor of \mathcal{H}/k . Only the cross-power spectrum of two different tracers produces an imaginary contribution that scales as $i(\mathcal{H}/k)P$ [89].¹

For a single tracer, the $(\mathcal{H}/k)^2$ relativistic signal in the galaxy *power* spectrum is not detectable, even for a cosmic-variance limited survey [118]. The galaxy bispectrum of a single tracer, with its $i(\mathcal{H}/k)$ relativistic contribution, improves the chances of detectability. In addition, the relativistic contribution in the bispectrum couples to short-scale Newtonian terms – which means that the signal is not confined to very large scales, unlike the case of the power spectrum. We confirmed the expectations of detectability by showing that the signal to noise on the imaginary relativistic part is $\mathcal{O}(10)$ for a Stage IV H α spectroscopic survey similar to Euclid [see Figure 3.4]. We checked that detectability is not compromised by including the uncertainties on two cosmological growth parameters, σ_8 and γ [Figure 3.9], assuming that other cosmological and nuisance parameters are determined by the Newtonian power spectrum and bispectrum.

The relativistic SNR depends on the $k_{\max}(z)$ assumed, because of the coupling of relativistic effects to short-scale Newtonian terms [Figure 3.5], and we made a con-

¹See also [92, 128–134] for the corresponding effect in the two-point correlation function, and see [135] for an imaginary short-scale contribution from neutrino drag on haloes.

3. Detectability in next-generation galaxy surveys

servative choice (3.27), which includes a redshift dependence to reflect the weakening of nonlinearity at higher z . Accurate modelling of nonlinear effects would allow us to increase the SNR – this is not at all specific to the relativistic signal, but is required for the standard analysis of RSD.

The relativistic SNR also relies on the largest available scales, but very little signal is lost if k_{\min}/k_f is increased by a factor up to 5, and even a factor of 10 increase leaves a detectable SNR [Figure 3.7].

By contrast, the SNR depends strongly on accurate modelling of the second-order part of the relativistic correction [Figure 3.8]. This includes both the theoretical form (2.7), and the two astrophysical parameters that do not appear in the Newtonian approximation of the galaxy bispectrum: the evolution bias b_e (measuring the deviation from comoving number conservation) and the magnification bias \mathcal{Q} (which is brought into play by a Doppler correction to standard lensing magnification). A key feature of our analysis is a physically self-consistent derivation of these quantities from the luminosity function [Figure 3.3 and (3.46), (3.47)]. We do this for an observationally motivated luminosity function model too, the so-called Model 3 [Figure 3.10]. We showed that the SNR is very sensitive to these parameters [Figure 3.6], which underlines the need for accurate physical modelling.

We assumed a Gaussian covariance in our computations, but we used the approximation of [123] to include non-Gaussian corrections.

It is important to note that using Gaussian covariance and Fisher matrix analysis are approximations that are not necessarily trustworthy in the case of low SNRs, as larger signal strengths correspond to lower statistical errors [136].

Further work should include the window function which we have neglected. The imaginary part of the galaxy bispectrum generates a dipole, as shown in [88]. This suggests a multipole analysis that uses the relativistic dipole in addition to the monopole and quadrupole, which are unaffected by relativistic effects at leading order. The window function can also have an imaginary part [137], which will need to be corrected for. The dipole from the imaginary part of the bispectrum vanishes in equilateral configurations [88], which may help to disentangle the relativistic dipole from that of the window function.

Our analysis, in common with other works on the Fourier bispectrum, implicitly uses the plane-parallel approximation, since the line-of-sight direction \mathbf{n} is fixed. At the cost of significant complexity, the approximation can be avoided, for example

3. Detectability in next-generation galaxy surveys

by using a Fourier-Bessel analysis of bispectrum multipoles [138]. Further work is needed to address this, but we note that errors from the approximation are mitigated in high redshift surveys such as the one considered here.

Finally, further work also needs to include the effects of lensing magnification, which are excluded in the standard Fourier analysis, but have been included in the galaxy angular bispectrum [103, 139–141] and in a spherical Bessel analysis [142].

3.4. 21cm intensity mapping surveys

In this work, we investigate the detectability of the relativistic signal in the bispectrum of various planned 21cm intensity mapping surveys at post-reionisation redshifts. The 21cm emission line of neutral hydrogen (HI) is measured without detecting the individual galaxies that contain HI. This results in brightness temperature maps that trace the large-scale structure with exquisite redshift precision. In Section 2 we discuss the leading order relativistic form of the temperature contrast up to second order, and its contribution to the bispectrum. Section 3 describes the signal, modelled using the tree-level bispectrum with the addition of a phenomenological model to account for RSD ‘fingers-of-god’ nonlinearity. Foreground contamination overwhelms the signal, and cleaning techniques must be applied which lead to a loss of signal in regions of Fourier space, which we take into account. We also discuss the effects of telescope beams and the instrumental noise. Our forecast signal to noise for future surveys is presented in Section 4, and we conclude in Section 5.

3.4.1. Relativistic effects in the 21cm IM bispectrum

The HI brightness temperature measured at redshift z in direction \mathbf{n} is related to the observed number of 21cm emitters per redshift per solid angle, N_{HI} , as follows (see [118, 143] for details):

$$T_{\text{HI}}(z, \mathbf{n}) = \text{const.} \frac{N_{\text{HI}}(z, \mathbf{n})}{d_A(z, \mathbf{n})^2}, \quad (3.64)$$

where d_A is the angular diameter distance.

3. Detectability in next-generation galaxy surveys

The background HI brightness temperature follows from (3.64) as [144]

$$\bar{T}_{\text{HI}}(z) = 189h \frac{(1+z)H_0}{\mathcal{H}(z)} \Omega_{\text{HI}}(z) \text{ mK.} \quad (3.65)$$

Here $h = H_0/(100 \text{ km/s})$, $\mathcal{H} = (\ln a)'$ is the conformal Hubble rate, and $\Omega_{\text{HI}}(z)$ is the comoving HI density in units of the critical density today, which is currently poorly constrained by observations and is modelled by simulations. We use the fit in [145]:

$$\bar{T}_{\text{HI}}(z) = 0.056 + 0.23z - 0.024z^2 \text{ mK.} \quad (3.66)$$

The temperature fractional perturbation is,

$$\Delta_{\text{HI}}(z, \mathbf{n}) = \frac{T_{\text{HI}}(z, \mathbf{n}) - \bar{T}_{\text{HI}}(z)}{\bar{T}_{\text{HI}}(z)}. \quad (3.67)$$

Using (3.64), this leads to the following perturbative expansion (our convention is $X + X^{(2)}/2$). (A clear and concise derivation of the following expressions for Δ and $\Delta^{(2)}$ is given in Appendix A of [95].)

- **At first order** [143]:

$$\Delta \equiv \Delta_{\text{HI}}^{(1)} = \Delta_N + \Delta_D, \quad \Delta_N = b_1 \delta_m - \frac{1}{\mathcal{H}} \partial_r(\mathbf{v} \cdot \mathbf{n}), \quad \Delta_D = A(\mathbf{v} \cdot \mathbf{n}). \quad (3.68)$$

Here r is the radial comoving distance and $\mathbf{v} = \nabla V$ is the peculiar velocity. Δ_N is the standard density + RSD term, which scales as δ_m . Δ_D is the dominant relativistic correction, scaling as $i(\mathcal{H}/k)\delta_m$ in Fourier space. This Doppler term has coefficient

$$A = b_e - 2 - \frac{\mathcal{H}'}{\mathcal{H}^2} = -\frac{d \ln [(1+z)\bar{T}_{\text{HI}}]}{d \ln(1+z)}, \quad (3.69)$$

where the evolution bias is [146],

$$b_e = -\frac{d \ln [(1+z)^{-1}\mathcal{H}\bar{T}_{\text{HI}}]}{d \ln(1+z)}. \quad (3.70)$$

We omit sub-leading relativistic corrections that scale as $(\mathcal{H}/k)^2\delta_m$.

- **At second order** [114] (see also [88, 95, 110, 140, 147]):

$$\Delta^{(2)} \equiv \Delta_{\text{HI}}^{(2)} = \Delta_N^{(2)} + \Delta_D^{(2)}, \quad (3.71)$$

3. Detectability in next-generation galaxy surveys

$$\Delta_N^{(2)} = b_1 \delta_m^{(2)} + b_2 (\delta_m)^2 + b_{s^2} s^2 + \text{RSD}^{(2)}, \quad (3.72)$$

$$\begin{aligned} \Delta_D^{(2)} = & A(\mathbf{v}^{(2)} \cdot \mathbf{n}) + 2 \left[b_1(A+f) + \frac{b'_1}{\mathcal{H}} \right] (\mathbf{v} \cdot \mathbf{n}) \delta_m + \frac{1}{\mathcal{H}} (8 - 4A - 3\Omega_m) \\ & \cdot (\mathbf{v} \cdot \mathbf{n}) \partial_r (\mathbf{v} \cdot \mathbf{n}) + \frac{2}{\mathcal{H}^2} [(\mathbf{v} \cdot \mathbf{n}) \partial_r^2 \Phi - \Phi \partial_r^2 (\mathbf{v} \cdot \mathbf{n})] - \frac{2}{\mathcal{H}} \partial_r (\mathbf{v} \cdot \mathbf{v}) \\ & + 2 \frac{b_1}{\mathcal{H}} \Phi \partial_r \delta_m. \end{aligned} \quad (3.73)$$

In (3.72), $b_{s^2} s^2$ is the tidal bias contribution and RSD⁽²⁾ is the standard second-order RSD contribution (see [114] for details). The bias parameters are computed via a halo model and are shown in Figure 3.12, together with the evolution bias. In (3.73), we see the Doppler terms and the line-of-sight gradients that make up the dominant relativistic contribution. Φ is the gravitational potential and $\Omega_m = \Omega_{m0}(1+z)H_0^2/\mathcal{H}^2$. We neglect sub-dominant relativistic effects in $\Delta^{(2)}$ that scale as $(\mathcal{H}/k)^2(\delta_m)^2$.

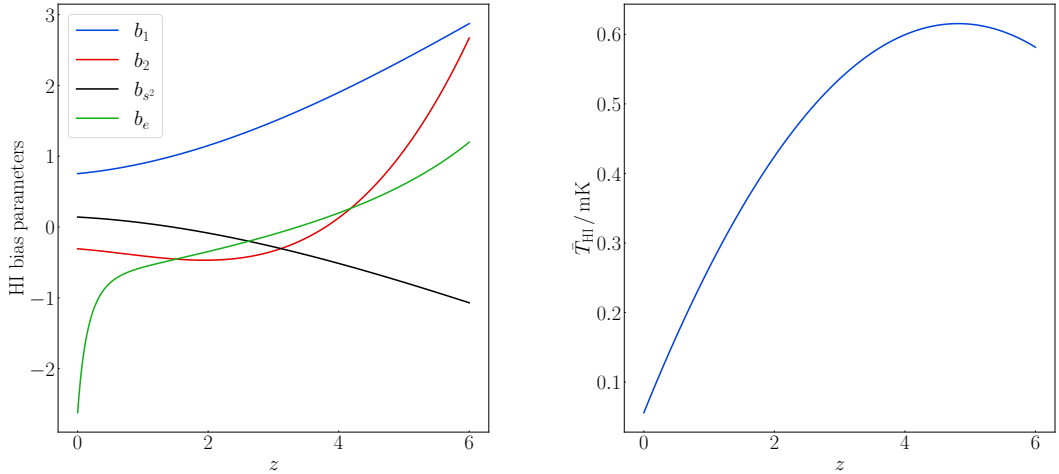


Figure 3.12.: HI clustering and evolution bias parameters (*left*) and background temperature (*right*).

- **Lensing contribution:**

At first order, there is no lensing contribution to Δ [143]. The general case of galaxy number density contrast contains a lensing contribution $2(Q-1)\kappa$ to Δ_g , where κ is the convergence [90]. For HI emitters in intensity mapping, the magnification bias satisfies

$$Q \equiv -\frac{\partial \ln \bar{N}_{\text{HI}}}{\partial \ln L} \Big|_c = 1, \quad (3.74)$$

3. Detectability in next-generation galaxy surveys

where c indicates evaluation at the luminosity cut.

At second order, (3.64) shows that there is also no contribution to $\Delta^{(2)}$ from lensing convergence [140, 148]. We can recover this result from the full general expression for second-order number density contrast [98–101, 149], by imposing (3.74) together with the conditions [140]

$$\frac{\partial^2 \ln \bar{N}_{\text{HI}}}{\partial (\ln L)^2} \Big|_c = 0, \quad \frac{\partial b_1}{\partial \ln L} \Big|_c = 0. \quad (3.75)$$

There remains however a lensing deflection contribution $\nabla_{\perp a} \Delta \nabla_{\perp}^a \phi$ to $\Delta^{(2)}$, where $\nabla_{\perp a}$ is a screen-space gradient and ϕ is the lensing potential [110, 140, 148]. In the bispectrum the contribution of this term is negligible for equal-redshift correlations [140, 150]. Since we only consider the bispectrum at equal redshifts, we can safely neglect this term.

In addition to this, recent work presented in [151] derived the expected contribution from the lensing-ISW bispectrum to the 21cm bispectrum. This is due to the evolution of the density field along the line-of-sight. As it turns out, the lensing-ISW bispectrum introduces negligible bias to the parameter constraints, and hence can be safely ignored.

In Fourier space, the HI bispectrum at tree level is defined by,

$$\langle \Delta(z, \mathbf{k}_1) \Delta(z, \mathbf{k}_2) \Delta^{(2)}(z, \mathbf{k}_3) \rangle + 2 \text{ cp} = 2(2\pi)^3 B_{\text{HI}}(z, \mathbf{k}_1, \mathbf{k}_2, \mathbf{k}_3) \delta^{\text{Dirac}}(\mathbf{k}_1 + \mathbf{k}_2 + \mathbf{k}_3), \quad (3.76)$$

where cp denotes cyclic permutation. It follows that,

$$B_{\text{HI}}(z, \mathbf{k}_1, \mathbf{k}_2, \mathbf{k}_3) = \mathcal{K}^{(1)}(z, \mathbf{k}_1) \mathcal{K}^{(1)}(z, \mathbf{k}_2) \mathcal{K}^{(2)}(z, \mathbf{k}_1, \mathbf{k}_2, \mathbf{k}_3) P_{\text{m}}(z, k_1) P_{\text{m}}(z, k_2) + 2 \text{ cp}, \quad (3.77)$$

where P_{m} is the linear matter power spectrum (computed using CLASS [152]). From now on, we often drop the z dependence for brevity. The bispectrum kernels are as follows:

- **Standard (Newtonian) kernels:**

$$\mathcal{K}_{\text{N}}^{(1)}(\mathbf{k}_1) = b_1 + f \mu_a^2, \quad (3.78)$$

$$\begin{aligned} \mathcal{K}_{\text{N}}^{(2)}(\mathbf{k}_1, \mathbf{k}_2, \mathbf{k}_3) &= b_1 F_2(\mathbf{k}_1, \mathbf{k}_2) + b_2 + f \mu_3^2 G_2(\mathbf{k}_1, \mathbf{k}_2) + f \mathcal{Z}_2(\mathbf{k}_1, \mathbf{k}_2) \\ &\quad + b_{s^2} S_2(\mathbf{k}_1, \mathbf{k}_2), \end{aligned} \quad (3.79)$$

3. Detectability in next-generation galaxy surveys

where f is the linear matter growth rate, $\mu_a = \hat{\mathbf{k}}_a \cdot \mathbf{n}$ and the standard $F_2, G_2, \mathcal{Z}_2, S_2$ kernels are given in [114].

- **Leading-order relativistic kernels:**

$$\mathcal{K}_{\text{D}}^{(1)}(\mathbf{k}_1) = i \mathcal{H} f A \frac{\mu_a}{k_a}, \quad (3.80)$$

$$\begin{aligned} \mathcal{K}_{\text{D}}^{(2)}(\mathbf{k}_1, \mathbf{k}_2, \mathbf{k}_3) = & i \mathcal{H} f \left\{ A \frac{\mu_3}{k_3} G_2(\mathbf{k}_1, \mathbf{k}_2) + \left[b_1 (A + f) + \frac{b'_1}{\mathcal{H}} \right] \left(\frac{\mu_1}{k_1} + \frac{\mu_2}{k_2} \right) \right. \\ & - \frac{3}{2} \Omega_m \left(\mu_1^3 \frac{k_1}{k_2^2} + \mu_2^3 \frac{k_2}{k_1^2} \right) + \left[\frac{3}{2} \Omega_m (1 + f) + 2f (A - 2) \right] \cdot \\ & \left. \mu_1 \mu_2 \left(\frac{\mu_1}{k_2} + \frac{\mu_2}{k_1} \right) + 2f \hat{\mathbf{k}}_1 \cdot \hat{\mathbf{k}}_2 \left(\frac{\mu_1}{k_1} + \frac{\mu_2}{k_2} \right) \right. \\ & \left. - \frac{3 \Omega_m b_1}{2f} \left(\mu_1 \frac{k_1}{k_2^2} + \mu_2 \frac{k_2}{k_1^2} \right) \right\}, \end{aligned} \quad (3.81)$$

$$\begin{aligned} & \mu_1 \mu_2 \left(\frac{\mu_1}{k_2} + \frac{\mu_2}{k_1} \right) + 2f \hat{\mathbf{k}}_1 \cdot \hat{\mathbf{k}}_2 \left(\frac{\mu_1}{k_1} + \frac{\mu_2}{k_2} \right) \\ & - \frac{3 \Omega_m b_1}{2f} \left(\mu_1 \frac{k_1}{k_2^2} + \mu_2 \frac{k_2}{k_1^2} \right) \end{aligned} \quad (3.82)$$

where A is given by (3.69). These follow from (3.68) and (3.73), and agree with [114] when we impose (3.69), (3.74) and (3.75).

- **Complex bispectrum:**

From (3.78)–(3.82) we see that B_{HI} is complex: the imaginary part is given purely by local relativistic corrections, while at leading order, i.e. neglecting relativistic terms of $\mathcal{O}(\mathcal{H}^2/k^2)$, the real part is given purely by the standard Newtonian bispectrum:

$$\text{Re}(B_{\text{HI}}) = B_{\text{N}} = \mathcal{K}_{\text{N}}^{(1)}(\mathbf{k}_1) \mathcal{K}_{\text{N}}^{(1)}(\mathbf{k}_2) \mathcal{K}_{\text{N}}^{(2)}(\mathbf{k}_1, \mathbf{k}_2, \mathbf{k}_3) P_{\text{m}}(k_1) P_{\text{m}}(k_2) + 2 \text{ cp}, \quad (3.83)$$

$$\begin{aligned} i \text{Im}(B_{\text{HI}}) = B_{\text{D}} = & \left\{ \left[\mathcal{K}_{\text{N}}^{(1)}(\mathbf{k}_1) \mathcal{K}_{\text{D}}^{(1)}(\mathbf{k}_2) + \mathcal{K}_{\text{D}}^{(1)}(\mathbf{k}_1) \mathcal{K}_{\text{N}}^{(1)}(\mathbf{k}_2) \right] \mathcal{K}_{\text{N}}^{(2)}(\mathbf{k}_1, \mathbf{k}_2, \mathbf{k}_3) \right. \\ & \left. + \mathcal{K}_{\text{N}}^{(1)}(\mathbf{k}_1) \mathcal{K}_{\text{N}}^{(1)}(\mathbf{k}_2) \mathcal{K}_{\text{D}}^{(2)}(\mathbf{k}_1, \mathbf{k}_2, \mathbf{k}_3) \right\} P_{\text{m}}(k_1) P_{\text{m}}(k_2) + 2 \text{ cp}. \end{aligned} \quad (3.84)$$

It is apparent that $B_{\text{N}} \sim P_{\text{m}}^2$ while $B_{\text{D}} \sim i(\mathcal{H}/k)P_{\text{m}}^2$. Equation (3.84) makes explicit the coupling of relativistic and Newtonian terms in the bispectrum.

3. Detectability in next-generation galaxy surveys

HI bias parameters

We follow [110] to compute b_1 and b_2 from a halo-model approach,

$$b_1 = 1 + \left\langle \frac{2p + (q\nu - 1) [1 + (q\nu)^p]}{\delta_{\text{cr}} [1 + (q\nu)^p]} \right\rangle_m, \quad (3.85)$$

$$b_2 = \frac{8}{21} (b_1 - 1) + \left\langle \frac{2p (2p + 2\nu q - 1) + q\nu (q\nu - 3) [1 + (q\nu)^p]}{\delta_{\text{cr}}^2 [1 + (q\nu)^p]} \right\rangle_m, \quad (3.86)$$

where the parameters p , q and ν are related to the Sheth-Tormen distribution function (see [153–155] for more details), and δ_{cr} is the critical density at which halos collapse spherically [156],

$$\delta_{\text{cr}}(z) = \frac{3(12\pi)^{2/3}}{20} [1 + 0.0123 \log \Omega_m(z)] \dots \quad (3.87)$$

The mass average is defined by

$$\langle X_h(z, \mathbf{x}) \rangle_m = \frac{\int_{M_-}^{M_+} dM X_h(z, \mathbf{x}, M) M_{\text{HI}}(M) n_h(z, \mathbf{x}, M)}{\int_{M_-}^{M_+} dM M_{\text{HI}}(M) n_h(z, \mathbf{x}, M)}, \quad (3.88)$$

where M is the mass of halos that can host HI gas, and M_{\pm} are the lower and upper mass limits, which are related to the circular velocities of the galaxies [157]. n_h is the halo mass function [153, 154, 158], and M_{HI} is the HI mass function, which is assumed to follow a power law [159],

$$M_{\text{HI}}(M) \propto M^{0.6}. \quad (3.89)$$

Figure 3.2 shows the numerical results from (3.85) and (3.86). Fitting formulas for the bias parameters are

$$b_1(z) = 0.754 + 0.0877z + 0.0607z^2 - 0.00274z^3, \quad (3.90)$$

$$b_2(z) = -0.308 - 0.0724z - 0.0534z^2 + 0.0247z^3. \quad (3.91)$$

Assuming that halo formation is a local process in Lagrangian space and that there is no initial tidal bias, the tidal bias is [158],

$$b_{s^2} = \frac{4}{7} (1 - b_1). \quad (3.92)$$

3.4.2. Effects of foregrounds

Foreground contamination is the major systematic confronting 21cm intensity mapping. All sources of radio emission within our observing band make up the contamination – except of course the cosmological signal of interest. The main contaminant is the galactic synchrotron radiation. Other contaminants include free-free emission, bright radio point sources, and unresolved point sources [160]. The effect of these other sources of foreground contamination is subdominant to that of synchrotron radiation, but may still dominate over the fainter cosmological signal, and hence are important to take into consideration. Cleaning techniques are very efficient at recovering the cosmological signal in regions of $(k_{\parallel}, k_{\perp})$ space (see e.g. [157, 159, 161–171]). A realistic model of bispectrum measurements should include modelling of foreground removal. However, our focus is on the relativistic signal in the bispectrum and so we take a simpler approach – by excising the regions of $(k_{\parallel}, k_{\perp})$ space where foreground cleaning does not recover the signal efficiently.

HI intensity mapping surveys are planned for next-generation radio dish arrays, including MeerKAT², SKA1-MID³, and HIRAX⁴. We will also consider surveys with PUMA⁵ in its initial phase (Petite) (note that PUMA is currently still a proposal).

Intensity mapping surveys can be done in 2 survey modes:

- Single-dish (SD) mode: auto-correlation signals from single dishes are added.
- Interferometer (IF) mode: cross-correlation signals from array elements are combined.

In both SD- and IF-mode surveys, foreground cleaning effectively removes large-scale radial modes because of the smoothness in frequency of the main foreground emissions. In order to model the effects of foreground cleaning, we remove radial modes $k_{\parallel} \equiv \mu k$ that are smaller than a critical scale $k_{\parallel fg}$ [71]. We impose this via an exponential damping factor [157],

$$D_{fg}(k, \mu) = 1 - \exp \left[- \left(\frac{\mu k}{k_{\parallel fg}} \right)^2 \right] \quad \text{for SD and IF survey modes.} \quad (3.93)$$

²www.sarao.ac.za/science/meerkat/

³www.skatelescope.org/

⁴hirax.ukzn.ac.za/

⁵www.puma.bnl.gov/

3. Detectability in next-generation galaxy surveys

Then,

$$P_{\text{HI}}(k, \mu, z) \rightarrow D_{\text{fg}}(k, \mu) P_{\text{HI}}(k, \mu, z), \quad (3.94)$$

$$B_{\text{HI}}(k_a, \mu_a, z) \rightarrow D_{\text{fg}}(k_1, \mu_1) D_{\text{fg}}(k_2, \mu_2) D_{\text{fg}}(k_3, \mu_3) B_{\text{HI}}(k_a, \mu_a, z). \quad (3.95)$$

The value of $k_{\parallel \text{fg}}$ can be reduced by techniques which reconstruct long modes from the information in measured short modes. This technique has been applied to HI intensity mapping by [172, 173]. Taking into account reconstruction, we choose,

$$k_{\parallel \text{fg}} = 0.01 h \text{ Mpc}^{-1}, \quad (3.96)$$

but we will also consider an optimistic case, $k_{\parallel \text{fg}} = 0.005 h \text{ Mpc}^{-1}$, that anticipates further developments of the reconstruction technique.

IF-mode surveys lose additional signal due to the fact that interferometers are chromatic, i.e. a fixed physical baseline length probes different angular scales at different frequencies. This causes smooth foregrounds to leak into high- k_{\perp} modes [166, 167, 174]. The signal loss may be accounted for by excluding the region known as the foreground wedge [161, 163]:

$$|k_{\parallel}| > k_{\text{wedge}}(z) k_{\perp} \quad \text{for IF survey mode}, \quad (3.97)$$

where $k_{\perp} = \sqrt{1 - \mu^2} k$ and k_{wedge} is modelled as,

$$k_{\text{wedge}}(z) = r(z) \mathcal{H}(z) \sin [0.61 N_w \theta_b(z)]. \quad (3.98)$$

The beam (defining the IF field of view) is given for a dish array by,

$$\theta_b(z) = 1.22 \frac{\lambda(z)}{D_d}, \quad (3.99)$$

where $\lambda(z) = \lambda_{21}(1 + z)$ and D_d is the dish diameter. N_w is the number of primary beams away from the beam centre that contaminate the signal. The wedge effect is a technical problem that can be mitigated (and in principle removed) by calibration of baselines [175]. Following [176], we take

$$N_w = 0, 1, 3, \quad (3.100)$$

where 0 is the most optimistic possibility (wedge removed by calibration) and 3 is a pessimistic case.

3.4.3. Maximum and minimum scales probed

The nonlinearity limit $k \leq k_{\max}(z)$ given in (3.27), defines a minimum wavelength $2\pi/k_{\max}(z)$ that is independent of surveys and is determined purely by dark matter clustering. It applies to both SD- and IF-mode surveys. However, in the case of IF-mode surveys, there is also a lower limit on angular scales, i.e. an upper limit on transverse wavenumbers, via $k_{\perp} = 2\pi/(r\theta)$. This arises because the maximum baseline D_{\max} determines the angular resolution and the upper limit can be roughly estimated by a cut-off [150, 157, 174, 176],

$$k_{\perp \max}^{\text{IF}}(z) \approx \frac{2\pi D_{\max}}{r(z) \lambda(z)}. \quad (3.101)$$

In our computations, we do not use this cut-off since it is effectively imposed by the baseline density factor (see Section 3.4.4).

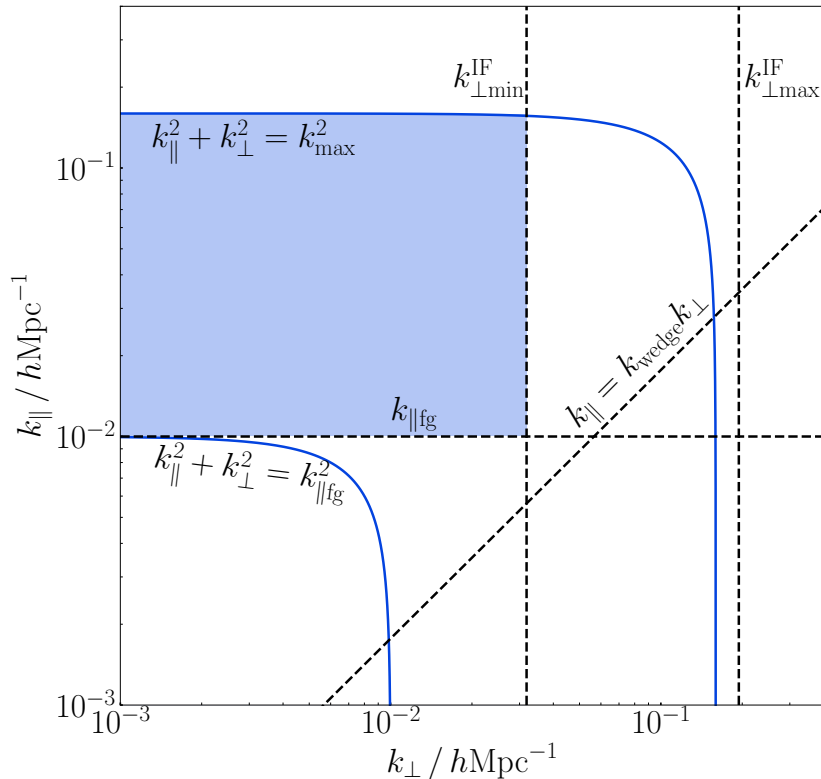


Figure 3.13.: Schematic of important scales in the k_{\parallel}, k_{\perp} -plane at fixed z . Shading indicates the included region for SD mode (light) and IF mode (dark).

3. Detectability in next-generation galaxy surveys

In principle, the maximum wavelength probed by HI intensity surveys at redshift z is $2\pi/k_f(z)$, where the fundamental mode k_f is determined by the comoving volume of the redshift bin, via equation 3.20. However, foreground cleaning imposes on both SD- and IF-mode surveys the limiting minimum radial wavenumber $k_{\parallel\text{fg}}$, given by (3.96). Since $k^2 = k_{\parallel}^2 + k_{\perp}^2$, this means that

$$k > k_{\parallel\text{fg}} \quad \text{which implies} \quad k > k_{\min} = \max \{k_f(z), k_{\parallel\text{fg}}\}. \quad (3.102)$$

In IF-mode surveys there is a further minimum wavenumber, corresponding to the maximum angular scale that can be probed. This limit depends on the minimum baseline and is given by [150, 157, 174, 176],

$$k_{\perp\min}^{\text{IF}}(z) = \frac{2\pi}{r(z)\theta_b(z)}. \quad (3.103)$$

Since $k > k_{\perp}$, we have

$$k > k_{\min} = \max \{k_{\perp\min}^{\text{IF}}(z), k_f(z), k_{\parallel\text{fg}}\} \quad \text{for IF surveys.} \quad (3.104)$$

The scales from foreground cleaning and the maximum and minimum scales are shown schematically in Figure 3.13. This does not include the effects of the beam in SD mode; see Figure 3.17.

3.4.4. Instrumental noise

In HI intensity mapping for the scales and redshifts we consider, the shot noise is much smaller than the instrumental noise for next-generation surveys⁶ and can be safely neglected [144, 178]. The noise power spectrum for the fractional temperature perturbation is then determined by instrumental noise and is given by [157, 174]:⁷

$$P_{\text{noise}}(z) = \frac{2\pi f_{\text{sky}}}{\nu_{21} t_{\text{tot}}} \frac{(1+z)r(z)^2}{\mathcal{H}(z)} \left[\frac{T_{\text{sys}}(z)}{\bar{T}_{\text{HI}}(z)} \right]^2 \frac{\alpha(z, k_{\perp})}{\beta(z, k_{\perp})^2} h^{-3} \text{Mpc}^3. \quad (3.105)$$

⁶For the futuristic PUMA (Full) survey, the noise is low enough to be comparable to the shot noise [177].

⁷It is also possible to put the beam factor β in the signal, rather than in the noise; see e.g. [179] for a discussion.

3. Detectability in next-generation galaxy surveys

Here t_{tot} is the total observing time, and the system temperature may be modelled as [167]:

$$T_{\text{sys}}(z) = T_{\text{d}}(z) + T_{\text{sky}}(z) = T_{\text{d}}(z) + 2.7 + 25 \left[\frac{400 \text{ MHz}}{\nu_{21}} (1+z) \right]^{2.75} \text{ K}, \quad (3.106)$$

where T_{d} is the dish receiver temperature. (We consider only dish arrays.)

In (3.105), the dish density factor α and the effective beam β depend on the survey mode as follows [150, 157, 166, 167, 180],

$$\alpha_{\text{SD}} = \frac{1}{N_{\text{d}}}, \quad \beta_{\text{SD}} = \exp \left[-\frac{k_{\perp}^2 r(z)^2 \theta_{\text{b}}(z)^2}{16 \ln 2} \right], \quad (3.107)$$

$$\alpha_{\text{IF}} = \left[\frac{\lambda(z)^2}{A_{\text{e}}} \right]^2 \frac{1}{n_{\text{b}}(z, k_{\perp})}, \quad \beta_{\text{IF}} = \theta_{\text{b}}(z). \quad (3.108)$$

Here N_{d} is the number of dishes and A_{e} is the effective beam area,

$$A_{\text{e}} = 0.7 A_{\text{d}}, \quad A_{\text{d}} = \frac{\pi}{4} D_{\text{d}}^2. \quad (3.109)$$

The dimensionless n_{b} is the baseline density in the image plane (assuming azimuthal symmetry), which is determined by the array distribution. The total number of baselines is $\int d^2 \mathbf{u} n_{\text{b}}(u) = N_{\text{d}}(N_{\text{d}} - 1)/2$. A physical baseline length L is related to an image-plane scale u as

$$L = u \lambda = \frac{k_{\perp} r}{2\pi} \lambda. \quad (3.110)$$

Then the image-plane and physical distributions of the array are related by [167],

$$n_{\text{b}}(z, u) = \lambda(z)^2 n_{\text{b}}^{\text{phys}}(L). \quad (3.111)$$

3.4.5. Future 21cm IM surveys

We consider surveys proposed for the following dish arrays:

- SD mode: MeerKAT, SKA1-MID.
- IF mode: HIRAX, PUMA (Petite).

The survey specifications are given in Table 3.2, based on [145, 169, 176, 181, 182]. Limiting wavenumbers for large wavelengths are shown for these surveys in Fig-

3. Detectability in next-generation galaxy surveys

ure 3.15: the fundamental wavenumber 3.20, the minimum radial wavenumber (3.96) from foreground cleaning and the IF-mode minimum wavenumber (3.103).

Table 3.2.: HI intensity mapping survey specifications. (For *, see Table 3.4.)

Survey	z -range	f_{sky}	t_{tot} [10^3 hr]	T_d [K]	D_d [m]	N_d	D_{max} [m]
MeerKAT L Band	0.10–0.58	0.10	4	*	13.5	64	—
MeerKAT UHF Band	0.40–1.45	0.10	4	*	13.5	64	—
SKA1-MID Band 1	0.35–3.05	0.48	10	*	15.0	197	—
SKA1-MID Band 2	0.10–0.49	0.48	10	*	15.0	197	—
HIRAX	0.75–2.00	0.36	10	50	6.0	1024	270
PUMA (Petite)	2.00–6.00	0.50	40	50	6.0	5000	600

Table 3.3.: Parameters in (3.112) (from [167]).

Survey	a	b	c	d	e	N_s
HIRAX	0.4847	−0.3300	1.3157	1.5974	6.8390	32
PUMA (Petite)	0.5698	−0.5274	0.8358	1.6635	7.3177	100

For the system temperature, we use the results of measurements and simulations for MeerKAT and SKA1-MID, given below in Table 3.4 and Figure 3.14. For HIRAX and PUMA, we use the fit (3.106).

In IF mode, HIRAX is assumed to be a square-packed array, while PUMA is taken as hexagonal-packed in a circular area, with 50% fill factor. We follow [176] and use the fitting formula from [167] for the baseline density of such arrays,

$$n_b^{\text{phys}}(L) = \left(\frac{N_s}{D_d} \right)^2 \frac{a + b(L/L_s)}{1 + c(L/L_s)^d} \exp[-(L/L_s)^e], \quad (3.112)$$

where $L_s = N_s D_d$ and $N_s^2 = N_d$. The parameters in (3.112) are given in Table 3.3, and $n_b^{\text{phys}}(L)$ is shown in Figure 3.16.

In the case of PUMA, we take account of the 50% fill factor as follows. We use double the number of dishes to define N_s for the computation of (3.112), i.e. $N_s^2 = 2 \cdot 5000$. Then we remove half of the dishes without changing the baseline, i.e. without changing the shape and ground-area of the array.

The noise power spectra of the surveys at fixed redshift are displayed in Figure 3.17. For SD-mode surveys, the poor angular resolution is reflected in the blow-up of noise due to the beam in (3.107). The minimum transverse scale for IF-mode surveys is shown as a sharp cut-off, as in (3.103), with effectively infinite noise. Figure 3.17 also shows the smooth blow-up of IF-mode noise on small transverse scales, which

3. Detectability in next-generation galaxy surveys

Table 3.4.: System temperatures for MeerKAT and SKA1-MID, used in Figure 3.3 (from [183]).

z	MeerKAT L Band	MeerKAT UHF Band	SKA1-MID Band 1	SKA1-MID Band 2
z	$T_{\text{sys}} / \text{K}$	$T_{\text{sys}} / \text{K}$	$T_{\text{sys}} / \text{K}$	$T_{\text{sys}} / \text{K}$
0.136	19.2	0.420	20.3	0.403
0.183	19.7	0.495	21.0	0.470
0.235	20.3	0.578	21.7	0.539
0.291	20.9	0.671	22.5	0.612
0.352	21.5	0.775	23.5	0.767
0.420	22.3	0.893	24.7	0.850
0.495	23.1	1.03	26.1	0.938
0.578	24.0	1.18	27.9	1.03
		1.37	30.3	1.12
		1.45	31.5	1.22
				1.33
				1.44
				1.55
				1.67
				1.80
				1.93
				2.07
				2.22
				2.37
				2.54
				2.69
				2.87
				3.05
				74.8

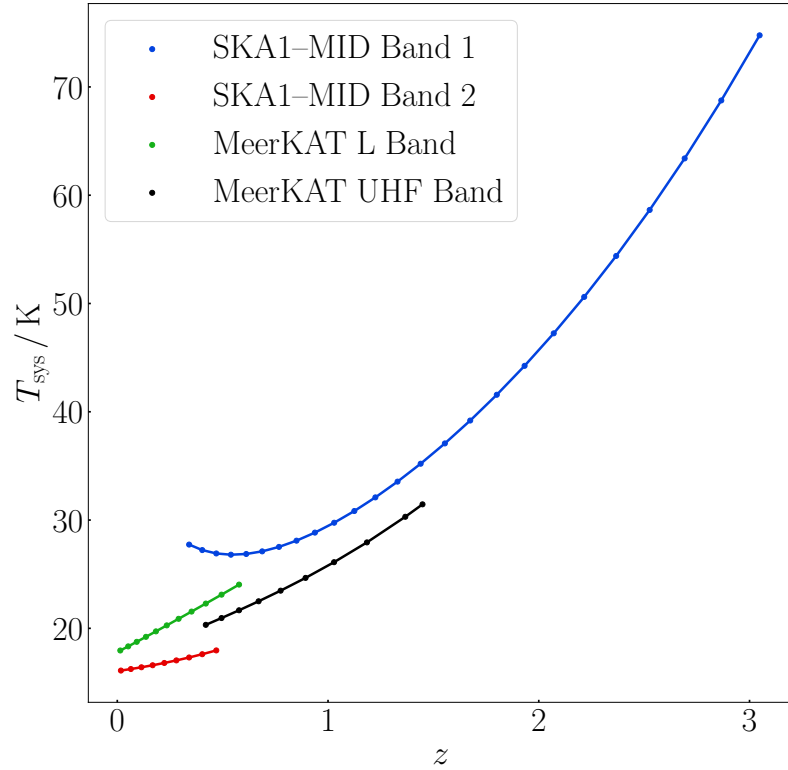


Figure 3.14.: T_{sys} for the different frequency bands of MeerKAT and SKA1 (from Table 3.4).

results from the fact that $n_b \rightarrow 0$ as the baseline approaches its maximum D_{max} (see Figure 3.16). The unbounded increase of noise kills the signal, corresponding to the approximate cut-off scale (3.101).

3.4.6. Forecasts for the relativistic signal-to-noise ratio

Single-dish mode experiments

The SNR of the relativistic part of the bispectrum is shown in Figure 3.18, per z -bin and cumulative.

The total SNR for the HI IM surveys in SD mode is $3 \lesssim \text{SNR} \lesssim 7$, with the high- z_{max} bands giving higher SNR. Table 3.5 displays the predicted total SNR for the SD-mode HI IM surveys. We can slightly improve the best total SNR by combining measurements in the two bands, for both MeerKAT and SKA. In general, since

3. Detectability in next-generation galaxy surveys

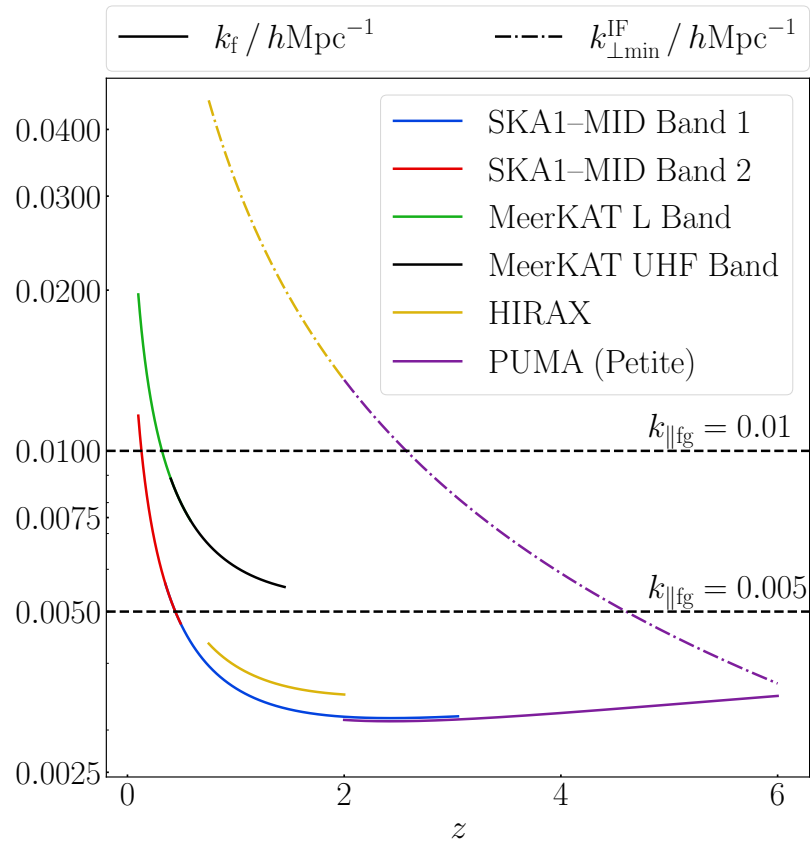


Figure 3.15.: Minimum wavenumbers for the surveys, where k is subject to (3.7) (SD) or (3.104) (IF).

3. Detectability in next-generation galaxy surveys

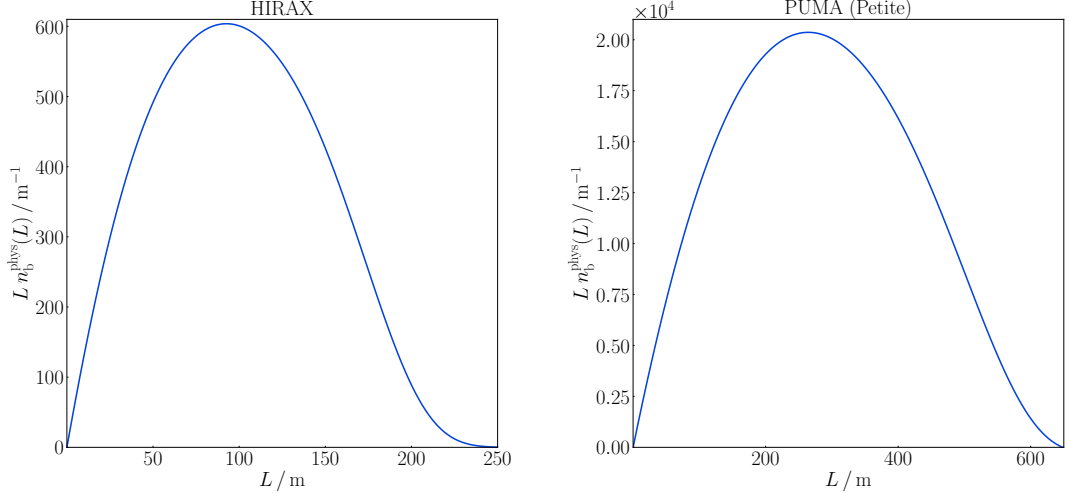


Figure 3.16.: Physical baseline density models for HIRAX (*left*) and PUMA (*right*).

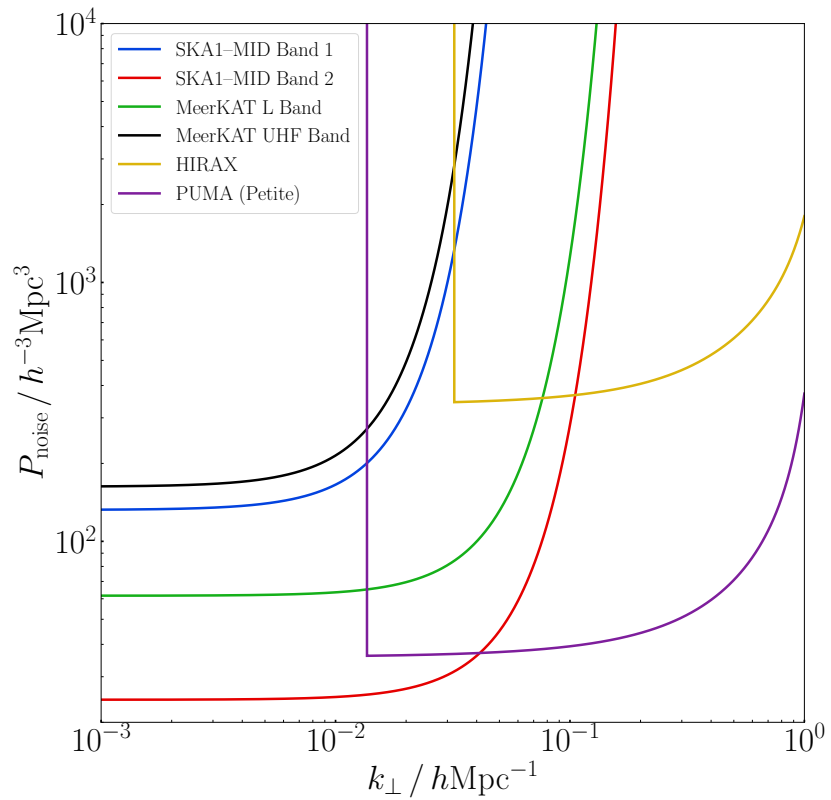


Figure 3.17.: Noise power spectra of the SD-mode surveys (at $z = 0.4$ for low- z_{max} bands and $z = 1$ for high- z_{max} bands) and IF-mode surveys (HIRAX at $z = 1$, PUMA at $z = 2$).

we ignore cross-redshift correlations, we can sum in quadrature the per-bin values,

3. Detectability in next-generation galaxy surveys

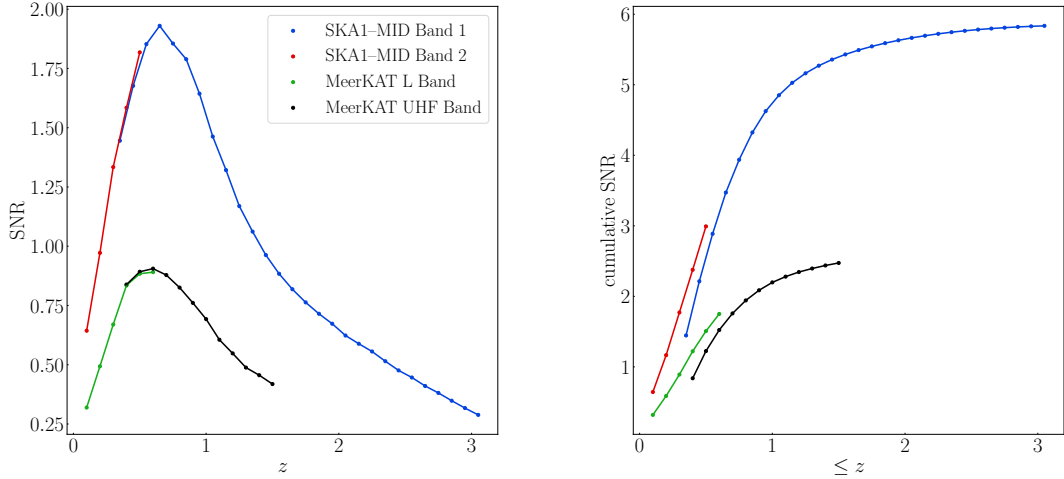


Figure 3.18.: SNR of the relativistic bispectrum per z -bin (*left*) and cumulative (*right*) for SD-mode surveys.

Table 3.5.: Total SNR for single-dish mode surveys.

Survey	Total SNR
MeerKAT UHF Band	2.5
MeerKAT L Band	1.8
MeerKAT L+UHF Bands	3.0
SKA1-MID Band 1	5.8
SKA1-MID Band 2	3.0
SKA1-MID Bands 1+2	6.6

$\text{SNR}(z_i)$, as if they were a collection of bins from the same set of observations. However, it must be noted that the two bands overlap in the redshift range $0.40 \leq z \leq 0.58$ for MeerKAT and $0.35 \leq z \leq 0.49$ for SKA. In that range, we follow a conservative approach and only consider the band yielding the largest value of SNR. The values obtained are shown in Table 3.5.

The best case, SKA1 Bands 1+2 gives a total SNR ~ 6 that is detectable, a few times smaller than the SNR predicted for a Stage IV H α (similar to *Euclid*) spectroscopic survey [114].

Interferometer mode experiments

Figure 3.19 shows the forecasts of the relativistic bispectrum SNR for HIRAX and PUMA, using three values of the wedge parameter N_w . HIRAX predicts SNR values

3. Detectability in next-generation galaxy surveys

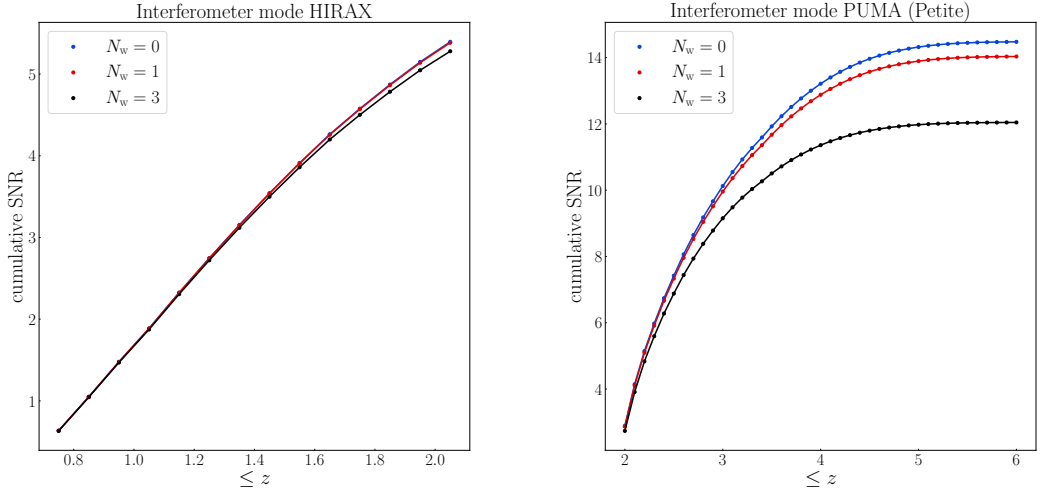


Figure 3.19.: Cumulative SNR of the relativistic bispectrum for IF-mode surveys.

slightly lower than an SKA SD-mode survey. The proposed PUMA survey (the ‘Petite’ or PUMA–5K phase of the full or PUMA–32K proposal) gives the highest SNR, at a level similar to a Stage IV H α (*Euclid-like*) spectroscopic survey. This SNR would safely detect the relativistic signal. Note that PUMA is more sensitive than HIRAX to the N_w parameter. Table 3.6 gives the predicted total SNR for the IF-mode surveys.

Table 3.6.: Total SNR for interferometer-mode surveys.

Survey \ N_w	0	1	3
HIRAX	5.4	5.4	5.3
PUMA (Petite)	14.5	14.0	12.0

Reducing the radial foreground cut

We investigate how much improvement in SNR results if we increase the number of very large scale modes by reducing the radial foreground cut to $k_{\parallel\text{fg}} = 0.005 h\text{Mpc}^{-1}$. Such a reduction may be achieved by future advances in reconstruction techniques.

It turns out that the SNR is relatively insensitive to this reduction in $k_{\parallel\text{fg}}$: very little gain in SNR is achieved, as shown in Tables 3.7 and 3.8.

3. Detectability in next-generation galaxy surveys

Table 3.7.: Total SNR for single-dish mode surveys with $k_{\parallel \text{fg}} = 0.005 \text{ hMpc}^{-1}$.

Survey	Total SNR
MeerKAT UHF Band	2.8
MeerKAT L Band	2.0
MeerKAT L+UHF Bands	3.4
SKA1-MID Band 1	6.5
SKA1-MID Band 2	3.4
SKA1-MID Bands 1+2	7.3

Table 3.8.: Total SNR for interferometer-mode surveys with $k_{\parallel \text{fg}} = 0.005 \text{ hMpc}^{-1}$.

Survey \ N_w	0	1	3
HIRAX	5.6	5.6	5.5
PUMA (Petite)	15.2	14.6	12.5

3.5. Conclusions

The imaginary part of the galaxy bispectrum at leading order is a unique signal that is purely relativistic [88] – and that can be readily extracted from the full bispectrum. In Fourier space, the leading-order local lightcone effects that generate the Doppler-type signal scale as $i(\mathcal{H}/k)$ (see (3.80) and (3.82)). In the galaxy power spectrum for a single tracer, these Doppler-type contributions only occur squared, thus scaling as \mathcal{H}^2/k^2 . Only a cross-power spectrum analysis of two different tracers will generate an imaginary contribution [89]. For single tracers, the relativistic Doppler-type signal in the power spectrum is therefore highly suppressed and not detectable, even for a cosmic-variance limited survey [118].

However, in the bispectrum of a single tracer, the $i(\mathcal{H}/k)$ relativistic signal survives because it couples with the Newtonian terms [88]. This increases the chance of detectability and, as shown by [114], the SNR forecast for a Stage IV H α galaxy spectroscopic survey (similar to *Euclid*) is ~ 17 .

We extended the analysis of [114] to HI intensity mapping spectroscopic surveys, which requires significant additions in order to deal with foreground contamination and the complexities of instrumental noise (that dominates over shot noise). As expected, loss of signal due to foreground cleaning and telescope beam effects reduces the SNR for the next-generation surveys on MeerKAT, SKA1-MID and HIRAX. We forecast a detectable SNR ~ 6 for SKA1 and ~ 5 for HIRAX. The proposed PUMA

3. Detectability in next-generation galaxy surveys

survey in its Petite or 5,000-dish first phase (before the futuristic full survey with 32,000 dishes) delivers a SNR ~ 14 , comparable to that of a Stage IV H α galaxy survey.

Surveys in single-dish mode (MeerKAT, SKA1) suffer from poor angular resolution so that the Newtonian short-scale transverse modes are suppressed. On the other hand, the interferometer-mode surveys (HIRAX, PUMA) do not probe ultra-large scales as well as SD-mode surveys because the maximum length scale is determined by the minimum baseline (3.103), as shown in Figure 3.17.

We investigated the effect of a more optimistic radial wavenumber cut and found that the improvement in SNR is small. This means that detection of the relativistic signal in the bispectrum does not require scales with $k \lesssim 0.01h/\text{Mpc}$.

There are some caveats to our results and pointers for future work:

- In common with nearly all work on the Fourier-space bispectrum that includes RSD, we implicitly make a flat-sky assumption, based on the fixed global direction \mathbf{n} . This is an issue when probing ultra-large scales – which applies not only to our case but also to all work on constraining primordial non-Gaussianity via the Fourier bispectrum. The flat-sky analysis loses accuracy as θ increases, where θ is the maximum opening angle to the three-point correlations at the given redshift. The corresponding comoving transverse scale is $k_{\perp}(z) = 2\pi / [r(z)\theta]$. There is a threshold scale θ_{fs} , beyond which the approximation fails – i.e., for $\theta > \theta_{\text{fs}}$, or equivalently, $k_{\perp} < k_{\perp\text{fs}}$, the SNR is not reliable.

For IF-mode surveys, the flat-sky assumption is reasonable if $\theta_{\text{fs}} > \theta_b$, where θ_b is the beam, given by (3.99). If we estimate that $\theta_{\text{fs}} \sim 10^\circ$ (see [184]), then this condition holds for HIRAX, and for PUMA up to redshift 3 (see Figure 3.15). Consequently, the flat-sky assumption is reasonable for HIRAX. However for PUMA at $z > 3$ and for the SD-mode surveys, there are modes with $k_{\perp} < k_{\perp\text{fs}}$ and the accuracy of the SNR will be affected for these modes.

Including wide-angle effects is a key target for future work that constrains relativistic effects or primordial non-Gaussianity via the bispectrum. In fact, this is also important for standard cosmological constraints. Corrections to the global flat-sky analysis of the Fourier bispectrum can be made by using a local flat-sky approximation [185, 186]. Such corrections are typically approximate and do not incorporate the full wide-angle effect. Ultimately, one needs to

3. Detectability in next-generation galaxy surveys

use the full-sky 3-point correlation function or the full-sky angular bispectrum (see e.g. [103, 139, 141, 150]) to properly include all wide-angle correlations. These alternatives are computationally much more intensive than the Fourier analysis.

- Also in common with other work on the Fourier power spectrum and bispectrum, we neglect cross-correlations among redshift bins. This is justified by the exquisite redshift accuracy of HI intensity mapping, allowing for sharp-edged redshift bins, which in turn implies small or no overlap between them. Integrated effects will in principle induce correlations along the line-of-sight direction, but this is not going to be relevant in our case since the dominant integrated contribution is weak lensing magnification, which vanishes in HI intensity mapping [118, 140, 143, 148]. Ultimately, only approximate solutions are possible in Fourier space and a complete treatment would require the angular bispectrum or 3-point correlation function.
- In the absence of a simulation-based model for the bispectrum RSD damping parameter σ_B , we set it equal to the power spectrum damping parameter σ_P , for which we used a fit from simulations given in [187]. Realistically, we expect that $\sigma_B > \sigma_P$. We tested the impact on the SNR of increasing σ_B to $\sigma_B = 1.5 \sigma_P$ and found that it leads to only a small decrease in SNR.

4. Higher order relativistic effects in the bispectrum

In this chapter, we summarise previous work on relativistic projection effects in the observed galaxy bispectrum [102, 107–109] going beyond the $\mathcal{O}(\mathcal{H}/k)$ approximation used in the previous chapters. The leading order effects examined in the previous chapters are unique in a sense that they are less suppressed on small scales than the leading order relativistic corrections to the power spectrum of a single tracer, which scale as $\mathcal{O}(\mathcal{H}^2/k^2)$. The higher order effects in the bispectrum will become significant on larger scales, and need to be taken into account for a fully consistent theoretical analysis.

Where appropriate, we define the gauges used, but a full and technical discussion on the different gauges used in cosmological perturbation theory is beyond the scope of this work.

For the bispectrum, similar to the power spectrum, effects from observing on the past lightcone need to be taken into account, as they distort the information which is contained in the underlying distribution of dark matter. These lightcone projection effects themselves can also provide new information. The major difference between the power spectrum and bispectrum analyses however, is that for the bispectrum, projection effects up to second order in perturbation theory are required.

Previously, the GR effects on the angular bispectrum of galaxies arising from lensing convergence has been computed in [140], which neglects other ultra-large scale GR corrections to the galaxy overdensity. In [139], a separate-universe approximation is used to compute the angular bispectrum of galaxies in the squeezed limit only, but including all GR lightcone effects. In Section 4.1 we discuss the Fourier-space observed galaxy bispectrum including corrections from local projection effects and relativistic corrections from nonlinear dynamical evolution on large scales, which contribute significantly. At second order in general relativity, scalar perturbations

4. Higher order relativistic effects in the bispectrum

also generate second-order tensor and vector modes [188, 189], and these modes enter the observed galaxy number density contrast at second order [98–101, 149]. However, the power in these second-order tensor and vector modes is much smaller than the power from the scalar modes, and is neglected in forthcoming chapters— a brief discussion on the vector and tensor modes can be found in Section 4.3.

4.1. Lightcone projection effects in the galaxy number density

In this section, we will discuss the observed galaxy bispectrum including relativistic corrections going beyond the leading \mathcal{H}/k approximation. These leading order corrections are introduced in Chapter 2 in more detail— they give rise to a purely imaginary correction to the bispectrum of a single tracer, are potentially detectable (Chapter 3), and will be a smoking gun signal for relativistic effects. However, when one wants to carry out a more complete theoretical analysis, for example to include primordial non-Gaussianity (Chapter 6), the leading-order approximation no longer is sufficient. Local PNG in the bispectrum and the scale-dependent bias it gives rise to have a scale dependence starting at $\mathcal{O}(\mathcal{H}^2/k^2)$ (and higher). As a result, on ultra-large scales, higher-order relativistic corrections in the bispectrum can mimic the effects due to PNG. Hence, they are crucial for a complete theoretical description.

The observed galaxy bispectrum at tree level involves projection effects at both first and second order. These effects, which arise from observing on our past lightcone, include local contributions from Doppler and gravitational potential terms, integrated contributions such as lensing, and at nonlinear order there are also couplings between almost all of these projection effects.

Since we work in Fourier space, which is common with much of the literature on the galaxy bispectrum, we necessarily neglect terms involving lensing and other line-of-sight integrals, i.e. only local relativistic projection effects are included. Furthermore, another approximation which is a direct consequence of working in Fourier space is the plane-parallel approximation, neglecting wide-angle correlations. These need to be included for improved theoretical accuracy. When using an angular harmonic or three-point correlation function analysis, the wide-angle effects would be automatically included, but it poses further computational challenges [142].

4. Higher order relativistic effects in the bispectrum

To be able to compute the observed tree-level bispectrum including local projection effects, we need the observed galaxy number count contrast $\Delta_g^{(2)}$. The full expression for $\Delta_g^{(2)}$ [98–101, 149] is very long and complicated, even when integrated contributions are omitted. All terms at the observer are neglected too, since they do not contribute to the bispectrum.

4.1.1. Observed galaxy number density contrast

The observed number density contrast Δ_g is defined through,

$$\frac{dN(z, \mathbf{n} > \ln L)}{dz d\Omega_o} = \frac{\chi^2(z)}{(1+z)^4 \mathcal{H}(z)} \bar{\mathcal{N}}(z, > \ln L) [1 + \Delta_g(z, \mathbf{n}, > \ln L)], \quad (4.1)$$

where dN is the observed count of galaxies above threshold luminosity L , in direction of observation \mathbf{n} , within redshift interval dz and within solid angle element $d\Omega_o$. $\mathcal{H}(\eta) = a'(\eta)/a(\eta)$ is the conformal hubble rate, $\bar{\mathcal{N}}$ is the background magnitude-limited number density, and χ is the comoving line-of-sight distance. Expanding Δ_g up to second order in perturbation theory as,

$$\Delta_g(z, \mathbf{n}) = \Delta_g^{(1)}(z, \mathbf{n}) + \frac{1}{2} [\Delta_g^{(2)}(z, \mathbf{n}) - \langle \Delta_g^{(2)}(z, \mathbf{n}) \rangle], \quad (4.2)$$

where we have dropped the dependence of the density contrast on luminosity for brevity, and subtract $\langle \Delta_g^{(2)} \rangle$ to ensure that $\langle \Delta_g \rangle = 0$.

The observed number density contrast can be split into Newtonian and relativistic parts at each order r in perturbation theory,

$$\Delta_g^{(r)} = \Delta_{gN}^{(r)} + \Delta_{gGR}^{(r)}, \quad (4.3)$$

which is convenient for our purpose here.

The comoving-synchronous gauge (C) is the gauge that coincides with the matter rest frame, and is treated as the Lagrangian frame in GR. C-gauge overdensities of matter and galaxy counts are denoted as δ_{mC} and δ_{gC} . At first order, the Poisson and continuity equations are,

$$\nabla^2 \Phi^{(1)} = \frac{3}{2} \Omega_m \mathcal{H}^2 \delta_{mC}^{(1)} \quad (4.4)$$

$$\delta_{mC}^{(1)'} = -\nabla^2 v^{(1)}. \quad (4.5)$$

4. Higher order relativistic effects in the bispectrum

These lead to the following relations for the velocity and metric potentials,

$$\Phi^{(1)} = -\frac{3}{2}\Omega_m \frac{\mathcal{H}^2}{k^2} \delta_{mC}^{(1)}, \quad (4.6)$$

where $\Phi^{(1)}(a, \mathbf{k}) = \frac{D(a)}{a} \Phi^{(1)}(1, \mathbf{k})$, and,

$$\mathcal{H}v^{(1)} = f \frac{\mathcal{H}^2}{k^2} \delta_{mC}^{(1)}, \quad (4.7)$$

where $f = \frac{d \ln D}{d \ln a}$ and $\delta_{mC}^{(1)}(a, \mathbf{k}) = D(a) \delta_{mC}^{(1)}(1, \mathbf{k})$.

Galaxy overdensity at first order in perturbation theory

The first-order observed galaxy number density contrast $\Delta_g^{(1)}$ is given by [107],

$$\begin{aligned} \Delta_g^{(1)} &= b_1 \delta_{mT} - \frac{1}{\mathcal{H}} \partial_{\parallel}^2 v^{(1)} + \left[b_e - 2\mathcal{Q} + \frac{2(\mathcal{Q}-1)}{\chi \mathcal{H}} - \frac{\mathcal{H}'}{\mathcal{H}^2} \right] [\partial_{\parallel} v^{(1)} - \Phi^{(1)}] + (2\mathcal{Q}-1) \Phi^{(1)} \\ &\quad + \frac{1}{\mathcal{H}} \Phi^{(1)\prime} + (3-b_e) \mathcal{H}v^{(1)}, \end{aligned} \quad (4.8)$$

where subscript T denotes the total matter gauge. There is no unique gauge defined in the Eulerian frame, but the T gauge is a convenient choice, as the transformation from C to T gauge is simply a purely spatial transformation. The first-order observed galaxy number density contrast can be split into a Newtonian and a relativistic part as,

$$\Delta_{gN}^{(1)} = b_1 \delta_{mT} - \frac{1}{\mathcal{H}} \partial_{\parallel}^2 v^{(1)}, \quad (4.9)$$

$$\begin{aligned} \Delta_{gGR}^{(1)} &= \left[b_e - 2\mathcal{Q} + \frac{2(\mathcal{Q}-1)}{\chi \mathcal{H}} - \frac{\mathcal{H}'}{\mathcal{H}^2} \right] [\partial_{\parallel} v^{(1)} - \Phi^{(1)}] - (2\mathcal{Q}-1) \Phi^{(1)} + \frac{1}{\mathcal{H}} \Phi^{(1)\prime} \\ &\quad + (3-b_e) \mathcal{H}v^{(1)}. \end{aligned} \quad (4.10)$$

The Newtonian part in the above equation consists of the T-gauge density contrast term + Kaiser RSD. The GR part consists of Dopper + potential + velocity potential terms.

Galaxy overdensity at second order in perturbation theory

At second order, the expression for Δ_g is a lot more involved, because it includes both the second-order generalisations of effects included at first order, as well as quadratic

4. Higher order relativistic effects in the bispectrum

couplings between the first-order terms themselves. Various groups have computed the second order observed galaxy number counts, in different formalisms [99–101, 149, 190]. A full comparison of the different results has yet to be done, see for example [191] in which the leading order corrections are compared.

Here we use the expression given by [98], which includes the evolution and magnification biases— we neglect the integrated effects that are given, and we include our gauge-independent model of second-order galaxy bias. The resulting expression for $\Delta_g^{(2)}$ is,

$$\begin{aligned}
\Delta_g^{(2)} = & b_1 \delta_{mT}^{(2)} + b_2 \left[\delta_{mT}^{(1)} \right]^2 + \left[(b_e - 3)^2 \mathcal{H}^2 + b'_e \mathcal{H} + (b_e - 3) \mathcal{H}' \right] \left[v^{(1)} \right]^2 \\
& + (b_e - 3) \mathcal{H} v^{(1)} v^{(1)\prime} + 2b_1 (3 - b_e) \mathcal{H} v^{(1)} \delta_{mT}^{(1)} - 2v^{(1)} \left[b_1 \delta_{mT}^{(1)\prime} + b'_1 \delta_{mT}^{(1)} \right] \\
& + (3 - b_e) \mathcal{H} \nabla^{-2} \left[v^{(1)} \nabla^2 v^{(1)\prime} - v^{(1)\prime} \nabla^2 v^{(1)} - 6\partial_i \Phi^{(1)} \partial^i v^{(1)} - 6\Phi^{(1)} \nabla^2 v^{(1)} \right] \\
& - \frac{1}{\mathcal{H}} \partial_{\parallel}^2 v^{(2)} + (3 - b_e) \mathcal{H} v^{(2)} + \left[b_e - 2\mathcal{Q} - \frac{2(1 - \mathcal{Q})}{\chi \mathcal{H}} - \frac{\mathcal{H}'}{\mathcal{H}^2} \right] \left[\partial_{\parallel} v^{(2)} - \Phi^{(2)} \right] \\
& + 2(\mathcal{Q} - 1) \Psi^{(2)} + \Phi^{(2)} + \frac{1}{\mathcal{H}} \Psi^{(2)\prime} + \left[b_e - 2\mathcal{Q} - \frac{\mathcal{H}'}{\mathcal{H}^2} - (1 - \mathcal{Q}) \frac{2}{\chi \mathcal{H}} \right] \cdot \\
& \left[3 \left[\Phi^{(1)} \right]^2 - \left[\partial_{\parallel} v^{(1)} \right]^2 + \partial_{\perp i} v^{(1)} \partial_{\perp}^i v^{(1)} - 2\partial_{\parallel} v^{(1)} \Phi^{(1)} - \frac{2}{\mathcal{H}} \left(\Phi^{(1)} - \partial_{\parallel} v^{(1)} \right) \cdot \right. \\
& \left. \left(\Phi^{(1)\prime} - \partial_{\parallel}^2 v^{(1)} \right) \right] + 2(2\mathcal{Q} - 1) \Phi^{(1)} \delta_g^{(1)} - \frac{2}{\mathcal{H}} \delta_g^{(1)} \partial_{\parallel}^2 v^{(1)} + \frac{2}{\mathcal{H}} \delta_g^{(1)} \Phi^{(1)\prime} \\
& + \left(4\mathcal{Q} - 5 + 4\mathcal{Q}^2 - 4 \frac{\partial \mathcal{Q}}{\partial \ln \bar{L}} \right) \left[\Phi^{(1)} \right]^2 + \frac{2}{\mathcal{H}} \left(2\mathcal{Q} + \frac{\mathcal{H}'}{\mathcal{H}^2} \right) \Phi^{(1)} \Phi^{(1)\prime} \\
& - \frac{2}{\mathcal{H}} \left(1 + 2\mathcal{Q} + \frac{\mathcal{H}'}{\mathcal{H}^2} \right) \Phi^{(1)} \partial_{\parallel}^2 v^{(1)} + \frac{2}{\mathcal{H}^2} \left[\Phi^{(1)\prime} \right]^2 + \frac{2}{\mathcal{H}^2} \left[\partial_{\parallel}^2 v^{(1)} \right]^2 \\
& + \frac{2}{\mathcal{H}^2} \partial_{\parallel} v^{(1)} \partial_{\parallel}^2 \Phi^{(1)} + \frac{4}{\mathcal{H}} \partial_{\parallel} v^{(1)} \partial_{\parallel} \Phi^{(1)} - \frac{2}{\mathcal{H}^2} \Phi^{(1)} \partial_{\parallel}^3 v^{(1)} - \frac{2}{\mathcal{H}} \Phi^{(1)} \partial_{\parallel} \Phi^{(1)} \\
& + \frac{2}{\mathcal{H}^2} \Phi^{(1)} \frac{d\Phi^{(1)\prime}}{d\chi} - \frac{2}{\mathcal{H}^2} \partial_{\parallel} v^{(1)} \frac{d\Phi^{(1)\prime}}{d\chi} + \frac{2}{\mathcal{H}} \left(1 + \frac{\mathcal{H}'}{\mathcal{H}^2} \right) \partial_{\parallel} v^{(1)} \partial_{\parallel}^2 v^{(1)} \\
& - \frac{2}{\mathcal{H}^2} \Phi^{(1)} \partial_{\parallel}^2 \Phi^{(1)} + \frac{2}{\mathcal{H}} \left(1 - \frac{\mathcal{H}'}{\mathcal{H}^2} \right) \partial_{\parallel} v^{(1)} \Phi^{(1)\prime} - \frac{4}{\mathcal{H}^2} \partial_{\parallel}^2 v^{(1)} \Phi^{(1)\prime} \\
& + \frac{2}{\mathcal{H}} \partial_{\perp i} v^{(1)} \partial_{\perp}^i \Phi^{(1)} - \frac{4}{\mathcal{H}} \partial_{\perp i} v^{(1)} \partial_{\perp}^i \partial_{\parallel} v^{(1)} + \left(\frac{4}{\chi \mathcal{H}} - 1 \right) \partial_{\perp i} v^{(1)} \partial_{\perp}^i v^{(1)} \\
& + \frac{2}{\mathcal{H}^2} \partial_{\parallel} v^{(1)} \partial_{\parallel}^3 v^{(1)} + \left\{ \left[4b_e \mathcal{Q} - 2b_e - 4\mathcal{Q} - 8\mathcal{Q}^2 + 8 \frac{\partial \mathcal{Q}}{\partial \ln \bar{L}} + 4 \frac{\partial \mathcal{Q}}{\partial \ln \bar{a}} \right. \right. \\
& \left. \left. + 2 \frac{\mathcal{H}'}{\mathcal{H}^2} (1 - 2\mathcal{Q}) + \frac{4}{\chi \mathcal{H}} \left(\mathcal{Q} - 1 + 2\mathcal{Q}^2 - 2 \frac{\partial \mathcal{Q}}{\partial \ln \bar{L}} \right) \right] \Phi^{(1)} + 2[b_e - 2\mathcal{Q}] \right. \\
& \left. - \frac{\mathcal{H}'}{\mathcal{H}^2} - \frac{2}{\chi \mathcal{H}} (1 - \mathcal{Q}) \right] \delta_g^{(1)} - \frac{2}{\mathcal{H}} \frac{d\delta_g^{(1)}}{d\chi} + \frac{2}{\mathcal{H}} \left[2\mathcal{Q} - b_e + \frac{\mathcal{H}'}{\mathcal{H}^2} + \frac{2}{\chi \mathcal{H}} (1 - \mathcal{Q}) \right].
\end{aligned}$$

4. Higher order relativistic effects in the bispectrum

$$\begin{aligned}
& \partial_{\parallel}^2 v^{(1)} + \frac{2}{\mathcal{H}} \left[b_e - 2 - \frac{2}{\chi \mathcal{H}} (1 - \mathcal{Q}) - \frac{\mathcal{H}'}{\mathcal{H}^2} \right] \Phi^{(1)\prime} - \frac{4}{\mathcal{H}} \mathcal{Q} \partial_{\parallel} \Phi \Big\} [\partial_{\parallel} v^{(1)} - \Phi^{(1)}] \\
& + \left\{ b_e^2 - b_e + \frac{\partial b_e}{\partial \ln \bar{a}} + 6\mathcal{Q} - 4\mathcal{Q}b_e + 4\mathcal{Q}^2 - 4 \frac{\partial \mathcal{Q}}{\partial \ln \bar{L}} - 4 \frac{\partial \mathcal{Q}}{\partial \ln \bar{a}} + \frac{6}{\chi} \frac{\mathcal{H}'}{\mathcal{H}^3} (1 - \mathcal{Q}) \right. \\
& + (1 - 2b_e + 4\mathcal{Q}) \frac{\mathcal{H}'}{\mathcal{H}^2} - \frac{\mathcal{H}''}{\mathcal{H}^3} + 3 \frac{\mathcal{H}'^2}{\mathcal{H}^4} + \frac{2}{\chi^2 \mathcal{H}^2} \left(1 - \mathcal{Q} + 2\mathcal{Q}^2 - 2 \frac{\partial \mathcal{Q}}{\partial \ln \bar{L}} \right) \\
& \left. + \frac{2}{\chi \mathcal{H}} \left[1 - 2b_e - \mathcal{Q} + 2b_e \mathcal{Q} - 4\mathcal{Q}^2 + 4 \frac{\partial \mathcal{Q}}{\partial \ln \bar{L}} + 2 \frac{\partial \mathcal{Q}}{\partial \ln \bar{a}} \right] \right\} [\partial_{\parallel} v^{(1)} - \Phi^{(1)}]^2 \\
& + 4 \left[\left(1 - \frac{1}{\chi \mathcal{H}} \right) \partial_{\parallel} v^{(1)} - \left(2 - \frac{1}{\chi \mathcal{H}} \right) \Phi^{(1)} \right] \frac{\partial \delta_g^{(1)}}{\partial \ln \bar{L}}. \tag{4.11}
\end{aligned}$$

Similarly to the first-order observed galaxy number density contrast, $\Delta_g^{(2)}$ can be split into Newtonian and GR parts. The Newtonian part consists of the density contrast and the Kaiser RSD terms, plus couplings thereof,

$$\begin{aligned}
\Delta_{gN}^{(2)} = & b_1 \delta_{mT}^2 + b_2 [\delta_{mT}^{(1)}]^2 - \frac{1}{\mathcal{H}} \partial_{\parallel}^2 v^{(2)} - 2 \frac{b_1}{\mathcal{H}} \left[\delta_{mT}^{(1)} \partial_{\parallel}^2 v^{(1)} + \partial_{\parallel} v^{(1)} \partial_{\parallel} \delta_{mT}^{(1)} \right] \\
& \frac{2}{\mathcal{H}^2} \left[[\partial_{\parallel}^2 v^{(1)}]^2 + \partial_{\parallel} v^{(1)} \partial_{\parallel}^3 v^{(1)} \right]. \tag{4.12}
\end{aligned}$$

The GR part of $\Delta_g^{(2)}$ then is formed by all the remaining terms. For notational brevity we define coefficients that depend on the background coefficients only, such that we get,

$$\begin{aligned}
\Delta_{gGR}^{(2)} = & \mathcal{H}(3 - b_e)v^{(2)} + \left[(9 - 6b_e + b_e^2)\mathcal{H}^2 + b'_e \mathcal{H} + (b_e - 3)\mathcal{H}' \right] [v^{(1)}]^2 \\
& + (b_e - 3)\mathcal{H}v^{(1)}v^{(1)\prime} - (b_e - 3)\mathcal{H}\nabla^{-2} [v^{(1)}\nabla^2 v^{(1)\prime} - v^{(1)\prime}\nabla^2 v^{(1)}] \\
& - 6\partial_i \Phi^{(1)} \partial^i v^{(1)} - 6\Phi^{(1)} \nabla^2 v^{(1)}] + 2(3 - b_e)b_1 \mathcal{H}v^{(1)}\delta_{mT}^{(1)} \\
& - 2v^{(1)} \left(b'_1 \delta_{mT}^{(1)} + b_1 \delta_{mT}^{(1)\prime} \right) + \left[b_e - 2\mathcal{Q} - \frac{2(1 - \mathcal{Q})}{\chi \mathcal{H}} - \frac{\mathcal{H}'}{\mathcal{H}^2} \right] \partial_{\parallel} v^{(2)} \\
& + \left[1 - b_e + 2\mathcal{Q} + \frac{2(1 - \mathcal{Q})}{\chi \mathcal{H}} + \frac{\mathcal{H}'}{\mathcal{H}^2} \right] \Phi^{(2)} - 2(1 - \mathcal{Q})\Psi^{(2)} + \frac{1}{\mathcal{H}}\Psi^{(2)\prime} \\
& + \frac{2}{\mathcal{H}} \left[b_1 \delta_{mT}^{(1)\prime} \partial_{\parallel} v^{(1)} + (f - 2 + 2\mathcal{Q})\Phi^{(1)} \partial_{\parallel} \Phi^{(1)} + (2 - f - 2\mathcal{Q})\partial_{\parallel} v^{(1)} \partial_{\parallel} \Phi^{(1)} \right. \\
& \left. - b_1 \Phi^{(1)} \delta_{mT}^{(1)\prime} + b_1 \Phi^{(1)} \partial_{\parallel} \delta_{mT}^{(1)} - 2\partial_i v^{(1)} \partial_{(1)} \partial^i v^{(1)} + \partial_i v^{(1)} \partial^i \Phi^{(1)} \right] \\
& + \frac{2}{\mathcal{H}^2} \left[\partial_{\parallel} v^{(1)} \partial_{\parallel}^2 \Phi^{(1)} - \Phi^{(1)} \partial_{\parallel}^2 \Phi^{(1)} - \Phi^{(1)} \partial_{\parallel}^3 v^{(1)} \right] - 2(3 - b_e)v^{(1)} \partial_{\parallel}^2 v^{(1)} \\
& + 2 \left[b_1 \left(b_e - 2\mathcal{Q} - \frac{2(1 - \mathcal{Q})}{\chi \mathcal{H}} - \frac{\mathcal{H}'}{\mathcal{H}^2} \right) + \frac{b'_1}{\mathcal{H}} + 2 \left(1 - \frac{1}{\chi \mathcal{H}} \right) \frac{\partial b_1}{\partial \ln \bar{L}} \right] \cdot \\
& \delta_{mT}^{(1)} \partial_{\parallel} v^{(1)} + \frac{2}{\mathcal{H}} \left[3 - 2b_e + 4\mathcal{Q} + \frac{4(1 - \mathcal{Q})}{\mathcal{H}\chi} + \frac{3\mathcal{H}'}{\mathcal{H}} \right] \partial_{\parallel} v^{(1)} \partial_{\parallel}^2 v^{(1)}
\end{aligned}$$

4. Higher order relativistic effects in the bispectrum

$$\begin{aligned}
& + 2 \left[b_1 \left(f - 2 - b_e + 4\mathcal{Q} + \frac{2(1-\mathcal{Q})}{\chi\mathcal{H}} + \frac{\mathcal{H}'}{\mathcal{H}^2} \right) - \frac{b'_1}{\mathcal{H}} - 2 \left(2 - \frac{1}{\chi\mathcal{H}} \right) \frac{\partial b_1}{\partial \ln \bar{L}} \right] \\
& \Phi^{(1)} \delta_{mT}^{(1)} + \left[b_e - 1 - 2\mathcal{Q} - \frac{2(1-\mathcal{Q})}{\chi\mathcal{H}} - \frac{\mathcal{H}'}{\mathcal{H}^2} \right] \partial_i v^{(1)} \partial^i v^{(1)} + \frac{2}{\mathcal{H}} [1 - 2f + 2b_e \\
& - 6\mathcal{Q} - \frac{4(1-\mathcal{Q})}{\chi\mathcal{H}} - \frac{3\mathcal{H}'}{\mathcal{H}^2}] \Phi^{(1)} \partial_{\parallel}^2 v^{(1)} + \mathcal{A} [\Phi^{(1)}]^2 + \mathcal{B} v^{(1)} \partial_{\parallel} v^{(1)} + \mathcal{C} \Phi^{(1)} v^{(1)} \\
& + \mathcal{D} \Phi^{(1)} \partial_{\parallel} v^{(1)} + \mathcal{E} [\partial_{\parallel} v^{(1)}]^2. \tag{4.13}
\end{aligned}$$

The coefficients $\mathcal{A}, \mathcal{B}, \mathcal{C}, \mathcal{D}, \mathcal{E}$ are defined as,

$$\begin{aligned}
\mathcal{A} = & -3 + 2f \left(2 - 2b_e + 4\mathcal{Q} + \frac{4(1-\mathcal{Q})}{\chi\mathcal{H}} + \frac{2\mathcal{H}'}{\mathcal{H}^2} \right) - \frac{2f'}{\mathcal{H}} + b_e^2 + 6b_e - 8b_e\mathcal{Q} \\
& + 4\mathcal{Q} + 16\mathcal{Q}^2 - 16 \frac{\partial \mathcal{Q}}{\partial \ln \bar{L}} - 8 \frac{\mathcal{Q}'}{\mathcal{H}} + \frac{b'_e}{\mathcal{H}} + \frac{2}{\chi^2 \mathcal{H}^2} \left(1 - \mathcal{Q} + 2\mathcal{Q}^2 - 2 \frac{\partial \mathcal{Q}}{\partial \ln \bar{L}} \right) \\
& - \frac{2}{\chi\mathcal{H}} \left[4 + 2b_e - 2b_e\mathcal{Q} - 4\mathcal{Q} + 8\mathcal{Q}^2 - \frac{3\mathcal{H}'}{\mathcal{H}^2}(1-\mathcal{Q}) - 8 \frac{\partial \mathcal{Q}}{\partial \ln \bar{L}} - 2 \frac{\mathcal{Q}'}{\mathcal{H}} \right] \\
& + \frac{\mathcal{H}'}{\mathcal{H}^2} \left(-8 - 2b_e + 8\mathcal{Q} + \frac{3\mathcal{H}'}{\mathcal{H}^2} \right) - \frac{\mathcal{H}''}{\mathcal{H}^3}, \tag{4.14}
\end{aligned}$$

$$\begin{aligned}
\mathcal{B} = & 2\mathcal{H} \left[-3 + 4b_e + 2b_e \frac{(1-\mathcal{Q})}{\chi\mathcal{H}} - b_e^2 + 2b_e\mathcal{Q} - 6\mathcal{Q} - \frac{b'_e}{\mathcal{H}} - \frac{6(1-\mathcal{Q})}{\chi\mathcal{H}} \right. \\
& \left. + 2 \left(1 - \frac{1}{\chi\mathcal{H}} \right) \frac{\mathcal{Q}'}{\mathcal{H}} \right], \tag{4.15}
\end{aligned}$$

$$\begin{aligned}
\mathcal{C} = & 2\mathcal{H} \left[-3 + f(3 - b_e) - 3b_e - 2b_e \frac{(1-\mathcal{Q})}{\chi\mathcal{H}} + \frac{b'_e}{\mathcal{H}} + b_e^2 - 4b_e\mathcal{Q} + 12\mathcal{Q} \right. \\
& \left. + \frac{6(1-\mathcal{Q})}{\chi\mathcal{H}} - 2 \left(2 - \frac{1}{\chi\mathcal{H}} \right) \frac{\mathcal{Q}'}{\mathcal{H}} \right], \tag{4.16}
\end{aligned}$$

$$\begin{aligned}
\mathcal{D} = & 4 + 2f \left[-3 + f + 2b_e - 3\mathcal{Q} - \frac{4(1-\mathcal{Q})}{\chi\mathcal{H}} - \frac{2\mathcal{H}'}{\mathcal{H}^2} \right] + \frac{2f'}{\mathcal{H}} - 6b_e - 2b_e^2 + 12b_e\mathcal{Q} \\
& - 8\mathcal{Q} - 16\mathcal{Q}^2 + 16 \frac{\partial \mathcal{Q}}{\partial \ln \bar{L}} + 12 \frac{\mathcal{Q}'}{\mathcal{H}} - 2 \frac{b'_e}{\mathcal{H}} - \frac{4}{\chi^2 \mathcal{H}^2} \left(1 - \mathcal{Q} + 2\mathcal{Q}^2 - 2 \frac{\partial \mathcal{Q}}{\partial \ln \bar{L}} \right) \\
& - \frac{4}{\chi\mathcal{H}} \left[-1 - 2b_e + 2b_e\mathcal{Q} + \mathcal{Q} - 6\mathcal{Q}^2 + \frac{3\mathcal{H}'}{\mathcal{H}^2}(1-\mathcal{Q}) + 6 \frac{\partial \mathcal{Q}}{\partial \ln \bar{L}} + 2 \frac{\mathcal{Q}'}{\mathcal{H}} \right] \\
& + \frac{2\mathcal{H}'}{\mathcal{H}^2} \left(3 + 2b_e - 6\mathcal{Q} - \frac{3\mathcal{H}'}{\mathcal{H}^2} \right) + \frac{2\mathcal{H}''}{\mathcal{H}^3}, \tag{4.17}
\end{aligned}$$

$$\begin{aligned}
\mathcal{E} = & -4 - b_e + b_e^2 - 4b_e\mathcal{Q} + 6\mathcal{Q} + 4\mathcal{Q}^2 - 4 \frac{\partial \mathcal{Q}}{\partial \ln \bar{L}} - 4 \frac{\mathcal{Q}'}{\mathcal{H}} + \frac{b'_e}{\mathcal{H}} \\
& + \frac{2}{\chi^2 \mathcal{H}^2} \left(1 - \mathcal{Q} + 2\mathcal{Q}^2 - 2 \frac{\partial \mathcal{Q}}{\partial \ln \bar{L}} \right) + \frac{2}{\chi\mathcal{H}} [3 - 2b_e + 2b_e\mathcal{Q} - 3\mathcal{Q} - 4\mathcal{Q}^2 \\
& + \frac{3\mathcal{H}'}{\mathcal{H}^2}(1-\mathcal{Q}) + 4 \frac{\partial \mathcal{Q}}{\partial \ln \bar{L}} + 2 \frac{\mathcal{Q}'}{\mathcal{H}}] + \frac{\mathcal{H}'}{\mathcal{H}^2} \left(3 - 2b_e + 4\mathcal{Q} + \frac{3\mathcal{H}'}{\mathcal{H}^2} \right) - \frac{\mathcal{H}''}{\mathcal{H}^3}. \tag{4.18}
\end{aligned}$$

4. Higher order relativistic effects in the bispectrum

The expressions for $\Delta_{gN}^{(2)}$ and $\Delta_{g\text{GR}}^{(2)}$ as given in equations (4.12) and (4.13), plus the background coefficients, are derived from equation (4.11), which is the general formula for $\Delta_g^{(2)}$ in Poisson gauge neglecting terms with line-of-sight integrals. We choose Poisson gauge here, because at higher orders in perturbation theory, the choice of a gauge for the metric becomes important as the complexity of the calculations increases.

4.1.2. The galaxy number density contrast in Fourier space

We only consider correlations at the same fixed observed redshift z . At this fixed redshift, the perturbative variables depend on the direction of observation \mathbf{n} , and are computed in Fourier space at fixed $\eta(z)$. At fixed redshift and fixed observed direction, we transform $\mathbf{x} = [\eta_0 - \eta(z)]\mathbf{n} + \mathbf{x}_0 \rightarrow \mathbf{k}$, which is equivalent to transforming over all observer positions \mathbf{x}_0 . We denote the T-gauge matter density $\delta_{mT} \equiv \delta$ and expand it in perturbation theory as,

$$\delta = \delta^{(1)} + \frac{1}{2}\delta^{(2)}. \quad (4.19)$$

The second-order matter density contrast is given by,

$$\delta^{(2)}(\mathbf{k}) = \int \frac{d^3k_1}{(2\pi)^3} \frac{d^3k_2}{(2\pi)^3} \delta^{(1)}(\mathbf{k}_1)\delta^{(1)}(\mathbf{k}_2)F_2(\mathbf{k}_1, \mathbf{k}_2)(2\pi)^3\delta^D(\mathbf{k}_1 + \mathbf{k}_2 - \mathbf{k}), \quad (4.20)$$

where F_2 is the kernel for the dark matter perturbations in a matter-dominated model. The velocity and metric potentials can be split into Newtonian and GR parts, $\mathbf{v}^{(2)} = v_N^{(2)} + v_{\text{GR}}^{(2)}$ and similarly for $\Phi^{(2)}$ and $\Psi^{(2)}$. In a Newtonian approximation, these are given by [62],

$$v_N^{(2)}(\mathbf{k}) = f \frac{\mathcal{H}}{k^2} \int \frac{d^3k_1}{(2\pi)^3} \frac{d^3k_2}{(2\pi)^3} \delta^{(1)}(\mathbf{k}_1)\delta^{(1)}(\mathbf{k}_2)G_2(\mathbf{k}_1, \mathbf{k}_2)(2\pi)^3\delta^D(\mathbf{k}_1 + \mathbf{k}_2 - \mathbf{k}), \quad (4.21)$$

$$\Phi_N^{(2)}(\mathbf{k}) = \Psi_N^{(2)}(\mathbf{k}) = -\frac{3}{2}\Omega_m \frac{\mathcal{H}^2}{k^2} \delta^{(2)}(\mathbf{k}). \quad (4.22)$$

The relativistic parts, assuming ΛCDM and Gaussian initial conditions, are given in real space and Poisson gauge by [106],

$$v_{\text{GR}}^{(2)}(\mathbf{x}) = \alpha D' g \left[\left(1 - \frac{10}{3} \frac{g_{\text{in}}}{g} \right) \varphi_0^2(\mathbf{x}) - 12\Theta_0(\mathbf{x}) \right], \quad (4.23)$$

4. Higher order relativistic effects in the bispectrum

$$\Phi_{\text{GR}}^{(2)}(\mathbf{x}) = \left(3g^2 - \frac{5}{3}g g_{\text{in}} + \frac{\alpha D'^2}{a}\right) \varphi_0^2(\mathbf{x}) + 12 \left(2g^2 - \frac{5}{3}g g_{\text{in}} + \frac{\alpha D'^2}{a}\right) \Theta_0(\mathbf{x}), \quad (4.24)$$

$$\Psi_{\text{GR}}^{(2)}(\mathbf{x}) = - \left(g^2 + \frac{5}{3}g g_{\text{in}} - \frac{\alpha D'^2}{a}\right) \varphi_0^2(\mathbf{x}) + 12 \left(g^2 - \frac{5}{3}g g_{\text{in}}\right) \Theta_0(\mathbf{x}). \quad (4.25)$$

The above expressions can be simplified using that,

$$\alpha = \frac{2}{2\Omega_{m0}H_0^2} = \frac{2}{3\Omega_m \mathcal{H}^2 a}, \quad (4.26)$$

$$g = \frac{D}{a}, \quad D(\eta) = \frac{\delta_T^{(1)}(\eta, \mathbf{x})}{\delta_T(\eta_0, \mathbf{x})}, \quad g\varphi_0 = \Phi^{(1)} = \Psi^{(1)}, \quad (4.27)$$

$$\Theta_0(\mathbf{x}) = \frac{1}{2} \nabla^{-2} \left[\frac{1}{3} \varphi_0^i \varphi_{0,i} - \nabla^{-2} (\varphi_0^i \varphi_0^j)_{,ij} \right], \quad (4.28)$$

$$\frac{g_{\text{in}}}{g} = \frac{1}{5} \left(3 + 2 \frac{f}{\Omega_m}\right), \quad f = \frac{d \ln D}{d \ln a}, \quad (4.29)$$

where g_{in} is the initial values in the matter-dominated era, subscript 0 denotes the value at redshift $z = 0$, and $a_0 = D_0 = g_0 = 1$. We then obtain,

$$\mathcal{H}v_{\text{GR}}^{(2)}(\mathbf{x}) = -g^2 \frac{2f}{3\Omega_m} \left[\left(1 + \frac{4f}{3\Omega_m}\right) \varphi_0^2(\mathbf{x}) + 12\Theta_0(\mathbf{x}) \right], \quad (4.30)$$

$$\Phi_{\text{GR}}^{(2)}(\mathbf{x}) = g^2 \left[2 - \frac{2f}{3\Omega_m} + \frac{2f^2}{3\Omega_m}\right] \varphi_0^2(\mathbf{x}) + 12g^2 \left[1 - \frac{2f}{3\Omega_m} + \frac{2f^2}{3\Omega_m}\right], \quad (4.31)$$

$$\Psi_{\text{GR}}^{(2)}(\mathbf{x}) = -g^2 \left[2 + \frac{2f}{3\Omega_m} - \frac{2f^2}{3\Omega_m}\right] \varphi_0^2(\mathbf{x}) - 8g^2 \frac{f}{\Omega_m} \Theta_0(\mathbf{x}). \quad (4.32)$$

The matter density contrast is,

$$\delta^{(1)} = \alpha D \nabla^2 \varphi_0, \quad (4.33)$$

which in combination with the relations (4.26) and (4.27) can be used to obtain the Fourier transforms,

$$\varphi_0^{(2)}(\mathbf{k}_3) = \left(\frac{3\Omega_m \mathcal{H}^2}{2g}\right)^2 \int d(\mathbf{k}_1, \mathbf{k}_2, \mathbf{k}_3) \frac{1}{k_1^2 k_2^2}, \quad (4.34)$$

$$\Theta_0(\mathbf{k}_3) = \left(\frac{3\Omega_m \mathcal{H}^2}{2gk_3}\right)^2 \int d(\mathbf{k}_1, \mathbf{k}_2, \mathbf{k}_3) \left\{ \frac{\mathbf{k}_1 \cdot \mathbf{k}_2}{6k_1^2 k_2^2} - \frac{1}{2k_3^2} \left[1 + \frac{\mathbf{k}_1 \cdot \mathbf{k}_2}{k_1 k_2} \left(\frac{k_1}{k_2} + \frac{k_2}{k_1}\right) + \frac{(\mathbf{k}_1 \cdot \mathbf{k}_2)^2}{k_1^2 k_2^2}\right] \right\}. \quad (4.35)$$

We can then define a new Fourier kernel function which scales as k^0 (similarly to

4. Higher order relativistic effects in the bispectrum

the kernels F_2 and G_2),

$$E_2(\mathbf{k}_1, \mathbf{k}_2, \mathbf{k}_3) = \frac{k_1^2 k_2^2}{k_3^4} \left[3 + 2 \frac{\mathbf{k}_1 \cdot \mathbf{k}_2}{k_1 k_2} \left(\frac{k_1}{k_2} + \frac{k_2}{k_1} \right) + \frac{(\mathbf{k}_1 \cdot \mathbf{k}_2)^2}{k_1^2 k_2^2} \right]. \quad (4.36)$$

Combining all of the above expressions, the GR parts of second-order velocity and metric potentials become,

$$\mathcal{H}v_{\text{GR}}^{(2)}(\mathbf{k}_3) = 3\Omega_m \mathcal{H}^4 f \int d(\mathbf{k}_1, \mathbf{k}_2, \mathbf{k}_3) \frac{1}{k_1 k_2} \left[-\frac{1}{6} \left(3 + \frac{4f}{\Omega_m} \right) + E_2(\mathbf{k}_1, \mathbf{k}_2, \mathbf{k}_3) \right], \quad (4.37)$$

$$\Phi_{\text{GR}}^{(2)}(\mathbf{k}_3) = 3\Omega_m \mathcal{H}^4 \int d(\mathbf{k}_1, \mathbf{k}_2, \mathbf{k}_3) \frac{1}{k_1^2 k_2^2} \left[\frac{1}{2} (3\Omega_m - f + f^2) - \frac{1}{2} (3\Omega_m - 2f + 2f^2) \cdot E_2(\mathbf{k}_1, \mathbf{k}_2, \mathbf{k}_3) \right], \quad (4.38)$$

$$\Psi_{\text{GR}}^{(2)}(\mathbf{k}_3) = 3\Omega_m \mathcal{H}^4 \int d(\mathbf{k}_1, \mathbf{k}_2, \mathbf{k}_3) \frac{1}{k_1^2 k_2^2} \left[\frac{1}{2} (3\Omega_m + f - f^2) + f E_2(\mathbf{k}_1, \mathbf{k}_2, \mathbf{k}_3) \right]. \quad (4.39)$$

From equations (4.22) and (4.39) we can get the time derivatives,

$$\Phi_{\text{N}}^{(2)\prime}(\mathbf{k}) = (2f - 1) \mathcal{H} \Phi^{(2)}, \quad (4.40)$$

$$\begin{aligned} \Psi_{\text{GR}}^{(2)\prime}(\mathbf{k}_3) = & 3\Omega_m \mathcal{H}^5 \int d(\mathbf{k}_1, \mathbf{k}_2, \mathbf{k}_3) \frac{1}{k_1^2 k_2^2} \left\{ \frac{1}{2} (1 - f) [6\Omega_m + f(1 - 2f) \right. \\ & \left. - 2f \frac{\mathcal{H}'}{\mathcal{H}^2}] + \frac{1}{2} (2f - 1) \frac{f'}{\mathcal{H}} + \left[f \left(2f - 1 + \frac{2\mathcal{H}'}{\mathcal{H}^2} \right) + \frac{f'}{\mathcal{H}} \right] E_2(\mathbf{k}_1, \mathbf{k}_2, \mathbf{k}_3) \right\}. \end{aligned} \quad (4.41)$$

To Fourier transform the observed galaxy density contrast, we write $\Delta_g^{(1,2)}$ in terms of Fourier space kernels as,

$$\Delta_g^{(1)}(\mathbf{k}_2) = \int \frac{d^3 k_1}{(2\pi)^3} \mathcal{K}^{(1)}(\mathbf{k}_1) \delta^{(1)}(\mathbf{k}_1) (2\pi)^3 \delta^D(\mathbf{k}_1 - \mathbf{k}_2), \quad (4.42)$$

$$\begin{aligned} \Delta_g^{(2)}(\mathbf{k}_3) = & \int \frac{d^3 k_1}{(2\pi)^3} \frac{d^3 k_2}{(2\pi)^3} \mathcal{K}^{(2)}(\mathbf{k}_1, \mathbf{k}_2, \mathbf{k}_3) \delta^{(1)}(\mathbf{k}_1) \delta^{(1)}(\mathbf{k}_2) (2\pi)^3 \delta^D(\mathbf{k}_1 + \mathbf{k}_2 - \mathbf{k}_3) \\ & - \delta^{(D)}(\mathbf{k}_3) \langle \Delta_g^{(2)} \rangle, \end{aligned} \quad (4.43)$$

subtracting off the ensemble average of Δ_g in the last line,

$$\langle \Delta_g^{(2)} \rangle = \int \frac{d^3 k_1}{(2\pi)^3} P(k_1) \mathcal{K}^{(2)}(\mathbf{k}_1, -\mathbf{k}_1, 0), \quad (4.44)$$

4. Higher order relativistic effects in the bispectrum

where $P(k) \equiv P_{\delta^{(1)}}(k)$ is the linear dark matter power spectrum, such that $\langle \Delta_g \rangle = 0$.

We then split the kernels into Newtonian and GR parts as $\mathcal{K}^{(1,2)} = \mathcal{K}_{\text{N}}^{(1,2)} + \mathcal{K}_{\text{GR}}^{(1,2)}$.

The first-order Newtonian and GR Fourier-space kernels are given by,

$$\mathcal{K}_{\text{N}}^{(1)}(\mathbf{k}) = b_1 + f\mu^2, \quad (4.45)$$

$$\mathcal{K}_{\text{GR}}^{(1)}(\mathbf{k}) = i\frac{\mu}{k}\gamma_1 + \frac{\gamma_2}{k^2} \quad (4.46)$$

where $\mu = \hat{\mathbf{k}} \cdot \mathbf{n}$ is the projection of normalised wavevector \mathbf{k} onto line-of-sight \mathbf{n} and γ_1 and γ_2 are redshift-dependent functions of background coefficients,

$$\frac{\gamma_1}{\mathcal{H}} = f \left[b_e - 2\mathcal{Q} - \frac{2(1-\mathcal{Q})}{\chi\mathcal{H}} - \frac{\mathcal{H}'}{\mathcal{H}^2} \right], \quad (4.47)$$

$$\frac{\gamma_2}{\mathcal{H}^2} = f(3-b_e) + \frac{3}{2}\Omega_m \left[2 + b_e - f - 4\mathcal{Q} - 2\frac{(1-\mathcal{Q})}{\chi\mathcal{H}} - \frac{\mathcal{H}'}{\mathcal{H}^2} \right]. \quad (4.48)$$

The second-order Newtonian part of the kernel is,

$$\begin{aligned} \mathcal{K}_{\text{N}}^{(2)}(\mathbf{k}_1, \mathbf{k}_2, \mathbf{k}_3) &= b_1 F_2(\mathbf{k}_1, \mathbf{k}_2) + b_2 + f G_2(\mathbf{k}_1, \mathbf{k}_2) \mu_3^2 \\ &+ f^2 \frac{\mu_1 \mu_2}{k_1 k_2} (\mu_1 k_1 + \mu_2 k_2)^2 + b_1 \frac{f}{k_1 k_2} [(\mu_1^2 + \mu_2^2) k_1 k_2 + \mu_1 \mu_2 (k_1^2 + k_2^2)], \end{aligned} \quad (4.49)$$

where similarly to before we have $\mu_i = \hat{\mathbf{k}}_i \cdot \mathbf{n}$. The second line incorporates the non-linear Kaiser RSD contribution to the kernel [96, 192].

Finally, the second-order relativistic kernel can be written as,

$$\begin{aligned} \mathcal{K}_{\text{GR}}^{(2)}(\mathbf{k}_1, \mathbf{k}_2, \mathbf{k}_3) &= \frac{1}{k_1^2 k_2^2} \left\{ \beta_1 + E_2(\mathbf{k}_1, \mathbf{k}_2) \beta_2 + i(\mu_1 k_1 + \mu_2 k_2) \beta_3 \right. \\ &+ i\mu_3 k_3 [\beta_4 + E_2(\mathbf{k}_1, \mathbf{k}_2) \beta_5] + \frac{k_1^2 k_2^2}{k_3^2} [F_2(\mathbf{k}_1, \mathbf{k}_2) \beta_6 + G_2(\mathbf{k}_1, \mathbf{k}_2) \beta_7] \\ &+ (\mu_1 k_1 \mu_2 k_2) \beta_8 + \mu_3^2 k_3^2 (\beta_9 + E_2(\mathbf{k}_1, \mathbf{k}_2, \mathbf{k}_3) \beta_{10}) + (\mathbf{k}_1 \cdot \mathbf{k}_2) \beta_{11} \\ &+ (k_1^2 + k_2^2) \beta_{12} + (\mu_1^2 k_1^2 + \mu_2^2 k_2^2) \beta_{13} + i \left[(\mu_1 k_1^3 + \mu_2 k_2^3) \beta_{14} \right. \\ &+ (\mu_1 k_1 + \mu_2 k_2) (\mathbf{k}_1 \cdot \mathbf{k}_2) \beta_{15} + k_1 k_2 (\mu_1 k_2 + \mu_2 k_1) \beta_{16} \\ &+ (\mu_1^3 k_1^3 + \mu_2^3 k_2^3) \beta_{17} + \mu_1 \mu_2 k_1 k_2 (\mu_1 k_1 + \mu_2 k_2) \beta_{18} \\ &\left. \left. + \mu_3 \frac{k_1^2 k_2^2}{k_3} G_2(\mathbf{k}_1, \mathbf{k}_2) \beta_{19} \right] \right\}. \end{aligned} \quad (4.50)$$

4. Higher order relativistic effects in the bispectrum

In the above expression, we have defined 19 redshift-dependent coefficients β_I —not to be confused with the RSD parameter $\beta = f/b_1$. These coefficients are given in full in Appendix A.

To demonstrate how the second-order relativistic kernel is obtained from (4.13), we shall include an example Fourier transform of one of the terms of the second-order observed galaxy overdensity here, and include a table in Appendix B. Taking, for example, $\mathcal{C}\Phi^{(1)}v^{(1)}$, where \mathcal{C} is a background coefficient as defined in equation (4.16). In our Fourier convention we have,

$$[\Phi^{(1)}v^{(1)}](\mathbf{x}) = \int \frac{d^3k}{(2\pi)^3} e^{i\mathbf{k}\cdot\mathbf{x}} [\Phi^{(1)}v^{(1)}](\mathbf{k}), \quad (4.51)$$

and,

$$[\Phi^{(1)}v^{(1)}](\mathbf{k}) = \int d^3x e^{-i\mathbf{k}\cdot\mathbf{x}} [\Phi^{(1)}v^{(1)}](\mathbf{x}). \quad (4.52)$$

Symmetrising, we get,

$$\begin{aligned} [\Phi^{(1)}v^{(1)}](\mathbf{k}) &= \frac{1}{2} \int d^3x \int \frac{d^3k_1}{(2\pi)^3} \int \frac{d^3k_2}{(2\pi)^3} [\Phi^{(1)}(\mathbf{k}_1)v^{(1)}(\mathbf{k}_2) + \Phi^{(1)}(\mathbf{k}_2)v^{(1)}(\mathbf{k}_1)] \cdot \\ &\quad e^{-i\mathbf{k}\cdot\mathbf{x}} e^{i\mathbf{k}_1\cdot\mathbf{x}} e^{i\mathbf{k}_2\cdot\mathbf{x}} \end{aligned} \quad (4.53)$$

$$\Rightarrow \frac{1}{2} \int \frac{d^3k_1}{(2\pi)^3} \int \frac{d^3k_2}{(2\pi)^3} [\Phi^{(1)}(\mathbf{k}_1)v^{(1)}(\mathbf{k}_2) + \Phi^{(1)}(\mathbf{k}_2)v^{(1)}(\mathbf{k}_1)] (2\pi)^3 \delta^D(\mathbf{k}_1 + \mathbf{k}_2 - \mathbf{k}), \quad (4.54)$$

where in the second line we have performed the integral over x and the exponentials. Then, expand the perturbative variables in terms of $\delta^{(1)}$ using the relations,

$$\mathcal{H}v^{(1)}(\mathbf{k}) = f \frac{\mathcal{H}^2}{k^2} \delta^{(1)}(\mathbf{k}), \quad (4.55)$$

$$\Phi^{(1)}(\mathbf{k}) = -\frac{3}{2} \Omega_m \frac{\mathcal{H}^2}{k^2} \delta^{(1)}(\mathbf{k}), \quad (4.56)$$

as,

$$[\Phi^{(1)}(\mathbf{k}_1)v^{(1)}(\mathbf{k}_2) + \Phi^{(1)}(\mathbf{k}_2)v^{(1)}(\mathbf{k}_1)] \quad (4.57)$$

$$= -\frac{3}{2} \Omega_m \frac{\mathcal{H}^2}{k_1^2} \delta^{(1)}(\mathbf{k}_1) f \frac{\mathcal{H}}{k_2^2} \delta^{(1)}(\mathbf{k}_2) - \frac{3}{2} \Omega_m \frac{\mathcal{H}^2}{k_2^2} \delta^{(1)}(\mathbf{k}_2) f \frac{\mathcal{H}}{k_1^2} \delta^{(1)}(\mathbf{k}_1) \quad (4.58)$$

$$= -\frac{6}{2} \Omega_m \frac{\mathcal{H}^3}{k_1^2 k_2^2} f \delta^{(1)}(\mathbf{k}_1) \delta^{(1)}(\mathbf{k}_2). \quad (4.59)$$

4. Higher order relativistic effects in the bispectrum

Using the above, we can write the Fourier transformed term as,

$$[\Phi^{(1)}v^{(1)}](\mathbf{k}) = \int \frac{d^3k_1}{(2\pi)^3} \int \frac{d^3k_2}{(2\pi)^3} \mathcal{F}[\Phi^{(1)}v^{(1)}](2\pi)^3 \delta^D(\mathbf{k}_1 + \mathbf{k}_2 - \mathbf{k}), \quad (4.60)$$

where we can identify the Fourier kernel,

$$\mathcal{F}[\Phi^{(1)}v^{(1)}] = \frac{1}{2} \left(-\frac{6}{2} \Omega_m \frac{\mathcal{H}^3}{k_1^2 k_2^2} f \right) \quad (4.61)$$

$$= \frac{-3\Omega_m \mathcal{H}^3 f}{2k_1^2 k_2^2}, \quad (4.62)$$

with coefficient \mathcal{C} . In Appendix B, a table of terms and the corresponding Fourier space kernels and coefficients can be found.

4.2. Construction of the galaxy bispectrum

The Fourier space observed galaxy bispectrum at a fixed redshift is given by,

$$\langle \Delta_g(\mathbf{k}_1) \Delta_g(\mathbf{k}_2) \Delta_g(\mathbf{k}_3) \rangle = (2\pi)^3 B_g(\mathbf{k}_1, \mathbf{k}_2, \mathbf{k}_3) \delta^D(\mathbf{k}_1 + \mathbf{k}_2 + \mathbf{k}_3). \quad (4.63)$$

The only terms that contribute to the tree-level bispectrum at second order are,

$$2\langle \Delta_g(\mathbf{k}_1) \Delta_g(\mathbf{k}_2) \Delta_g(\mathbf{k}_3) \rangle = \langle \Delta_g^{(1)}(\mathbf{k}_1) \Delta_g^{(1)}(\mathbf{k}_2) \Delta_g^{(2)}(\mathbf{k}_3) \rangle + 2 \text{ cyc. perm.}, \quad (4.64)$$

where the factor of 2 on the left hand side originates from the factor of 1/2 in our perturbative expansion of the observed galaxy density contrast. Since we expand Δ_g into Newtonian and GR parts, the terms that contribute to the tree-level Fourier space bispectrum can be made more explicit by writing,

$$\begin{aligned} & \langle \Delta_g^{(1)}(\mathbf{k}_1) \Delta_g^{(1)}(\mathbf{k}_2) \Delta_g^{(2)}(\mathbf{k}_3) \rangle + 2 \text{ cyclic permutations} \\ &= \frac{1}{2} \left[\langle \Delta_{gN}^{(1)}(\mathbf{k}_1) \Delta_{gN}^{(1)}(\mathbf{k}_2) \Delta_{gN}^{(2)}(\mathbf{k}_3) \rangle + \langle \Delta_{gGR}^{(1)}(\mathbf{k}_1) \Delta_{gGR}^{(1)}(\mathbf{k}_2) \Delta_{gGR}^{(2)}(\mathbf{k}_3) \rangle \right. \\ &+ \langle \Delta_{gN}^{(1)}(\mathbf{k}_1) \Delta_{gN}^{(1)}(\mathbf{k}_2) \Delta_{gGR}^{(2)}(\mathbf{k}_3) \rangle + \langle \Delta_{gGR}^{(1)}(\mathbf{k}_1) \Delta_{gGR}^{(1)}(\mathbf{k}_2) \Delta_{gN}^{(2)}(\mathbf{k}_3) \rangle \Big] \\ &+ \left[\langle \Delta_{gN}^{(1)}(\mathbf{k}_1) \Delta_{gGR}^{(1)}(\mathbf{k}_2) \Delta_{gN}^{(1)}(\mathbf{k}_3) \rangle + \langle \Delta_{gN}^{(1)}(\mathbf{k}_1) \Delta_{gGR}^{(1)}(\mathbf{k}_2) \Delta_{gGR}^{(2)}(\mathbf{k}_3) \rangle \right] \\ &+ 2 \text{ cyc. perm.} \end{aligned} \quad (4.65)$$

4. Higher order relativistic effects in the bispectrum

The expression above shows the separation of the bispectrum into the Newtonian and relativistic observed galaxy number counts—illustrating that there is a split into a purely Newtonian and a purely GR part (the first two terms on the right hand side of the equality sign), and cross-correlations between Newtonian and GR terms.

The galaxy bispectrum in terms of Fourier space then follows as,

$$B_g(\mathbf{k}_1, \mathbf{k}_2, \mathbf{k}_3) = \mathcal{K}^{(1)}(\mathbf{k}_1)\mathcal{K}^{(1)}(\mathbf{k}_2)\mathcal{K}^{(2)}(\mathbf{k}_1, \mathbf{k}_2, \mathbf{k}_3)P(k_1)P(k_2) + 2 \text{ cyc. perm.}, \quad (4.66)$$

The Fourier space kernels that appear on the right hand side in the above equation then can be split into Newtonian and relativistic parts, analogous to the split into Newtonian and Doppler parts as considered in the first part of this thesis. Hence, we can write,

$$\mathcal{K}^{(1,2)} = \mathcal{K}_{\text{N}}^{(1,2)} + \mathcal{K}_{\text{GR}}^{(1,2)}. \quad (4.67)$$

The GR parts of the kernels here are composed of all relativistic corrections at all orders of \mathcal{H}/k . From products between the first- and second-order Fourier space kernels, more suppressed contributions are generated also. All of these are considered henceforth.

Figure 4.1 shows the monopole of the bispectrum including local GR effects for different triangular configurations, compared to the monopole in the Newtonian approximation. On large scales (small k), the departure of the GR monopole from the Newtonian approximation becomes large.

A Newtonian analysis of the bispectrum, in the case where equality scales and larger are probed, could suffer from serious bias when GR projection effects are ignored. To illustrate this, a simple estimate for the effective f_{NL} can be made, considering PNG in the Newtonian bispectrum (ignoring scale-dependent bias), taken directly from [108]. Writing the Newtonian non-Gaussian bispectrum as,

$$B_{g,\text{N}}^{\text{nG}}(\mathbf{k}_1, \mathbf{k}_2, \mathbf{k}_3) = \mathcal{K}_{\text{N}}^{(1)}(\mathbf{k}_1)\mathcal{K}_{\text{N}}^{(2)}(\mathbf{k}_2) \left[\mathcal{K}_{\text{N}}^{(2)}(\mathbf{k}_1, \mathbf{k}_2, \mathbf{k}_3) + 2f_{\text{NL}}\mathcal{K}_{\text{N}}^{(1)}(\mathbf{k}_3)\frac{\mathcal{M}(k_3)}{\mathcal{M}(k_1)\mathcal{M}(k_2)} \right] P(k_1)P(k_2) + 2 \text{ c.p..} \quad (4.68)$$

Here, \mathcal{M} is the scale-dependent function that relates the late-time matter density contrast to the primordial potential, which we briefly met before in Chapter 1, and will be defined in Chapter 6. Using this expression for the Newtonian PNG bispectrum, a rough estimate for the effective f_{NL} from ignoring GR projection

4. Higher order relativistic effects in the bispectrum

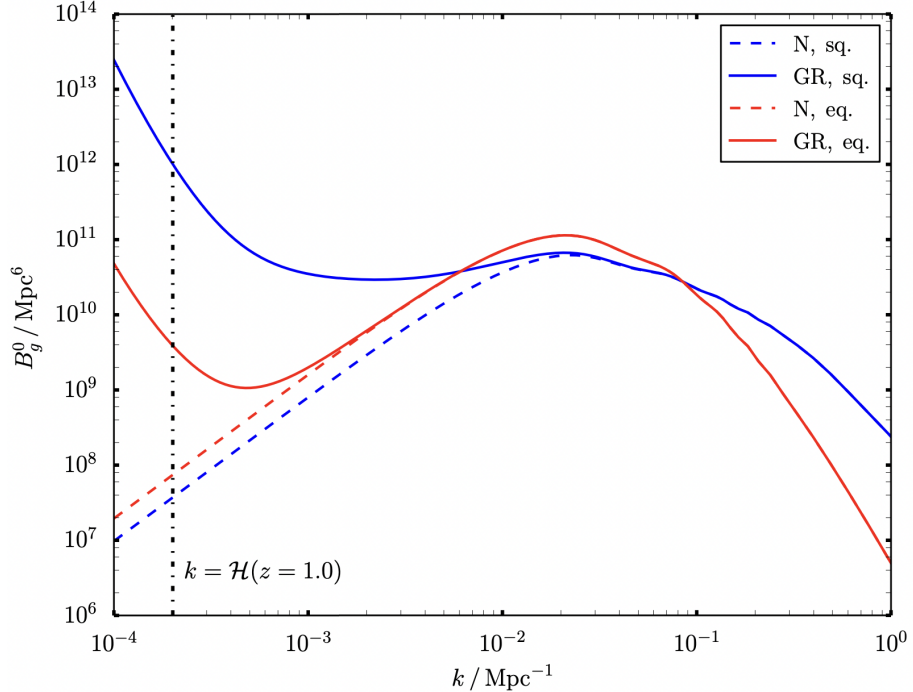


Figure 4.1.: Monopole of the bispectrum at $z = 1$, taken from [108]. The different colours denote the different triangle shapes considered—blue representing a squeezed shape (chosen such that $k_3 \approx k/16$), and red denotes the equilateral shape. The shape is held fixed, and the overall scale of the triangle is varied (k along the x -axis). Dashed lines denote the Newtonian approximation, and the solid lines include local GR effects.

effects would be,

$$f_{\text{NL}}^{\text{eff}} = \left\{ \left[\mathcal{K}_{\text{GR}}^{(1)}(\mathbf{k}_1) \mathcal{K}^{(1)}(\mathbf{k}_2) \mathcal{K}^{(2)}(\mathbf{k}_1, \mathbf{k}_2, \mathbf{k}_3) + \mathcal{K}_{\text{N}}^{(1)}(\mathbf{k}_1) \mathcal{K}_{\text{GR}}^{(1)}(\mathbf{k}_2) \mathcal{K}^{(2)}(\mathbf{k}_1, \mathbf{k}_2, \mathbf{k}_3) \right. \right. \\ \left. \left. \mathcal{K}_{\text{N}}^{(1)}(\mathbf{k}_1) \mathcal{K}_{\text{N}}^{(1)}(\mathbf{k}_2) \mathcal{K}_{\text{GR}}^{(2)}(\mathbf{k}_1, \mathbf{k}_2, \mathbf{k}_3) \right] P(k_1) P(k_2) + 2 \text{ c.p.} \right\} \\ \cdot \left\{ 2 \mathcal{K}_{\text{N}}^{(1)}(\mathbf{k}_1) \mathcal{K}_{\text{N}}^{(1)}(\mathbf{k}_2) \mathcal{K}_{\text{N}}^{(1)}(\mathbf{k}_3) \frac{\mathcal{M}(k_3)}{\mathcal{M}(k_1) \mathcal{M}(k_2)} P(k_1) P(k_2) + 2 \text{ c.p.} \right\}^{-1}. \quad (4.69)$$

Figure 4.2 shows the effective non-Gaussianity from neglecting local GR projection effects from comparison to a Newtonian analysis, as described above. At equality scales, this leads to an effective f_{NL} of ~ 1.4 for equilateral shapes and ~ 9 for squeezed shapes. This means that when GR effects are neglected and a false Newtonian analysis is used, one would conclude that the primordial universe was significantly non-Gaussian (of course, this estimate neglects scale-dependent bias, the effects of which are similar to the lightcone effects, and we will discuss this properly in Chapter 6).

4. Higher order relativistic effects in the bispectrum

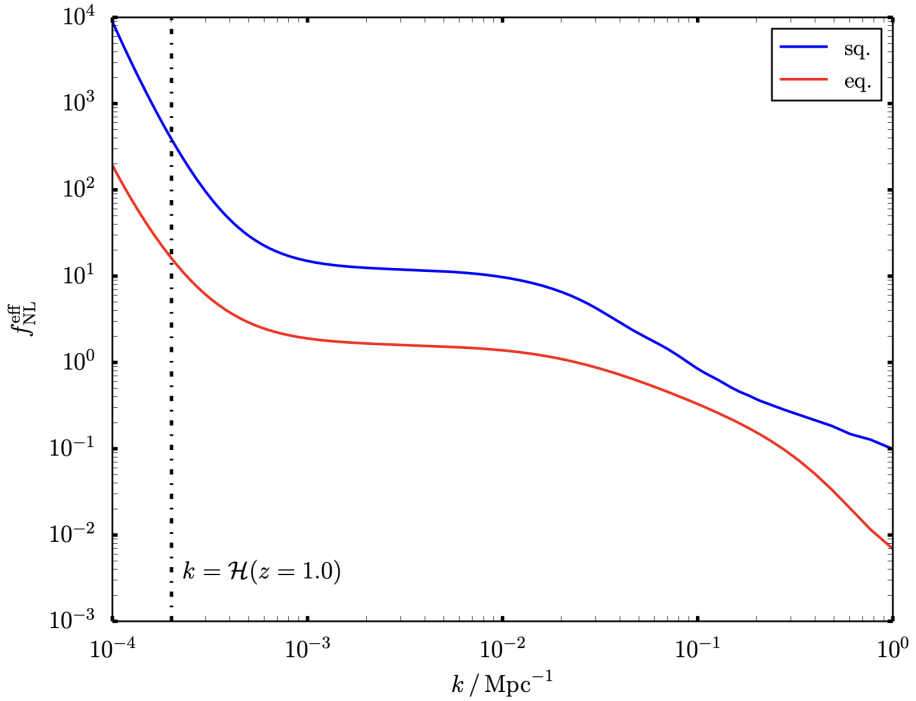


Figure 4.2.: Effective f_{NL} due to neglecting GR projection effects, from comparison to a Newtonian bispectrum analysis but ignoring scale-dependent bias. The red solid line corresponds to the equilateral shape, and the blue solid line denotes the squeezed shape, as in Figure 4.1. This figure is taken from [108].

4.3. Contributions from second-order vector and tensor modes

Around and above the equality scale, the bispectrum receives local contributions from the generated vector and tensor background, which is generated by scalar modes [193–199]. In this section we will discuss these second-order vector and tensor contributions, which for the Fourier-space galaxy bispectrum were first derived in [109]. These contributions are subdominant in the relativistic bispectrum, and will be neglected in subsequent chapters of this thesis.

The metric in Poisson gauge and conformal time η can be written as,

$$ds^2 = a^2 \left[- (1 + 2\Phi^{(1)}) d\eta^2 + \omega_i^{(2)} dx^i d\eta + \left[(1 - 2\Psi^{(1)}) \delta_{ij} + \frac{1}{2} h_{ij}^{(2)} \right] dx^i dx^j \right], \quad (4.70)$$

where we include only first order scalar perturbations that source the second-order vector and tensor perturbations $\omega_i^{(2)}$ and $h_{ij}^{(2)}$. Vector and tensor modes are charac-

4. Higher order relativistic effects in the bispectrum

terised by being divergence-free. We also have that $\Phi^{(1)} = \Psi^{(1)}$, which we write as Φ for brevity. The first-order vector and tensor modes are purely decaying modes and are neglected [200–202]. The solutions for the vector mode is given by [199],

$$\nabla^2 \omega_i(\mathbf{x}) = \frac{16}{3\Omega_m \mathcal{H}} [\nabla^2 \Phi(\mathbf{x}) \partial_i \Phi(\mathbf{x})]^V \quad (4.71)$$

where V denotes the vector part, and we have dropped the superscript (2) for brevity. The other second-order contribution comes from generation of tensor modes as structure forms, which are found by projecting out the tensor part of the ij part of the Einstein field equations. These modes are considered in [193–195, 197, 200, 203–210]. Adapting from [197] to include a cosmological constant, we obtain for the tensor projection (superscript (T)),

$$h_{ij}'' + 2\mathcal{H}h_{ij}' - \nabla^2 h_{ij} = S_{ij}(\mathbf{x}) = 8 \left[\partial_i \Phi \partial_j \Phi + \frac{1}{4\pi G a^2 \rho} \partial_i (\Phi' + \mathcal{H}\Phi) \partial_j (\Phi' + \mathcal{H}\Phi) \right]^T \quad (4.72)$$

$$= 8 \left[1 + \frac{2f^2}{3\Omega_m} \right] [\partial_i \Phi \partial_j \Phi]^T. \quad (4.73)$$

When including these second-order vector and tensor modes in the observed galaxy number counts, we can expand $\Delta_g^{(2)}$ to include explicitly these contributions as,

$$\Delta_g^{(2)} = \Delta_{gN}^{(2)} + \Delta_{gS}^{(2)} + \Delta_{gV}^{(2)} + \Delta_{gT}^{(2)}, \quad (4.74)$$

where as before subscript N denotes the Newtonian part, subscript S here denotes the local parts of the non-Newtonian scalar contribution (which were referred to by subscript GR throughout this chapter), and V and T denote the contributions to the observed number counts from the second-order vector and tensor perturbations.

It can be shown that the second-order local contributions of vectors and tensors respectively to the galaxy number count are given by [98],

$$\Delta_{gV}^{(2)}(\mathbf{x}) = \left[-b_e + 2\mathcal{Q} + \frac{2(1-\mathcal{Q})}{\chi\mathcal{H}} + \frac{\mathcal{H}'}{\mathcal{H}^2} + \frac{1}{\mathcal{H}} \partial_{||} \right] \omega_{||}(\mathbf{x}), \quad (4.75)$$

$$\Delta_{gT}^{(2)}(\mathbf{x}) = -\frac{1}{2}(1-\mathcal{Q})h_{||}(\mathbf{x}) - \frac{1}{2\mathcal{H}}h'_{||}(\mathbf{x}), \quad (4.76)$$

where $\omega_{||} = n^i \omega_i$ is the longitudinal component of the vector perturbation, $h_{||} = h_{ij} n^i n^j$, and we have suppressed redshift dependence (for we consider correlations at the same redshift only) as well as superscript (2) on the vector and tensor modes.

4. Higher order relativistic effects in the bispectrum

In Fourier space, these contributions to the observed density contrast can be written as integrals over kernels,

$$\Delta_{gV}^{(2)}(\mathbf{k}_3) = \int d(\mathbf{k}_1, \mathbf{k}_2, \mathbf{k}_3) \mathcal{K}_V^{(2)}(\mathbf{k}_1, \mathbf{k}_2, \mathbf{k}_3), \quad (4.77)$$

$$\Delta_{gT}^{(2)}(\mathbf{k}_3) = \int d(\mathbf{k}_1, \mathbf{k}_2, \mathbf{k}_3) \mathcal{K}_T^{(2)}(\mathbf{k}_1, \mathbf{k}_2, \mathbf{k}_3). \quad (4.78)$$

The explicit forms of the kernels are derived in [109]. For the vector modes, it is,

$$\begin{aligned} \mathcal{K}_V^{(2)}(\mathbf{k}_1, \mathbf{k}_2, \mathbf{k}_3) = & 12\Omega_m \mathcal{H}^2 f \left(\frac{\mu_3}{k_3} - i \frac{\mathcal{H}}{k_3^2} \left[-b_e + 2\mathcal{Q} + \frac{2(1-Q)}{\chi\mathcal{H}} + \frac{\mathcal{H}'}{\mathcal{H}^2} \right] \right) \\ & \cdot \left[\mathbf{n} \cdot \mathbf{e}(\mathbf{k}_3) \left(\frac{\mathbf{k}_1 \cdot \mathbf{e}(\mathbf{k}_3)}{k_1^2} + \frac{\mathbf{k}_2 \cdot \mathbf{e}(\mathbf{k}_3)}{k_2^2} \right) + \mathbf{n} \cdot \bar{\mathbf{e}} \left(\frac{\mathbf{k}_1 \cdot \bar{\mathbf{e}}(\mathbf{k}_3)}{k_1^2} + \frac{\mathbf{k}_2 \cdot \bar{\mathbf{e}}(\mathbf{k}_3)}{k_2^2} \right) \right], \end{aligned} \quad (4.79)$$

where \mathbf{e} and $\bar{\mathbf{e}}$ are the 2 polarisation vectors associated with the vector mode. The kernel is symmetric on $\mathbf{k}_1 \leftrightarrow \mathbf{k}_2$, and complex, with the real part having a k -dependence of $\mathcal{O}(k^{-2})$ and the imaginary part a k -dependence of $\mathcal{O}(k^{-3})$. For an equilateral triangular configuration in which case $k_1 = k_2 = k_3 = k$, it can easily be seen that the above kernel vanishes, since in this case $\mathbf{k}_1 \cdot \mathbf{e}(\mathbf{k}_3) = -\mathbf{k}_2 \cdot \mathbf{e}(\mathbf{k}_3)$. The physical reason behind it is that the equilateral configuration of the bispectrum probes vector modes that are generated by scalar modes at the same wavelength. However, as shown in [196], only when 2 scalar modes have different wavelengths they can generate vector modes, otherwise the interaction will not generate any angular momentum. For the tensor modes, the kernel is,

$$\begin{aligned} \mathcal{K}_T^{(2)}(\mathbf{k}_1, \mathbf{k}_2, \mathbf{k}_3) = & 3\Omega_m \mathcal{H}^4 \left\{ \left[-3\Omega_m(1+\mathcal{Q}) - 2f^2\mathcal{Q} - (3\Omega_m - 2f^2) \frac{\mathcal{H}'}{\mathcal{H}^2} + 4 \frac{ff'}{\mathcal{H}} \right] \right. \\ & \cdot \mathcal{G}(\eta, k_3) + \frac{3\Omega_m + 2f^2}{\mathcal{H}} \mathcal{G}'(\eta, k_3) \Big\} \\ & \cdot \frac{e^{ij}(\mathbf{k}_3) k_{1i} k_{2j} n^\ell n^m e_{\ell m}(\mathbf{k}_3) + \bar{e}^{ij}(\mathbf{k}_3) k_{1i} k_{2j} n^\ell n^m \bar{e}_{\ell m}(\mathbf{k}_3)}{k_1^2 k_2^2 k_3^2}, \end{aligned} \quad (4.80)$$

where e_{ij} and \bar{e}_{ij} are orthogonal polarisation tensors and function $\mathcal{G}(\eta, k)$ comes from solving the tensor wave equation,

$$\mathcal{G}(\eta, k) = 1 + \frac{3[k\eta \cos(k\eta) - \sin(k\eta)]}{(k\eta)^3}, \quad (4.81)$$

see [109] for a detailed derivation. For both kernels, products of the polarisations

4. Higher order relativistic effects in the bispectrum

with the wavevectors is complicated and requires a coordinate system, resulting in different expressions for each of the permutations.

In order to illustrate that these contributions due to the second-order vector and tensor modes are subdominant and therefore safely neglected in our further treatment of the galaxy bispectrum, we will plot the monopole of the bispectrum for the various cases; purely Newtonian, local relativistic effects from scalar modes only, and those due to the vector and tensor modes. From the definition of the galaxy bispectrum in terms of Fourier-space kernels as before, we can split the second-order kernel as,

$$\mathcal{K}^{(2)} = \mathcal{K}_N^{(2)} + \mathcal{K}_{GR}^{(2)} + \mathcal{K}_V^{(2)} + \mathcal{K}_T^{(2)}, \quad (4.82)$$

where now we have taken to explicitly state the separate terms due to the scalar contributions as Newtonian (N) and relativistic (GR). The second-order vector and tensor contributions to the bispectrum then are given by,

$$B_{gV}(\mathbf{k}_1, \mathbf{k}_2, \mathbf{k}_3) = \mathcal{K}^{(1)}(\mathbf{k}_1)\mathcal{K}^{(1)}(\mathbf{k}_2)\mathcal{K}_V^{(2)}(\mathbf{k}_1, \mathbf{k}_2, \mathbf{k}_3)P(k_1)P(k_2) + 2 \text{ c.p.}, \quad (4.83)$$

$$B_{gT}(\mathbf{k}_1, \mathbf{k}_2, \mathbf{k}_3) = \mathcal{K}^{(1)}(\mathbf{k}_1)\mathcal{K}^{(1)}(\mathbf{k}_2)\mathcal{K}_T^{(2)}(\mathbf{k}_1, \mathbf{k}_2, \mathbf{k}_3)P(k_1)P(k_2) + 2 \text{ c.p.}, \quad (4.84)$$

where in each of the above expressions we keep the full GR part in the first-order kernels. The ‘scalar’ part of the bispectrum, which consists of the Newtonian part as well as the local scalar relativistic corrections, is given by,

$$B_{gS}(\mathbf{k}_1, \mathbf{k}_2, \mathbf{k}_3) = \mathcal{K}^{(1)}(\mathbf{k}_1)\mathcal{K}^{(1)}(\mathbf{k}_2)\mathcal{K}_S^{(2)}(\mathbf{k}_1, \mathbf{k}_2, \mathbf{k}_3)P(k_1)P(k_2) + 2 \text{ c.p.}, \quad (4.85)$$

where similarly to above the full $\mathcal{O}(1)$ GR kernel is included, and $\mathcal{K}_S^{(2)} = \mathcal{K}_N^{(2)} + \mathcal{K}_{GR}^{(2)}$.

Taking the monopole of the bispectrum as,

$$B_g^0(k_1, k_2, k_3) = \frac{1}{\sqrt{4\pi}} \int_0^{2\pi} d\varphi \int_{-1}^1 d\mu_1 B_g(k_1, k_2, k_3, \mu, \varphi), \quad (4.86)$$

which can be computed for the bispectrum vector/tensor/scalar contributions separately. For reference, the monopole of the ‘full’ relativistic bispectrum is included too, which is defined as,

$$B_{gfull}(\mathbf{k}_1, \mathbf{k}_2, \mathbf{k}_3) = \mathcal{K}^{(1)}(\mathbf{k}_1)\mathcal{K}^{(1)}(\mathbf{k}_2)\mathcal{K}^{(2)}(\mathbf{k}_1, \mathbf{k}_2, \mathbf{k}_3)P(k_1)P(k_2) + 2 \text{ c.p.}, \quad (4.87)$$

which includes all contributions discussed in this section. The result is shown in

4. Higher order relativistic effects in the bispectrum

figure 4.3, at fixed redshift $z = 1$, with a simplified toy model of galaxy bias for illustrative purposes only, which is, [107]

$$\begin{aligned} b_1 &= \sqrt{1+z}, & b_2 &= -0.1\sqrt{1+z}, \\ b_e &= \mathcal{Q} = 0, & b_s &= -\frac{4}{7}(b_1 - 1). \end{aligned} \quad (4.88)$$

Cosmological parameters chosen here are $\Omega_{m0} = 1 - \Omega_{\Lambda0} = 0.308$, $h = 0.678$. The bispectrum configuration is fixed to be a moderately squeezed triangle with $k_1 = k_2 = k$ and $k_3 \approx k/16$, with long mode k_3 plotted along the x -axis. The dashed lines indicate negative values (the sign of the bispectrum monopole indicates whether overdensities are more or less clustered relative to voids than in a Gaussian random field).

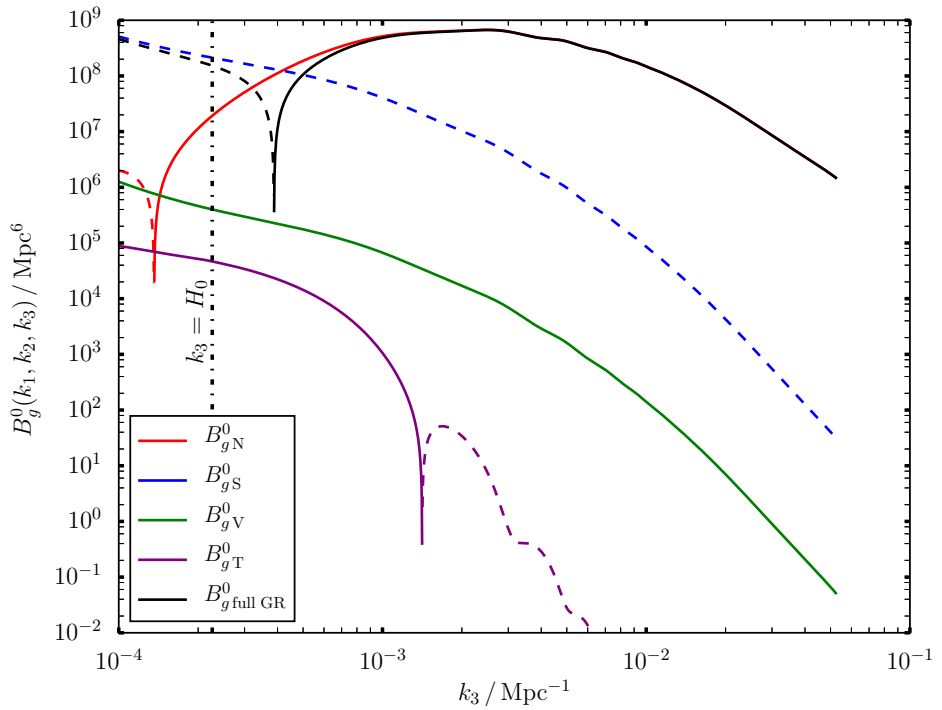


Figure 4.3.: The separated vector, tensor, and scalar contributions to the monopole of the galaxy bispectrum, with the full GR bispectrum in black for reference. The vector and tensor modes are subdominant at a factor of about 3 orders of magnitude smaller than the scalar contributions, except outside the Hubble radius (and where unobservable) where they grow due to their k -dependence and where the Newtonian contribution becomes negative as a result of the tidal bias. The tensor contributions (purple) oscillate at small scales as they pick up the BAO.

4. Higher order relativistic effects in the bispectrum

Figure 4.3 shows that the contributions due to vector and tensor modes are small on all scales, as expected. They grow only towards the Hubble radius (indicated on the figure with a dash-dotted vertical line) due to their k -dependence, with the leading behaviour scaling as $(\mathcal{H}/k)^2$. While the vector contribution is larger than the contribution due to the second-order tensor modes, it is still about three orders of magnitude below the scalar contribution. When the long mode k_3 is outside the Hubble radius (and hence unobservable) it does grow larger than the Newtonian contribution—this is due to the tidal bias causing a sign change in the Newtonian contribution at these scales. A final thing to note is that the tensor contribution oscillates on small scales, picking up the BAO.

As the vector and tensor modes are subdominant compared to the scalar contributions to the bispectrum, they may safely be ignored. Integrated contributions from these sources may alter this conclusion, however due to computational complexity any integrated contributions are left for future work.

5. Multipoles of the bispectrum

In previous chapters, we have examined the leading-order relativistic effect in more detail, which induces a dipole with respect to the observer’s line-of-sight. A full multipole decomposition including all orders of local relativistic effects is presented in this chapter, which is taken from [211]. The chapter is organised as follows. We introduce the relativistic Fourier space bispectrum in section 5.1, and present the multipole expansion of the relativistic bispectrum in section 5.2. An analysis of the multipoles can be found in section 5.3. Finally, we summarise our conclusions in section 5.4.

5.1. The relativistic bispectrum

Galaxy number count fluctuations are distorted due to the fact that we observe on the past lightcone. A well-known effect is the Kaiser redshift-space distortion (RSD) effect [96, 105]. Further distortions are due to lensing convergence, as well as due to Doppler, Sachs-Wolfe, Integrated Sachs-Wolfe (ISW), and time delay effects; all of which are suppressed on sub-equality scales. There are also couplings between these effects when one goes up to non-linear order.

The observed galaxy power spectrum at tree level involves only the projection effects at first order. However, the bispectrum, even at tree level, involves both first- and second-order relativistic projection effects. These have all been introduced in Chapter 4.

Above the equality scale the galaxy bispectrum will be a key probe for measuring primordial non-Gaussianity which can help differentiate between different inflationary models and other theories of the early universe. On these scales a variety of relativistic effects come into play once the galaxy number-count fluctuation is projected onto our past lightcone. By decomposing the Fourier-space bispectrum into invariant multipoles about the observer’s line of sight we examine in detail how the

5. Multipoles of the bispectrum

relativistic effects contribute to these. We show how to perform this decomposition analytically, which is significantly faster for subsequent computations. While all multipoles receive a contribution from the relativistic part, odd multipoles arising from the imaginary part of the bispectrum have no Newtonian contribution, making the odd multipoles a smoking gun for a relativistic signature in the bispectrum for single tracers. The dipole and the octopole are significant on equality scales and above where the Newtonian approximation breaks down. This breakdown is further signified by the fact that the even multipoles receive a significant correction on very large scales.

The bispectrum will play a key role in future galaxy surveys as an important probe of large-scale structure and for measuring primordial non-Gaussianity and galaxy bias [212–214]. It can help discriminate between different inflationary models and other theories of the early universe, and contains information that is complementary and additional to what is contained in the power spectrum. On super-equality scales, a variety of relativistic effects come into play once the galaxy number-count fluctuation is projected onto the past light cone. In the density contrast up to second order, relativistic effects arise from observing on the past lightcone, and they include all redshift, volume and lensing distortions and couplings between these. In Poisson gauge, these effects can be attributed to velocities (Doppler), gravitational potentials (Sachs-Wolfe, integrated SW, time delay) and lensing magnification and shear. In addition, there are corrections arising from a GR definition of galaxy bias [149]. These effects generate corrections to the Newtonian approximation at order $\mathcal{O}(\mathcal{H}/k)$ and higher. Non-Gaussianity generated by these relativistic projection effects could closely mimic the signature of f_{NL} on large scales which gives a correction in the halo bias $\mathcal{O}((\mathcal{H}/k)^2)$, indicating the importance of precisely including all $\mathcal{O}(\mathcal{H}/k)$ and higher effects in theoretical modelling. So far, a variety of relativistic effects in the galaxy Fourier bispectrum has been taken into account, see [88, 102, 107–109, 114] under the assumption of the plane parallel approximation, and neglecting integrated effects. Other groups are working on this from different angles and approaches, for example by a spherical-Fourier formalism [142], and calculating the angular galaxy bispectrum [103, 141]. Crucially, we have shown that the relativistic part should be detectable in a survey like *Euclid* without resorting to the multi-tracer technique, which is needed for the power spectrum [114].

Once an observable like the galaxy number-count fluctuation is projected onto the past lightcone the orientation of the triangle in the Fourier space bispectrum becomes important. Analogously to how the Legendre multipole expansion is used for power

5. Multipoles of the bispectrum

spectrum analysis, one can expand the galaxy bispectrum in spherical harmonics, thus isolating the different invariant multipoles with respect to the observer's line of sight \mathbf{n} . We use the full spherical harmonics for the bispectrum rather than the Legendre polynomial expansion usually adopted for the power spectrum because of the azimuthal degrees of freedom associated with the orientation of the triangle with respect to the line of sight direction vector in Fourier space. In the power spectrum limit, there is only one angular degree of freedom after ensemble averaging. For the bispectrum, we have one angular and one azimuthal degree of freedom which when expanded in spherical harmonics leads to $(2\ell + 1)$ independent harmonics for each multipole value ℓ .

This has been done for the Newtonian bispectrum, which generates non-zero multipoles only for even ℓ (up to $\ell = 8$) due to redshift-space distortions [96, 97]. Contrary to the Newtonian bispectrum, the relativistic galaxy bispectrum generates non-zero multipoles for both even and odd ℓ up to $\ell = 8$ and $m = 6$ where the odd multipoles are induced by the general relativistic effects only. This means that these multipoles are a crucial signature of relativistic projection effects. We provide, for the first time, a multipole decomposition of the Fourier space galaxy bispectrum with relativistic effects included. Additionally we show that the coefficients of this expansion can be worked out analytically. We provide an exact analytic formula for this multipole expansion of the galaxy bispectrum. Previously, we examined for the first time the dipole of the galaxy bispectrum in detail, showing that its amplitude can be more than 10% of that of the monopole even at equality scales [88]. In order to eliminate possible biases when analysing large scale structure data, it is important to include the relativistic effects. In addition to this, a variety of the effects that appear in the bispectrum are relativistic effects that have not been measured elsewhere and hence are interesting to study. By analysing the non-zero multipoles of the galaxy bispectrum both for a *Euclid*-like galaxy survey, and for an SKA-like HI intensity mapping survey, we show the behaviour of the higher multipoles and their corrections to the Newtonian bispectrum. In follow-up work, we are investigating possibilities of detecting the higher multipoles of the bispectrum. See for example [114] for detection prospects of the leading order relativistic effects; the dipole is expected to have the strongest GR signature.

In Fourier space, the observed galaxy bispectrum B_g at a fixed redshift z is given by [102, 107]

$$\langle \Delta_g(z, \mathbf{k}_1) \Delta_g(z, \mathbf{k}_2) \Delta_g(z, \mathbf{k}_3) \rangle = (2\pi)^3 B_g(z, \mathbf{k}_1, \mathbf{k}_2, \mathbf{k}_3) \delta^D(\mathbf{k}_1 + \mathbf{k}_2 + \mathbf{k}_3), \quad (5.1)$$

5. Multipoles of the bispectrum

where $\Delta_g(z, \mathbf{k}_1)$ is the number count contrast at redshift z (see [102] for the full expression). Here we work in the Poisson gauge; note that $\Delta_g = \delta_g + \text{RSD} + \text{GR}$ projection effects, where the RSD term is the Kaiser RSD up to second order, which is part of the Newtonian approximation. Since redshift is fixed, in what follows we drop redshift dependence for brevity. Furthermore, since the observed direction \mathbf{n} is fixed in what follows, the plane-parallel approximation is necessarily assumed. Then, at tree level, and for Gaussian initial conditions, the following combinations of terms contribute,

$$\langle \Delta_g(\mathbf{k}_1) \Delta_g(\mathbf{k}_2) \Delta_g(\mathbf{k}_3) \rangle = \frac{1}{2} \langle \Delta_g^{(1)}(\mathbf{k}_1) \Delta_g^{(1)}(\mathbf{k}_2) \Delta_g^{(2)}(\mathbf{k}_3) \rangle + 2 \text{ c.p.} \quad (5.2)$$

Using Wick's theorem, this gives an expression for the galaxy bispectrum [102]

$$B_g(\mathbf{k}_1, \mathbf{k}_2, \mathbf{k}_3) = \mathcal{K}^{(1)}(\mathbf{k}_1) \mathcal{K}^{(1)}(\mathbf{k}_2) \mathcal{K}^{(2)}(\mathbf{k}_1, \mathbf{k}_2, \mathbf{k}_3) P(\mathbf{k}_1) P(\mathbf{k}_2) + 2 \text{ c.p.}, \quad (5.3)$$

where P is the power spectrum of $\delta_{\text{T}}^{(1)}$, the first order dark matter density contrast in the total-matter gauge, which corresponds to an Eulerian frame. The first order kernel can be split into a Newtonian and a relativistic part as [116]

$$\mathcal{K}^{(1)} = \mathcal{K}_{\text{N}}^{(1)} + \mathcal{K}_{\text{GR}}^{(1)}, \quad \mathcal{K}_{\text{N}}^{(1)} = b_1 + f\mu^2, \quad \mathcal{K}_{\text{GR}}^{(1)} = i\mu \frac{\gamma_1}{k} + \frac{\gamma_2}{k^2}, \quad (5.4)$$

with $\mu = \hat{\mathbf{k}} \cdot \mathbf{n}$ ($\hat{\mathbf{k}} = \mathbf{k}/k$), b_1 is the first-order Eulerian galaxy bias coefficient, f is the linear growth rate of matter perturbations, and redshift-dependent coefficients γ_i are [116],

$$\frac{\gamma_1}{\mathcal{H}} = f \left[b_e - 2\mathcal{Q} - \frac{2(1-\mathcal{Q})}{\chi\mathcal{H}} - \frac{\mathcal{H}'}{\mathcal{H}^2} \right], \quad (5.5)$$

$$\frac{\gamma_2}{\mathcal{H}^2} = f(3-b_e) + \frac{3}{2}\Omega_m \left[2 + b_e - f - 4\mathcal{Q} - \frac{2(1-\mathcal{Q})}{\chi\mathcal{H}} - \frac{\mathcal{H}'}{\mathcal{H}^2} \right]. \quad (5.6)$$

In equations (5.5) and (5.6), \mathcal{H} is the conformal Hubble rate $(\ln a)'$, where a prime denotes a derivative with respect to conformal time; b_e and \mathcal{Q} are the galaxy evolution and magnification biases respectively, χ is the line-of-sight comoving distance and $\Omega_m = \Omega_{m0}(1+z)H_0^2/\mathcal{H}^2$ is the matter density parameter. At first order, the gauge-independent GR definition of galaxy bias is made in the common comoving frame of galaxies and matter,

$$\delta_{g\text{C}}^{(1)} = b_1 \delta_{\text{C}}^{(1)} = b_1 \delta_{\text{T}}^{(1)}, \quad (5.7)$$

5. Multipoles of the bispectrum

where subscript C is for the comoving gauge and T is for total matter gauge, which is a gauge corresponding to standard Newtonian perturbation theory. The bias relation in Poisson gauge is then obtained by transforming (5.7) to Poisson gauge [107, 149]:

$$\delta_g^{(1)} = \delta_{gC}^{(1)} + (3 - b_e)\mathcal{H}v^{(1)} = b_1\delta_T^{(1)} + (3 - b_e)\mathcal{H}v^{(1)}, \quad (5.8)$$

where $v^{(1)}$ is the velocity potential. Since $v^{(1)} = f\mathcal{H}\delta_T^{(1)}/k^2$, the last term on the right of equation (5.8) leads to the $f(3 - b_e)$ term in γ_2/\mathcal{H}^2 , equation (5.6).

Similarly to the first order kernel, the second order kernel can be split into a Newtonian and a relativistic part. The second order part of the Newtonian kernel is well studied and is given as [62, 71, 96, 105]

$$\mathcal{K}_N^{(2)}(\mathbf{k}_1, \mathbf{k}_2, \mathbf{k}_3) = b_1 F_2(\mathbf{k}_1, \mathbf{k}_2) + b_2 + f\mu_3^2 G_2(\mathbf{k}_1, \mathbf{k}_2) + fZ_2(\mathbf{k}_1, \mathbf{k}_2) + b_{s^2} S_2(\mathbf{k}_1, \mathbf{k}_2), \quad (5.9)$$

where $\mu_i = \hat{\mathbf{k}}_i \cdot \mathbf{n}$, b_2 is the second-order Eulerian bias parameter, and b_{s^2} is the tidal bias. F_2 and G_2 are the Fourier-space Eulerian kernels for second-order density contrast and velocity respectively [102, 106];

$$\begin{aligned} F_2(\mathbf{k}_1, \mathbf{k}_2) &= 1 + \frac{F}{D^2} + \left(\hat{\mathbf{k}}_1 \cdot \hat{\mathbf{k}}_2\right) \left(\frac{k_1}{k_2} + \frac{k_2}{k_1}\right) + \left(1 - \frac{F}{D^2}\right) \left(\hat{\mathbf{k}}_1 \cdot \hat{\mathbf{k}}_2\right)^2, \\ G_2(\mathbf{k}_1, \mathbf{k}_2) &= \frac{F'}{DD'} + \left(\hat{\mathbf{k}}_1 \cdot \hat{\mathbf{k}}_2\right) \left(\frac{k_1}{k_2} + \frac{k_2}{k_1}\right) + \left(2 - \frac{F'}{DD'}\right) \left(\hat{\mathbf{k}}_1 \cdot \hat{\mathbf{k}}_2\right)^2, \end{aligned} \quad (5.10)$$

where F is a second-order growth factor, which is given by the growing mode solution of,

$$F'' + \mathcal{H}F' - \frac{3}{2} \frac{H_0^2 \Omega_{m0}}{a} F = \frac{3}{2} \frac{H_0^2 \Omega_{m0}}{a} D^2. \quad (5.11)$$

In an Einstein-de Sitter background, $F = 3D^2/7$, which is a very good approximation for Λ CDM which we use here. The second-order RSD part of the Newtonian kernel is comprised of G_2 above and the kernel Z_2 [96, 105],

$$Z_2(\mathbf{k}_1, \mathbf{k}_2) = f \frac{\mu_1 \mu_2}{k_1 k_2} (\mu_1 k_1 + \mu_2 k_2)^2 + \frac{b_1}{k_1 k_2} [(\mu_1^2 + \mu_2^2) k_1 k_2 + \mu_1 \mu_2 (k_1^2 + k_2^2)]. \quad (5.12)$$

Finally, $S_2(\mathbf{k}_1, \mathbf{k}_2)$ is the kernel for the tidal bias,

$$S_2(\mathbf{k}_1, \mathbf{k}_2) = (\hat{\mathbf{k}}_1 \cdot \hat{\mathbf{k}}_2)^2 - \frac{1}{3}. \quad (5.13)$$

5. Multipoles of the bispectrum

The Newtonian bias model is

$$\delta_{gT}^{(2)} = b_1 \delta_T^{(2)} + b_2 \left[\delta_T^{(1)} \right]^2 + b_{s^2} s^2, \quad (5.14)$$

where $s^2 = s_{ij} s^{ij}$, and $s_{ij} = \Phi_{,ij} - \delta_{ij} \nabla^2 \Phi / 3$.

The relativistic part of the second order kernel was first derived in [108] in the simplest case and extended in [102, 107, 109]. Neglecting sub-dominant vector and tensor contributions, we have

$$\begin{aligned} \mathcal{K}_{\text{GR}}^{(2)}(\mathbf{k}_1, \mathbf{k}_2, \mathbf{k}_3) = & \frac{1}{k_1^2 k_2^2} \left\{ \beta_1 + E_2(\mathbf{k}_1, \mathbf{k}_2, \mathbf{k}_3) \beta_2 + i (\mu_1 k_1 + \mu_2 k_2) \beta_3 \right. \\ & + i \mu_3 k_3 [\beta_4 + E_2(\mathbf{k}_1, \mathbf{k}_2, \mathbf{k}_3) \beta_5] + \frac{k_1^2 k_2^2}{k_3^2} [F_2(\mathbf{k}_1, \mathbf{k}_2) \beta_6 + G_2(\mathbf{k}_1, \mathbf{k}_2) \beta_7] \\ & + (\mu_1 k_1 \mu_2 k_2) \beta_8 + \mu_3^2 k_3^2 (\beta_9 + E_2(\mathbf{k}_1, \mathbf{k}_2, \mathbf{k}_3) \beta_{10}) + (\mathbf{k}_1 \cdot \mathbf{k}_2) \beta_{11} \\ & + (k_1^2 + k_2^2) \beta_{12} + (\mu_1^2 k_1^2 + \mu_2^2 k_2^2) \beta_{13} + i \left[(\mu_1 k_1^3 + \mu_2 k_2^3) \beta_{14} \right. \\ & + (\mu_1 k_1 + \mu_2 k_2) (\mathbf{k}_1 \cdot \mathbf{k}_2) \beta_{15} + k_1 k_2 (\mu_1 k_2 + \mu_2 k_1) \beta_{16} \\ & + (\mu_1^3 k_1^3 + \mu_2^3 k_2^3) \beta_{17} + \mu_1 \mu_2 k_1 k_2 (\mu_1 k_1 + \mu_2 k_2) \beta_{18} \\ & \left. \left. + \mu_3 \frac{k_1^2 k_2^2}{k_3} G_2(\mathbf{k}_1, \mathbf{k}_2) \beta_{19} \right] \right\}. \end{aligned} \quad (5.15)$$

We have collected terms according to the overall powers of k involved. The β_i here are redshift- and bias-dependent coefficients, given in full in Appendix A, which updates expressions in previous papers. We have defined the kernel E_2 which scales as k^0 (like F_2 , G_2 , and \mathcal{Z}_2 do),

$$E_2(\mathbf{k}_1, \mathbf{k}_2, \mathbf{k}_3) = \frac{k_1^2 k_2^2}{k_3^4} \left[3 + 2 \left(\hat{\mathbf{k}}_1 \cdot \hat{\mathbf{k}}_2 \right) \left(\frac{k_1}{k_2} + \frac{k_2}{k_1} \right) + \left(\hat{\mathbf{k}}_1 \cdot \hat{\mathbf{k}}_2 \right)^2 \right], \quad (5.16)$$

which incorporates some of the relativistic dynamical corrections to the intrinsic second-order terms.

At second order, the GR bias model, which corrects the Newtonian bias model (5.14) is given by [215],

$$\delta_{gT}^{(2)} = b_1 \delta_T^{(2)} + b_2 \left[\delta_T^{(1)} \right]^2 + b_{s^2} s^2 + \delta_{C,\text{GR}}^{(2)}, \quad (5.17)$$

where the last term maintains gauge invariance on ultra-large scales, and is given

5. Multipoles of the bispectrum

by (using $\delta_{\text{C}}^{(1)} = \delta_{\text{T}}^{(1)}$)

$$\delta_{\text{C,GR}}^{(2)} = 2\mathcal{H}^2(3\Omega_m + 2f) \left[\delta_{\text{T}}^{(1)} \nabla^{-2} \delta_{\text{T}}^{(1)} - \frac{1}{4} \partial_i \nabla^{-2} \delta_{\text{T}}^{(1)} \partial^i \nabla^{-2} \delta_{\text{T}}^{(1)} \right]. \quad (5.18)$$

The GR correction (5.18) to the Newtonian bias model is contained in the GR kernel (5.15). Then, we also need to transform $\delta_{g\text{T}}^{(2)}$ to the Poisson gauge $\delta_g^{(2)}$, the expression for this is given in [102],

$$\begin{aligned} \delta_g^{(2)} = & \delta_{g\text{T}}^{(2)} + (3 - b_e)\mathcal{H}v^{(2)} + [(b_e - 3)\mathcal{H}' + b'_e\mathcal{H} + (b_e - 3)^2\mathcal{H}^2] [v^{(1)}]^2 \\ & + (b_e - 3)\mathcal{H}v^{(1)}v^{(1)'} + 2(3 - b_e)\mathcal{H}v^{(1)}\delta_{g\text{T}}^{(1)} - 2v^{(1)}\delta_{g\text{T}}^{(1)'} + 3(b_e - 3)\mathcal{H}v^{(1)}\Phi^{(1)}. \end{aligned} \quad (5.19)$$

All of the terms after $\delta_{g\text{T}}^{(2)}$ on the right of equation (5.19) scale as $(\mathcal{H}/k)^n [\delta_{\text{T}}^{(1)}]^2$, where $n = 2, 4$. Therefore they are omitted in the Newtonian approximation. These GR correction terms maintain gauge-independence on ultra-large scales, and they are included in the GR kernel (5.15).

5.2. Extracting the multipoles

Our goal is to extract the spherical harmonic multipoles of B_g with respect to the observer's line of sight. That is, for a fixed line of sight and triangle shape, the rotation of the plane of the triangle about \mathbf{n} generates invariant moments, the sum of which add up to the full bispectrum. This means that

$$B_g = \sum_{\ell m} B_{\ell m} Y_{\ell m}(\mathbf{n}), \quad (5.20)$$

where we follow [96, 97] in our choice of decomposition of the bispectrum (an alternative basis can be found in [186]). To define the $B_{\ell m}$ we need to define an orientation for the $Y_{\ell m}$ to give the polar and azimuthal angles over which to integrate. We choose a coordinate basis for the vectors that span the triangle as follows:

$$\mathbf{k}_1 = (0, 0, k_1) \quad (5.21)$$

$$\mathbf{k}_2 = (0, k_2 \sin \theta, k_2 \cos \theta), \quad (5.22)$$

$$\mathbf{k}_3 = (0, -k_2 \sin \theta, -k_1 - k_2 \cos \theta), \quad (5.23)$$

$$\mathbf{n} = (\sin \theta_1 \cos \varphi, \sin \theta_1 \sin \varphi, \cos \theta_1). \quad (5.24)$$

5. Multipoles of the bispectrum

That is, we fix \mathbf{k}_1 along the z -axis, and require the other triangle vectors to lie in the y - z plane, see Figure 5.1 for a sketch of the relevant vectors. Then we define $\mu_1 = \cos \theta_1$ and use φ , which is the azimuthal angle giving the orientation of the triangle relative to \mathbf{n} . $\theta_{12} = \theta$ is the angle between vectors \mathbf{k}_1 and \mathbf{k}_2 , and we define $\mu = \cos \theta = \hat{\mathbf{k}}_1 \cdot \hat{\mathbf{k}}_2$.

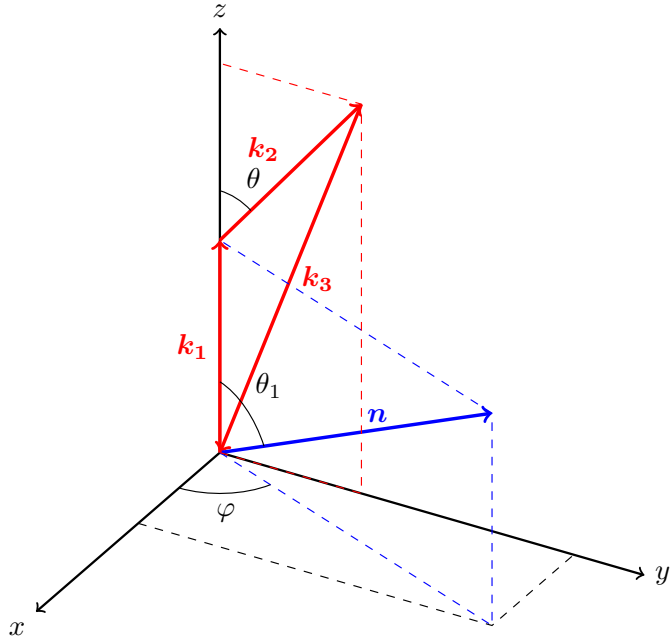


Figure 5.1.: Recap of the overview of the relevant vectors and angles for the Fourier-space bispectrum.

The bispectrum can then be expressed in terms of five variables, φ , μ_1 , θ , k_1 and k_2 , by using

$$\mu_2 = \sqrt{1 - \mu_1^2} \sin \theta \sin \varphi + \mu_1 \cos \theta, \quad (5.25)$$

$$\mu_3 = -\frac{k_1}{k_3} \mu_1 - \frac{k_2}{k_3} \mu_2. \quad (5.26)$$

Then

$$B_g(\theta, k_1, k_2, \mu_1, \varphi) = \sum_{\ell m} B_{\ell m}(\theta, k_1, k_2) Y_{\ell m}(\mu_1, \varphi), \quad (5.27)$$

where we use standard orthonormal spherical harmonics,

$$Y_{\ell m}(\mu_1, \varphi) = \sqrt{\frac{2\ell+1}{4\pi}} \sqrt{\frac{(\ell-m)!}{(\ell+m)!}} P_{\ell}^m(\mu_1) e^{im\varphi}, \quad (5.28)$$

5. Multipoles of the bispectrum

where the P_ℓ^m are the associated Legendre polynomials,

$$P_\ell^m(\mu_1) = \frac{(-1)^m}{2^\ell \ell!} (1 - \mu_1^2)^{m/2} \frac{d^{\ell+m}}{d\mu_1^{\ell+m}} (\mu_1^2 - 1)^\ell. \quad (5.29)$$

At this stage we can extract the multipoles numerically once a bias model and cosmological parameters are given. It is actually significantly quicker to perform this extraction algebraically however, as we now explain.

The bispectrum in general can be considered as a function of $k_1, k_2, k_3, \mu, \mu_1, \mu_2, \mu_3$ and φ . An alternative to the expansion (5.27) is

$$B_g(\mu, k_1, k_2; \mu_1, \mu_2) = \sum_{a=0}^6 \sum_{b=0}^6 \mathcal{B}_{ab}(\mu, k_1, k_2) (i\mu_1)^a (i\mu_2)^b, \quad (5.30)$$

where we used μ_2 instead of φ and $a, b = 0 \dots 6$, which is the maximum power of μ_1, μ_2 that can arise. This factors out all the angular dependence from the functions $\mathcal{B}_{ab}(\mu, k_1, k_2)$, where $\mu = \cos \theta$, which just depend on the triangle shape (and the cosmology). Note that by explicitly including factors of i in the sum, we have only real coefficients \mathcal{B}_{ab} . Schematically we can visualise \mathcal{B}_{ab} in matrix form, split into Newtonian and relativistic contributions as (a bullet denotes a non-zero entry, open circles denote zero entries, and dots are non-existent entries; here that means $a + b > 8$ as higher powers don't occur):

$$\mathcal{B}_{ab} \sim \underbrace{\begin{pmatrix} \bullet & \circ & \bullet & \circ & \bullet & \circ & \circ \\ \circ & \bullet & \circ & \bullet & \circ & \bullet & \circ \\ \bullet & \circ & \bullet & \circ & \bullet & \circ & \bullet \\ \circ & \bullet & \circ & \bullet & \circ & \bullet & \cdot \\ \bullet & \circ & \bullet & \circ & \bullet & \cdot & \cdot \\ \circ & \bullet & \circ & \bullet & \cdot & \cdot & \cdot \\ \circ & \circ & \bullet & \cdot & \cdot & \cdot & \cdot \end{pmatrix}}_{\text{Newtonian}} + \underbrace{\begin{pmatrix} \bullet & \bullet & \bullet & \bullet & \bullet & \bullet & \bullet \\ \bullet & \bullet & \bullet & \bullet & \bullet & \bullet & \bullet \\ \bullet & \bullet & \bullet & \bullet & \bullet & \bullet & \circ \\ \bullet & \bullet & \bullet & \bullet & \bullet & \circ & \cdot \\ \bullet & \bullet & \bullet & \bullet & \circ & \cdot & \cdot \\ \bullet & \bullet & \bullet & \circ & \cdot & \cdot & \cdot \\ \bullet & \bullet & \circ & \cdot & \cdot & \cdot & \cdot \end{pmatrix}}_{\text{Relativistic}}. \quad (5.31)$$

(Note that the matrix row and column labelling start at $a, b = 0, 0$ for the top left element.) Thus, the Newtonian contributions always have $a + b = \text{even} \leq 8$, contributing only to the real part of B_g , while there are relativistic contributions present for all $a + b \leq 7$. When $a + b$ is odd, this implies an imaginary component to the full bispectrum.

In terms of the powers of \mathcal{H}/k involved, we can visualise the maximum powers that

5. Multipoles of the bispectrum

appear in matrix form as follows:

$$\mathcal{B}_{ab} \sim \begin{pmatrix} k^{-8} & k^{-7} & k^{-6} & k^{-5} & k^{-4} & k^{-3} & k^{-2} \\ k^{-7} & k^{-6} & k^{-5} & k^{-4} & k^{-3} & k^{-2} & k^{-1} \\ k^{-6} & k^{-5} & k^{-4} & k^{-3} & k^{-2} & k^{-1} & k^0 \\ k^{-5} & k^{-4} & k^{-3} & k^{-2} & k^{-1} & k^0 & . \\ k^{-4} & k^{-3} & k^{-2} & k^{-1} & k^0 & . & . \\ k^{-3} & k^{-2} & k^{-1} & k^0 & . & . & . \\ k^{-2} & k^{-1} & k^0 & . & . & . & . \end{pmatrix}. \quad (5.32)$$

As in the matrix (5.31), the matrix row and column labelling in (5.32) starts at $(a, b) = (0, 0)$. We see that higher powers n of $(\mathcal{H}/k)^n$ appear for lower $a + b$. Newtonian contributions are all $(\mathcal{H}/k)^0$. Each element has only odd powers of \mathcal{H}/k if $a + b$ is odd, and similarly only even powers if $a + b$ is even.

The advantage of writing the bispectrum in this form is that we can derive analytic formulas for the multipoles. We need to find

$$\begin{aligned} B_{\ell m} &= \int d\Omega B_g Y_{\ell m}^* \\ &= \sum_{a,b} \mathcal{B}_{ab} X_{\ell m}^{ab}, \end{aligned} \quad (5.33)$$

where

$$X_{\ell m}^{ab} = \int_0^{2\pi} d\varphi \int_{-1}^1 d\mu_1 (i\mu_1)^a (i\mu_2)^b Y_{\ell m}^*(\mu_1, \varphi). \quad (5.34)$$

The derivation is as follows. Our aim is analytic integration of,

$$X_{\ell m}^{ab} = \int_0^{2\pi} d\varphi \int_{-1}^1 d\mu_1 (i\mu_1)^a (i\mu_2)^b Y_{\ell m}^*(\mu_1, \varphi). \quad (5.35)$$

In the above, we have used that $\mu_1 = \cos \theta$, such that $Y_{\ell m}(\theta, \varphi) = Y_{\ell, m}(\mu_1, \varphi)$. The standard orthonormal spherical harmonics are defined as,

$$Y_{\ell m}(\mu_1, \varphi) = \sqrt{\frac{2\ell+1}{4\pi}} \sqrt{\frac{(\ell-m)!}{(\ell+m)!}} P_{\ell m}(\mu_1) e^{im\varphi}, \quad (5.36)$$

and the spherical harmonics are related to their complex conjugate as,

$$Y_{\ell, -m} = (-1)^m Y_{\ell, m}^*, \quad Y_{\ell, m}^* = (-1)^m Y_{\ell, -m}. \quad (5.37)$$

5. Multipoles of the bispectrum

Equation (5.35) is separable. We can make this explicit as follows. First expressing μ_2 in terms of μ_1 using $\mu_2 = \sqrt{1 - \mu_1^2} \sin \theta \sin \varphi + \mu_1 \cos \theta$, where $\theta \equiv \theta_{12} \neq \theta_1$ – it is the angle between vectors \mathbf{k}_1 and \mathbf{k}_2 . Then we can expand $(i\mu_2)^b$ using the binomial series,

$$\begin{aligned} (i\mu_2)^b &= i^b (\sqrt{1 - \mu_1^2} \sin \theta \sin \varphi + \mu_1 \cos \theta)^b \\ &= i^b \sum_{g=0}^b \binom{b}{g} \left[\sqrt{1 - \mu_1^2} \sin \theta \sin \varphi \right]^g [\mu_1 \cos \theta]^{b-g} \\ &= i^b \sum_{g=0}^b \binom{b}{g} (1 - \mu_1^2)^{g/2} \mu_1^{b-g} \sin^g \varphi \sin^g \theta \cos^{b-g} \theta. \end{aligned} \quad (5.38)$$

Using this, we have,

$$\begin{aligned} X_{\ell m}^{ab} &= i^{a+b} \sum_{g=0}^b \sin^g \theta \cos^{b-g} \theta \binom{b}{g} \int_0^{2\pi} d\varphi \int_{-1}^1 d\mu (1 - \mu^2)^{g/2} \mu^{a+b-g} \\ &\quad \sin^g \varphi Y_{\ell m}^*(\mu, \varphi), \end{aligned} \quad (5.39)$$

where we have dropped subscript on $\mu_1 \equiv \mu$ for brevity. Now using the definition of the complex-conjugated standard spherical harmonics,

$$\begin{aligned} Y_{\ell m}^* &= (-1)^m Y_{\ell, -m} \\ &= (-1)^m \sqrt{\frac{2\ell+1}{4\pi}} \sqrt{\frac{(\ell+m)!}{(\ell-m)!}} P_{\ell, -m}(\mu) e^{-im\varphi} \end{aligned} \quad (5.40)$$

and the associated Legendre polynomials $P_{\ell m}$ can be rewritten for negative m as,

$$P_{\ell, -m} = (-1)^m \frac{(\ell-m)!}{(\ell+m)!} P_{\ell, m}, \quad (5.41)$$

such that,

$$Y_{\ell m}^* = \sqrt{\frac{2\ell+1}{4\pi}} \sqrt{\frac{(\ell-m)!}{(\ell+m)!}} P_{\ell m}(\mu) e^{-im\varphi}. \quad (5.42)$$

This makes the separability of the integral (5.35) explicit,

$$\begin{aligned} X_{\ell m}^{ab} &= i^{a+b} \sum_{g=0}^b \binom{b}{g} \sin^g \theta \cos^{b-g} \theta \sqrt{\frac{2\ell+1}{4\pi}} \sqrt{\frac{(\ell-m)!}{(\ell+m)!}} \int_0^{2\pi} d\varphi \sin^g \varphi e^{-im\varphi} \\ &\quad \int_{-1}^1 d\mu (1 - \mu^2)^{g/2} \mu^{a+b-g} P_{\ell m}(\mu). \end{aligned} \quad (5.43)$$

5. Multipoles of the bispectrum

Now these two integrals can be solved independently. Starting with the integral over μ , splitting the interval $\int_{-1}^1 = \int_{-1}^0 + \int_0^1$, the \int_{-1}^1 term can be rewritten using a change of variables and the parity of the associated Legendre polynomials as,

$$\begin{aligned} & \int_{-1}^0 d\mu (1 - \mu^2)^{g/2} \mu^{a+b-g} P_{\ell m}(\mu) \\ &= - \int_0^{-1} d\mu (1 - \mu^2)^{g/2} \mu^{a+b-g} P_{\ell m}(\mu) \\ &= \int_0^1 d\tilde{\mu} (1 - \tilde{\mu}^2)^{g/2} (-\tilde{\mu})^{a+b-g} P_{\ell m}(-\tilde{\mu}) \\ &= (-1)^{\ell+m+a+b-g} \int_0^1 d\mu (1 - \mu)^{g/2} \mu^{a+b-g} P_{\ell m}(\mu), \end{aligned} \quad (5.44)$$

where we have used that $P_{\ell m}(-x) = (-1)^{\ell+m} P_{\ell m}(x)$, and renamed $\tilde{\mu} = \mu$ in the last line. The full integral over μ then can be written as,

$$[1 + (-1)^{\ell+m+a+b-g}] \int_0^1 d\mu (1 - \mu^2)^{g/2} \mu^{a+b-g} P_{\ell m}(\mu). \quad (5.45)$$

The associated Legendre polynomials can be written in closed form, using,

$$\begin{aligned} P_{\ell m}(\mu) &= (-1)^m P_{\ell}^m \\ &= (-1)^m (-1)^m 2^{\ell} (1 - \mu^2)^{m/2} \sum_{k=m}^{\ell} \frac{k!}{(k-m)!} \mu^{k-m} \binom{\ell}{k} \binom{\frac{1}{2}(\ell+k-1)}{\ell} \\ &\quad \cdot 2^{\ell} (1 - \mu^2)^{m/2} \sum_{k=m}^{\ell} \frac{k!}{(k-m)!} \mu^{k-m} \binom{\ell}{k} \binom{\frac{1}{2}(\ell+k-1)}{\ell}, \end{aligned} \quad (5.46)$$

such that,

$$\begin{aligned} & [1 + (-1)^{\ell+m+a+b-g}] (-1)^m 2^{\ell} \sum_{k=m}^{\ell} \frac{k!}{(k-m)!} \binom{\ell}{k} \binom{\frac{1}{2}(\ell+k-1)}{\ell} \\ & \int_0^1 d\mu (1 - \mu^2)^{\frac{1}{2}(m+g)} \mu^{a+b+k-g-m}. \end{aligned} \quad (5.47)$$

Changing variables $\xi = \mu^2$, omitting the prefactor for brevity, we get,

$$\int_0^1 d\xi \frac{1}{2} (1 - \xi)^{\frac{1}{2}(m+g)} \xi^{\frac{1}{2}(a+b+k-g-m-1)}. \quad (5.48)$$

5. Multipoles of the bispectrum

Comparing to the Beta function,

$$B(x, y) = \int_0^1 dt (1-t)^{y-1} t^{x-1}, \quad (5.49)$$

we can identify $x = \frac{1}{2}(a + b + k - g - m + 1)$ and $y = \frac{1}{2}(m + g + 2)$. The Beta function can be expressed in terms of Gamma functions $B(x, y) = \frac{\Gamma(x)\Gamma(y)}{\Gamma(x+y)}$, which in turn can be written in terms of factorials, for any positive integer n this relation is $\Gamma(n) = (n-1)!$. We will express the result in terms of Gamma functions as,

$$\begin{aligned} & \int_{-1}^1 d\mu (1-\mu^2)^{g/2} \mu^{a+b-g} P_{\ell m}(\mu) \\ &= [1 + (-1)^{\ell+m+a+b-g}] (-1)^m 2^\ell \sum_{k=m}^{\ell} \frac{k!}{(k-m)!} \binom{\ell}{k} \binom{\frac{1}{2}(\ell+k-1)}{\ell} \\ & \left\{ \Gamma \left[\frac{1}{2}(m+g+2) \right] \Gamma \left[\frac{1}{2}(a+b+k-g-m+1) \right] \right\} \cdot \left\{ \Gamma \left[\frac{1}{2}(a+b+k+3) \right] \right\}^{-1}. \end{aligned} \quad (5.50)$$

Now to solve the integral over φ ,

$$\int_0^{2\pi} d\varphi \sin^g \varphi e^{-im\varphi}. \quad (5.51)$$

Write $\sin^g \varphi$ in terms of e using the usual trig identities and binomial expansion as,

$$\sin^g \varphi = \frac{1}{(2i)^g} \sum_{n=0}^g \binom{g}{n} e^{i(g-n)\varphi} (-1)^n e^{-in\varphi} \quad (5.52)$$

to get,

$$\begin{aligned} & \int_0^{2\pi} d\varphi \frac{1}{(2i)^g} \sum_{n=0}^g \binom{g}{n} (-1)^n e^{i\varphi(g-m-2n)} \\ &= \frac{1}{(2i)^g} \sum_{n=0}^g \binom{g}{n} (-1)^n \int_0^{2\pi} d\varphi e^{i\varphi(g-m-2n)} \\ &= \frac{1}{(2i)^g} \sum_{n=0}^g \binom{g}{n} (-1)^n (2\pi) \delta_{g-m-2n,0}. \end{aligned} \quad (5.53)$$

The Kronecker δ picks out the term in the sum which satisfies $g - m - 2n = 0 \Rightarrow$

5. Multipoles of the bispectrum

$$n = \frac{1}{2}(g - m), \text{ s.t.}$$

$$\int_0^{2\pi} d\varphi \sin^g \varphi e^{-i m \varphi} = \frac{1}{(2i)^g} \binom{g}{\frac{1}{2}(g-m)} (2\pi) (-1)^{\frac{1}{2}(g-m)} \quad (5.54)$$

where n must be a positive integer (or zero), so $g \geq m$ and $g - m$ even.

Putting together all these results and simplifying leads to the identity for $m \geq 0$,

$$X_{\ell m}^{ab} = 2^{\ell+m-1} i^{a+b+m} \sqrt{\frac{\pi(2\ell+1)(\ell-m)!}{(\ell+m)!}} \cdot \sum_{p=m}^{\frac{1}{2}(b+m)} \sum_{q=m}^{\ell} \frac{[1 + (-1)^{a+b+q}] b! \cos^{b+m-2p} \theta \sin^{2p-m} \theta}{4^p (b+m-2p)! (\ell-q)! (p-m)! (q-m)!} \quad (5.55)$$

$$\cdot \frac{\Gamma[\frac{1}{2}(q+\ell+1)] \Gamma[\frac{1}{2}(a+b+q-2p+1)]}{\Gamma[\frac{1}{2}(q-\ell+1)]} \frac{\Gamma[\frac{1}{2}(a+b+q+3)]}{\Gamma[\frac{1}{2}(a+b+q+1)]} \quad (5.56)$$

for $m \leq b$ and zero otherwise. For $m < 0$, the result follows a similar pattern, using the simple relation $X_{\ell-m}^{ab} = (-1)^{a+b+m} X_{\ell m}^{ab*}$.

The resulting expressions for $B_{\ell m}$ are rather massive, in part because the cyclic permutations become mixed together, so we do not present them here. We can visualise these in matrix form split into their Newtonian and relativistic contributions:

$$B_{\ell m} = \underbrace{\begin{pmatrix} \bullet & \cdot \\ \circ & \circ & \cdot \\ \bullet & \bullet & \bullet & \cdot & \cdot & \cdot & \cdot & \cdot & \cdot \\ \circ & \circ & \circ & \circ & \cdot & \cdot & \cdot & \cdot & \cdot \\ \bullet & \bullet & \bullet & \bullet & \bullet & \cdot & \cdot & \cdot & \cdot \\ \circ & \circ & \circ & \circ & \circ & \circ & \cdot & \cdot & \cdot \\ \bullet & \cdot & \cdot \\ \circ & \cdot \\ \bullet & \circ \end{pmatrix}}_{\text{Newtonian}} + \underbrace{\begin{pmatrix} \bullet & \cdot \\ \bullet & \bullet & \cdot \\ \bullet & \bullet & \bullet & \cdot & \cdot & \cdot & \cdot & \cdot & \cdot \\ \bullet & \bullet & \bullet & \bullet & \bullet & \cdot & \cdot & \cdot & \cdot \\ \bullet & \cdot & \cdot \\ \bullet & \bullet \\ \bullet & \bullet \\ \circ & \circ \end{pmatrix}}_{\text{Relativistic}}. \quad (5.57)$$

Again, the matrix indices start at $(0, 0)$ in the top left, $(\ell, m) = (0, 0)$. In the matrix (5.57), consistent with previous matrix visualisations, a closed bullet represents a non-zero entry, while an open circle denotes a vanishing entry. The dots denote the non-existent elements of the matrix, here they are matrix elements where $m > \ell$ and hence do not exist. So, the Newtonian bispectrum only induces even multipoles

5. Multipoles of the bispectrum

up to and including $\ell = 8$, while the relativistic part induces even and odd multipoles up to $\ell = 7$ with multipoles higher than $\ell = 8$ vanishing exactly. Both the Newtonian and the relativistic part terminate at $m = \pm 6$, because $m \leq b \leq 6$, as can be seen from (5.55). Note that for $m < 0$ the pattern is the same. In terms of (\mathcal{H}/k) powers, the highest that appear for each ℓ is $(\mathcal{H}/k)^{8-\ell}$, while the leading contribution is $(\mathcal{H}/k)^0$ or ¹ if the leading contribution is Newtonian or relativistic. These powers are even (odd) if ℓ is even (odd), as explained previously along with the visualisation of the powers \mathcal{H}/k in equation (5.32).

Presentation of the matrix \mathcal{B}_{ab}

Here we describe in more detail how to calculate the matrix of coefficients \mathcal{B}_{ab} . These are far too large to write down, but most of the complexity comes from the k_i permutations and the fact that they are made irreducible from substituting for μ_3 . However, the core part can be shown from which they can easily be calculated. First we note that once μ_3 is substituted for, we can write the first cyclic permutation of the product of the kernels as

$$\begin{aligned} \mathcal{K}_{123} &= \mathcal{K}^{(1)}(k_1, \mu_1)\mathcal{K}^{(1)}(k_2, \mu_2)\mathcal{K}^{(2)}(k_1, k_2, k_3, \mu_1, \mu_2) \\ &= \sum_{a=0}^5 \sum_{b=0}^5 (\mathrm{i}\mu_1)^a (\mathrm{i}\mu_2)^b \mathcal{K}_{ab}(k_1, k_2, k_3), \end{aligned} \quad (5.58)$$

where $\mathcal{K}_{ab}(k_1, k_2, k_3) = \mathcal{K}_{ab}(k_2, k_1, k_3)$ is a set of real μ -independent coefficients which we give below, and here the maximum value of $a, b = 5$. Given \mathcal{K}_{123} we can derive the permutations \mathcal{K}_{321} and \mathcal{K}_{312} as

$$\mathcal{K}_{321} = \sum_{a,b} \sum_{c=0}^a \binom{a}{c} \frac{k_1^{a-c} k_2^c}{k_3^a} (-1)^a (\mathrm{i}\mu_1)^{a-c} (\mathrm{i}\mu_2)^{b+c} \mathcal{K}_{ab}(k_3, k_2, k_1), \quad (5.59)$$

$$\mathcal{K}_{312} = \sum_{a,b} \sum_{c=0}^a \binom{a}{c} \frac{k_1^{a-c} k_2^c}{k_3^a} (-1)^a (\mathrm{i}\mu_1)^{a+b-c} (\mathrm{i}\mu_2)^c \mathcal{K}_{ab}(k_3, k_1, k_2), \quad (5.60)$$

where, as in general, the range of $a, b = 0 \dots 6$. Given these, the full bispectrum is just $B_g = \mathcal{K}_{123} P_1 P_2 + 2$ permutations, but now explicitly written in terms of sums over powers of μ_1, μ_2 . From this \mathcal{B}_{ab} can be found by inspection. The difference in dimension between the permutations originates from the other cyclic permutations being added, where one substitutes $\mu_3 = -(k_1\mu_1 + k_2\mu_2)/k_3$. In (5.59) the largest power of μ_2 is 6, and (5.60) has the largest power of μ_1 as 6.

5. Multipoles of the bispectrum

To present $\mathcal{K}_{ab}(k_1, k_2, k_3)$ we will show powers of \mathcal{H}/k separately, and write $\mathcal{K}_{ab}(k_1, k_2, k_3) = \sum_{n=0}^8 \mathcal{K}_{ab}^{(n)}(k_1, k_2, k_3)$ where n represents the power of \mathcal{H}/k . Then the Newtonian and leading GR correction part look like (again, a bullet denotes a non-zero entry)

$$\mathcal{K}_{ab}^{(0)} = \begin{pmatrix} \bullet & \circ & \bullet & \circ & \bullet & \circ \\ \circ & \bullet & \circ & \bullet & \circ & \bullet \\ \bullet & \circ & \bullet & \circ & \bullet & \circ \\ \circ & \bullet & \circ & \bullet & \circ & \bullet \\ \bullet & \circ & \bullet & \circ & \bullet & \circ \\ \circ & \bullet & \circ & \bullet & \circ & \circ \end{pmatrix} \quad \mathcal{K}_{ab}^{(1)} = \begin{pmatrix} \circ & \bullet & \circ & \bullet & \circ & \bullet \\ \bullet & \circ & \bullet & \circ & \bullet & \circ \\ \circ & \bullet & \circ & \bullet & \circ & \bullet \\ \bullet & \circ & \bullet & \circ & \bullet & \circ \\ \circ & \bullet & \circ & \bullet & \circ & \circ \\ \bullet & \circ & \bullet & \circ & \circ & \circ \end{pmatrix} \quad (5.61)$$

where, writing $F = F_2(\mathbf{k}_1, \mathbf{k}_2)$, $G = G_2(\mathbf{k}_1, \mathbf{k}_2)$, $S = S_2(\mathbf{k}_1, \mathbf{k}_2)$,

$$\mathcal{K}_{00}^{(0)} = b_1^2 (b_{s^2} S + b_2) + F b_1^3 \quad (5.62)$$

$$\mathcal{K}_{02}^{(0)} = -b_1 f \left[b_1^2 + b_{s^2} S + b_2 + \left(F + \frac{G k_2^2}{k_3^2} \right) b_1 \right] \quad (5.63)$$

$$\mathcal{K}_{04}^{(0)} = b_1 f^2 \left(\frac{G k_2^2}{k_3^2} + b_1 \right) \quad (5.64)$$

$$\mathcal{K}_{11}^{(0)} = -b_1^2 f \left[\frac{(k_1^2 + k_2^2) b_1}{k_1 k_2} + \frac{2 G k_1 k_2}{k_3^2} \right] \quad (5.65)$$

$$\mathcal{K}_{13}^{(0)} = b_1 f^2 \left[\frac{(k_1^2 + 2 k_2^2) b_1}{k_1 k_2} + \frac{2 G k_1 k_2}{k_3^2} \right] \quad (5.66)$$

$$\mathcal{K}_{15}^{(0)} = -\frac{b_1 f^3 k_2}{k_1} \quad (5.67)$$

$$\mathcal{K}_{20}^{(0)} = -b_1 f \left[b_1^2 + b_{s^2} S + b_2 + \left(F + \frac{G k_1^2}{k_3^2} \right) b_1 \right] \quad (5.68)$$

$$\mathcal{K}_{22}^{(0)} = f^2 \left[4 b_1^2 + b_{s^2} S + b_2 + \left(F + \frac{G (k_1^2 + k_2^2)}{k_3^2} \right) b_1 \right] \quad (5.69)$$

$$\mathcal{K}_{24}^{(0)} = -f^3 \left(\frac{G k_2^2}{k_3^2} + 3 b_1 \right) \quad (5.70)$$

$$\mathcal{K}_{31}^{(0)} = b_1 f^2 \left[\frac{b_1 (2 k_1^2 + k_2^2)}{k_1 k_2} + \frac{2 G k_1 k_2}{k_3^2} \right] \quad (5.71)$$

$$\mathcal{K}_{33}^{(0)} = -f^3 \left[\frac{2 b_1 (k_1^2 + k_2^2)}{k_1 k_2} + \frac{2 G k_1 k_2}{k_3^2} \right] \quad (5.72)$$

$$\mathcal{K}_{35}^{(0)} = \frac{f^4 k_2}{k_1} \quad (5.73)$$

$$\mathcal{K}_{40}^{(0)} = b_1 f^2 \left(b_1 + \frac{G k_1^2}{k_3^2} \right) \quad (5.74)$$

5. Multipoles of the bispectrum

$$\mathcal{K}_{42}^{(0)} = -f^3 \left(3b_1 + \frac{Gk_1^2}{k_3^2} \right) \quad (5.75)$$

$$\mathcal{K}_{44}^{(0)} = 2f^4 \quad (5.76)$$

$$\mathcal{K}_{51}^{(0)} = -\frac{b_1 f^3 k_1}{k_2} \quad (5.77)$$

$$\mathcal{K}_{53}^{(0)} = \frac{f^4 k_1}{k_2}. \quad (5.78)$$

Similarly, the leading GR correction $\mathcal{O}(\mathcal{H}/k)$ coefficients are,

$$\mathcal{K}_{01}^{(1)} = b_1 \gamma_1 \frac{(b_2 + b_{s^2} S)}{k_2} + b_1^2 \left(\frac{F\gamma_1 + \beta_{16}}{k_2} + \frac{\beta_{15}\mu}{k_1} + \frac{\beta_{14}k_2}{k_1^2} - \frac{\beta_{19}Gk_2}{k_3^2} \right) \quad (5.79)$$

$$\mathcal{K}_{03}^{(1)} = b_1 f \left[\frac{(\beta_{19} - \gamma_1) Gk_2}{k_3^2} - \frac{\beta_{16}}{k_2} - \frac{\beta_{15}\mu}{k_1} - \frac{\beta_{14}k_2}{k_1^2} \right] - b_1^2 \left(\frac{f\gamma_1}{k_2} + \frac{\beta_{17}k_2}{k_1^2} \right) \quad (5.80)$$

$$\mathcal{K}_{05}^{(1)} = \frac{b_1 f \beta_{17} k_2}{k_1^2} \quad (5.81)$$

$$\mathcal{K}_{10}^{(1)} = b_1 \gamma_1 \frac{(b_2 + b_{s^2} S)}{k_1} + b_1^2 \left[\left(-\frac{G\beta_{19}}{k_3^2} + \frac{\beta_{14}}{k_2^2} \right) k_1 + \frac{\beta_{15}\mu}{k_2} + \frac{F\gamma_1 + \beta_{16}}{k_1} \right] \quad (5.82)$$

$$\begin{aligned} \mathcal{K}_{12}^{(1)} &= -\gamma_1 f \frac{(b_{s^2} S + b_2)}{k_1} - b_1^2 \left[\gamma_1 f \left(\frac{k_1}{k_2^2} + \frac{2}{k_1} \right) + \frac{\beta_{18}}{k_1} \right] \\ &\quad + b_1 f \left\{ \left[\left(-\frac{2k_1}{k_3^2} - \frac{k_2^2}{k_1 k_3^2} \right) \gamma_1 + \frac{k_1 \beta_{19}}{k_3^2} \right] G - \frac{F\gamma_1}{k_1} - \frac{\beta_{14}k_1}{k_2^2} - \frac{\beta_{15}\mu}{k_2} - \frac{\beta_{16}}{k_1} \right\} \end{aligned} \quad (5.83)$$

$$\mathcal{K}_{14}^{(1)} = b_1 f \frac{2\gamma_1 f + \beta_{18}}{k_1} + \frac{Gk_2^2 \gamma_1 f^2}{k_1 k_3^2} \quad (5.85)$$

$$\begin{aligned} \mathcal{K}_{21}^{(1)} &= -\gamma_1 f \frac{(b_{s^2} S + b_2)}{k_2} - b_1^2 \left[\gamma_1 f \left(\frac{2}{k_2} + \frac{k_2}{k_1^2} \right) + \frac{\beta_{18}}{k_2} \right] \\ &\quad + b_1 f \left\{ \left[\left(-\frac{k_1^2}{k_2 k_3^2} - \frac{2k_2}{k_3^2} \right) \gamma_1 + \frac{k_2 \beta_{19}}{k_3^2} \right] G - \frac{F\gamma_1}{k_2} - \frac{\beta_{16}}{k_2} - \beta_{14} \left(\frac{\mu}{k_1} + \frac{k_2}{k_1^2} \right) \right\} \end{aligned} \quad (5.86)$$

$$\begin{aligned} \mathcal{K}_{23}^{(1)} &= b_1 f \left[\left(\frac{4}{k_2} + \frac{2k_2}{k_1^2} \right) \gamma_1 f + \frac{\beta_{18}}{k_2} + \frac{\beta_{17}k_2}{k_1^2} \right] + f^2 \left[G (3\gamma_1 - \beta_{19}) \frac{k_2}{k_3^2} + \frac{\beta_{16}}{k_2} \right. \\ &\quad \left. + \frac{\beta_{15}\mu}{k_1} + \frac{\beta_{14}k_2}{k_1^2} \right] \end{aligned} \quad (5.88)$$

$$\mathcal{K}_{25}^{(1)} = -f^2 (\gamma_1 f + \beta_{17}) \frac{k_2}{k_1^2} \quad (5.89)$$

$$\mathcal{K}_{30}^{(1)} = -b_1^2 \left(\frac{f\gamma_1}{k_1} + \frac{\beta_{17}k_1}{k_2^2} \right) + b_1 f \left[G (-\gamma_1 + \beta_{19}) \frac{k_1}{k_3^2} - \frac{\beta_{14}k_1}{k_2^2} - \frac{\beta_{15}\mu}{k_2} - \frac{\beta_{16}}{k_1} \right] \quad (5.90)$$

5. Multipoles of the bispectrum

$$\begin{aligned} \mathcal{K}_{32}^{(1)} = & b_1 f \left[\left(\frac{2k_1}{k_2^2} + \frac{4}{k_1} \right) \gamma_1 f + \frac{\beta_{17} k_1}{k_2^2} + \frac{\beta_{18}}{k_1} \right] + f^2 \left[G (3\gamma_1 - \beta_{19}) \frac{k_1}{k_3^2} + \frac{\beta_{14} k_1}{k_2^2} \right. \\ & \left. + \frac{\beta_{15} \mu}{k_2} + \frac{\beta_{16}}{k_1} \right] \end{aligned} \quad (5.91)$$

$$\mathcal{K}_{34}^{(1)} = - \frac{f^2 (3f\gamma_1 + \beta_{18})}{k_1} \quad (5.92)$$

$$\mathcal{K}_{41}^{(1)} = b_1 f \frac{(2\gamma_1 f + \beta_{18})}{k_2} + \frac{G\gamma_1 f^2 k_1^2}{k_2 k_3^2} \quad (5.93)$$

$$\mathcal{K}_{43}^{(1)} = - \frac{f^2 (3f\gamma_1 + \beta_{18})}{k_2} \quad (5.94)$$

$$\mathcal{K}_{50}^{(1)} = \frac{b_1 \beta_{17} f k_1}{k_2^2} \quad (5.95)$$

$$\mathcal{K}_{52}^{(1)} = - \frac{f^2 k_1 (f\gamma_1 + \beta_{17})}{k_2^2}. \quad (5.96)$$

The remaining matrices are of the form,

$$\begin{aligned} \mathcal{K}_{ab}^{(2)} &= \begin{pmatrix} \bullet & \circ & \bullet & \circ & \bullet & \circ \\ \circ & \bullet & \circ & \bullet & \circ & \bullet \\ \bullet & \circ & \bullet & \circ & \bullet & \circ \\ \circ & \bullet & \circ & \bullet & \circ & \circ \\ \bullet & \circ & \bullet & \circ & \circ & \circ \\ \circ & \bullet & \circ & \circ & \circ & \circ \end{pmatrix} & \mathcal{K}_{ab}^{(3)} &= \begin{pmatrix} \circ & \bullet & \circ & \bullet & \circ & \bullet \\ \bullet & \circ & \bullet & \circ & \bullet & \circ \\ \circ & \bullet & \circ & \bullet & \circ & \circ \\ \bullet & \circ & \bullet & \circ & \circ & \circ \\ \circ & \bullet & \circ & \circ & \circ & \circ \\ \bullet & \circ & \circ & \circ & \circ & \circ \end{pmatrix} \\ \mathcal{K}_{ab}^{(4)} &= \begin{pmatrix} \bullet & \circ & \bullet & \circ & \bullet & \circ \\ \circ & \bullet & \circ & \bullet & \circ & \circ \\ \bullet & \circ & \bullet & \circ & \circ & \circ \\ \circ & \bullet & \circ & \circ & \circ & \circ \\ \bullet & \circ & \circ & \circ & \circ & \circ \\ \circ & \circ & \circ & \circ & \circ & \circ \end{pmatrix} & \mathcal{K}_{ab}^{(5)} &= \begin{pmatrix} \circ & \bullet & \circ & \bullet & \circ & \circ \\ \bullet & \circ & \bullet & \circ & \circ & \circ \\ \circ & \bullet & \circ & \circ & \circ & \circ \\ \bullet & \circ & \circ & \circ & \circ & \circ \\ \circ & \circ & \circ & \circ & \circ & \circ \\ \bullet & \circ & \circ & \circ & \circ & \circ \end{pmatrix} \\ \mathcal{K}_{ab}^{(6)} &= \begin{pmatrix} \bullet & \circ & \bullet & \circ & \circ & \circ \\ \circ & \bullet & \circ & \circ & \circ & \circ \\ \bullet & \circ & \circ & \circ & \circ & \circ \\ \circ & \circ & \circ & \circ & \circ & \circ \\ \circ & \circ & \circ & \circ & \circ & \circ \\ \circ & \circ & \circ & \circ & \circ & \circ \end{pmatrix} & \mathcal{K}_{ab}^{(7)} &= \begin{pmatrix} \circ & \bullet & \circ & \circ & \circ & \circ \\ \bullet & \circ & \circ & \circ & \circ & \circ \\ \circ & \circ & \circ & \circ & \circ & \circ \\ \circ & \circ & \circ & \circ & \circ & \circ \\ \circ & \circ & \circ & \circ & \circ & \circ \\ \circ & \circ & \circ & \circ & \circ & \circ \end{pmatrix} \end{aligned}$$

5. Multipoles of the bispectrum

$$\mathcal{K}_{ab}^{(8)} = \begin{pmatrix} \bullet & \circ & \circ & \circ & \circ & \circ \\ \circ & \circ & \circ & \circ & \circ & \circ \\ \circ & \circ & \circ & \circ & \circ & \circ \\ \circ & \circ & \circ & \circ & \circ & \circ \\ \circ & \circ & \circ & \circ & \circ & \circ \\ \circ & \circ & \circ & \circ & \circ & \circ \end{pmatrix}. \quad (5.97)$$

Their coefficients are extracted in similar fashion, and can be found in full in Appendix D.

5.3. Analysis of the multipoles

Here we present an analysis of the behaviour of the multipoles.

5.3.1. Co-linear, squeezed and equilateral limits

To help understand further the multipoles we can evaluate their equilateral ($k_1 = k_2 = k_3$), co-linear ($\theta = 0$ or $\theta = \pi$) and squeezed limits analytically. Non-zero co-linear multipoles exist only for $m = 0$ components. This is the one limit that is easy to evaluate by hand – it follows directly from (5.55). The equilateral case is significantly more complicated to evaluate. Non-zero equilateral multipoles exist for all even m , for any ℓ , the one exception being the $m = 0$ part of the dipole, for which the equilateral configuration is identically zero. These are summarised in Fig. 5.2, together with the powers of k which appear in each multipole.

The squeezed limit was explicitly evaluated in [88] for the leading $\mathcal{O}(\mathcal{H}/k_L)$ contribution, where k_L is the long mode, which we expand further here. Note that in what follows, we have assumed that the small-scale modes are sufficiently sub-equality scale, and that the large-scale modes are larger than the equality scale. The leading corrections in the even multipoles require us going beyond leading order $\mathcal{O}(\mathcal{H}/k_L)$ in the squeezed limit. We let

$$k_1 = k_2 = k_S, \quad k_3 = \epsilon k_S, \quad (5.98)$$

5. Multipoles of the bispectrum

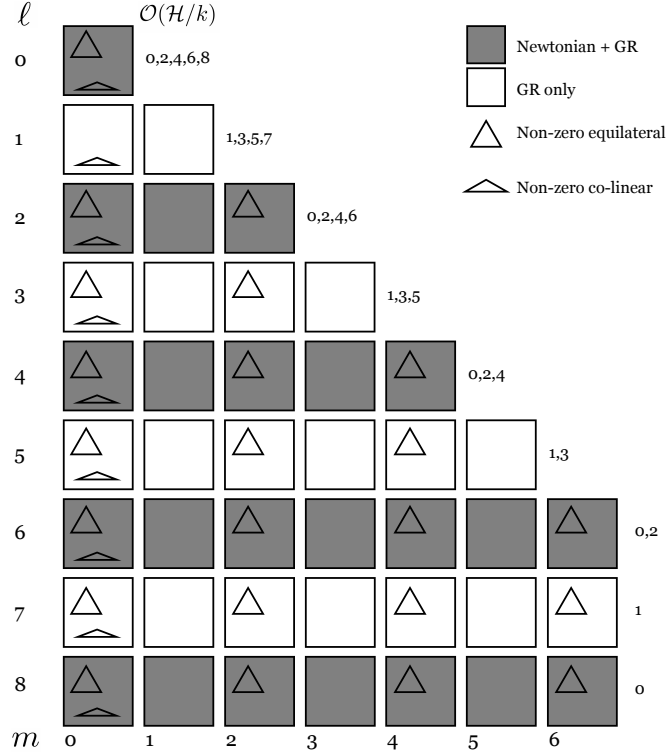


Figure 5.2.: Overview of all non-zero multipoles for the bispectrum, which includes ℓ from 0 to 8, and m from $-\ell$ to ℓ ; the pattern here is the same for $m < 0$, so only $m \geq 0$ are displayed. Denoted in the figure are whether components are Newtonian+GR or GR only, triangle shapes indicating whether given components are non-vanishing in flattened (co-linear) or equilateral limits. Note how the dipole is unique in having the equilateral case vanish for every value of m . Also given is which powers of \mathcal{H}/k appear in each of the multipoles.

to write the wavenumber in terms of the short mode $k_S \gg k_L$, which implies

$$\mu = -1 + \frac{\epsilon^2}{2}. \quad (5.99)$$

We then take the limit as $\epsilon \rightarrow 0$ with the short mode k_S fixed, and keep only the leading terms in \mathcal{H}/k_L , neglecting factors of \mathcal{H}/k_S and $P(k_S)^2$. For each multipole we are then left with the squeezed limit as a polynomial in \mathcal{H}/k_L . The leading

5. Multipoles of the bispectrum

contributions are:

Here, the matrices represent the ℓ, m values from $\ell = 0, m = 0$ (top left entry). We see that the Newtonian part has non-zero squeezed limits for some even m , terminating at $m = 4$. GR corrections come in up to $m = 3$ for $\ell \leq 7$. For odd m these contributions come in for the leading terms $\mathcal{O}(\mathcal{H}/k)$, while for m even the order is lower, $\mathcal{O}((\mathcal{H}/k)^2)$. Note that we assume primordial Gaussianity. In the presence of primordial non-Gaussianity, the squeezed limit has higher powers of \mathcal{H}/k . Current work investigates how primordial non-Gaussianity will change our

5. Multipoles of the bispectrum

results. The effect of local primordial non-Gaussianity on the Newtonian galaxy bispectrum is presented in [108].

5.3.2. Numerical analysis for next-generation surveys

Here we present a numerical analysis of the multipoles of the galaxy bispectrum. We use three different survey models, two of which are appropriate for future surveys; i.e. SKA HI intensity mapping, and a Stage IV H α spectroscopic galaxy survey similar to *Euclid*. The third model we consider is a simplified ‘toy model’ for illustrative purposes. The parameters we use are introduced below.

Evolution and magnification bias are defined as [118],

$$b_e = -\frac{\partial \ln n_g}{\partial \ln(1+z)}, \quad \mathcal{Q} = -\left.\frac{\partial \ln n_g}{\partial \ln L}\right|_c, \quad (5.101)$$

where n_g is the comoving galaxy number density, L the luminosity, and $|_c$ denotes evaluation at the flux cut.

For an HI intensity mapping survey, we estimate the bias from the halo model following [110]. This yields the following fitting formulae for first and second order bias,

$$b_1^{\text{HI}}(z) = 0.754 + 0.0877z + 0.0607z^2 - 0.00274z^3, \quad (5.102)$$

$$b_2^{\text{HI}}(z) = -0.308 - 0.0724z - 0.0534z^2 + 0.0247z^3. \quad (5.103)$$

For the tidal bias, we assume zero initial tidal bias which relates b_{s^2} to b_1 as,

$$b_{s^2}^{\text{HI}}(z) = -\frac{4}{7}(b_1(z) - 1), \quad (5.104)$$

so that,

$$b_{s^2}^{\text{HI}}(z) = 0.141 - 0.0501z - 0.0347z^2 + 0.00157z^3. \quad (5.105)$$

The HI intensity mapping evolution bias is given by the background HI brightness temperature [111],

$$b_e^{\text{HI}}(z) = -\frac{d \ln [(1+z)^{-1} \mathcal{H} \bar{T}_{\text{HI}}]}{d \ln [1+z]}, \quad (5.106)$$

where \bar{T}_{HI} is given by the fitting formula,

$$\bar{T}_{\text{HI}}(z) = (5.5919 + 23.242z - 2.4136z^2) \cdot 10^{-2} \text{ mK}. \quad (5.107)$$

5. Multipoles of the bispectrum

The effective magnification bias for HI intensity mapping is [111]

$$\mathcal{Q}^{\text{HI}} = 1.0, \quad (5.108)$$

and clustering bias is independent of luminosity,

$$\frac{\partial b_1^{\text{HI}}}{\partial \ln L} = 0. \quad (5.109)$$

We consider a Stage IV H α spectroscopic survey similar to *Euclid*, and use the clustering biases given in [114],

$$b_1^{H\alpha}(z) = 0.9 + 0.4z, \quad (5.110)$$

$$b_2^{H\alpha}(z) = -0.741 - 0.125z + 0.123z^2 + 0.00637z^3, \quad (5.111)$$

$$b_{s^2}^{H\alpha}(z) = 0.0409 - 0.199z - 0.0166z^2 + 0.00268z^3. \quad (5.112)$$

The magnification bias and evolution bias are [114],

$$\mathcal{Q}^{H\alpha}(z) = \frac{y_c(z)^{\alpha+1} \exp[-y_c(z)]}{\Gamma(\alpha+1, y_c(z))}, \quad (5.113)$$

$$b_e^{H\alpha}(z) = -\frac{d \ln \Phi_*(z)}{d \ln(1+z)} + \frac{d \ln y_c(z)}{d \ln(1+z)} \mathcal{Q}^{H\alpha}(z), \quad (5.114)$$

where $\alpha = -1.35$, Γ is the upper incomplete gamma function, Φ_* is given in [114] and $y_c(z) = [\chi(z)/(2.97h \cdot 10^3) (\text{Mpc}/h)]^2$. Table 1 in [114] summarises the numerical values of the bias parameters discussed above. Finally, we follow [114] and take

$$\left. \frac{\partial b_1^{H\alpha}}{\partial \ln L} \right|_c = 0. \quad (5.115)$$

For the simple model of galaxy bias, we use

$$b_1(z) = \sqrt{1+z}, \quad (5.116)$$

$$b_2(z) = -0.3\sqrt{1+z}, \quad (5.117)$$

$$b_{s^2}(z) = -\frac{4}{7}(b_1(z) - 1), \quad (5.118)$$

$$b_e = 0, \quad (5.119)$$

$$\mathcal{Q} = 0. \quad (5.120)$$

5. Multipoles of the bispectrum

For cosmological parameters we use Planck 2018 [8], giving the best-fit parameters $h = 0.6766$, $\Omega_{m0} = 0.3111$, $\Omega_{b0}h^2 = 0.02242$, $\Omega_{c0}h^2 = 0.11933$, $n_s = 0.9665$, $\gamma = \ln f / \ln \Omega_m = 0.545$. The linear matter power spectrum is calculated using CAMB [61].

We examine numerically three different triangular configurations, the squeezed, co-linear, and equilateral triangles, as a function of triangle size. For our numerical analysis, we choose a moderately squeezed triangle shape with $\theta \approx 178^\circ$, which corresponds to $k_3 = k$, $k_1 = k_2 = 28k$ (such that long mode k_3 is the reference wavevector, and the other vectors are defined in relation to the long mode). For the co-linear case, we use flattened isosceles triangles with $\theta \approx 2.3^\circ$, corresponding to $k_3 = k$, $k_1 = k_2 = 0.5001k$. All plots are at redshift $z = 1$, with the exception of Figure 5.9, where we look at the amplitude as a function of redshift.

Firstly, we consider the total amplitude of the different multipoles with respect to the Newtonian monopole, plotting the total power contained in each of the multipoles and normalising by the Newtonian monopole of the galaxy bispectrum,

$$b_\ell(k_1, k_2, \theta) = \frac{1}{B_{N,00}(k_1, k_2, \theta)} \sqrt{\frac{1}{2\ell+1} \sum_{m=-\ell}^{\ell} |B_{\ell m}(k_1, k_2, \theta)|^2}. \quad (5.121)$$

We present this for all multipoles $\ell = 0 \dots 8$ and separately for each of the triangle shapes introduced above (i.e. fixing triangle shape, and varying size by varying k), as well as for both bias models which are relevant for future surveys. The results can be viewed in Figures 5.3, 5.4 and 5.5.

We have created colour-intensity plots to give an overview of the relative amplitudes of the first few multipoles of the galaxy bispectrum, $\ell = 0 \dots 3$. Because of the simple relationship between $B_{\ell,m}$ and $B_{\ell,-m}$, we do not show plots for negative m . These as well are done for both HI intensity mapping bias and $H\alpha$ bias. The results are shown in Figures 5.6 and 5.7 for the *Euclid*-like survey and for SKA intensity mapping respectively.

To further investigate the dependence on triangle shape we investigate the reduced bispectrum. The reduced bispectrum divides out the dependence of the bispectrum amplitude on the squares of the power spectrum, and hence provides an alternative picture of the contributions of the Fourier space kernels \mathcal{K} on the total amplitude of the bispectrum. While not a physical signal, it is a useful complementary analysis alongside the standard numerical bispectrum analyses, as most of the amplitude of the bispectrum ($\mathcal{O}(10^6)$) generally comes from the power spectrum ($\mathcal{O}(10^3)$ ·

5. Multipoles of the bispectrum

$\mathcal{O}(10^3)$), and the reduced bispectrum is commonly studied in literature on the galaxy bispectrum. We define the reduced bispectrum as

$$Q_{\ell m}(k_1, k_2, \theta) = \frac{B_{\ell m}(k_1, k_2, \theta)}{P_0(k_1)P_0(k_2) + P_0(k_2)P_0(k_3) + P_0(k_1)P_0(k_3)}, \quad (5.122)$$

where P_0 is the monopole of the galaxy power spectrum,

$$P_0(k) = \frac{1}{2} \int_{-1}^1 d\mu P_g(\mathbf{k}), \quad (5.123)$$

with the galaxy power spectrum $P_g(\mathbf{k}) = (b_1 + f\mu^2)^2 P$, P being the linear dark matter power spectrum. (An alternative definition would be to use the relativistic galaxy power spectrum which would induce small changes $\mathcal{O}((\mathcal{H}/k)^2)$ on Hubble scales.) The reduced bispectrum Q is hence dependent on magnitude of wavevectors \mathbf{k}_1 and \mathbf{k}_2 , and the angle between these $(\pi - \theta)$. We fix $k_1 = 0.1 \text{ Mpc}^{-1}$ and $k_1 = 0.01 \text{ Mpc}^{-1}$, and use differently coloured lines to indicate the ratio of k_2/k_1 , which ranges from isosceles triangles in which $k_1 = k_2$, to $k_2/k_1 = 4.5$. The angle θ ranges from $[0, \pi]$, except for the isosceles shape, for which we stop at $\theta = \pi - 0.01$ (for $k_1 = 0.1 \text{ Mpc}^{-1}$), and at $\theta = \pi - 0.02$ (for $k_1 = 0.01 \text{ Mpc}^{-1}$). The reason for this is the inclusion of relativistic \mathcal{H}/k contributions, which cause unobservable divergences as $k \rightarrow 0$, occurring here for the isosceles shape when the angle between \mathbf{k}_1 and \mathbf{k}_2 goes to π and $k_3 \rightarrow 0$.

The bias used is again that for the *Euclid*-like H α spectroscopic survey. Results are in Figure 5.8. The layout is similar to Figures 5.6 and 5.7, with $\ell = 0 \dots 3$ plotted. Once again, negative m are not shown.

Lastly, we fix triangle shape and size, and plot the relative total power (as defined in (5.121)) as a function of redshift, where redshift ranges from $z = 0.1 \dots 2.0$. This is done for the toy model for bias only. The three panels in Figure 5.9 show the results for $\ell = 0 \dots 3$, for each of the three wavevector triangles discussed earlier; equilateral, squeezed and flattened shapes. Solid and dashed lines indicate the relative total power for $k_1 = 0.1 \text{ Mpc}^{-1}$ and $k_1 = 0.01 \text{ Mpc}^{-1}$ respectively.

5. Multipoles of the bispectrum

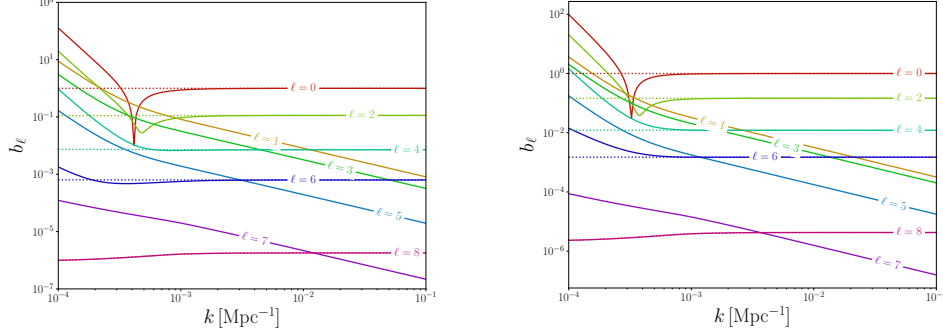


Figure 5.3.: Normalised total power for squeezed configuration for *Euclid*-like (*left*) and SKA HI intensity mapping (*right*) surveys. Long mode k_3 is plotted along the x -axis.

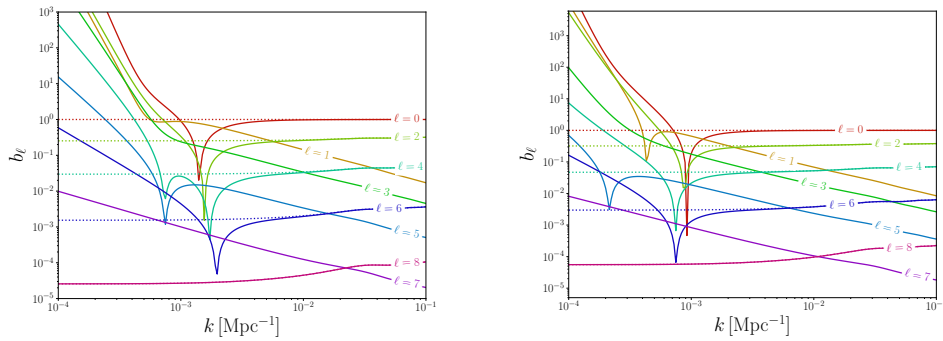


Figure 5.4.: Total power for flattened configuration for *Euclid*-like (*left*) and SKA HI intensity mapping (*right*) surveys. Long mode k_3 is plotted along the x -axis.

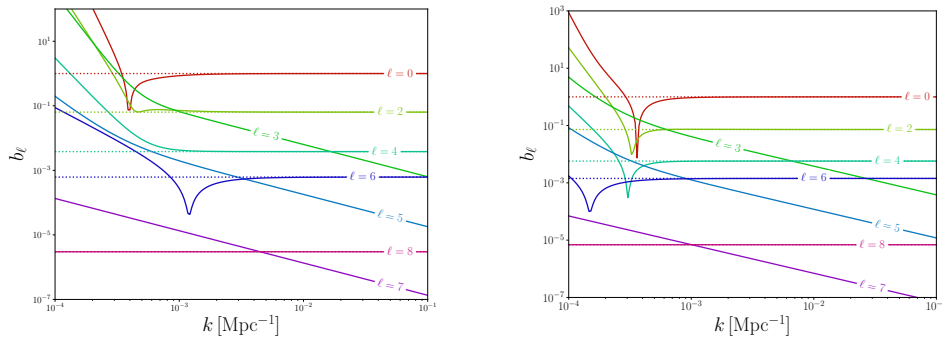


Figure 5.5.: Total power for equilateral configuration for *Euclid*-like (*left*) and SKA HI intensity mapping (*right*) surveys. Since the dipole vanishes in this limit, the $\ell = 1$ line is absent.

5. Multipoles of the bispectrum

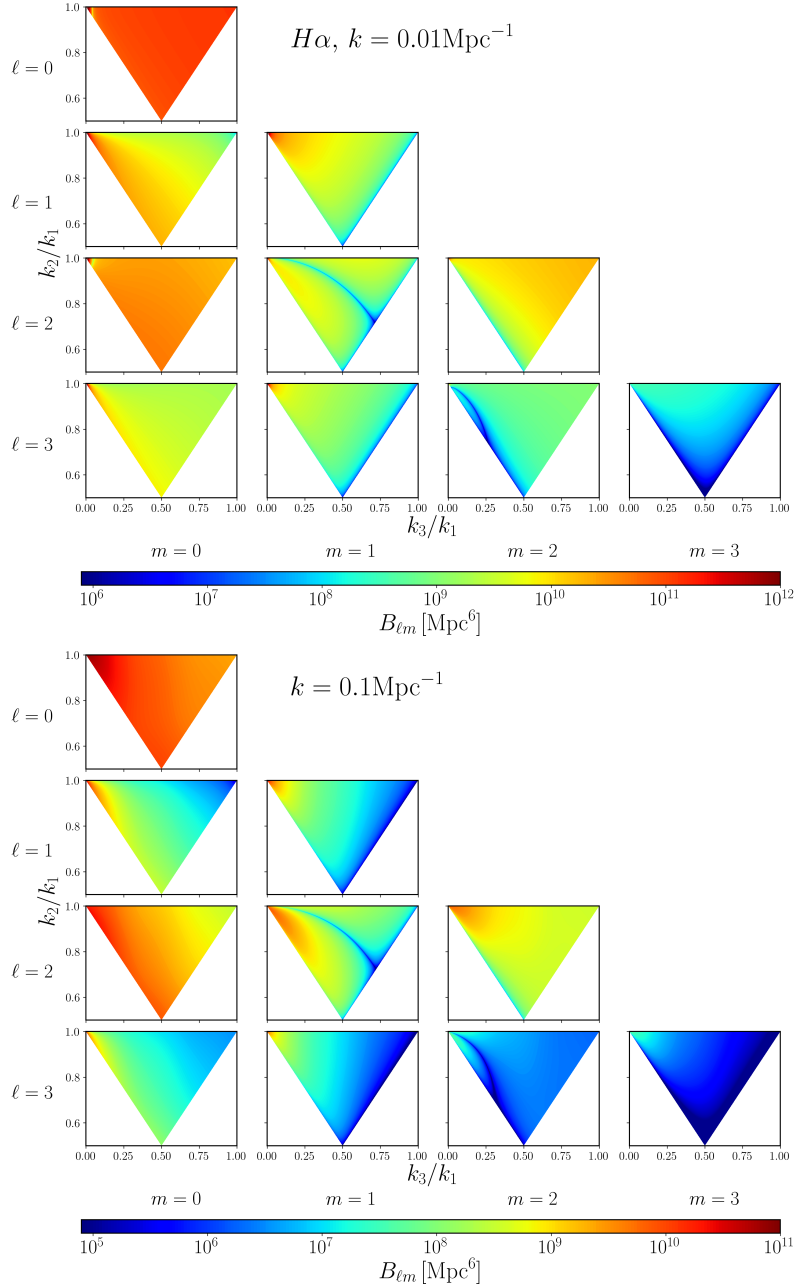


Figure 5.6.: A selection of multipoles of the galaxy bispectrum, $B_{\ell m}$, with $\ell = 0 \dots 3$ and $m = 0 \dots \ell$ as indicated in the figure. Bias model used is that for an $H\alpha/Euclid$ -like survey. k_1 is kept fixed, the value of which is given alongside the plot, and the x and y axes vary respectively k_3 and k_2 with respect to the fixed k_1 . The upper left corner of the wedge shape is the squeezed limit, the upper right corner is the equilateral configuration, and the lower corner is the co-linear configuration. Note the difference in range of the colour bars.

5. Multipoles of the bispectrum

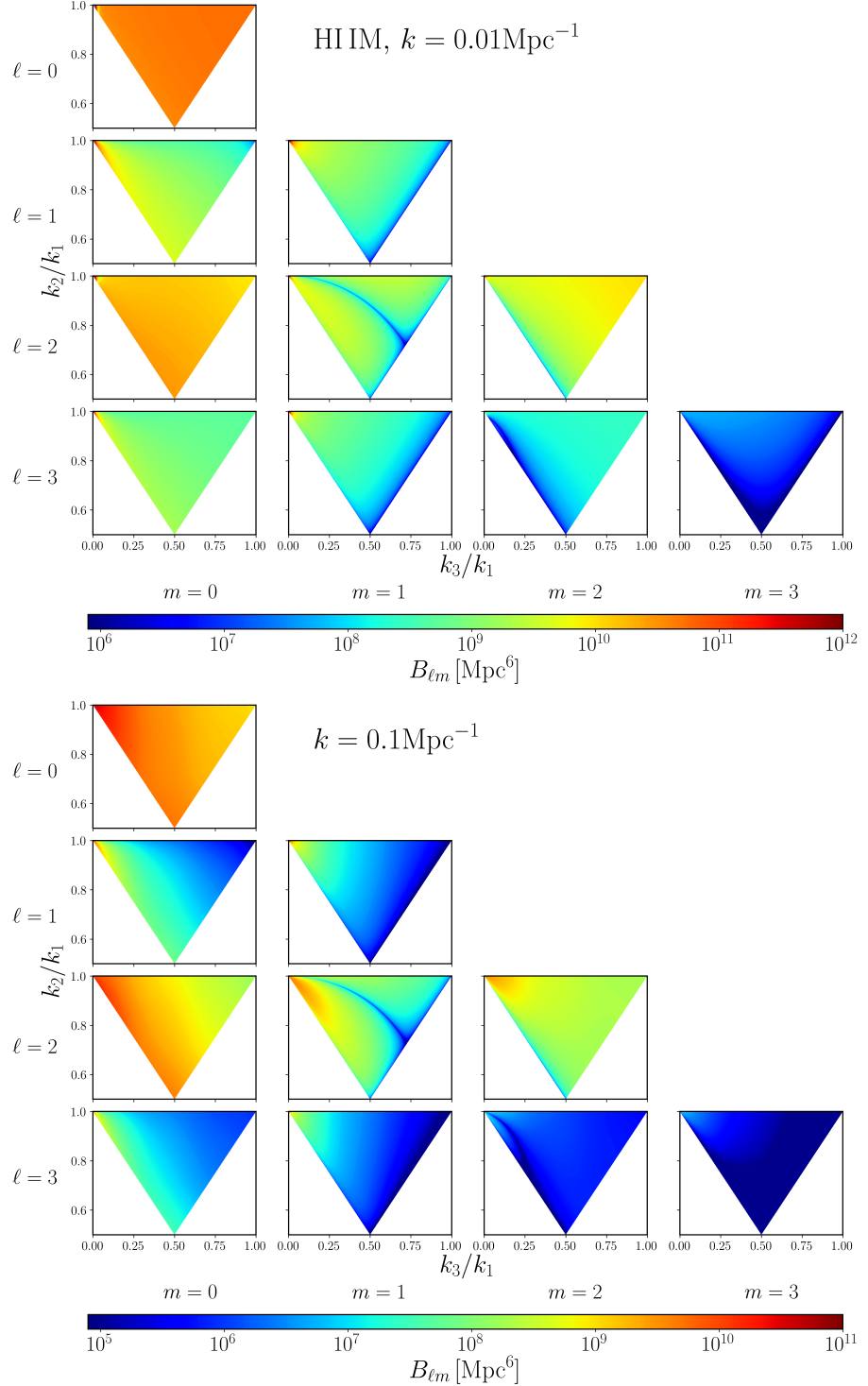


Figure 5.7.: Selected multipoles of the galaxy bispectrum, similar to Figure 5.6, but with the bias model appropriate for intensity mapping. The value of fixed k_1 is indicated on the figures. The upper left corner of a wedge shape is the squeezed limit, the upper right corner is the equilateral configuration, and the lower corner is the co-linear configuration.

5. Multipoles of the bispectrum

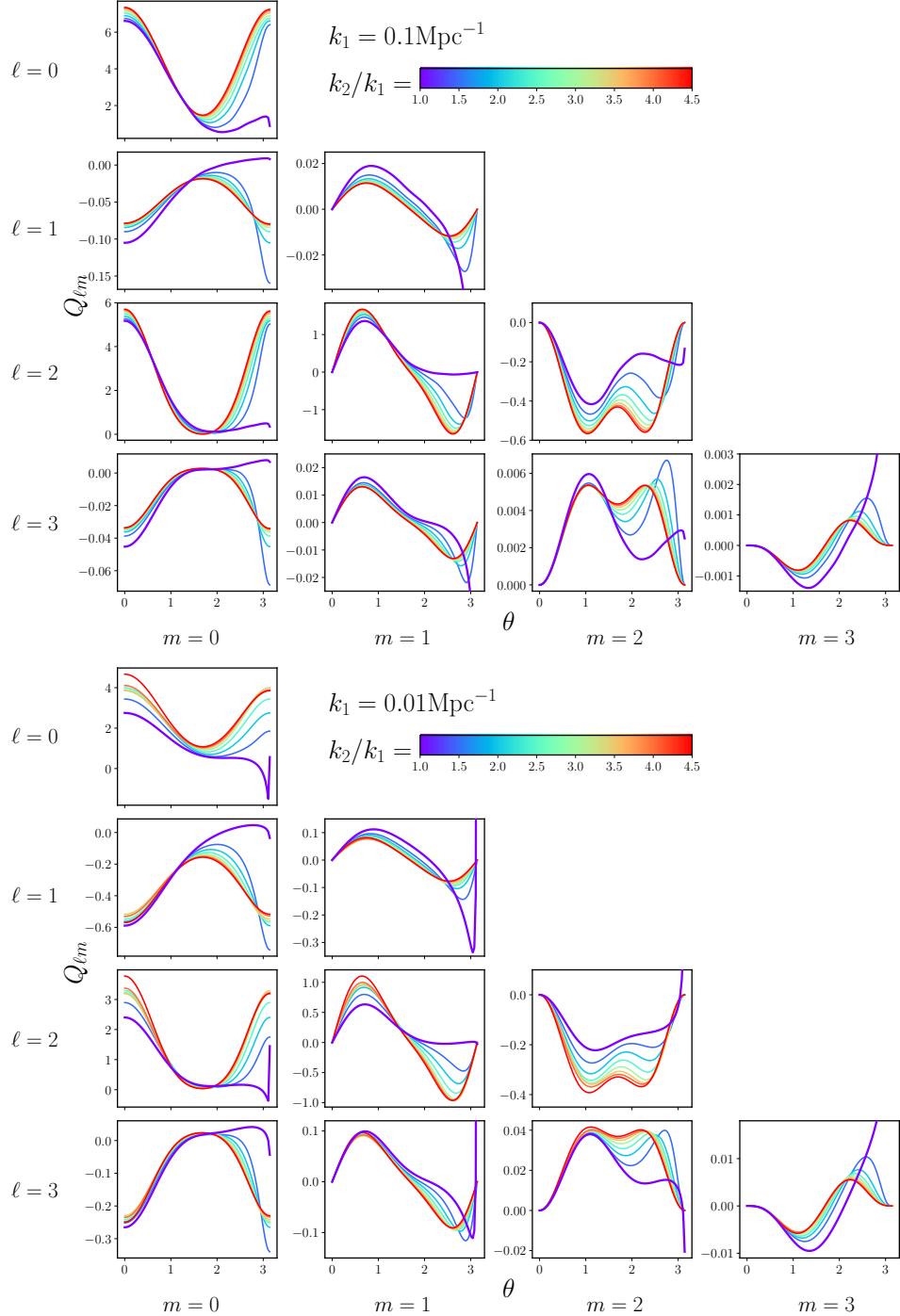


Figure 5.8.: Results for the reduced bispectrum $Q_{\ell m}$, where $\ell = 0 \dots 3$ and negative m not shown. The multipoles ℓ, m are indicated on the figure, as well as the value of k_1 which is kept fixed. The colourbar and different colours denote the ratio of k_2/k_1 , where the slightly thicker purple line is the isosceles triangle, which diverges as $\theta \rightarrow \pi$ since there $k_3 \rightarrow 0$.

5. Multipoles of the bispectrum

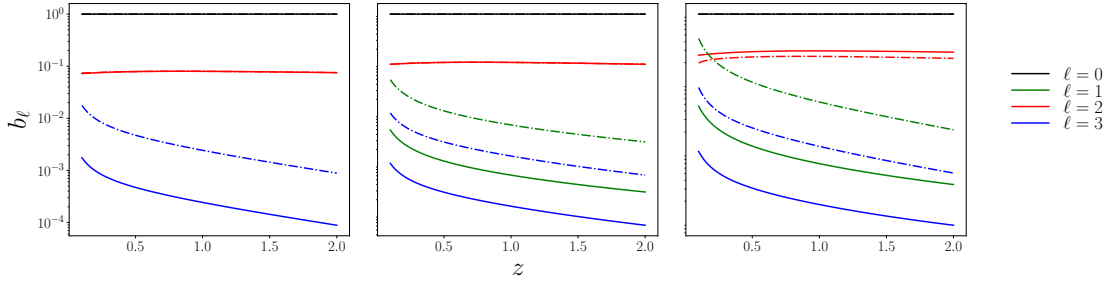


Figure 5.9.: Total power contained in the relativistic bispectrum normalised by the Newtonian monopole as a function of redshift z ranging from 0.1 to 2. The three panels are the equilateral configuration (*left*, with $\ell = 1$ vanishing), squeezed (*middle*) and co-linear flattened configuration (*right*). Solid lines for $k = 0.1 \text{ Mpc}^{-1}$, and dash-dotted for $k = 0.01 \text{ Mpc}^{-1}$.

Figures 5.3, 5.4 and 5.5 show the amplitude of the total power as defined in (5.121). For each ℓ this contains all orientations per multipole divided by the amplitude of the Newtonian monopole. Values of ℓ are labelled on the figure, with the dotted lines denoting the Newtonian contribution (for even ℓ only). For small scales (larger wavenumber k), the Newtonian contributions are generally larger than the relativistic b_ℓ (i.e. odd ℓ), however at larger scales, above equality, the relative power contained in relativistic contributions increases. This shows up in the even multipoles as a divergence between the dotted (purely Newtonian) lines and solid (GR-corrected) lines. In the odd multipoles, we see an increase in amplitude, which at the largest scales become larger than the purely Newtonian signal. This is dependent on bias model and triangular configuration.

The colour-intensity maps in figures 5.6 and 5.7 show the amplitude of the relativistic bispectrum over the k_3/k_1 , k_2/k_1 plane. The amplitude of the bispectrum signal peaks in the squeezed limit where $k_1 = k_2$, $k_3 \rightarrow 0$ which is in the top left corner in these plots. For the odd multipoles $\ell = 1$ and $\ell = 3$, the amplitude of the dipole is higher than the $\ell = 3$ case in most configurations. The amplitude of the relativistic bispectrum is also higher for larger scales (smaller k). For $\ell = 1$, the equilateral configuration, which lies in the upper right corner of the plots, is vanishing as we established analytically. A further feature to note is dark blue lines (zero crossings—lower than the cutoff value) appearing for some multipole numbers as smooth lines across the colour-intensity map. These zero crossings are due to our choice of bias model—specifically it is our modelling of tidal bias, which has a sign change. We can also observe from these plots that there is a rough trend that more power is contained in the lower m multipoles.

5. Multipoles of the bispectrum

The reduced bispectrum is plotted in Figure 5.8, showing large relativistic contributions to the bispectrum odd-multipoles especially at large scales. This also shows the significant dependence on the triangle shape, depending on the orientation of the harmonic.

Finally, Figure 5.9 shows the total power divided by the Newtonian monopole, as a function of redshift. The model for bias used here is not physically realistic, but this illustrates the generic behaviour with redshift we can expect. It is interesting to observe how, when going towards lower redshift, the power in the relativistic corrections to the bispectrum grows compared to the Newtonian signal. This is especially noticeable in squeezed and flattened shapes where the dipole approaches or surpasses the $\ell = 2$ line. Of course, at low redshift the plane-parallel assumption that we have used becomes a worse approximation.

5.4. Conclusion

We have considered in detail for the first time the multipole decomposition of the observed relativistic galaxy bispectrum. In section 5.2 we have shown how the multipoles may be derived analytically, with an analytic formula given in equation (5.55), and have illustrated how they behave in the squeezed, equilateral and co-linear limits (which includes the flattened case) in section 5.3. We have shown how the amplitude of the relativistic signals behaves for two types of upcoming surveys – a *Euclid*-like galaxy survey, and an SKA intensity mapping survey. Our key findings are:

odd multipoles Relativistic effects generate a hierarchy of odd multipoles which are absent in the Newtonian picture, plus an additional contribution to all multipoles up to $\ell = 7$. In particular we find that the octopole is similar in amplitude to the dipole; it is only about a factor of 5 or so smaller than the dipole. These are both larger than the Newtonian hexadecapole on large scales. Higher multipoles are suppressed. This effect can be seen clearly in figures 5.3, 5.4, 5.5.

powers of k The leading power of the relativistic correction in each ℓ harmonic is $(\mathcal{H}/k)^1$ for odd multipoles and $(\mathcal{H}/k)^2$, for even multipoles. Furthermore, all odd multipoles contain the leading (\mathcal{H}/k) correction, while lower values of ℓ contain the higher powers of \mathcal{H}/k , going up to $(\mathcal{H}/k)^7$ for $\ell = 1$ (though these

5. Multipoles of the bispectrum

are probably unobservable). An overview of occurring powers of k is given in Figure 5.2.

special limits the co-linear case ($\theta = 0$ or π) only generates non-zero $m = 0$ multipoles and vanishes for all other values of m . The equilateral case is always zero for m odd, and is always zero for the special case of the dipole. For the squeezed limit we have leading (\mathcal{H}/k) relativistic corrections for ℓ and $m \leq 3$ odd.

multipoles with shape We computed the amplitude of each ℓ, m over the range of triangle shapes in figures 5.6, 5.7. For each ℓ most of the power is contained in the lower m multipoles.

multipoles with scale We analysed the total power in each multipole as a function of scale for 3 triangle shapes at $z = 1$. Roughly speaking the even- ℓ are dominated by the Newtonian part and have little scale dependence relative to the Newtonian monopole, though this changes approaching the Hubble scale. For odd- ℓ the leading relativistic part dominates and the dipole reaches the size of the Newtonian quadrupole around equality scales.

redshift dependence Relative to the Newtonian monopole, all the relativistic multipoles decay with redshift, while the quadrupole is roughly constant. For large squeezed triangles the dipole is comparable in size to the quadrupole for small redshift as shown in Figure 5.9.

Of course, the analysis here is limited by the fact we have neglected wide angle effects which will alter the multipoles. Integrated effects will also contribute, but their effect will be suppressed when we analyse the multipoles. We leave these contributions for future work.

6. Local primordial non-Gaussianity in the bispectrum

Next-generation galaxy and 21cm intensity mapping surveys will rely on a combination of the power spectrum and bispectrum for high-precision measurements of primordial non-Gaussianity. In turn, these measurements will allow us to distinguish between various models of inflation. However, precision observations require theoretical precision at least at the same level. We extend the theoretical understanding of the galaxy bispectrum by incorporating a consistent general relativistic model of galaxy bias at second order, in the presence of local primordial non-Gaussianity. The influence of primordial non-Gaussianity on the bispectrum extends beyond the galaxy bias and the dark matter density, due to redshift-space effects. The standard redshift-space distortions at first and second order produce a well-known primordial non-Gaussian imprint on the bispectrum. Relativistic corrections to redshift-space distortions generate new contributions to this primordial non-Gaussian signal, arising from: (1) a coupling of first-order scale-dependent bias with first-order relativistic observational effects, and (2) linearly evolved non-Gaussianity in the second-order velocity and metric potentials which appear in relativistic observational effects. Our analysis allows for a consistent separation of the relativistic ‘contamination’ from the primordial signal, in order to avoid biasing the measurements by using an incorrect theoretical model. We show that the bias from using a Newtonian analysis of the squeezed bispectrum could be $\Delta f_{\text{NL}} \sim 5$ for a Stage IV H α survey.

The content discussed in this chapter is taken from [216]. The chapter is structured as follows. Section 6.2.4 reviews the relativistic correction to the galaxy bias, including the case of local PNG. In addition, we show how the linearly evolved second-order metric and velocity potentials carry a primordial non-Gaussian signal, which is imprinted in the bispectrum by relativistic projection effects. In Section 6.3,

6. Local primordial non-Gaussianity in the bispectrum

after presenting the relativistic correction to the matter bispectrum, we discuss the number density contrast in redshift space, which brings into play the relativistic projection effects. We combine the various results to derive the relativistic galaxy bispectrum, including all local PNG effects, and we show examples of the galaxy bispectrum for a Stage IV H α spectroscopic survey. We summarise and conclude in Section 6.4.

6.1. Galaxy clustering statistics and primordial non-Gaussianity

Galaxy number counts are distorted by projection effects that arise from observing on the past lightcone. The dominant perturbative effect on sub-Hubble scales is from redshift-space distortions (RSD) [46, 217], which constitute the standard Newtonian approximation to projection effects. Lensing magnification produces the best-known relativistic correction to RSD [218], but there are further relativistic effects [90, 117, 219, 220]. The basic idea is the following. The number of sources, dN , above the luminosity threshold that are counted by the observer in a solid angle element about unit direction \mathbf{n} and in a redshift interval about a central redshift z , is given by

$$dN = N_g dz d\Omega_{\mathbf{n}} = n_g dV. \quad (6.1)$$

The second equality relates the observed quantities to those measured in the rest frame of the source. N_g is the number that is counted by the observer per redshift per solid angle, while n_g is the number per proper volume, which is not observed by the observer but is the quantity that would be measured at the source. Similarly, dV is not the observed volume element but the corresponding proper volume element at the source.

Then the observed number density contrast, $\Delta_g = (N_g - \bar{N}_g)/\bar{N}_g$, is related to the proper number density contrast at the source, $\delta_g = (n_g - \bar{n}_g)/\bar{n}_g$, by volume, redshift and luminosity perturbations. At first order in Poisson gauge, the gauge-independent relation (6.1) leads to

$$\Delta_g = \delta_g + \text{RSD} + \text{lensing effect} + \text{other relativistic effects}$$

6. Local primordial non-Gaussianity in the bispectrum

$$= \delta_g - \frac{1}{\mathcal{H}} \mathbf{n} \cdot \nabla (\mathbf{v} \cdot \mathbf{n}) + 2(1 - \mathcal{Q})\kappa + A(\mathbf{v} \cdot \mathbf{n}) + B\Psi + \int d\chi C\Psi' + \int d\chi E\Psi. \quad (6.2)$$

Here $\mathcal{H} = d \ln a / d\eta = (\ln a)'$ is the conformal Hubble rate, $\mathbf{v} = \nabla V$ is the peculiar velocity (V is not to be confused with the often-used alternative $v = |\mathbf{v}|$), κ is the integrated lensing convergence, \mathcal{Q} is the magnification bias, χ is the comoving line-of-sight distance and the integrals are from source to observer. The perturbed metric is given by

$$a^{-2} ds^2 = -(1 + 2\Phi)d\eta^2 + (1 - 2\Psi)d\mathbf{x}^2, \quad (6.3)$$

and we have assumed $\Phi = \Psi$. The time-dependent factors A, B, C, E in (6.2) correspond respectively to Doppler, Sachs-Wolfe, integrated Sachs-Wolfe and time-delay effects. In Fourier space the Doppler term scales as $\partial V \propto (\mathcal{H}/k)\delta_m$, while the remaining terms scale as $\Psi \propto (\mathcal{H}/k)^2\delta_m$. Thus the other relativistic effects are suppressed on sub-Hubble scales, unlike the lensing effect, which scales as $\partial^2\Psi \propto \delta_m$.

The case of 21cm intensity mapping follows from the number count expressions by using the ‘dictionary’ given in [118, 143, 146] at first order and in [110, 113, 140] at second order.

The physical definition of linear Gaussian galaxy bias is in the joint matter-galaxy rest frame, which corresponds to the comoving gauge (‘C gauge’),¹ so that (omitting luminosity dependence for brevity),

$$\delta_{gC}(a, \mathbf{x}) = b_1(a)\delta_{mC}(a, \mathbf{x}). \quad (6.4)$$

This relation is gauge-independent because C gauge corresponds to the physical rest frame. When transforming to other gauges, δ_g is in general no longer proportional to δ_m [90, 116, 221]. For example, in the Poisson gauge of (6.2) and (6.3),

$$\delta_g = b_1\delta_{mC} + (3 - b_e)\mathcal{H}V, \quad b_e = \frac{\partial \ln(a^3\bar{n}_g)}{\partial \ln a}, \quad (6.5)$$

where b_e is known as the evolution bias, which encodes the non-conservation of the background comoving galaxy number density. The velocity potential V scales as Ψ by the Euler equation, $V \propto \Psi \propto (\mathcal{H}/k)^2\delta_m$, and therefore the gauge correction $(3 - b_e)\mathcal{H}V$ is only non-negligible on Hubble scales and may be neglected in a

¹In the Λ CDM model the comoving and synchronous gauges coincide.

6. Local primordial non-Gaussianity in the bispectrum

Newtonian approximation.

Local primordial non-Gaussianity (PNG) generates scale-dependent linear bias, with constant parameter f_{NL} [222, 223]:

$$b_1(a) \rightarrow b_1(a) + 3\delta_{\text{crit}}\Omega_{m0}H_0^2 \frac{[b_1(a) - 1]}{D(a)} g_{\text{in}} \frac{f_{\text{NL}}}{T(k)k^2}. \quad (6.6)$$

The threshold density contrast for collapse is usually taken to be $\delta_{\text{crit}} = 1.686$, and the growth factor D is normalised to 1 today ($a_0 = 1$), i.e. $\delta_m(a, \mathbf{k}) = D(a)\delta_{m0}(\mathbf{k})$. The growth suppression factor for the potential Ψ is $g = D/a$, which is thus also normalised as $g_0 = 1$, with initial value g_{in} deep in the matter era, and T is the transfer function. Note that (6.6) follows the CMB convention for f_{NL} [86, 213]; g_{in} can be removed from (6.6) if D is normalised as $D_{\text{in}} = a_{\text{in}}$. In a Λ CDM model we have the useful relation [106]

$$\frac{g_{\text{in}}}{g} = \frac{3}{5} \left(1 + \frac{2f}{3\Omega_m} \right), \quad (6.7)$$

where the growth rate of linear matter perturbations, $f = d \ln D / d \ln a$, is very well approximated by $f(a) = \Omega_m(a)^{0.545}$.

The PNG component of galaxy bias in (6.6) scales as H_0^2/k^2 on ultra-large scales, i.e. above the equality scale, $k < k_{\text{eq}}$, where $T \approx 1$. It is strongly suppressed on scales $k \gg k_{\text{eq}}$ by $T(k)$. PNG has a similar impact on the power spectrum to the impact of ultra-large-scale relativistic effects. This means that relativistic effects contaminate the primordial signal – leading to biases if a Newtonian approximation is used to model the galaxy power spectrum (see [116, 221, 224]). The relativistic galaxy power spectrum has been used to analyse and predict the capability of future galaxy and intensity mapping surveys to measure the local PNG parameter f_{NL} , while avoiding the bias that is inherent in a Newtonian analysis (see e.g. [93, 111, 116, 118, 146, 221, 224–236]).

The tree-level bispectrum requires the number counts in redshift space up to second order. In the Newtonian approximation, the projection effects are the second-order RSD terms (see e.g. [69]). The relativistic corrections to RSD at second-order are extremely complicated, since they involve quadratic couplings of all the first-order terms, as well as introducing new terms that do not enter at first order, such as the transverse peculiar velocity, the lensing deflection angle and the lensing shear [98–101, 149]. There are further relativistic corrections that are not projection ef-

6. Local primordial non-Gaussianity in the bispectrum

fects. Firstly, the Newtonian model of second-order galaxy bias in the comoving frame requires a relativistic correction, unlike the first-order bias (see Section 6.2). Secondly, and similar to the first-order case, the second-order galaxy bias relation needs relativistic gauge corrections when using non-comoving gauges such as the Poisson gauge. These are second-order extensions of equations like (6.5). In summary, the second-order relativistic corrections to the galaxy bispectrum in the Gaussian case are:

- relativistic projection corrections to the Newtonian RSD [98–101, 149];
- relativistic corrections to the Newtonian bias model in the comoving frame at second order, which were only recently derived [215, 237];
- relativistic gauge corrections to the second-order number density when using non-comoving gauges [99, 149].

As in the case of the power spectrum, local PNG affects the bispectrum on very large scales, which is also where the relativistic effects are strongest. This leads again to a contamination of the primordial signal by relativistic effects, necessitating a relativistic analysis. A Gaussian primordial universe could be mistakenly interpreted as non-Gaussian if a Newtonian model is used for the bispectrum in analysis of the data, as shown by [102, 108, 139, 238].

There are important differences between the power spectrum and bispectrum:

- At first order, there is no relativistic correction to the bias model in comoving gauge – the relativistic correction arises at second order [215, 237]. Therefore the tree-level bispectrum contains a relativistic correction to the bias model, but the tree-level power spectrum does not.
- There is no PNG signal in the primordial *matter* power spectrum at tree level, so that the local PNG signal in the tree-level galaxy power spectrum is sourced only by scale-dependent bias.
- By contrast, local PNG in the galaxy bispectrum is sourced by scale-dependent bias, by the primordial matter bispectrum and by RSD at second order (see [69] and Section 6.2.4 below).
- Second-order relativistic corrections to RSD induce new local PNG effects in the bispectrum, via (1) a coupling of first-order scale-dependent bias to first-order relativistic projection effects, and (2) the linearly evolved PNG

6. Local primordial non-Gaussianity in the bispectrum

in second-order velocity and metric potentials, which appear in relativistic projection effects (absent in the standard Newtonian analysis).

Since local PNG affects the power spectrum and bispectrum differently, a Newtonian analysis could mistakenly identify inconsistencies between the power spectrum and bispectrum f_{NL} measurements, which could wrongly lead to an inference of hidden systematics or deviations from general relativity.

PNG in the galaxy bispectrum has been extensively investigated in the Newtonian approximation. Most work has used the Fourier bispectrum, implicitly incorporating a plane-parallel assumption (see e.g. [66, 67, 69, 71, 79, 83, 86, 158, 176, 192, 213, 239–245]) and we follow this approximation. Our previous work [108] included the local (non-integrated) relativistic effects in the Fourier bispectrum for the first time. This was extended by our work [88, 102, 107, 109, 113, 114, 211, 246], all in the case of primordial Gaussianity. Here we incorporate local PNG into the relativistic bispectrum. This involves applying the recent results of [215, 237] on relativistic corrections to the second-order galaxy bias model. In addition, we derive the new local PNG terms induced by a coupling of first-order scale-dependent bias and first-order relativistic projection effects and by linearly evolved second-order relativistic projection effects.

Conventions used: We assume a flat Λ CDM model, based on general relativity and perturbed up to second order, in which the matter is pressure-free and irrotational on perturbative scales. Generalisations to allow dynamical dark energy and relativistic modified gravity are straightforward, but are not included. For numerical calculations, we use the Planck 2018 best-fit parameters [8]. Perturbed quantities are expanded as $X + X^{(2)}/2$, and may be split as $X_N + X_{\text{GR}} + X_{\text{nG}}$, and similarly at second order, where N denotes the Newtonian approximation, GR denotes the relativistic correction and nG denotes the local PNG contribution. GR corrections are highlighted in magenta. Our definition of the metric potentials in (6.3) leads to the first-order Poisson equation

$$\nabla^2 \Psi = +\frac{3}{2} \Omega_m \mathcal{H}^2 \delta_C, \quad (6.8)$$

where $\Phi = \Psi$ in Λ CDM. Here and in the remainder of the paper, we omit the subscript m on the matter density contrast for brevity. At second order, the perturbed metric in Poisson gauge is given by

$$a^{-2} ds^2 = -[1 + 2\Psi + \Phi^{(2)}] d\eta^2 + [1 - 2\Psi - \Psi^{(2)}] d\mathbf{x}^2. \quad (6.9)$$

6. Local primordial non-Gaussianity in the bispectrum

Here we have neglected the relativistic vector and tensor modes that are generated by scalar mode coupling, so that we only consider the relativistic scalar contribution to the bispectrum. This approximation is justified by the fact that the relativistic vector contribution to the bispectrum is typically 2 orders of magnitude below the relativistic scalar contribution on observable scales, while the relativistic tensor contribution is typically an order of magnitude below that of the vector contribution (see [109]).

6.2. Local primordial non-Gaussianity in the galaxy bias

Local PNG is defined as a simple form of nonlinearity in the primordial curvature perturbation, which is local in configuration space. In terms of the gravitational potential deep in the matter era, we have

$$-\left[\Psi_{\text{in}}(\mathbf{x}) + \frac{1}{2}\Psi_{\text{in}}^{(2)}(\mathbf{x})\right] = \varphi_{\text{in}}(\mathbf{x}) + f_{\text{NL}}\left[\varphi_{\text{in}}(\mathbf{x})^2 - \langle\varphi_{\text{in}}^2\rangle\right], \quad (6.10)$$

where φ_{in} is the first-order Gaussian part. The standard definition of f_{NL} uses a convention for Ψ that is different to ours, with a minus on the right of the Poisson equation (6.8). In order to keep the standard sign of f_{NL} , we made a sign change on the left of (6.10). (f_{NL} in [106, 237, 238] is of opposite sign to the standard sign that we use.)

6.2.1. First-order bias

In (6.10), the Gaussian part of the potential deep in the matter era (but after decoupling) is related to the linear primordial potential by the transfer function:

$$\varphi_{\text{in}}(\mathbf{k}) = T(k)\varphi_{\text{p}}(\mathbf{k}) \quad \text{for } a_{\text{p}} \ll a_{\text{eq}} \ll a_{\text{in}}. \quad (6.11)$$

Here $\varphi_{\text{p}}(\mathbf{k}) = -9\Psi(a_{\text{p}}, \mathbf{k})/10$, where the factor 9/10 ensures conservation of the curvature perturbation on super-Hubble scales. After equality, the potential evolves with the growth suppression factor, so that

$$\varphi(a, \mathbf{k}) = \frac{g(a)}{g_{\text{in}}}\varphi_{\text{in}}(\mathbf{k}) \quad \text{for } a \geq a_{\text{in}} > a_{\text{dec}}. \quad (6.12)$$

6. Local primordial non-Gaussianity in the bispectrum

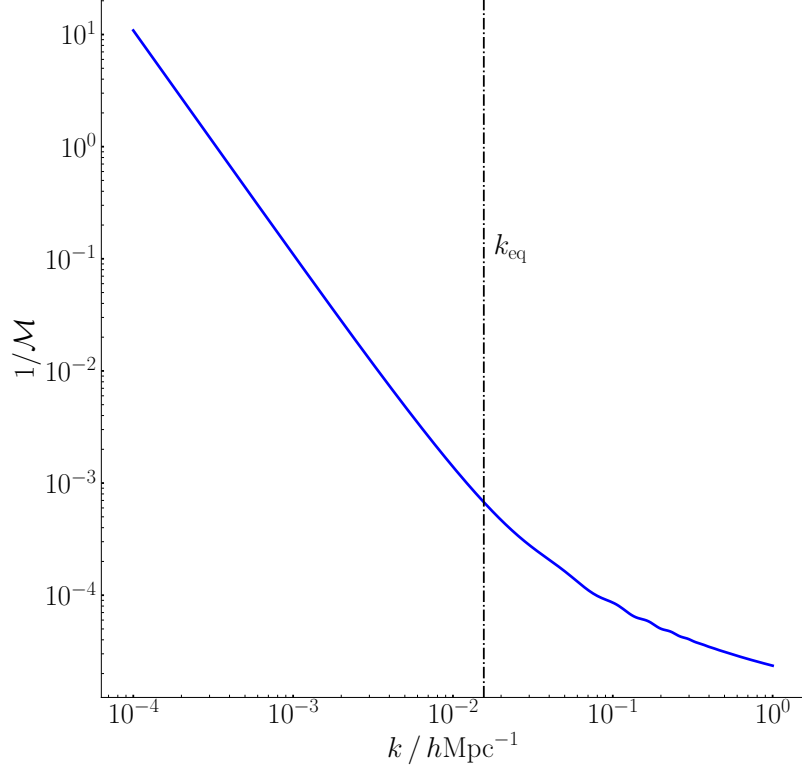


Figure 6.1.: $\mathcal{M}^{-1} = \varphi_p / \delta_C^{(1)}$ at $z = 1$.

We relate the late-time matter density contrast to the primordial potential via the Poisson equation (6.8), using (6.7), (6.11) and (6.12):

$$\delta_C(a, \mathbf{k}) = \mathcal{M}(a, k) \varphi_p(\mathbf{k}) \quad \text{where} \quad \mathcal{M}(a, k) = \frac{10}{3\mathcal{H}(a)^2 [3\Omega_m(a) + 2f(a)]} k^2 T(k). \quad (6.13)$$

This relation is illustrated in Figure 6.1. The matter and number density contrasts can be written as

$$\delta_C = \delta_{C,N} \quad \text{and} \quad \delta_{gC} = \delta_{gC,N} + \delta_{gC,nG}. \quad (6.14)$$

This follows since there is no GR correction to either contrast and no PNG in the Gaussian matter density contrast:

$$\delta_{C,GR} = 0 = \delta_{gC,GR}, \quad \delta_{C,nG} = 0. \quad (6.15)$$

6. Local primordial non-Gaussianity in the bispectrum

Then it follows that

$$\delta_{gC} = \delta_{gC,N} + \delta_{gC,nG} = b_{10} \delta_C + b_{01} \varphi_p , \quad (6.16)$$

where the Gaussian and non-Gaussian bias coefficients are

$$b_{10} = b_1 , \quad b_{01} = 2f_{NL}\delta_{\text{crit}}(b_{10} - 1) . \quad (6.17)$$

The relations (6.13)–(6.17) then recover (6.6).

At first order, there is *no* GR correction to the bias relation expressed in the matter-galaxy rest frame. This is no longer true at second order.

The first-order metric potential is Gaussian by (6.10) and has no GR correction by (6.15) and the Poisson equation. From the Euler equation ($V' + \mathcal{H}V = -\Psi$) it follows that the velocity also has no GR and no PNG corrections:

$$\Psi = \Psi_N , \quad V = V_N . \quad (6.18)$$

6.2.2. Second-order bias: Newtonian approximation

At second order, the galaxy bias is physically defined in comoving gauge, but any gauge may be used in general relativity. Standard Newtonian perturbation theory is often given in an Eulerian frame, and so it is useful for comparison to express the bias in a suitable Eulerian frame. We use Poisson gauge here, following [88, 102, 107–109, 114, 211, 247], but with the galaxy and matter density contrasts in total-matter gauge (‘T gauge’). The total-matter gauge is a convenient Eulerian choice for the density contrasts, since it has the same spatial coordinates as the Poisson gauge at first order and the same time-slicing as the comoving gauge at first and second orders [106, 247, 248]. As a result, at first order the total-matter density contrasts coincide with those of the comoving gauge: $\delta_T = \delta_C$, $\delta_{gT} = \delta_{gC}$, and we can rewrite (6.16) as

$$\delta_{gT} = \delta_{gT,N} + \delta_{gT,nG} \quad (6.19)$$

$$= b_{10} \delta_T + b_{01} \varphi_p = \left(b_{10} + \frac{b_{01}}{\mathcal{M}} \right) \delta_T . \quad (6.20)$$

At second order, the total-matter and Poisson matter density contrasts agree in the Newtonian approximation: $\delta_{T,N}^{(2)} = \delta_N^{(2)}$, while the comoving and total-matter

6. Local primordial non-Gaussianity in the bispectrum

Newtonian density contrasts are related via a purely spatial gauge transformation [102, 106, 215, 249]:

$$\delta_{\text{T,N}}^{(2)} = \delta_{\text{C,N}}^{(2)} + 2\xi^i \partial_i \delta_{\text{C}}, \quad \delta_{g\text{T,N}}^{(2)} = \delta_{g\text{C,N}}^{(2)} + 2\xi^i \partial_i \delta_{g\text{C}}, \quad (6.21)$$

where

$$\xi^i = \partial^i \nabla^{-2} \delta_{\text{C}} = \partial^i \nabla^{-2} \delta_{\text{T}}. \quad (6.22)$$

(The GR parts of the second-order density contrasts in comoving and total-matter gauges are equal; see below.)

For the small scales involved in local clustering of matter density, the Poisson equation at second order has the same Newtonian form as at first order. Then we can extend (6.13) up to second order to define the linearly evolved local PNG part of the density contrast, whose nonlinearity is purely primordial:

$$\delta_{\text{T,nG}}^{(2)} = \mathcal{M} \varphi_{\text{p}}^{(2)} = 2f_{\text{NL}} \mathcal{M} \varphi_{\text{p}} * \varphi_{\text{p}}, \quad (6.23)$$

where the $*$ denotes a convolution in Fourier space. This leads to

$$\delta_{\text{T,nG}}^{(2)} = 2f_{\text{NL}} \mathcal{M}(a, k) \int \frac{d\mathbf{k}'}{(2\pi)^3} \frac{\delta_{\text{T}}(a, \mathbf{k}')}{\mathcal{M}(a, k')} \frac{\delta_{\text{T}}(a, \mathbf{k} - \mathbf{k}')}{\mathcal{M}(a, |\mathbf{k} - \mathbf{k}'|)}. \quad (6.24)$$

In order to include the nonlinearity due to gravitational evolution, we add the standard Newtonian contribution for Gaussian initial conditions to the local PNG part:

$$\begin{aligned} & \delta_{\text{T,N}}^{(2)}(a, \mathbf{k}) + \delta_{\text{T,nG}}^{(2)}(a, \mathbf{k}) \\ &= \int \frac{d\mathbf{k}'}{(2\pi)^3} \left[F_2(a, \mathbf{k}', \mathbf{k} - \mathbf{k}') + 2f_{\text{NL}} \frac{\mathcal{M}(a, k')}{\mathcal{M}(a, k') \mathcal{M}(a, |\mathbf{k} - \mathbf{k}'|)} \right] \delta_{\text{T}}(a, \mathbf{k}') \delta_{\text{T}}(a, \mathbf{k} - \mathbf{k}'). \end{aligned} \quad (6.25)$$

The standard Newtonian mode-coupling kernel for Λ CDM is [106]:

$$F_2(a, \mathbf{k}_1, \mathbf{k}_2) = 1 + \frac{F(a)}{D(a)^2} + \left(\frac{k_1}{k_2} + \frac{k_2}{k_1} \right) \hat{\mathbf{k}}_1 \cdot \hat{\mathbf{k}}_2 + \left[1 - \frac{F(a)}{D(a)^2} \right] (\hat{\mathbf{k}}_1 \cdot \hat{\mathbf{k}}_2)^2, \quad (6.26)$$

where F is the second-order growth factor. The Einstein–de Sitter relation $F/D^2 = 3/7$ is a very good approximation in Λ CDM. We use this approximation, in which F_2 is effectively time independent.

At second order, the standard Newtonian bias model, including tidal bias in the Gaussian part and all local PNG contributions, is given by (see [86] for a comprehen-

6. Local primordial non-Gaussianity in the bispectrum

hensive treatment):

$$\delta_{gT,N}^{(2)} + \delta_{gT,nG}^{(2)} = b_{10} \delta_{T,N}^{(2)} + b_{20} (\delta_T)^2 + b_s s^2 + b_{10} \delta_{T,nG}^{(2)} + b_{11} \delta_T \varphi_p + b_n \xi^i \partial_i \varphi_p + b_{02} (\varphi_p)^2. \quad (6.27)$$

The (Eulerian) bias parameters in the case of Gaussian initial conditions are in the first line on the right-hand side: the linear and quadratic biases, b_{10} and b_{20} , and the tidal bias b_s , where

$$s^2 = s_{ij} s^{ij}, \quad s_{ij} = \left(\partial_i \partial_j - \frac{1}{3} \delta_{ij} \nabla^2 \right) \nabla^{-2} \delta_T. \quad (6.28)$$

The second line of (6.27) contains the local PNG contribution, with three new bias parameters b_{11}, b_n, b_{02} . The first term is the primordial dark matter contribution, from (6.25); note that $\tilde{\delta}_{T,N}^{(2)}$ is proportional to f_{NL} . The b_{11}, b_n terms scale as $(\mathcal{H}^2/k^2)(\delta_T)^2$, while the b_{02} term is $\mathcal{O}(\mathcal{H}^4/k^4)$. The new bias parameters vanish when $f_{NL} = 0$; in the presence of local PNG, they are given by [86, 158, 237]:

$$b_{11} = 4f_{NL} \left[\delta_{\text{crit}} b_{20} + \left(\frac{13}{21} \delta_{\text{crit}} - 1 \right) (b_{10} - 1) + 1 \right], \quad (6.29)$$

$$b_n = 4f_{NL} \left[\delta_{\text{crit}} (1 - b_{10}) + 1 \right], \quad (6.30)$$

$$b_{02} = 4f_{NL}^2 \delta_{\text{crit}} \left[\delta_{\text{crit}} b_{20} - 2 \left(\frac{4}{21} \delta_{\text{crit}} + 1 \right) (b_{10} - 1) \right]. \quad (6.31)$$

Note that the expressions for the bias coefficients in (6.29)–(6.31), as well as for b_{01} in (6.17), are based on a universal halo mass function. (For recent work on the limits of the universality assumption, see [250, 251].)

6.2.3. Second-order bias: relativistic corrections

The relativistic second-order galaxy bias model has been derived in [215] (Gaussian case) and [237] (with local PNG). The key feature to bear in mind is the following:

GR corrections in the galaxy number density contrast $\delta_{gT}^{(2)}$ do not change the galaxy bias terms in (6.27), which contain all the local PNG effects.

This separation between GR effects and local PNG in the number density can be understood as follows.

- The intrinsic nonlinearity of GR modulates the galaxy number density via large-scale modes. However, this does not affect small-scale clustering: GR

6. Local primordial non-Gaussianity in the bispectrum

effects do *not* modulate the variance of small-scale density modes [238, 252, 253].

- By contrast, local PNG imprints a primordial long-short coupling that induces a long-mode modulation of the variance and thus changes the galaxy bias.

As a consequence, we expect that relativistic corrections to the bias relation should be independent of non-Gaussianity and apply only on ultra-large scales (for a different view, see [254]). These two features are consistent with the behaviour of (6.27) under change of gauge:

The Newtonian bias relation (6.27) is gauge-independent only on small scales.

Relativistic corrections to (6.27) are needed to enforce gauge-independence of the bias relation on ultra-large scales.

As shown in [215, 237], gauge-independence requires the addition to (6.27) of the relativistic part of the second-order matter density contrast. The relativistic modes are super-Hubble at equality and arise from nonlinear GR corrections to the Newtonian Poisson equation [106, 247, 248, 255]:

$$\delta_{\text{C,GR}}^{(2)} = \delta_{\text{T,GR}}^{(2)} = \frac{20}{3} \delta_{\text{T}} \hat{\varphi}_{\text{in}} - \frac{5}{3} \xi^i \partial_i \hat{\varphi}_{\text{in}} \equiv \delta_{g\text{T,GR}}^{(2)}. \quad (6.32)$$

Here $\hat{\varphi}_{\text{in}}$ is the ultra-large scale potential deep in the matter era,

$$\hat{\varphi}_{\text{in}}(\mathbf{k}) = \varphi_{\text{in}}(\mathbf{k} \mid k < k_{\text{eq}}). \quad (6.33)$$

When we relate $\hat{\varphi}_{\text{in}}$ to the density contrast today, via (6.11) and (6.13), we need to impose $T = 1$ on the transfer function, by (6.33).

The relativistic second-order galaxy bias model of [237] can be written in T-gauge as

$$\delta_{g\text{T}}^{(2)} = \delta_{g\text{T,N}}^{(2)} + \delta_{g\text{T,nG}}^{(2)} + \delta_{g\text{T,GR}}^{(2)}, \quad (6.34)$$

where

$$\delta_{g\text{T,N}}^{(2)} = b_{10} \delta_{\text{T,N}}^{(2)} + b_{20} (\delta_{\text{T}})^2 + b_s s^2, \quad (6.35)$$

$$\delta_{g\text{T,nG}}^{(2)} = b_{10} \delta_{\text{T,nG}}^{(2)} + b_{11} \delta_{\text{T}} \varphi_{\text{p}} + b_n \xi^i \partial_i \varphi_{\text{p}} + b_{02} (\varphi_{\text{p}})^2, \quad (6.36)$$

$$\delta_{g\text{T,GR}}^{(2)} = \frac{20}{3} \delta_{\text{T}} \hat{\varphi}_{\text{in}} - \frac{5}{3} \xi^i \partial_i \hat{\varphi}_{\text{in}}. \quad (6.37)$$

6. Local primordial non-Gaussianity in the bispectrum

Here (6.35) and (6.36) recover the Newtonian relation (6.27).

Both the local PNG and GR terms scale as $(\mathcal{H}^2/k^2)(\delta_T)^2$, so that the GR correction *cannot* be neglected. Although they are of the same order of magnitude, there is a key distinction between them: local PNG induces a short-long mode coupling, and thus affects the primordial potential φ_p on small scales, while the GR corrections affect only the ultra-large-scale primordial modes. In the absence of local PNG, i.e. for $f_{NL} = 0$, the GR terms survive and constitute the relativistic bias correction in the case of Gaussian initial conditions, as derived in [215].

Finally, we transform (6.20) and (6.34) to Poisson gauge:

$$\delta_g = \delta_{gT} + (3 - b_e)\mathcal{H}V, \quad (6.38)$$

$$\begin{aligned} \delta_g^{(2)} &= \delta_{gT}^{(2)} + (3 - b_e)\mathcal{H}V^{(2)} + \left[(b_e - 3)\mathcal{H}' + (b_e - 3)(b_e - 4)\mathcal{H}^2 + b'_e\mathcal{H} \right] (V)^2 \\ &\quad + 2(3 - b_e)\mathcal{H}V \delta_{gT} - 2V \delta'_{gT} + 2(3 - b_e)\mathcal{H}V \Psi, \end{aligned} \quad (6.39)$$

where the GR corrections in magenta scale as $(\mathcal{H}^2/k^2)\delta_T$ at first order, and as $(\mathcal{H}^2/k^2)(\delta_T)^2$ or $(\mathcal{H}^4/k^4)(\delta_T)^2$ at second order. For (6.39) we followed [102, 149, 211], but we significantly simplified their expressions, using the first-order Euler equation $V' + \mathcal{H}V = -\Psi$ and the relation

$$V = -\frac{2f}{3\Omega_m\mathcal{H}}\Psi, \quad (6.40)$$

which follows from the continuity equation, $\delta'_T = -\nabla^2 V$, and the Poisson equation. We also included the evolution bias terms that are omitted in [237].

6.2.4. Second-order metric and velocity potentials

At second order, the number density contrast has a GR correction in addition to a PNG correction, as shown in (6.34). Unlike the first-order case, the metric and velocity potentials at second order also have nonzero GR and PNG corrections:

$$\Psi^{(2)} = \Psi_N^{(2)} + \Psi_{GR}^{(2)} + \Psi_{nG}^{(2)}, \quad (6.41)$$

$$\Phi^{(2)} = \Phi_N^{(2)} + \Phi_{GR}^{(2)} + \Psi_{nG}^{(2)}, \quad (6.42)$$

$$V^{(2)} = V_N^{(2)} + V_{GR}^{(2)} + V_{nG}^{(2)}, \quad (6.43)$$

6. Local primordial non-Gaussianity in the bispectrum

where we note that

$$\Phi_N^{(2)} = \Psi_N^{(2)} \quad \text{and} \quad \Phi_{nG}^{(2)} = \Psi_{nG}^{(2)}. \quad (6.44)$$

The GR corrections are derived in [106] (which only considers modes $k < k_{\text{eq}}$). Here we derive the PNG contributions, which include modes $k > k_{\text{eq}}$.

The PNG corrections to metric and velocity potentials are linearly evolved, i.e., their nonlinearity is purely primordial, the same as in the case of the density contrast. They follow from constraint and energy conservation equations applied to the linearly evolved PNG part of the matter density contrast, $\delta_{T,nG}^{(2)}$. As we argued in deriving (6.24), $\delta_{T,nG}^{(2)}$ obeys the linear Newtonian Poisson equation. The same applies to the linearly evolved $\Psi_{nG}^{(2)}$. From the Newtonian Poisson equation we find that

$$\begin{aligned} \Psi_{nG}^{(2)}(a, \mathbf{k}) &= -\frac{3\Omega_m(a)\mathcal{H}(a)^2}{2k^2}\delta_{T,nG}^{(2)}(a, \mathbf{k}) \\ &= -\frac{10}{3}f_{\text{NL}}\left[1 + \frac{2f(a)}{3\Omega_m(a)}\right]^{-1}T(k)(\varphi_p * \varphi_p)(\mathbf{k}), \end{aligned} \quad (6.45)$$

where we used (6.13) and (6.24).

By (6.45), $\Psi_{nG}^{(2)}$ grows as $(1 + 2f/3\Omega_m)^{-1}$, and thus

$$\Psi_{nG}^{(2)\prime} = -\frac{2f}{(3\Omega_m + 2f)}\left(\frac{f'}{f} + \mathcal{H} + 2\frac{\mathcal{H}'}{\mathcal{H}}\right)\Psi_{nG}^{(2)}. \quad (6.46)$$

The first-order linear equation (6.40), based on energy conservation and the Poisson equation, extends to second order for the linearly evolved PNG parts of the velocity and the potential. This determines the PNG part of the velocity:

$$V_{nG}^{(2)} = -\frac{2f}{3\Omega_m\mathcal{H}}\Psi_{nG}^{(2)}. \quad (6.47)$$

The linearly evolved PNG part of the second-order RSD term then follows as

$$\partial_{\parallel}^2 V_{nG}^{(2)}(a, \mathbf{k}) = -2f_{\text{NL}}\mathcal{H}(a)f(a)\mu^2\mathcal{M}(a, k)(\varphi_p * \varphi_p)(\mathbf{k}), \quad (6.48)$$

where $\partial_{\parallel} = \mathbf{n} \cdot \boldsymbol{\nabla}$ and $\mu = \hat{\mathbf{k}} \cdot \mathbf{n}$. Finally, the first-order linear relation $\Phi = \Psi$ extends to second order for the linearly evolved PNG part of $\Phi^{(2)}$, giving the second equality of (6.44).

6. Local primordial non-Gaussianity in the bispectrum

6.3. Local primordial non-Gaussianity in the relativistic bispectrum

6.3.1. Matter bispectrum

The primordial contribution of matter, independent of halo formation, is given by the Newtonian approximation (6.25), corrected by the GR contribution in (6.32):

$$\delta_T^{(2)} = \delta_{T,N}^{(2)} + \delta_{T,nG}^{(2)} + \frac{20}{3} \delta_T \hat{\varphi}_{\text{in}} - \frac{5}{3} \xi^i \partial_i \hat{\varphi}_{\text{in}}. \quad (6.49)$$

The kernels in Fourier space corresponding to the GR terms in (6.49) are:

$$\delta_T \hat{\varphi}_{\text{in}} \rightarrow - \frac{(k_1^2 + k_2^2)}{2k_1^2 k_2^2}, \quad \xi^i \partial_i \hat{\varphi}_{\text{in}} \rightarrow - \frac{\mathbf{k}_1 \cdot \mathbf{k}_2}{k_1^2 k_2^2}. \quad (6.50)$$

Then the tree-level matter bispectrum $\langle \delta_T \delta_T \delta_T^{(2)} \rangle$ at equal times is given by

$$B_m(\mathbf{k}_1, \mathbf{k}_2, \mathbf{k}_3) = \left\{ F_2(\mathbf{k}_1, \mathbf{k}_2) + 2f_{\text{NL}} \frac{\mathcal{M}(k_3)}{\mathcal{M}(k_1)\mathcal{M}(k_2)} \right. \\ \left. - (3\Omega_m + 2f) \mathcal{H}^2 \frac{[2(k_1^2 + k_2^2) - \mathbf{k}_1 \cdot \mathbf{k}_2]}{2k_1^2 k_2^2} \right\} P(k_1)P(k_2) + 2 \text{ cp}, \quad (6.51)$$

where we omit the time dependence for brevity, and ‘cp’ denotes cyclic permutation. Here $P \equiv P_T$ is the linear matter power spectrum and

$$\frac{\mathcal{M}(k_3)}{\mathcal{M}(k_1)\mathcal{M}(k_2)} = \frac{3}{10} (3\Omega_m + 2f) \mathcal{H}^2 \frac{T(k_3)}{T(k_1)T(k_2)} \frac{k_3^2}{k_1^2 k_2^2}. \quad (6.52)$$

The standard Newtonian result (see e.g. [158]) is modified in GR by the magenta terms in (6.51). For Gaussian initial conditions, the GR correction is suppressed by \mathcal{H}^2/k^2 relative to the Newtonian approximation, but *in the non-Gaussian case, the GR correction is of the same order of magnitude as the local PNG term.*

6.3.2. Observed number density

The observed number density contrast is $\Delta_g + \Delta_g^{(2)}/2$, which modifies the source quantity $\delta_g + \delta_g^{(2)}/2$ by RSD and other redshift space effects. It can be split into

6. Local primordial non-Gaussianity in the bispectrum

Newtonian, relativistic and non-Gaussian parts as follows.

- The **first order** parts are:

$$\Delta_{gN} = b_{10}\delta_{T,N} - \frac{1}{\mathcal{H}}\partial_{\parallel}^2 V, \quad (6.53)$$

$$\Delta_{gnG} = b_{01}\varphi_p, \quad (6.54)$$

$$\begin{aligned} \Delta_{gGR} = & \left[b_e - 2\mathcal{Q} + \frac{2(\mathcal{Q}-1)}{\chi\mathcal{H}} - \frac{\mathcal{H}'}{\mathcal{H}^2} \right] (\partial_{\parallel} V - \Psi) \\ & + (2\mathcal{Q}-1)\Psi + \frac{1}{\mathcal{H}}\Psi' + (3-b_e)\mathcal{H}V. \end{aligned} \quad (6.55)$$

Recall that δ_T , V and Ψ have no GR and no PNG corrections, by (6.15) and (6.18).

- The **second-order Newtonian** part of the observed number density contrast is formed from the density contrast and RSD terms and their couplings:

$$\begin{aligned} \Delta_{gN}^{(2)} = & \delta_{gT,N}^{(2)} - \frac{1}{\mathcal{H}}\partial_{\parallel}^2 V_N^{(2)} \\ & - 2\frac{b_{10}}{\mathcal{H}} \left[\delta_T \partial_{\parallel}^2 V + \partial_{\parallel} V \partial_{\parallel} \delta_T \right] + \frac{2}{\mathcal{H}^2} \left[(\partial_{\parallel}^2 V)^2 + \partial_{\parallel} V \partial_{\parallel}^3 V \right]. \end{aligned} \quad (6.56)$$

- The **second-order relativistic** part is [102, 107]:

$$\begin{aligned} \Delta_{gGR}^{(2)} = & \delta_{gT,GR}^{(2)} - \frac{1}{\mathcal{H}}\partial_{\parallel}^2 V_{GR}^{(2)} + \left[b_e - 2\mathcal{Q} + \frac{2(\mathcal{Q}-1)}{\chi\mathcal{H}} - \frac{\mathcal{H}'}{\mathcal{H}^2} \right] \\ & \cdot \left[\partial_{\parallel} V_{N+GR}^{(2)} - \Phi_{N+GR}^{(2)} \right] + 2(\mathcal{Q}-1)\Psi_{N+GR}^{(2)} + \Phi_{N+GR}^{(2)} + \frac{1}{\mathcal{H}}\Psi_{N+GR}^{(2)'} \\ & + (3-b_e)\mathcal{H}V_{N+GR}^{(2)} \\ & + \text{very many terms quadratic in first-order quantities}, \end{aligned} \quad (6.57)$$

where

$$V_{N+GR}^{(2)} \equiv V_N^{(2)} + \mathbf{V}_{GR}^{(2)}, \quad (6.58)$$

and similarly for the metric potentials.

The Newtonian parts of the metric potentials $\Psi^{(2)}, \Phi^{(2)}$ appear in the GR part of $\Delta_g^{(2)}$ because there is *no Newtonian projection effect involving these potentials*. For the velocity potential, the Newtonian part $V_N^{(2)}$ is present only in the RSD term in (6.56); the remaining velocity terms occur *only in the GR part of $\Delta_g^{(2)}$* and therefore $V_N^{(2)}$ is included in the GR terms.

6. Local primordial non-Gaussianity in the bispectrum

The quadratic terms in (6.57) are given in full by [102]. For convenience, Appendix A presents all of the terms in (6.57), correcting some errors in [102].

- The **second-order local PNG** part is

$$\begin{aligned}
\Delta_{gnG}^{(2)} = & \delta_{gT,nG}^{(2)} - \frac{1}{\mathcal{H}} \partial_{\parallel}^2 V_{nG}^{(2)} \\
& + \left[b_e - 2\mathcal{Q} + \frac{2(\mathcal{Q}-1)}{\chi\mathcal{H}} - \frac{\mathcal{H}'}{\mathcal{H}^2} \right] \left[\partial_{\parallel} V_{nG}^{(2)} - \Psi_{nG}^{(2)} \right] + (2\mathcal{Q}-1)\Psi_{nG}^{(2)} \\
& + \frac{1}{\mathcal{H}} \Psi_{nG}^{(2)\prime} + (3-b_e)\mathcal{H}V_{nG}^{(2)} \\
& - 2\frac{b_{01}}{\mathcal{H}} \left(\varphi_p \partial_{\parallel}^2 V + \partial_{\parallel} V \partial_{\parallel} \varphi_p \right) \\
& + b_{01} \left(c_1 \Psi \varphi_p + c_2 V \varphi_p + c_3 \varphi_p \partial_{\parallel} V + c_4 \Psi \partial_{\parallel} \varphi_p \right). \tag{6.59}
\end{aligned}$$

In this expression, lines 1, 2, and 3 contain the linearly evolved second-order terms whose nonlinearity is purely primordial. Lines 4 and 5 contain the quadratic coupling terms.

Line 1 is the Newtonian density + RSD part, given by (6.27) and (6.48).

Line 2 and 3 arise from *GR projection terms that are absent in the Newtonian approximation*: these terms are given by (6.44)–(6.48).

Line 4 arises from the first quadratic RSD term in line 2 of (6.56), given by the coupling of $\delta_{T,nG}$ to velocity gradients.

Line 5 arises from the *coupling of $\delta_{T,nG}$ to first-order GR projection terms*. The coefficients $c_I(a)$ are explicitly given below and in Appendix C.

Apart from the b_{02} term in $\delta_{gT,nG}^{(2)}$, the Newtonian terms in (6.59) scale as $(\mathcal{H}^2/k^2)(\delta_T)^2$ and dominate the GR correction terms, which scale as $i(\mathcal{H}^3/k^3)(\delta_T)^2$ or $(\mathcal{H}^4/k^4)(\delta_T)^2$.

In summary the local PNG part at second order has the following origins:

- * the primordial matter density contrast;
- * the scale-dependent bias;
- * the linearly evolved second-order projection effects in velocity and metric potentials – from RSD and from GR corrections;

6. Local primordial non-Gaussianity in the bispectrum

- * the coupling of first-order scale-dependent bias with first-order projection effects – from RSD and from GR corrections.

6.3.3. Galaxy bispectrum

At leading order the observed galaxy bispectrum is defined by [108]

$$2\langle \Delta_g(\mathbf{k}_1)\Delta_g(\mathbf{k}_2)\Delta_g^{(2)}(\mathbf{k}_3) \rangle + 2 \text{ cp} = (2\pi)^3 B_g(\mathbf{k}_1, \mathbf{k}_2, \mathbf{k}_3) \delta^{\text{Dirac}}(\mathbf{k}_1 + \mathbf{k}_2 + \mathbf{k}_3), \quad (6.60)$$

where here, and below, we omit the time dependence for brevity and we assume equal-time correlations. The bispectrum can be written in terms of Fourier kernels as

$$B_g(\mathbf{k}_1, \mathbf{k}_2, \mathbf{k}_3) = \mathcal{K}(\mathbf{k}_1) \mathcal{K}(\mathbf{k}_2) \mathcal{K}^{(2)}(\mathbf{k}_1, \mathbf{k}_2, \mathbf{k}_3) P(k_1)P(k_2) + 2 \text{ cp}, \quad (6.61)$$

where

$$\Delta_g(\mathbf{k}) = \mathcal{K}(\mathbf{k}) \delta_T(\mathbf{k}), \quad (6.62)$$

$$\Delta_g^{(2)}(\mathbf{k}_3) = \int \frac{d\mathbf{k}_1}{(2\pi)^3} d\mathbf{k}_2 \delta^{\text{Dirac}}(\mathbf{k}_1 + \mathbf{k}_2 - \mathbf{k}_3) \mathcal{K}^{(2)}(\mathbf{k}_1, \mathbf{k}_2, \mathbf{k}_3) \delta_T(\mathbf{k}_1) \delta_T(\mathbf{k}_2). \quad (6.63)$$

In [107], the Newtonian and GR kernels are presented, including all local relativistic effects, from projection, evolution and bias, but in the case of Gaussian initial conditions. Here we have updated these results and extended them to include the effects of local PNG. From Section 6.3.2, we find the following kernels.

- At **first order**, using (6.53)–(6.55) and (6.62):

$$\mathcal{K}_N(\mathbf{k}_a) = b_{10} + f\mu_a^2, \quad (6.64)$$

$$\mathcal{K}_{\text{GR}}(\mathbf{k}_a) = i\mu_a \frac{\gamma_1}{k_a} + \frac{\gamma_2}{k_a^2}, \quad (6.65)$$

$$\mathcal{K}_{\text{nG}}(\mathbf{k}_a) = \frac{b_{01}}{\mathcal{M}(k_a)}, \quad (6.66)$$

where $\mu_a = \hat{\mathbf{k}}_a \cdot \mathbf{n}$ and

$$\frac{\gamma_1}{\mathcal{H}} = f \left[b_e - 2\mathcal{Q} - \frac{2(1-\mathcal{Q})}{\chi\mathcal{H}} - \frac{\mathcal{H}'}{\mathcal{H}^2} \right], \quad (6.67)$$

$$\frac{\gamma_2}{\mathcal{H}^2} = f(3 - b_e) + \frac{3}{2}\Omega_m \left[2 + b_e - f - 4\mathcal{Q} - \frac{2(1-\mathcal{Q})}{\chi\mathcal{H}} - \frac{\mathcal{H}'}{\mathcal{H}^2} \right]. \quad (6.68)$$

6. Local primordial non-Gaussianity in the bispectrum

- The **second-order Newtonian part** follows from (6.56) and (6.63) (see e.g. [69]):

$$\begin{aligned}\mathcal{K}_{\text{N}}^{(2)}(\mathbf{k}_1, \mathbf{k}_2, \mathbf{k}_3) &= b_{10}F_2(\mathbf{k}_1, \mathbf{k}_2) + b_{20} + f\mu_3^2G_2(\mathbf{k}_1, \mathbf{k}_2) + b_sS_2(\mathbf{k}_1, \mathbf{k}_2) \quad (6.69) \\ &\quad + b_{10}f(\mu_1k_1 + \mu_2k_2)\left(\frac{\mu_1}{k_1} + \frac{\mu_2}{k_2}\right) + f^2\frac{\mu_1\mu_2}{k_1k_2}(\mu_1k_1 + \mu_2k_2)^2,\end{aligned}$$

where

$$G_2(\mathbf{k}_1, \mathbf{k}_2) = \frac{F'}{DD'} + \left(\frac{k_1}{k_2} + \frac{k_2}{k_1}\right)\hat{\mathbf{k}}_1 \cdot \hat{\mathbf{k}}_2 + \left(2 - \frac{F'}{DD'}\right)(\hat{\mathbf{k}}_1 \cdot \hat{\mathbf{k}}_2)^2, \quad (6.70)$$

$$S_2(\mathbf{k}_1, \mathbf{k}_2) = (\hat{\mathbf{k}}_1 \cdot \hat{\mathbf{k}}_2)^2 - \frac{1}{3}. \quad (6.71)$$

Since we use the approximation $F/D^2 = 3/7$ in F_2 , we have $F'/(DD') = 6/7$ in G_2 .

- The **second-order relativistic part** follows from (6.57) and (6.63) (see [107], with some errors that are corrected here):

$$\begin{aligned}\mathcal{K}_{\text{GR}}^{(2)}(\mathbf{k}_1, \mathbf{k}_2, \mathbf{k}_3) &= \frac{1}{k_1^2 k_2^2} \left\{ \beta_1 + E_2(\mathbf{k}_1, \mathbf{k}_2, \mathbf{k}_3) \beta_2 \quad (6.72) \right. \\ &\quad + i \left[(\mu_1 k_1 + \mu_2 k_2) \beta_3 + \mu_3 k_3 (\beta_4 + E_2(\mathbf{k}_1, \mathbf{k}_2, \mathbf{k}_3) \beta_5) \right] \\ &\quad + \frac{k_1^2 k_2^2}{k_3^2} \left[F_2(\mathbf{k}_1, \mathbf{k}_2) \beta_6 + G_2(\mathbf{k}_1, \mathbf{k}_2) \beta_7 \right] + (\mu_1 k_1 \mu_2 k_2) \beta_8 \\ &\quad + \mu_3^2 k_3^2 \left[\beta_9 + E_2(\mathbf{k}_1, \mathbf{k}_2, \mathbf{k}_3) \beta_{10} \right] + (\mathbf{k}_1 \cdot \mathbf{k}_2) \beta_{11} \\ &\quad + (k_1^2 + k_2^2) \beta_{12} + (\mu_1^2 k_1^2 + \mu_2^2 k_2^2) \beta_{13} \\ &\quad + i \left[(\mu_1 k_1^3 + \mu_2 k_2^3) \beta_{14} + (\mu_1 k_1 + \mu_2 k_2) (\mathbf{k}_1 \cdot \mathbf{k}_2) \beta_{15} \right. \\ &\quad + k_1 k_2 (\mu_1 k_2 + \mu_2 k_1) \beta_{16} + (\mu_1^3 k_1^3 + \mu_2^3 k_2^3) \beta_{17} \\ &\quad \left. \left. + \mu_1 \mu_2 k_1 k_2 (\mu_1 k_1 + \mu_2 k_2) \beta_{18} + \mu_3 \frac{k_1^2 k_2^2}{k_3} G_2(\mathbf{k}_1, \mathbf{k}_2) \beta_{19} \right] \right\},\end{aligned}$$

where

$$E_2(\mathbf{k}_1, \mathbf{k}_2, \mathbf{k}_3) = \frac{k_1^2 k_2^2}{k_3^4} \left[3 + 2 \left(\frac{k_1}{k_2} + \frac{k_2}{k_1} \right) \hat{\mathbf{k}}_1 \cdot \hat{\mathbf{k}}_2 + (\hat{\mathbf{k}}_1 \cdot \hat{\mathbf{k}}_2)^2 \right]. \quad (6.73)$$

6. Local primordial non-Gaussianity in the bispectrum

The kernel (6.72) is derived from the many terms in $\Delta_g^{(2)}(\mathbf{x})$, as given in [98, 99] (we neglect the integrated terms). For convenience, in Table B.1, Appendix B, we summarise which terms in $\Delta_g^{(2)}(\mathbf{x})$ contribute to which of the terms in (6.72). The time-dependent functions β_I are also given in Appendix A

- The **second-order local PNG part** follows from (6.59):

$$\begin{aligned} \mathcal{K}_{\text{nG}}^{(2)}(\mathbf{k}_1, \mathbf{k}_2, \mathbf{k}_3) = & 2 f_{\text{NL}} (b_{10} + f\mu_3^2) \frac{\mathcal{M}_3}{\mathcal{M}_1 \mathcal{M}_2} \\ & + f b_{01} (\mu_1 k_1 + \mu_2 k_2) \left(\frac{\mu_1}{k_1 \mathcal{M}_2} + \frac{\mu_2}{k_2 \mathcal{M}_1} \right) \\ & + b_n N_2(\mathbf{k}_1, \mathbf{k}_2) + \frac{b_{11}}{2} \left(\frac{1}{\mathcal{M}_1} + \frac{1}{\mathcal{M}_2} \right) + \frac{b_{02}}{\mathcal{M}_1 \mathcal{M}_2} \\ & + \frac{\mathcal{M}_3}{\mathcal{M}_1 \mathcal{M}_2} \left(\frac{\Upsilon_1}{k_3^2} + i \frac{\mu_3}{k_3} \Upsilon_2 \right) + \Upsilon_3 \left(\frac{1}{k_1^2 \mathcal{M}_2} + \frac{1}{k_2^2 \mathcal{M}_1} \right) \\ & + i \left[\Upsilon_4 \left(\frac{\mu_1 k_1}{k_2^2 \mathcal{M}_1} + \frac{\mu_2 k_2}{k_1^2 \mathcal{M}_2} \right) + \Upsilon_5 \left(\frac{\mu_1}{k_1 \mathcal{M}_2} + \frac{\mu_2}{k_2 \mathcal{M}_1} \right) \right], \end{aligned} \quad (6.74)$$

where $\mathcal{M}_a \equiv \mathcal{M}(k_a)$ and

$$N_2(\mathbf{k}_1, \mathbf{k}_2) = \frac{1}{2} \left(\frac{k_1}{k_2 \mathcal{M}_1} + \frac{k_2}{k_1 \mathcal{M}_2} \right) \hat{\mathbf{k}}_1 \cdot \hat{\mathbf{k}}_2. \quad (6.75)$$

In the first line of (6.74), the first term is a sum of the matter density term in line 2 of (6.27) and the linearly evolved PNG part of the second-order RSD term [line 1 of (6.59)]. The second term is the quadratic RSD term from line 3 of (6.59).

The second line gives the scale-dependent bias contribution from (6.27). The first two lines recover the Newtonian approximation (see [158]).

Lines 3 and 4 in magenta are the PNG contributions that arise from relativistic projection effects, as explained in Section 6.3.2. These projection terms in the non-Gaussian kernel involve new time-dependent functions Υ_I , which are given in Appendix C. The terms in $\Delta_g^{(2)}(\mathbf{x})$ corresponding to those in (6.74), lines 4 and 5, are summarised in Table C.1, Appendix C.

The Newtonian terms scale as $(\mathcal{H}^2/k^2)(\delta_T)^2$ except for the b_{02} term which scales as $(\mathcal{H}^4/k^4)(\delta_T)^2$. The relativistic Υ_1, Υ_3 terms scale as $(\mathcal{H}^4/k^4)(\delta_T)^2$, while the $\Upsilon_2, \Upsilon_4, \Upsilon_5$ terms are $\mathcal{O}(\mathcal{H}^3/k^3)$.

6. Local primordial non-Gaussianity in the bispectrum

Note that Υ_1, Υ_2 are proportional to f_{NL} , and $\Upsilon_3, \Upsilon_4, \Upsilon_5$ are proportional to b_{01} (which itself is proportional to f_{NL}).

For Gaussian initial conditions, $\mathcal{K}_{\text{nG}}^{(2)}$ vanishes:

$$f_{\text{NL}} = 0 \Rightarrow b_{01} = b_n = b_{11} = b_{02} = \Upsilon_I = 0 \Rightarrow \mathcal{K}_{\text{nG}}^{(2)}(\mathbf{k}_1, \mathbf{k}_2, \mathbf{k}_3) = 0. \quad (6.76)$$

6.3.4. Numerical examples

The GR corrections to the Newtonian bispectrum, for both Gaussian and local PNG cases, are sensitive to the following astrophysical parameters of the tracer: Gaussian bias b_{10} , PNG bias b_{01} , and magnification bias \mathcal{Q} , together with their first derivatives in time and luminosity; evolution bias b_e and its first time derivative. This can be seen from the kernels presented above, with the details given in Appendices B and C.

In order to illustrate the GR corrections, we need to use physically self-consistent values for these parameters, as well as for the second-order Newtonian clustering bias parameters b_{20} and b_s . For a Stage IV H α spectroscopic survey, similar to Euclid, we use [114] for the clustering biases, evolution bias and magnification bias. We neglect the luminosity derivatives of first-order clustering bias and magnification bias. For the PNG biases b_{11}, b_n, b_{02} we use (6.29)–(6.31).

We start by showing the contribution of GR corrections to the monopole of the reduced bispectrum,

$$Q_g^{00}(k_1, k_2, k_3) = \frac{B_g^{00}(k_1, k_2, k_3)}{P(k_1)P(k_2) + P(k_3)P(k_1) + P(k_2)P(k_3)}, \quad (6.77)$$

where [211]

$$B_g^{\ell m}(k_1, k_2, k_3) = \int_0^{2\pi} d\phi \int_{-1}^1 d\mu_1 B_g(k_1, k_2, k_3, \mu_1, \phi) Y_{\ell m}^*(\mu_1, \phi). \quad (6.78)$$

Here ϕ, μ_1 determine the orientation of the triangle relative to the line of sight. Figure 6.2 shows the monopole for squeezed configurations. We use fixed equal sides $k_1 = k_2 = 0.1 h/\text{Mpc}$ and varying long mode $k_3 < k_1 = k_2$. The isosceles triangle is increasingly squeezed as k_3 decreases. The left panel shows the Newtonian approximation (dash-dot lines) and the right panel shows the monopole without the GR bias correction (6.37).

6. Local primordial non-Gaussianity in the bispectrum

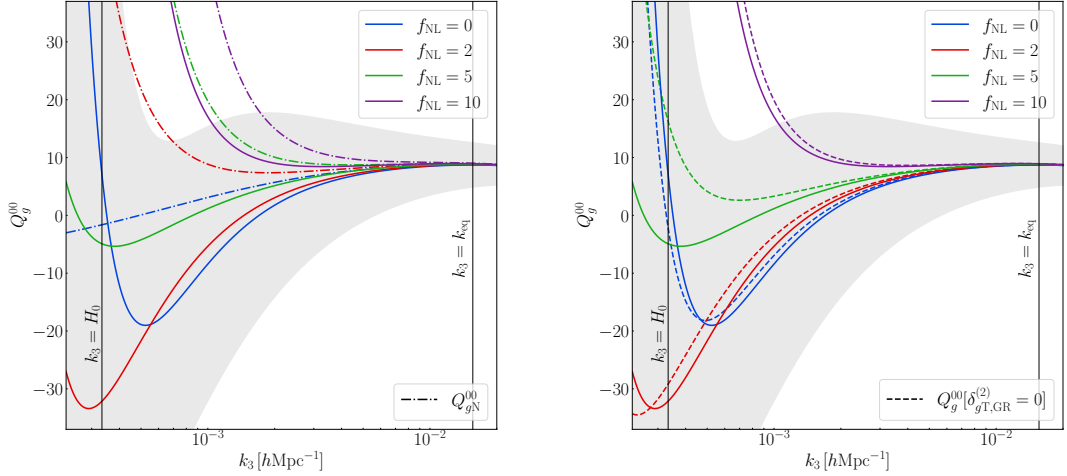


Figure 6.2.: Monopole of the reduced bispectrum for a Stage IV H α survey at $z = 1$, for various f_{NL} , with $k_1 = k_2 = 0.1 h/\text{Mpc}$. Shading indicates the 1σ uncertainty (neglecting shot noise) for the $f_{\text{NL}} = 0$ case (solid blue curve). *Left:* Comparing the full relativistic monopole to the Newtonian approximation (dash-dot curves). *Right:* Comparing the full relativistic monopole to the monopole without the GR correction to second-order galaxy bias, (6.32) (dashed curves).

The shading in Figure 6.2 is defined by the cosmic variance limited error σ_B on the $f_{\text{NL}} = 0$ monopole, given by [256]:

$$(\sigma_B)^2 = \frac{\mathcal{V}^{\text{com}}}{\pi k_1 k_2 k_3 \Delta k} \int d\mu_1 d\phi P_g(k_1, \mu_1) P_g(k_2, \mu_2) P_g(k_3, \mu_3), \quad (6.79)$$

where the galaxy power spectrum, from (6.64)–(6.66), is

$$P_g(k_a, \mu_a) = \left| b_{10} + f \mu_a^2 + \frac{\gamma_2}{k_a^2} + i \mu_a \frac{\gamma_1}{k_a} \right|^2 P(k_a). \quad (6.80)$$

In (6.79), \mathcal{V}^{com} is the comoving volume of the redshift bin, Δk is chosen as the fundamental mode, $2\pi(\mathcal{V}^{\text{com}})^{-1/3}$, $k_1 = k_2 = 0.1 h/\text{Mpc}$, and [88] $\mu_2 = \mu_1 \cos \theta_{12} + \sqrt{1 - \mu_1^2} \sin \theta_{12} \cos \phi$, $\mu_3 = -(k_1 \mu_1 + k_2 \mu_2)/k_3$. Here θ_{12} is the tail-to-tail angle between \mathbf{k}_1 and \mathbf{k}_2 , so that the squeezed limit is $\theta_{12} = \pi$.

The majority of curves corresponding to the different values of f_{NL} plotted in Figure 6.2 fall within the shaded region. This means that these curves fall within the uncertainty region for $f_{\text{NL}} = 0$, and would be indistinguishable. Only for higher values f_{NL} , one can see a departure from the shaded area when going towards larger

6. Local primordial non-Gaussianity in the bispectrum

scales, and would potentially be distinguishable from the $f_{\text{NL}} = 0$ case. However, one should keep in mind the Planck 2018 constraints suggesting a small negative value for f_{NL} as mentioned first in the Introduction chapter to this thesis 1.

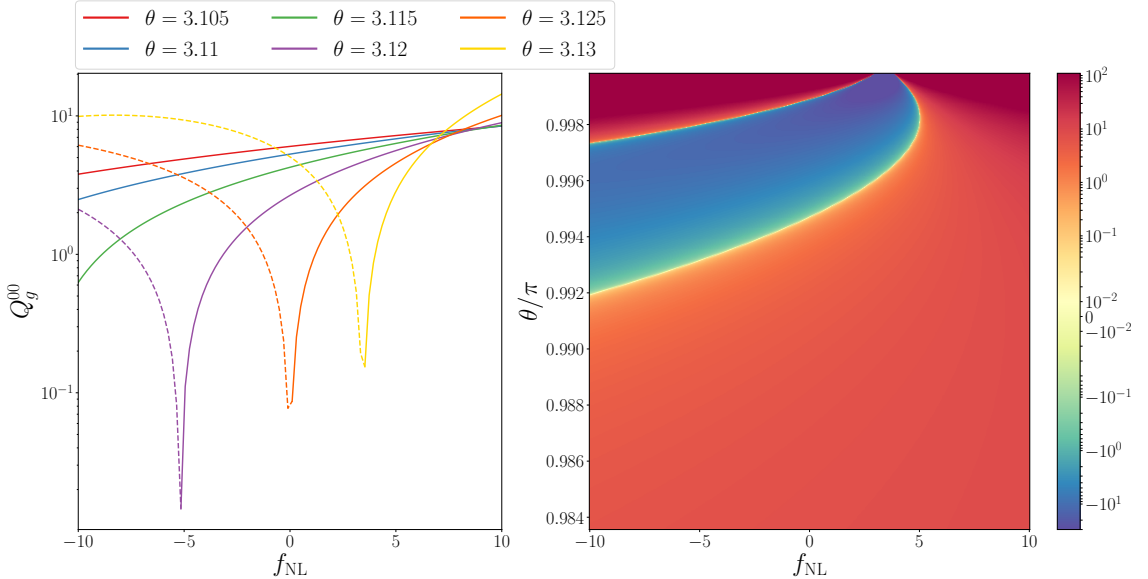


Figure 6.3.: Monopole of reduced bispectrum for isosceles triangles, as in Figure 6.2.
Left: As a function of f_{NL} , for various values of $\theta \equiv \theta_{12}$, where $\theta = \pi$ is the squeezed limit. Dashed curves indicate negative values. *Right:* 2D colour map as a function of f_{NL} and θ/π .

The effect of f_{NL} is strongest in the monopole and competes with the GR contribution on ultra-large scales, since they both affect the Newtonian Gaussian bispectrum at $\mathcal{O}(\mathcal{H}^2/k^2)$. We see this in Figure 6.2 left panel, which shows the monopole of the reduced bispectrum for an increasingly squeezed isosceles triangle. In the Gaussian case (blue) we see that the Newtonian reduced monopole (dot-dash blue) becomes negative when the long mode is close to the Hubble scale, due to the effects of second-order galaxy bias. The Gaussian GR correction to the Newtonian approximation is negative for super-equality long modes until close to the Hubble scale (this was pointed out in [109]). GR effects drive the reduced monopole (solid blue) below zero for $H_0 \lesssim k_3 \lesssim 0.002 h/\text{Mpc}$ (the locations of the zero-crossings are dependent on the Gaussian bias parameters, evolution bias and magnification bias).

As f_{NL} is increased above zero, the amplitude of the Newtonian reduced monopole (dot-dash curves) increases monotonically. When GR effects are taken into account, the reduced monopole is pushed upwards, but remains negative on observable scales for $f_{\text{NL}} \lesssim 5$, until it becomes always positive for $f_{\text{NL}} > 5$ – the precise turnaround value of f_{NL} depends on astrophysical parameters. This means that for $f_{\text{NL}} \lesssim 5$,

6. Local primordial non-Gaussianity in the bispectrum

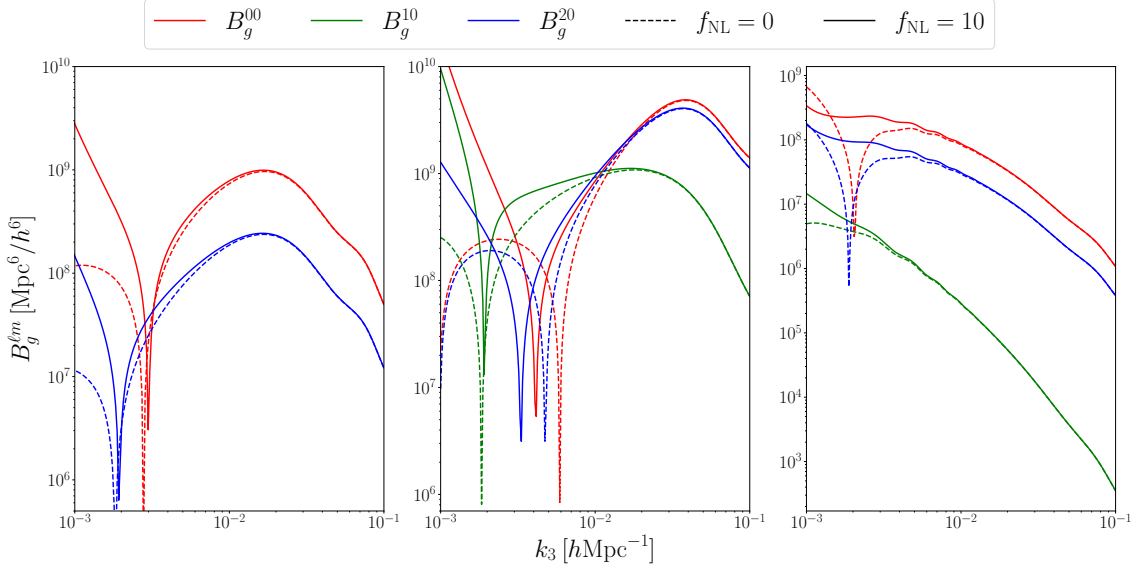


Figure 6.4.: First few nonzero multipoles for fixed triangle shape as a function of k_3 , with $f_{\text{NL}} = 10$ (solid) and $f_{\text{NL}} = 0$ (dashed). *Left:* Equilateral configuration, $k_1 = k_2 = k_3$. *Middle:* Flattened configuration, $k_1 = k_2 \approx k_3/2$, with $\theta_{12} = 2^\circ$. *Right:* Squeezed configuration with $\theta_{12} = 178^\circ$ and $k_1 = k_2 = k_3/(2 \sin \theta_{12}) \approx 14 k_3$.

local PNG *decreases* the amplitude of the reduced monopole on observable scales, in contrast to the Newtonian approximation. Comparing the green solid and blue dot-dash curves shows that *the Newtonian approximation is very close to the true reduced monopole with $f_{\text{NL}} \sim 5$* . For a universe with $f_{\text{NL}} \sim 5$, a Newtonian analysis of the squeezed bispectrum would conclude that the primordial universe is Gaussian. Similarly, a universe with $f_{\text{NL}} \sim 10$ would appear to have $f_{\text{NL}} \sim 5$ in a Newtonian approximation.

The GR contribution to the monopole is made up of: $\mathcal{O}(\mathcal{H}^2/k^2)$ Gaussian projection terms, $\mathcal{O}(\mathcal{H}^2/k^2)$ second-order galaxy bias correction (the same for Gaussian and PNG cases) and $\mathcal{O}(\mathcal{H}^4/k^4)$ second-order local PNG contributions from GR projection effects. The last contribution is effectively negligible on observable scales. In the right panel of Figure 6.2 we show that the GR bias correction is dominated by the Gaussian GR projection terms: the effect of removing the GR correction to second-order galaxy bias is small. Note that the GR bias correction has a similar effect to a small negative value of f_{NL} .

In Figure 6.3 we include negative f_{NL} and explore how local PNG changes the monopole of the reduced bispectrum as we approach the squeezed limit, $\theta_{12} \rightarrow \pi$. For $f_{\text{NL}} \geq 0$, the results provide a different perspective on Figure 6.2 left panel. For

6. Local primordial non-Gaussianity in the bispectrum

negative f_{NL} , local PNG and GR effects act together to drive the monopole negative, so that the zero-crossing of the monopole occurs for smaller θ_{12} , equivalently larger k_3 .

Figure 6.4 shows the effect of f_{NL} on the first three multipoles of the relativistic galaxy bispectrum, also including equilateral and flattened triangle shapes. In general, the Newtonian RSD effect induces only even multipoles, while the GR corrections modify the even multipoles and induce new odd multipoles. We show here the $m = 0$ dipole (absent without GR corrections) and quadrupole (mainly Newtonian), compared to the monopole.

For the equilateral shape (left panel), the dipole vanishes exactly in the Gaussian case [88, 211] and nonzero f_{NL} does not change this result. The effect of f_{NL} on the quadrupole is very similar to the case of the monopole.

For the flattened shape (middle panel), the dipole is the dominant part of the bispectrum for $0.002 \lesssim k_3/(h\text{Mpc}^{-1}) \lesssim 0.01$, and we see that $f_{\text{NL}} > 0$ increases this effect further. The dipole B_g^{1m} is purely relativistic: it vanishes in the Newtonian approximation [88, 113, 114].

Finally, in the squeezed case (right panel), the effect on the monopole of $f_{\text{NL}} = 10$ is consistent with Figure 6.2. The quadrupole has a similar behaviour, and dominates the dipole. It is interesting that the three multipoles are approximately equal at scales near $k = 0.002 h/\text{Mpc}$. Once again, this value is sensitive to astrophysical parameters.

6.4. Conclusions

Upcoming galaxy surveys and 21cm intensity mapping surveys will deliver high-precision cosmological measurements and constraints, based on a combination of the power spectrum and bispectrum. This advance demands a commensurate advance in theoretical precision. Here we contribute to the development of theoretical precision by deriving for the first time the local relativistic corrections to the tree-level redshift-space bispectrum in the presence of local primordial non-Gaussianity (PNG).

At first order in perturbations, there are no relativistic corrections to the comoving matter and galaxy density contrasts – and therefore no correction to the galaxy clustering bias relation. There are also no relativistic corrections to the velocity and

6. Local primordial non-Gaussianity in the bispectrum

metric potentials. Consequently, there is no relativistic contribution to local PNG. The only relativistic correction is to the Newtonian projection effect, i.e. standard redshift-space distortions (RSD).

At second-order, relativistic corrections go beyond projection effects to alter the galaxy bias relation and local PNG in the galaxy bispectrum. In summary, there are:

- relativistic projection corrections to the Newtonian RSD at first and second order;
- relativistic corrections to the Newtonian bias model in the comoving frame at second order;
- second-order relativistic projection corrections to the local PNG carried by Newtonian RSD – from a coupling of first-order scale-dependent bias to first-order relativistic projection effects, and from the linearly evolved local PNG in second-order velocity and metric potentials.

Our previous work [88, 102, 107–109, 113, 114, 211] presented local (non-integrated) relativistic effects in the case of primordial Gaussianity and without the relativistic correction to galaxy bias. We have made corrections to these earlier results. In addition, we have presented for the first time the galaxy bispectrum with relativistic corrections to galaxy clustering bias and new local PNG contributions that are encoded in relativistic projection effects. Our main results are given in Fourier space in (6.69)–(6.74), with further details in Appendices B and C.

In Figures 6.2 and 6.3 we show examples of the squeezed monopole of the reduced relativistic bispectrum for a Stage IV H α survey similar to Euclid, using physical models for the astrophysical parameters (clustering biases, evolution bias, magnification bias). These figures reveal various interesting relativistic features. In particular, they show the bias in the estimate of f_{NL} from using a Newtonian analysis. This bias is given by

$$f_{\text{NL}}^{\text{Newt}} = f_{\text{NL}} + \Delta f_{\text{NL}} . \quad (6.81)$$

For the Stage IV survey at $z = 1$, the bias can be roughly estimated by eye as $\Delta f_{\text{NL}} \sim 5$, for the long mode above the equality scale. Although the precise level of bias is sensitive to astrophysical parameters and redshift, the point is that next-generation precision demands that relativistic corrections are included in the bispectrum.

6. Local primordial non-Gaussianity in the bispectrum

In common with nearly all work on the Fourier-space bispectrum with RSD and PNG, we implicitly make a flat-sky assumption, based on the fixed global direction \mathbf{n} . As a consequence, wide-angle correlations are not included, so that the flat-sky analysis loses accuracy as θ increases, where θ is the maximum opening angle to the three-point correlations at the given redshift. This leads to a systematic bias in the separation of observational effects from the PNG signal, and therefore in the best-fit value of f_{NL} . Including wide-angle effects is a key target for future work. Corrections to the global flat-sky analysis of the Fourier bispectrum can be made by using a local or ‘moving’ line of sight [185, 186, 257]. However, corrections of this type are approximate and do not incorporate all the wide-angle effects. Ultimately, one needs to use the full-sky 3-point correlation function or the full-sky angular bispectrum (see e.g. [103, 139, 141, 150]) to properly include all wide-angle correlations. A major problem is that both of these alternatives are computationally more intensive.

7. Conclusions and Outlook

In this thesis, we have examined the relativistic contributions to the observed galaxy bispectrum. For the first part of this thesis, we focussed on the leading-order $\mathcal{O}(\mathcal{H}/k)$ corrections, which are absent in the power spectrum of a single tracer, but present in the bispectrum of single tracers and hence form a unique relativistic signature. In the second part of this thesis, we examined the higher-order relativistic corrections, and included local primordial non-Gaussianity in our theoretical description of the galaxy bispectrum. Local PNG and relativistic corrections have similar signatures (k -dependence) on large scales. Since detecting primordial non-Gaussianity is a key aim of next-generation (Stage IV) LSS surveys, it is crucial to include both relativistic effects and PNG in the theoretical description of the observed bispectrum, in order to avoid misinterpreting measurements.

In Chapter 1, we introduced the standard model of cosmology, ΛCDM , which is assumed throughout this work. We described the history of observational cosmology, and introduced two statistical tools that are employed to extract information from galaxy surveys: the power spectrum and the bispectrum, the latter of which is the main focus of this work. We briefly introduced primordial non-Gaussianity of the local type, which corresponds to squeezed shape triangles and is predicted by a wide range of inflationary scenarios. PNG gives rise to scale dependence in the galaxy bias, which we discussed next. This scale dependence comes in at next-to-leading-order in \mathcal{H}/k , and motivates the need for inclusion of relativistic corrections.

In Chapter 2, we analyse the \mathcal{H}/k effects in the bispectrum. We have shown that the relativistic galaxy bispectrum has a leading-order correction, which gives rise to a local dipole with respect to the observer's line-of-sight. This dipole exists even for the bispectrum of a single tracer, in contrast with the power spectrum. Even on equality scales, at redshift $z = 1$, the amplitude of this dipole is about 10% of that of the monopole. Although we have used Gaussian initial conditions in these predictions, the dipole will be unaffected by non-Gaussianity at leading order, since these corrections start at $\mathcal{O}(\mathcal{H}^2/k^2)$. As such, the dipole of the bispectrum

7. Conclusions and Outlook

is a unique signature of GR on cosmological scales, and offers a new observational window into modifications of GR.

In Chapter 3, we continue our consideration of the leading-order corrections first examined in Chapter 2. Since the relativistic contribution to the bispectrum couples to short-scale Newtonian terms, the signal is not confined to very large scales, unlike the case of the power spectrum. We confirmed the expectations of detectability of such a signal by showing that the signal-to-noise ratio on this relativistic part is $\mathcal{O}10$ for a Stage IV H α spectroscopic survey similar to *Euclid*. We checked that the detectability is not compromised by including the uncertainties on two cosmological growth parameters, σ_8 and γ , assuming that other cosmological and nuisance parameters are determined by the Newtonian power spectrum and bispectrum.

The relativistic SNR is dependent on the k_{\max} assumed, i.e. on the small scales where perturbation theory breaks down, because of the coupling of the relativistic effects to short-scale Newtonian terms. Further, the SNR depends on the largest available scales too, although not as strongly. Little signal is lost if k_{\min} is increased. In contrast, the SNR more strongly depends on accurate modelling of the second-order part of the relativistic correction, and in particular is dependent on two astrophysical parameters that do not appear in the Newtonian approximation: the evolution and magnification bias parameters b_e and \mathcal{Q} . A key feature of this work was the inclusion of physically self-consistent derivations of these quantities from the luminosity function, which we did for two luminosity function models relevant for future H α surveys.

HI intensity mapping surveys require significant additions to deal with foreground contamination and complexities of instrumental noise, which dominates over shot noise. The loss of signal due to foreground cleaning and telescope beam effects reduces the SNR for next-generation IM surveys on MeerKAT, SKA1-MID and HIRAX, with marginally detectable SNR forecasts of ~ 6 for SKA1 and ~ 5 for HIRAX. The PUMA survey, which is still in proposal stage, would deliver a SNR of ~ 14 in its Petite or first phase (before the futuristic full survey).

In Chapter 4, we summarised past work on the Fourier-space galaxy bispectrum including all orders of relativistic projection effects in the observed bispectrum. This meant going beyond the leading-order relativistic correction that was considered in the previous chapters. We included an overview of how the Fourier-space bispectrum of galaxies is constructed from observed galaxy overdensities, and motivate the inclusion of these higher order GR corrections, as they mimic the signal of PNG

7. Conclusions and Outlook

on large scales. We also showed that corrections that arise from vector and tensor modes are subdominant compared to scalar contributions, and hence can safely be ignored.

Next, in Chapter 5, we present a full analytic decomposition of the Fourier space bispectrum into invariant multipoles about the observer’s line-of-sight. We have found that relativistic corrections generate a hierarchy of odd multipoles, which are absent in the Newtonian picture. They also contribute to even multipoles. The leading power of the relativistic correction in each ℓ harmonic is $(\mathcal{H}/k)^1$ for odd multipoles and $(\mathcal{H}/k)^2$ for even multipoles. We have found that the co-linear configuration only generates non-zero $m = 0$ multipoles, and vanishes for all other values of m . Equilateral configurations are always zero for odd m , and always zero for the special case of the dipole. Relative to the Newtonian monopole, we have found that all relativistic multipoles decay with redshift. Depending on the scales of interest, higher-order Newtonian terms can exceed second-order GR terms in amplitude.

Finally, in Chapter 6, we have presented the local relativistic corrections to the tree-level redshift-space bispectrum of galaxies in the presence of local PNG. In summary, there are: relativistic projection corrections to the Newtonian RSD at first and second order, relativistic corrections to the Newtonian bias model in the comoving frame at second order, and second-order relativistic projection corrections to the local PNG carried by Newtonian RSD— from a coupling of first-order scale-dependent bias to first-order relativistic projection effects, and from the linearly evolved local PNG in second-order velocity and metric potentials. We have also shown the bias in the estimate of non-Gaussian parameter f_{NL} from using a Newtonian analysis, which for a Stage IV survey at $z = 1$ is about $\Delta f_{\text{NL}} \sim 5$, for the long mode above the equality scale. The precise level of bias is of course sensitive to astrophysical parameters and redshift, but the key result is that next-generation precision demands that relativistic corrections are included in the bispectrum.

Further work could take multiple different directions. Some lower-hanging fruits would be for example Fisher forecasts using the bispectrum to improve cosmological constraints, e.g. including f_{NL} and scale-dependent bias. Due to the sensitivity of the bispectrum on evolution and magnification bias b_e and \mathcal{Q} , it may offer potential for improved constraints on bias parameters. The bispectrum of multiple tracers is not yet fully understood either. The advantages and limitations of measuring parameters using the power spectrum of multiple tracers is already well understood, but it is

7. Conclusions and Outlook

unclear in what regimes and for what parameters the multi-tracer bispectrum would be a better suited observable.

In terms of predictions for detectability, it is necessary to include the window function, which we have neglected to do in our Chapter 3. The window function can also have an imaginary part, similar to the leading-order relativistic correction to the bispectrum. This will need to be corrected for. The dipole that arises from the imaginary part of the bispectrum vanishes identically for equilateral triangle configurations, which may help disentangle the relativistic dipole from that of the window function. There is also no simulation-based model for the bispectrum RSD damping parameter, which we have taken to be equal to the power spectrum damping parameter. From testing the impact of increasing the bispectrum damping parameter, it leads to only a small change in our results, but a complete analysis would require a consistent model of bispectrum RSD damping.

In common with other work on the Fourier-space bispectrum, our analysis as presented here implicitly uses the plane-parallel approximation, since we have fixed the line-of-sight direction \mathbf{n} . This approximation can be avoided, for example by using a Fourier-Bessel analysis of bispectrum multipoles, but this will come at the cost of a significant increase in complexity. Note however that errors from the plane-parallel approximation are mitigated in high redshift surveys such as considered in this thesis.

Further work also needs to include the effects of lensing magnification, which are excluded in the standard Fourier analysis. These have been included in work on the galaxy angular bispectrum, and in a spherical Bessel analysis of the bispectrum.

We also neglected cross-correlations among redshift bins throughout this thesis. This is justified by exquisite redshift accuracy in future surveys, which allows for sharp-edged redshift bins with little to no overlap between them. Integrated effects however will induce correlations along the line-of-sight direction. Ultimately, integrated effects and cross-bin correlations need to be included, which requires a complete treatment using the angular bispectrum or 3-point correlation function. The inclusion of integrated contributions may also change the impact that corrections due to vector and tensor modes have on the bispectrum, and may mean that these corrections can no longer be neglected.

A. Beta coefficients

In this appendix, we present the β_I functions that appear in the second-order relativistic Fourier space kernel of the galaxy bispectrum.

$$\begin{aligned}
\frac{\beta_1}{\mathcal{H}^4} = & \frac{9}{4}\Omega_m^2 \left[6 - 2f \left(2b_e - 4\mathcal{Q} - \frac{4(1-\mathcal{Q})}{\chi\mathcal{H}} - \frac{2\mathcal{H}'}{\mathcal{H}^2} \right) - \frac{2f'}{\mathcal{H}} + b_e^2 + 5b_e - 8b_e\mathcal{Q} \right. \\
& + 4\mathcal{Q} + 16\mathcal{Q}^2 - 16\frac{\partial\mathcal{Q}}{\partial\ln\bar{L}} - 8\frac{\mathcal{Q}'}{\mathcal{H}} + \frac{b'_e}{\mathcal{H}} + \frac{2}{\chi^2\mathcal{H}^2} \left(1 - \mathcal{Q} + 2\mathcal{Q}^2 - 2\frac{\partial\mathcal{Q}}{\partial\ln\bar{L}} \right) \\
& - \frac{2}{\chi\mathcal{H}} \left(3 + 2b_e - 2b_e\mathcal{Q} - 3\mathcal{Q} + 8\mathcal{Q}^2 - \frac{3\mathcal{H}'}{\mathcal{H}^2}(1-\mathcal{Q}) - 8\frac{\partial\mathcal{Q}}{\partial\ln\bar{L}} - 2\frac{\mathcal{Q}'}{\mathcal{H}} \right) \\
& + \frac{\mathcal{H}'}{\mathcal{H}^2} \left(-7 - 2b_e + 8\mathcal{Q} + \frac{3\mathcal{H}'}{\mathcal{H}^2} \right) - \frac{\mathcal{H}''}{\mathcal{H}^3} \Big] \\
& + \frac{3}{2}\Omega_m f \left[5 - 2f(4 - b_e) + \frac{2f'}{\mathcal{H}} + 2b_e \left(5 + \frac{2(1-\mathcal{Q})}{\chi\mathcal{H}} \right) - \frac{2b'_e}{\mathcal{H}} - 2b_e^2 + 8b_e\mathcal{Q} \right. \\
& - 28\mathcal{Q} - \frac{14(1-\mathcal{Q})}{\chi\mathcal{H}} - \frac{3\mathcal{H}'}{\mathcal{H}^2} + 4 \left(2 - \frac{1}{\chi\mathcal{H}} \right) \frac{\mathcal{Q}'}{\mathcal{H}} \Big] \\
& + \frac{3}{2}\Omega_m f^2 \left[-2 + 2f - b_e + 4\mathcal{Q} + \frac{2(1-\mathcal{Q})}{\chi\mathcal{H}} + \frac{3\mathcal{H}'}{\mathcal{H}^2} \right] \\
& + f^2 \left[12 - 7b_e + b_e^2 + \frac{b'_e}{\mathcal{H}} + (b_e - 3)\frac{\mathcal{H}'}{\mathcal{H}^2} \right] - \frac{3}{2}\Omega_m \frac{f'}{\mathcal{H}} \tag{A.1}
\end{aligned}$$

$$\begin{aligned}
\frac{\beta_2}{\mathcal{H}^4} = & \frac{9}{2}\Omega_m^2 \left[-1 + b_e - 2\mathcal{Q} - \frac{2(1-\mathcal{Q})}{\chi\mathcal{H}} - \frac{\mathcal{H}'}{\mathcal{H}^2} \right] \\
& + 3\Omega_m f \left[-1 + 2f - b_e + 4\mathcal{Q} + \frac{2(1-\mathcal{Q})}{\chi\mathcal{H}} + \frac{3\mathcal{H}'}{\mathcal{H}^2} \right] \\
& + 3\Omega_m f^2 \left[-1 + b_e - 2\mathcal{Q} - \frac{2(1-\mathcal{Q})}{\chi\mathcal{H}} - \frac{\mathcal{H}'}{\mathcal{H}^2} \right] + 3\Omega_m \frac{f'}{\mathcal{H}} \tag{A.2} \\
\frac{\beta_3}{\mathcal{H}^3} = & \frac{9}{4}\Omega_m^2(f - 2 + 2\mathcal{Q})
\end{aligned}$$

A. Beta coefficients

$$\begin{aligned}
& + \frac{3}{2} \Omega_m f \left[-2 - f \left(-3 + f + 2b_e - 3\mathcal{Q} - \frac{4(1-\mathcal{Q})}{\chi\mathcal{H}} - \frac{2\mathcal{H}'}{\mathcal{H}^2} \right) - \frac{f'}{\mathcal{H}} \right. \\
& + 3b_e + b_e^2 - 6b_e\mathcal{Q} + 4\mathcal{Q} + 8\mathcal{Q}^2 - 8 \frac{\partial\mathcal{Q}}{\partial \ln \bar{L}} - 6 \frac{\mathcal{Q}'}{\mathcal{H}} + \frac{b'_e}{\mathcal{H}} \\
& + \frac{2}{\chi^2\mathcal{H}^2} \left(1 - \mathcal{Q} + 2\mathcal{Q}^2 - 2 \frac{\partial\mathcal{Q}}{\partial \ln \bar{L}} \right) + \frac{2}{\chi\mathcal{H}} \left(-1 - 2b_e + 2b_e\mathcal{Q} + \mathcal{Q} - 6\mathcal{Q}^2 \right. \\
& \left. + \frac{3\mathcal{H}'}{\mathcal{H}^2}(1-\mathcal{Q}) + 6 \frac{\partial\mathcal{Q}}{\partial \ln \bar{L}} + 2 \frac{\mathcal{Q}'}{\mathcal{H}} \right) - \frac{\mathcal{H}'}{\mathcal{H}^2} \left(3 + 2b_e - 6\mathcal{Q} - \frac{3\mathcal{H}'}{\mathcal{H}^2} \right) - \frac{\mathcal{H}''}{\mathcal{H}^3} \Big] \\
& + f^2 \left[-3 + 2b_e \left(2 + \frac{(1-\mathcal{Q})}{\chi\mathcal{H}} \right) - b_e^2 + 2b_e\mathcal{Q} - 6\mathcal{Q} - \frac{b'_e}{\mathcal{H}} - \frac{6(1-\mathcal{Q})}{\chi\mathcal{H}} \right. \\
& \left. + 2 \left(1 - \frac{1}{\chi\mathcal{H}} \right) \frac{\mathcal{Q}'}{\mathcal{H}} \right] \tag{A.3}
\end{aligned}$$

$$\frac{\beta_4}{\mathcal{H}^3} = \frac{9}{2} \Omega_m f \left[-b_e + 2\mathcal{Q} + \frac{2(1-\mathcal{Q})}{\chi\mathcal{H}} + \frac{\mathcal{H}'}{\mathcal{H}^2} \right] \tag{A.4}$$

$$\frac{\beta_5}{\mathcal{H}^3} = 3\Omega_m f \left[b_e - 2\mathcal{Q} - \frac{2(1-\mathcal{Q})}{\chi\mathcal{H}} - \frac{\mathcal{H}'}{\mathcal{H}^2} \right] \tag{A.5}$$

$$\frac{\beta_6}{\mathcal{H}^2} = \frac{3}{2} \Omega_m \left[2 - 2f + b_e - 4\mathcal{Q} - \frac{2(1-\mathcal{Q})}{\chi\mathcal{H}} - \frac{\mathcal{H}'}{\mathcal{H}^2} \right] \tag{A.6}$$

$$\frac{\beta_7}{\mathcal{H}^2} = f(3 - b_e) \tag{A.7}$$

$$\begin{aligned}
& \frac{\beta_8}{\mathcal{H}^2} = 3\Omega_m f(2 - f - 2\mathcal{Q}) + f^2 \left[4 + b_e - b_e^2 + 4b_e\mathcal{Q} - 6\mathcal{Q} - 4\mathcal{Q}^2 + 4 \frac{\partial\mathcal{Q}}{\partial \ln \bar{L}} + 4 \frac{\mathcal{Q}'}{\mathcal{H}} \right. \\
& - \frac{b'_e}{\mathcal{H}} - \frac{2}{\chi^2\mathcal{H}^2} \left(1 - \mathcal{Q} + 2\mathcal{Q}^2 - 2 \frac{\partial\mathcal{Q}}{\partial \ln \bar{L}} \right) - \frac{2}{\chi\mathcal{H}} \left(3 - 2b_e + 2b_e\mathcal{Q} - \mathcal{Q} - 4\mathcal{Q}^2 \right. \\
& \left. + \frac{3\mathcal{H}'}{\mathcal{H}^2}(1-\mathcal{Q}) + 4 \frac{\partial\mathcal{Q}}{\partial \ln \bar{L}} + 2 \frac{\mathcal{Q}'}{\mathcal{H}} \right) - \frac{\mathcal{H}'}{\mathcal{H}^2} \left(3 - 2b_e + 4\mathcal{Q} + \frac{3\mathcal{H}'}{\mathcal{H}^2} \right) + \frac{\mathcal{H}''}{\mathcal{H}^3} \Big] \tag{A.8}
\end{aligned}$$

$$\frac{\beta_9}{\mathcal{H}^2} = -\frac{9}{2} \Omega_m f \tag{A.9}$$

$$\frac{\beta_{10}}{\mathcal{H}^2} = 3\Omega_m f \tag{A.10}$$

$$\frac{\beta_{11}}{\mathcal{H}^2} = 3\Omega_m \left(\frac{1}{2} + f \right) + f - f^2 \left[-1 + b_e - 2\mathcal{Q} - \frac{2(1+\mathcal{Q})}{\chi\mathcal{H}} - \frac{\mathcal{H}'}{\mathcal{H}^2} \right] \tag{A.11}$$

$$\begin{aligned}
& \frac{\beta_{12}}{\mathcal{H}^2} = \frac{3}{2} \Omega_m \left[-2 + b_1 \left(2 + b_e - 4\mathcal{Q} - \frac{2(1-\mathcal{Q})}{\chi\mathcal{H}} - \frac{\mathcal{H}'}{\mathcal{H}^2} \right) + \frac{b'_1}{\mathcal{H}} \right. \\
& \left. + 2 \left(2 - \frac{1}{\chi\mathcal{H}} \right) \frac{\partial b_1}{\partial \ln \bar{L}} \right] - f \left[2 + b_1(f - 3 + b_e) + \frac{b'_1}{\mathcal{H}} \right] \tag{A.12}
\end{aligned}$$

A. Beta coefficients

$$\frac{\beta_{13}}{\mathcal{H}^2} = \frac{9}{4}\Omega_m^2 + \frac{3}{2}\Omega_m f \left[1 - 2f + 2b_e - 6\mathcal{Q} - \frac{4(1-\mathcal{Q})}{\chi\mathcal{H}} - \frac{3\mathcal{H}'}{\mathcal{H}^2} \right] + f^2(3-b_e) \quad (\text{A.13})$$

$$\frac{\beta_{14}}{\mathcal{H}} = -\frac{3}{2}\Omega_m b_1 \quad (\text{A.14})$$

$$\frac{\beta_{15}}{\mathcal{H}} = 2f^2 \quad (\text{A.15})$$

$$\frac{\beta_{16}}{\mathcal{H}} = f \left[b_1 \left(f + b_e - 2\mathcal{Q} - \frac{2(1-\mathcal{Q})}{\chi\mathcal{H}} - \frac{\mathcal{H}'}{\mathcal{H}^2} \right) + \frac{b'_1}{\mathcal{H}} + 2 \left(1 - \frac{1}{\chi\mathcal{H}} \right) \frac{\partial b_1}{\partial \ln \bar{L}} \right] \quad (\text{A.16})$$

$$\frac{\beta_{17}}{\mathcal{H}} = -\frac{3}{2}\Omega_m f \quad (\text{A.17})$$

$$\frac{\beta_{18}}{\mathcal{H}} = \frac{3}{2}\Omega_m f - f^2 \left[3 - 2b_e + 4\mathcal{Q} + \frac{4(1-\mathcal{Q})}{\chi\mathcal{H}} + \frac{3\mathcal{H}'}{\mathcal{H}^2} \right] \quad (\text{A.18})$$

$$\frac{\beta_{19}}{\mathcal{H}} = f \left[b_e - 2\mathcal{Q} - \frac{2(1-\mathcal{Q})}{\chi\mathcal{H}} - \frac{\mathcal{H}'}{\mathcal{H}^2} \right] \quad (\text{A.19})$$

B. Beta coefficient tables

Here we present a table of individual terms in the observed density fluctuation $\Delta_g^{(2)}$, with the corresponding β function β_I in the second column (N for standard Newtonian terms), Fourier space kernel \mathcal{F} , and the coefficients of the terms that appear in $\Delta_g^{(2)}$ in the fourth column.

B. Beta coefficient tables

Table B.1.: Individual terms in the observed $\Delta_g^{(2)}(a, \mathbf{x})$ [see (6.56), (6.57)] for $f_{\text{NL}} = 0$ are shown in column 1. The related β_I functions in (6.72) are listed in column 2. The Fourier-space kernels \mathcal{F} corresponding to column 1, given by $\int d\mathbf{k}' \mathcal{F}(\mathbf{k}', \mathbf{k} - \mathbf{k}') \delta_T(\mathbf{k}') \delta_T(\mathbf{k} - \mathbf{k}') / (2\pi)^3$, are shown in column 3. Column 4 gives the coefficients of the terms in $\Delta_g^{(2)}$ (column 1). The line-of-sight derivative is $\partial_{\parallel} = \mathbf{n} \cdot \nabla$ and $\Phi = \Psi$. The superscript (1) on first-order quantities has been omitted and N denotes Newtonian. This table updates the one in [102].

TERM	β	FOURIER KERNEL	COEFFICIENT
$\delta_{T,N}^{(2)}$	N	$F_2(\mathbf{k}_1, \mathbf{k}_2)$	b_{10}
$(\delta_T)^2$	N	1	b_{20}
s^2	N	$S_2(\mathbf{k}_1, \mathbf{k}_2)$	b_s
$\partial_{\parallel}^2 V_N^{(2)}$	N	$f^2 \mathcal{H} \mu_3^2 G_2(\mathbf{k}_1, \mathbf{k}_2)$	$-1/\mathcal{H}$
$\delta_T \partial_{\parallel}^2 V$	N	$-f \mathcal{H} (\mu_1^2 + \mu_2^2)/2$	$-2b_{10}/\mathcal{H}$
$\partial_{\parallel} V \partial_{\parallel} \delta_T$	N	$-f \mathcal{H} \mu_1 \mu_2 (k_1^2 + k_2^2)/(2k_1 k_2)$	$-2b_{10}/\mathcal{H}$
$\partial_{\parallel} V \partial_{\parallel}^3 V$	N	$f^2 \mathcal{H}^2 (\mu_1 \mu_2^3 k_2^2 + \mu_2 \mu_1^3 k_1^2)/(k_1 k_2)$	$2/\mathcal{H}^2$

B. Beta coefficient tables

$[\partial_{\parallel}^2 V]^2$	N	$f^2 \mathcal{H}^2 \mu_1^2 \mu_2^2$	$2/\mathcal{H}^2$
$(\Psi)^2$	β_1	$9\Omega_m^2 \mathcal{H}^4 / (4k_1^2 k_2^2)$	\mathcal{A}_1
ΨV	β_1	$-3\Omega_m \mathcal{H}^3 f / (2k_1^2 k_2^2)$	\mathcal{A}_2
VV'	β_1	$f \mathcal{H}^3 (3\Omega_m - 2f) / (2k_1^2 k_2^2)$	$(b_e - 3)\mathcal{H}$
$(V)^2$	β_1	$f^2 \mathcal{H}^2 / (k_1^2 k_2^2)$	$(b_e - 3)^2 \mathcal{H}^2 + b'_e \mathcal{H} + (b_e - 3)\mathcal{H}'$
$V_{\text{GR}}^{(2)}$	β_1, β_2	$-3\Omega_m \mathcal{H}^3 [3 - 2E_2(\mathbf{k}_1, \mathbf{k}_2, \mathbf{k}_3)] / (4k_1^2 k_2^2)$	$(3 - b_e)\mathcal{H}$
$\Phi_{\text{GR}}^{(2)}$	β_1, β_2	$3\Omega_m \mathcal{H}^4 [f - \mathcal{C}_1 + \mathcal{C}_1 E_2(\mathbf{k}_1, \mathbf{k}_2, \mathbf{k}_3)] / (2k_1^2 k_2^2)$	$1 - b_e + 2\mathcal{Q} + \mathcal{R}$
$\Psi_{\text{GR}}^{(2)}$	β_1, β_2	$3\Omega_m \mathcal{H}^4 [\mathcal{C}_1 - 3f + 2f^2 + 2f E_2(\mathbf{k}_1, \mathbf{k}_2, \mathbf{k}_3)] / (2k_1^2 k_2^2)$	$2(\mathcal{Q} - 1)$
$\Psi_{\text{GR}}^{(2)\prime}$	β_1, β_2	$3\Omega_m \mathcal{H}^5 [\mathcal{C}_2 + \mathcal{C}_3 E_2(\mathbf{k}_1, \mathbf{k}_2, \mathbf{k}_3)] / (2k_1^2 k_2^2)$	$1/\mathcal{H}$
$V \partial_{\parallel} V$	β_3	$i f^2 \mathcal{H}^2 (\mu_1 k_1 + \mu_2 k_2) / (2k_1^2 k_2^2)$	\mathcal{A}_3
$\Psi \partial_{\parallel} V$	β_3	$-i 3f \Omega_m \mathcal{H}^3 (\mu_1 k_1 + \mu_2 k_2) / (4k_1^2 k_2^2)$	\mathcal{A}_4

B. Beta coefficient tables

$\Psi \partial_{\parallel} \Phi$	β_3	$i 9 \Omega_m^2 \mathcal{H}^4 (\mu_1 k_1 + \mu_2 k_2) / (8 k_1^2 k_2^2)$	$2(f - 2 + 2Q)/\mathcal{H}$
$\partial_{\parallel} V_{\text{GR}}^{(2)}$	β_4, β_5	$-i 3 \Omega_m \mathcal{H}^3 [3 - 2E_2(\mathbf{k}_1, \mathbf{k}_2, \mathbf{k}_3)] \mu_3 k_3 / (4 k_1^2 k_2^2)$	$b_e - 2Q - \mathcal{R}$
$\Psi_{\text{N}}^{(2)} = \Phi_{\text{N}}^{(2)}$ $\Psi_{\text{N}}^{(2)\prime} = \Phi_{\text{N}}^{(2)\prime}$	β_6 β_6	$-3 \Omega_m \mathcal{H}^2 F_2(\mathbf{k}_1, \mathbf{k}_2) / (2 k_3^2)$ $-3 \Omega_m \mathcal{H}^3 (2f - 1) F_2(\mathbf{k}_1, \mathbf{k}_2) / (2 k_3^2)$	$4Q - 1 - b_e + \mathcal{R}$ $1/\mathcal{H}$
$V_{\text{N}}^{(2)}$	β_7	$f \mathcal{H} G_2(\mathbf{k}_1, \mathbf{k}_2) / k_3^2$	$(3 - b_e) \mathcal{H}$
$(\partial_{\parallel} V)^2$ $\partial_{\parallel} V \partial_{\parallel} \Psi$	β_8 β_8	$-f^2 \mathcal{H}^2 \mu_1 \mu_2 / (k_1 k_2)$ $3 f \Omega_m \mathcal{H}^3 \mu_1 \mu_2 / (2 k_1 k_2)$	\mathcal{A}_5 $2(2 - f - 2Q)/\mathcal{H}$
$\partial_{\parallel}^2 V_{\text{GR}}^{(2)}$	β_9, β_{10}	$i 3 \Omega_m \mathcal{H}^3 [3 - 2E_2(\mathbf{k}_1, \mathbf{k}_2, \mathbf{k}_3)] \mu_3^2 k_3^2 / (4 k_1^2 k_2^2)$	$-1/\mathcal{H}$

B. Beta coefficient tables

$\partial_i V \partial^i V$	β_{11}	$b_e - 1 - 2\mathcal{Q} - \mathcal{R}$
$\partial_i V \partial^i \Psi$	β_{11}	$-f^2 \mathcal{H}^2 \mathbf{k}_1 \cdot \mathbf{k}_2 / (k_1^2 k_2^2)$
$\Psi \delta_T$	β_{12}	$3f \Omega_m \mathcal{H}^3 \mathbf{k}_1 \cdot \mathbf{k}_2 / (2k_1^2 k_2^2)$
$V \delta_T$	β_{12}	$-3\Omega_m \mathcal{H}^2 (k_1^2 + k_2^2) / (4k_1^2 k_2^2)$ $f \mathcal{H} (k_1^2 + k_2^2) / (2k_1^2 k_2^2)$
$\delta_{gT,GR}^{(2)}$	β_{11}, β_{12}	$(3\Omega_m + 2f) \mathcal{H}^2 [\mathbf{k}_1 \cdot \mathbf{k}_2 - 2(k_1^2 + k_2^2)] / (2k_1 k_2)$ 1
$\Psi \partial_{\parallel}^2 V$	β_{13}	$3f \Omega_m \mathcal{H}^3 (\mu_1^2 k_1^2 + \mu_2^2 k_2^2) / (4k_1^2 k_2^2)$ $-9\Omega_m^2 \mathcal{H}^4 (\mu_1^2 k_1^2 + \mu_2^2 k_2^2) / (4k_1^2 k_2^2)$
$V \partial_{\parallel}^2 \Psi$	β_{13}	$-2/f^2 \mathcal{H}^3 (\mu_1^2 k_1^2 + \mu_2^2 k_2^2) / (2k_1^2 k_2^2)$ $-i 3\Omega_m \mathcal{H}^2 (\mu_1 k_1^3 + \mu_2 k_2^3) / (4k_1^2 k_2^2)$
$\Psi \partial_{\parallel} \delta_T$	β_{14}	$2b_{10}/\mathcal{H}$
$\partial_i V \partial_{\parallel} \partial^i V$	β_{15}	$-i f^2 \mathcal{H}^2 \mathbf{k}_1 \cdot \mathbf{k}_2 (\mu_1 k_1 + \mu_2 k_2) / (2k_1^2 k_2^2)$ -4/\mathcal{H}

B. Beta coefficient tables

$\delta_T \partial_{\parallel} V$	β_{16}	$i f \mathcal{H} (\mu_1 k_2 + \mu_2 k_1) / (2k_1 k_2)$	$2b_{10}(f + b_e - 2Q - \mathcal{R}) + \mathcal{S}$
$\Phi \partial_{\parallel}^3 V$	β_{17}	$i 3f \Omega_m \mathcal{H}^3 (\mu_1^3 k_1^3 + \mu_2^3 k_2^3) / (4k_1^2 k_2^2)$	$-2/\mathcal{H}^2$
$\partial_{\parallel} V \partial_{\parallel}^2 V$	β_{18}	$-i f^2 \mathcal{H}^2 (\mu_1 \mu_2^2 k_2 + \mu_2 \mu_1^2 k_1) / (2k_1 k_2)$	$2[3 - 2b_e + 4Q + 2\mathcal{R} + (\mathcal{H}'/\mathcal{H}^2)]/\mathcal{H}$
$\partial_{\parallel} V \partial_{\parallel}^2 \Psi$	β_{18}	$i 3f \Omega_m \mathcal{H}^3 (\mu_1 \mu_2^2 k_2 + \mu_2 \mu_1^2 k_1) / (4k_1 k_2)$	$2/\mathcal{H}^2$
$\partial_{\parallel} V_N^{(2)}$	β_{19}	$i f \mathcal{H} \mu_3 G_2(\mathbf{k}_1, \mathbf{k}_2) / k_3$	$b_e - 2Q - \mathcal{R}$

B. Beta coefficient tables

Here the \mathcal{C} functions in the Fourier kernels are

$$\mathcal{C}_1 = 2f - f^2 - 3\Omega_m , \quad (\text{B.1})$$

$$\mathcal{C}_2 = 2f - 1 + (1-f) \left[6\Omega_m + f(1-2f) - 2f \frac{\mathcal{H}'}{\mathcal{H}^2} \right] , \quad (\text{B.2})$$

$$\mathcal{C}_3 = 2f \left(2f - 1 + \frac{\mathcal{H}'}{\mathcal{H}^2} \right) + 2 \frac{f'}{\mathcal{H}} , \quad (\text{B.3})$$

the \mathcal{A} functions in the coefficients are

$$\begin{aligned} \mathcal{A}_1 = & -3 + 2f \left(2 - 2b_e + 4\mathcal{Q} + \frac{4(1-\mathcal{Q})}{\chi\mathcal{H}} + \frac{2\mathcal{H}'}{\mathcal{H}^2} \right) - \frac{2f'}{\mathcal{H}} + b_e^2 + 6b_e\mathcal{Q} + 4\mathcal{Q} \\ & + 16\mathcal{Q}^2 - 16 \frac{\partial\mathcal{Q}}{\partial \ln L} - 8 \frac{\mathcal{Q}'}{\mathcal{H}} + \frac{b'_e}{\mathcal{H}} + \frac{2}{\chi^2\mathcal{H}^2} \left(1 - \mathcal{Q} + 2\mathcal{Q}^2 - 2 \frac{\partial\mathcal{Q}}{\partial \ln L} \right) \\ & - \frac{2}{\chi\mathcal{H}} \left[4 + 2b_e - 2b_e\mathcal{Q} - 4\mathcal{Q} + 8\mathcal{Q}^2 - \frac{3\mathcal{H}'}{\mathcal{H}^2}(1-\mathcal{Q}) - 8 \frac{\partial\mathcal{Q}}{\partial \ln L} - 2 \frac{\mathcal{Q}'}{\mathcal{H}} \right] \\ & + \frac{\mathcal{H}'}{\mathcal{H}^2} \left(-8 - 2b_e + 8\mathcal{Q} + \frac{3\mathcal{H}'}{\mathcal{H}^2} \right) - \frac{\mathcal{H}''}{\mathcal{H}^3} \end{aligned} \quad (\text{B.4})$$

$$\begin{aligned} \mathcal{A}_2 = & 2\mathcal{H} \left[-\frac{15}{2} + f(3-b_e) - \frac{3}{2}b_e - 2b_e \frac{(1-\mathcal{Q})}{\chi\mathcal{H}} + \frac{b'_e}{\mathcal{H}} + b_e^2 - 4b_e\mathcal{Q} + 12\mathcal{Q} \right. \\ & \left. + \frac{6(1-\mathcal{Q})}{\chi\mathcal{H}} - 2 \left(2 - \frac{1}{\chi\mathcal{H}} \right) \frac{\mathcal{Q}'}{\mathcal{H}} \right] , \end{aligned} \quad (\text{B.5})$$

$$\begin{aligned} \mathcal{A}_3 = & 2\mathcal{H} \left[-3 + 4b_e + \frac{2b_e(1-\mathcal{Q})}{\chi\mathcal{H}} - b_e^2 + 2b_e\mathcal{Q} - 6\mathcal{Q} - \frac{b'_e}{\mathcal{H}} - \frac{6(1-\mathcal{Q})}{\chi\mathcal{H}} \right. \\ & \left. + 2 \left(1 - \frac{1}{\chi\mathcal{H}} \right) \frac{\mathcal{Q}'}{\mathcal{H}} \right] , \end{aligned} \quad (\text{B.6})$$

$$\begin{aligned} \mathcal{A}_4 = & 4 + 2f \left[-3 + f + 2b_e - 3\mathcal{Q} - \frac{4(1-\mathcal{Q})}{\chi\mathcal{H}} - \frac{2\mathcal{H}'}{\mathcal{H}^2} \right] + \frac{2f'}{\mathcal{H}} - 6b_e - 2b_e^2 + 12b_e\mathcal{Q} \\ & - 8\mathcal{Q} - 16\mathcal{Q}^2 + 16 \frac{\partial\mathcal{Q}}{\partial \ln L} + 12 \frac{\mathcal{Q}'}{\mathcal{H}} - 2 \frac{b'_e}{\mathcal{H}} - \frac{4}{\chi^2\mathcal{H}^2} \left(1 - \mathcal{Q} + 2\mathcal{Q}^2 - 2 \frac{\partial\mathcal{Q}}{\partial \ln L} \right) \\ & - \frac{4}{\chi\mathcal{H}} \left(-1 - 2b_e + 2b_e\mathcal{Q} + \mathcal{Q} - 6\mathcal{Q}^2 + \frac{3\mathcal{H}'}{\mathcal{H}^2}(1-\mathcal{Q}) + 6 \frac{\partial\mathcal{Q}}{\partial \ln L} + 2 \frac{\mathcal{Q}'}{\mathcal{H}} \right) \\ & + \frac{2\mathcal{H}'}{\mathcal{H}^2} \left(3 + 2b_e - 6\mathcal{Q} - \frac{3\mathcal{H}'}{\mathcal{H}^2} \right) + \frac{2\mathcal{H}''}{\mathcal{H}^3} , \end{aligned} \quad (\text{B.7})$$

$$\begin{aligned} \mathcal{A}_5 = & -4 - b_e + b_e^2 - 4b_e\mathcal{Q} + 6\mathcal{Q} + 4\mathcal{Q}^2 - 4 \frac{\partial\mathcal{Q}}{\partial \ln L} - 4 \frac{\mathcal{Q}'}{\mathcal{H}} + \frac{b'_e}{\mathcal{H}} \\ & + \frac{2}{\chi^2\mathcal{H}^2} \left(1 - \mathcal{Q} + 2\mathcal{Q}^2 - 2 \frac{\partial\mathcal{Q}}{\partial \ln L} \right) \\ & + \frac{2}{\chi\mathcal{H}} \left[3 - 2b_e + 2b_e\mathcal{Q} - 3\mathcal{Q} - 4\mathcal{Q}^2 + \frac{3\mathcal{H}'}{\mathcal{H}^2}(1-\mathcal{Q}) + 4 \frac{\partial\mathcal{Q}}{\partial \ln L} + 2 \frac{\mathcal{Q}'}{\mathcal{H}} \right] \end{aligned}$$

B. Beta coefficient tables

$$+ \frac{\mathcal{H}'}{\mathcal{H}^2} \left(3 - 2b_e + 4\mathcal{Q} + \frac{3\mathcal{H}'}{\mathcal{H}^2} \right) - \frac{\mathcal{H}''}{\mathcal{H}^3}, \quad (\text{B.8})$$

and the functions \mathcal{R}, \mathcal{S} in the coefficients are

$$\mathcal{R} = \frac{2(1 - \mathcal{Q})}{\chi\mathcal{H}} + \frac{\mathcal{H}'}{\mathcal{H}^2}, \quad (\text{B.9})$$

$$\mathcal{S} = 4 \left(2 - \frac{1}{\chi\mathcal{H}} \right) \frac{\partial b_{10}}{\partial \ln L}. \quad (\text{B.10})$$

The magnification bias is defined by [114, 118, 140]:

$$\mathcal{Q} = - \left. \frac{\partial \ln \bar{n}_g}{\partial \ln L} \right|_c, \quad (\text{B.11})$$

where L is the background luminosity and the derivative is evaluated at the flux cut. Similarly, $\partial b_{10}/\partial \ln L$ is understood to be evaluated at the flux cut. We use a short-hand notation for the second luminosity derivative of \bar{n}_g :

$$\frac{\partial \mathcal{Q}}{\partial \ln L} \equiv - \left. \frac{\partial^2 \ln \bar{n}_g}{\partial (\ln L)^2} \right|_c. \quad (\text{B.12})$$

C. Upsilon coefficients

Υ_I functions in (6.74)

$$\begin{aligned} \frac{1}{f_{\text{NL}}} \frac{\Upsilon_1}{\mathcal{H}^2} &= 2(3 - b_e)f + 3\Omega_m \left[1 + b_e - 4\mathcal{Q} - \frac{2(1 - \mathcal{Q})}{\chi\mathcal{H}} - \frac{\mathcal{H}'}{\mathcal{H}^2} \right] \\ &\quad + \frac{6\Omega_m}{(3\Omega_m + 2f)} \left[\frac{f'}{\mathcal{H}} + \left(1 + 2\frac{\mathcal{H}'}{\mathcal{H}^2} \right) f \right] \end{aligned} \quad (\text{C.1})$$

$$\frac{1}{f_{\text{NL}}} \frac{\Upsilon_2}{\mathcal{H}} = 2f \left[b_e - 2\mathcal{Q} - \frac{2(1 - \mathcal{Q})}{\chi\mathcal{H}} - \frac{\mathcal{H}'}{\mathcal{H}^2} \right] \quad (\text{C.2})$$

$$\begin{aligned} \frac{1}{b_{01}} \frac{\Upsilon_3}{\mathcal{H}^2} &= \frac{3}{2}\Omega_m \left[2 + b_e - 4\mathcal{Q} + \frac{2(1 - \mathcal{Q})}{\chi\mathcal{H}} + \frac{\mathcal{H}'}{\mathcal{H}^2} + 2 \left(2 - \frac{1}{\chi\mathcal{H}} \right) \frac{\partial \ln b_{01}}{\partial \ln L} \right] \\ &\quad + f \left[3 - f - b_e + \frac{1}{2} \frac{\partial \ln b_{01}}{\partial \ln a} \right] \end{aligned} \quad (\text{C.3})$$

$$\frac{1}{b_{01}} \frac{\Upsilon_4}{\mathcal{H}} = -\frac{3}{2}\Omega_m \quad (\text{C.4})$$

$$\frac{1}{b_{01}} \frac{\Upsilon_5}{\mathcal{H}} = f \left[f + b_e - 2\mathcal{Q} - \frac{2(1 - \mathcal{Q})}{\chi\mathcal{H}} - \frac{\mathcal{H}'}{\mathcal{H}^2} + 2 \left(2 - \frac{1}{\chi\mathcal{H}} \right) \frac{\partial \ln b_{01}}{\partial \ln L} \right] \quad (\text{C.5})$$

Note that $\Upsilon_2 = 2f_{\text{NL}}\gamma_1$.

Table C.1.: The $f_{\text{NL}} \neq 0$ terms from relativistic projection effects [see (6.74)].

TERM	Υ	FOURIER KERNEL	COEFFICIENT
$V_{\text{nG}}^{(2)}$	Υ_1	$2f_{\text{NL}} \mathcal{H} f \mathcal{M}_3 / (\mathcal{M}_1 \mathcal{M}_2 k_3^2)$	$(3 - b_e) \mathcal{H}$
$\Psi_{\text{nG}}^{(2)} = \Phi_{\text{nG}}^{(2)}$	Υ_1	$-3f_{\text{NL}} \Omega_m \mathcal{H}^2 \mathcal{M}_3 / (\mathcal{M}_1 \mathcal{M}_2 k_3^2)$	$4\mathcal{Q} - 1 - b_e + \mathcal{R}$
$\Psi_{\text{nG}}^{(2)\prime}$	Υ_1	$6f_{\text{NL}} [f' + (\mathcal{H} + 2\mathcal{H}'/\mathcal{H})f] \Omega_m \mathcal{H}^2 \mathcal{M}_3 / [(3\Omega_m + 2f)(\mathcal{M}_1 \mathcal{M}_2 k_3^2)]$	$1/\mathcal{H}$
$\partial_{\parallel} V_{\text{nG}}^{(2)}$	Υ_2	$i 2f_{\text{NL}} \mathcal{H} f \mu_3 \mathcal{M}_3 / (\mathcal{M}_1 \mathcal{M}_2 k_3)$	$b_e - 2\mathcal{Q} - \mathcal{R}$
$\Psi \varphi_p$	Υ_3	$-3\Omega_m \mathcal{H}^2 [(k_1^2/\mathcal{M}_1) + (k_2^2/\mathcal{M}_2)] / (4k_1^2 k_2^2)$	$b_{01} [8\mathcal{Q} + 2\mathcal{R} - 2b_e - 4 - \mathcal{S}/(b_{10} - 1)]$
$V \varphi_p$	Υ_3	$f \mathcal{H} [(k_1^2/\mathcal{M}_1) + (k_2^2/\mathcal{M}_2)] / (2k_1^2 k_2^2)$	$b_{01} [2(3 - b_e - f) \mathcal{H} + b'_{10}/(b_{10} - 1)]$
$\Psi \partial_{\parallel} \varphi_p$	Υ_4	$-i 3\Omega_m \mathcal{H}^2 [(\mu_1 k_1^3/\mathcal{M}_1) + (\mu_2 k_2^3/\mathcal{M}_2)] / (4k_1^2 k_2^2)$	$2b_{01}/\mathcal{H}$
$\varphi_p \partial_{\parallel} V$	Υ_5	$i f \mathcal{H} [(\mu_1 k_2/\mathcal{M}_2) + (\mu_2 k_1/\mathcal{M}_1)] / (2k_1 k_2)$	$b_{01} [2f + 2b_e - 4\mathcal{Q} - 2\mathcal{R} + \mathcal{S}/(b_{10} - 1)]$

D. Presentation of kernel coefficients

Here we present the higher order \mathcal{H}/k kernels for the first of the cyclic permutations. It is worth noting that these cannot be exactly manipulated to obtain the coefficients for the other two cyclic permutations, since making the replacements $\mu_1 \rightarrow \mu_2, \mu_3$ introduces additional powers of μ_i , giving rise to slightly different coefficients \mathcal{K}_{ab} . It is however easy enough to extract the coefficients for these permutations following the same method. Below we focus on only the first of the cyclic permutations, that is, the 123 permutation, as outlined before. Schematic representations of the higher order Newtonian and GR kernels are given, along with their corresponding coefficients. Like before, for brevity we use shorthand notations; $F = F_2(\mathbf{k}_1, \mathbf{k}_2)$, $G = G_2(\mathbf{k}_1, \mathbf{k}_2)$, and $S = S_2(\mathbf{k}_1, \mathbf{k}_2)$. Superscript n on $\mathcal{K}_{ab}^{(n)}$ denotes the power $(\mathcal{H}/k)^n$.

$$\mathcal{K}_{ab}^{(2)} = \begin{pmatrix} \bullet & \circ & \bullet & \circ & \bullet & \circ \\ \circ & \bullet & \circ & \bullet & \circ & \bullet \\ \bullet & \circ & \bullet & \circ & \bullet & \circ \\ \circ & \bullet & \circ & \bullet & \circ & \circ \\ \bullet & \circ & \bullet & \circ & \circ & \circ \\ \circ & \bullet & \circ & \circ & \circ & \circ \end{pmatrix}, \quad (\text{D.1})$$

with coefficients,

$$\begin{aligned} \mathcal{K}_{00}^{(2)} &= b_1 b_{s^2} S \gamma_2 \left(\frac{1}{k_1^2} + \frac{1}{k_2^2} \right) + b_1^2 \left\{ [\gamma_2 (1 + F) + \beta_{12}] \left[\frac{1}{k_1^2} + \frac{1}{k_2^2} \right] + \frac{\mu \beta_{11}}{k_1 k_2} \right. \\ &\quad \left. + \frac{F \beta_6 + G \beta_7}{k_3^2} \right\} \\ \mathcal{K}_{02}^{(2)} &= \frac{f b_{s^2} S \gamma_2}{k_1^2} - b_1 f \left[\frac{\gamma_2 (1 + F) + \beta_{12}}{k_1^2} + \frac{G \gamma_2 k_2^2}{k_1^2 k_3^2} + \frac{\beta_{11} \mu}{k_1 k_2} + \frac{\beta_{12}}{k_2^2} \right] \end{aligned}$$

D. Presentation of kernel coefficients

$$\begin{aligned}
& + \frac{F\beta_6 + G(\beta_7 + \gamma_2)}{k_3^2} \Big] + b_1\gamma_1 \left[\frac{\beta_{14}}{k_1^2} + \frac{\mu\beta_{15}}{k_1 k_2} + \frac{\beta_{16}}{k_2^2} - \frac{G\beta_{19}}{k_3^2} \right] \\
& - b_1^2 \left[\frac{(\beta_9 + E\beta_{10} + \beta_{13})}{k_1^2} + f\gamma_2 \left(\frac{1}{k_1^2} + \frac{1}{k_2^2} \right) \right] \\
\mathcal{K}_{04}^{(2)} & = f^2\gamma_2 \left[\frac{b_1}{k_1^2} + \frac{Gk_2^2}{k_1^2 k_3^2} \right] + \frac{b_1}{k_1^2} [f(\beta_9 + E\beta_{10} + \beta_{13}) - \beta_{17}\gamma_1] \\
\mathcal{K}_{11}^{(2)} & = \frac{b_{s2}S\gamma_1^2}{k_1 k_2} + b_1 \left[\beta_{15}\gamma_1\mu \left(\frac{1}{k_1^2} + \frac{1}{k_2^2} \right) + \beta_{14}\gamma_1 \left(\frac{k_1}{k_2^3} + \frac{k_2}{k_1^3} \right) + \frac{2\beta_{16}\gamma_1 + \gamma_1^2(1+F)}{k_1 k_2} \right. \\
& \quad \left. - \frac{G(k_1^2 + k_2^2)(\beta_{19}\gamma_1 + 2f\gamma_2)}{k_1 k_2 k_3^2} \right] \\
\mathcal{K}_{13}^{(2)} & = f\gamma_1 \left[-\frac{k_2\beta_{14}}{k_1^3} - \frac{\beta_{15}\mu}{k_1^2} - \frac{\beta_{16}}{k_1 k_2} + Gk_2 \frac{(\beta_{19} - \gamma_1)}{k_1 k_3^2} \right] + b_1 \left[-\gamma_1 \left(\frac{k_2\beta_{17}}{k_1^3} + \frac{\beta_{18}}{k_1 k_2} \right) \right. \\
& \quad \left. + \frac{f}{k_1 k_2} (\beta_8 + 2\beta_9 + 2E\beta_{10} - \gamma_1^2) + 2f^2\gamma_2 \left(\frac{1}{k_1 k_2} + \frac{k_2}{k_1^3} \right) \right] \\
\mathcal{K}_{15}^{(2)} & = \frac{fk_2}{k_1^3} [\gamma_1\beta_{17} - \gamma_2] \\
\mathcal{K}_{20}^{(2)} & = -\frac{fb_{s2}S\gamma_2}{k_2^2} + b_1 \left[\frac{\beta_{16}\gamma_1 - f\beta_{12}}{k_1^2} + \frac{\beta_{14}\gamma_1 - f[\beta_{12} + \gamma_2(1+F)]}{k_2^2} \right. \\
& \quad \left. + \mu \frac{(-f\beta_{11} + \gamma_1\beta_{15})}{k_1 k_2} - f \frac{F\beta_6 + G(\beta_7 + \gamma_2)}{k_3^2} - \frac{fGk_1^2\gamma_2}{k_2^2 k_3^2} \right] \\
& - b_1^2 \left[\frac{\beta_9 + E\beta_{10} + \beta_{13}}{k_2^2} + f\gamma_2 \left(\frac{1}{k_1^2} + \frac{1}{k_2^2} \right) \right] \\
\mathcal{K}_{22}^{(2)} & = f\gamma_1 \left[-(\beta_{14} + \beta_{16}) \left(\frac{1}{k_1^2} + \frac{1}{k_2^2} \right) - \frac{2\beta_{15}\mu}{k_1 k_2} + \frac{2G(\beta_{19} - \gamma_1)}{k_3^2} \right] \\
& + f^2 \left[\beta_{12} \left(\frac{1}{k_1^2} + \frac{1}{k_2^2} \right) + \frac{\beta_{11}\mu}{k_1 k_2} + \frac{F\beta_6 + G(\beta_7 + 2\gamma_2)}{k_3^2} \right] \\
& + b_1 \left[(3f^2\gamma_2 - \beta_{18}\gamma_1) \left(\frac{1}{k_1^2} + \frac{1}{k_2^2} \right) \right. \\
& \quad \left. + f \frac{(k_1^2 + k_2^2)(\beta_9 + E\beta_{10} + \beta_{13} - \gamma_1^2)}{k_1^2 + k_2^2} \right] \\
\mathcal{K}_{24}^{(2)} & = \frac{f}{k_1^2} [\gamma_1(\beta_{17} + \beta_{18}) + f(-\beta_9 - E\beta_{10} - \beta_{13} + \gamma_1^2) - 2f^2\gamma_2] \\
\mathcal{K}_{31}^{(2)} & = -f\gamma_1 \left[\frac{k_1\beta_{14}}{k_2^3} + \frac{\beta_{15}\mu}{k_2^2} + \frac{\beta_{16}}{k_1 k_2} - \frac{Gk_1\beta_{19}}{k_2 k_3^2} \right] + [-f\gamma_1^2 + 2f^2\gamma_2] \frac{Gk_1}{k_2 k_3^2} \\
& + b_1 \left[\frac{k_1}{k_2^3} (-\beta_{17}\gamma_1 + 2f^2\gamma_2) + f \frac{\beta_8 + 2\beta_9 + 2E\beta_{10} - \gamma_1^2}{k_1 k_2} - \frac{\beta_{18}\gamma_1^2 - 2f^2\gamma_2}{k_1 k_2} \right] \\
\mathcal{K}_{33}^{(2)} & = \frac{f}{k_1 k_2} [2\beta_{18}\gamma_1 + f(-\beta_8 - 2\beta_9 - 2E\beta_{10} + 2\gamma_1^2) - 2f^2\gamma_2] \\
\mathcal{K}_{40}^{(2)} & = f^2\gamma_2 \frac{Gk_1^2}{k_2^2 k_3^2} - b_1\gamma_1 \frac{\beta_{17}}{k_2^2} + b_1 f \left[\frac{\beta_9 + E\beta_{10} + \beta_{13}}{k_2^2} \right] + b_1 f^2 \frac{\gamma_2}{k_2^2}
\end{aligned}$$

D. Presentation of kernel coefficients

$$\begin{aligned}\mathcal{K}_{42}^{(2)} &= f\gamma_1 \frac{(\beta_{17} + \beta_{18})}{k_2^2} + \frac{f^2}{k_2^2} [-\beta_9 - E\beta_{10}\beta_{13} + \gamma_1^2] - f^3 \frac{2\gamma_2}{k_2^2} \\ \mathcal{K}_{51}^{(2)} &= f \frac{k_1}{k_2^3} [\beta_{17}\gamma_1 - f^2\gamma_2].\end{aligned}$$

$$\mathcal{K}_{ab}^{(3)} = \begin{pmatrix} \circ & \bullet & \circ & \bullet & \circ & \bullet \\ \bullet & \circ & \bullet & \circ & \bullet & \circ \\ \circ & \bullet & \circ & \bullet & \circ & \circ \\ \bullet & \circ & \bullet & \circ & \circ & \circ \\ \circ & \bullet & \circ & \circ & \circ & \circ \\ \bullet & \circ & \circ & \circ & \circ & \circ \end{pmatrix}, \quad (\text{D.2})$$

with coefficients,

$$\begin{aligned}\mathcal{K}_{01}^{(3)} &= \gamma_1\gamma_2 \frac{b_{s2}S}{k_1^2 k_2} + b_1\gamma_1 \left[\frac{\beta_{12}(k_1^2 + k_2^2)}{k_1^2 k_2^3} + \frac{\beta_{11}\mu}{k_1 k_2^2} + \frac{F\beta_6 + G\beta_7}{k_2 k_3^2} \right] + b_1\gamma_2 \left[\frac{\beta_{14} + \beta_{16}}{k_1^2 k_2} \right. \\ &\quad \left. + \frac{\beta_{15}\mu}{k_1 k_2^2} + \frac{(k_2\beta_{14} + k_1\beta_{15}\mu)}{k_1^4} + \frac{\beta_{16}}{k_2^3} - G\beta_{19} \left(\frac{1}{k_2 k_3^2} + \frac{k_2}{k_1^2 k_3^2} \right) \right] + b_1\gamma_1\gamma_2 \frac{(1+F)}{k_1^2 k_2} \\ &\quad - b_1^2 \frac{(\beta_4 - \beta_3 + E\beta_5)}{k_1^2 k_2} \\ \mathcal{K}_{03}^{(3)} &= - \frac{f\gamma_2}{k_1^2} \left[\frac{k_2\beta_{14}}{k_1^2} + \frac{\beta_{15}\mu}{k_1} + \frac{\beta_{16}}{k_2} \right] + f\gamma_2 G k_2 \frac{[\beta_{19} - \gamma_1]}{k_1^2 k_3^2} - b_1 \left[\frac{k_2\beta_{17}\gamma_2}{k_1^4} \right. \\ &\quad \left. + [\gamma_2\beta_{17} - f(\beta_4 - \beta_3 + E\beta_5)] \right. \\ &\quad \left. + \gamma_1(\beta_9 + E\beta_{10} + \beta_{13}) + f\gamma_1\gamma_2 \right] \frac{1}{k_1^2 k_2} \\ \mathcal{K}_{05}^{(3)} &= f\gamma_2 \frac{k_2\beta_{17}}{k_1^4} \\ \mathcal{K}_{10}^{(3)} &= \gamma_1\gamma_2 \frac{b_{s2}S}{k_1 k_2^2} + b_1\gamma_1 \left[\frac{(k_1^2 + k_2^2)\beta_{12}}{k_1^3 k_2^2} + \frac{F\beta_6 + G\beta_7}{k_1 k_3^2} + \frac{\beta_{11}\mu}{k_1^2 k_2} \right] + b_1\gamma_2 \left[\frac{(k_1^2 + k_2^2)\beta_{16}}{k_1^3 k_2^2} \right. \\ &\quad \left. + \frac{(k_1^2 + k_2^2)(k_1\beta_{14} + k_2\beta_{15}\mu)}{k_1^2 k_2^4} - G\beta_{19} \frac{(k_1^2 + k_2^2)}{k_1 k_2^2 k_3^2} \right] + b_1\gamma_1\gamma_2 \frac{[1+F]}{k_1 k_2^2} \\ &\quad - b_1^2 \frac{[\beta_4 - \beta_3 + E\beta_5]}{k_1 k_2^2} \\ \mathcal{K}_{12}^{(3)} &= \gamma_1^2 \left[\frac{\beta_{14}}{k_1^3} + \frac{\beta_{15}\mu}{k_1^2 k_2} + \frac{\beta_{16}}{k_1 k_2^2} - G \frac{\beta_{19}}{k_1 k_3^2} \right] + f \left[-\gamma_1 \frac{(k_1^2 + k_2^2)\beta_{12}}{k_1^3 k_2^2} \right. \\ &\quad \left. - \gamma_1 \left(\frac{F\beta_6 + G[\beta_7 + 3\gamma_2]}{k_1 k_3^2} - \frac{\beta_{11}\mu}{k_1^2 k_2} \right) + \gamma_2 \left(-\frac{\beta_{14}}{k_1 k_2^2} - \frac{\beta_{15}\mu}{k_1^2 k_2} - \frac{\beta_{16}}{k_1^3} + 3 \frac{G\gamma_2}{k_1 k_3^2} \right) \right]\end{aligned}$$

D. Presentation of kernel coefficients

$$\begin{aligned}
& -b_1 \left[\frac{\beta_{13}\gamma_1}{k_1^3} + \frac{-f(\beta_4 - \beta_3 + E\beta_5) + \beta_8\gamma_1}{k_1 k_2^2} \right. \\
& \quad \left. + \frac{\gamma_1(2k_1^2 + k_2^2)}{k_1^3 k_2^2} (\beta_9 + E\beta_{10} + f\gamma_2) + \frac{(k_1^2 + k_2^2)\beta_{18}\gamma_2}{k_1^3 k_2^2} \right] \\
\mathcal{K}_{14}^{(3)} &= \gamma_1 \frac{-\beta_{17}\gamma_1 + f^2\gamma_2}{k_1^3} + f\gamma_1 \frac{[\beta_9 + E\beta_{10} + \beta_{13}]}{k_1^3} + f\gamma_2 \frac{\beta_{18}}{k_1^3} \\
\mathcal{K}_{21}^{(3)} &= \gamma_1^2 \left[\frac{\beta_{14}}{k_2^3} + \frac{\beta_{15}\mu}{k_1 k_2^2} + \frac{\beta_{16}}{k_1^2 k_2} - \frac{G\beta_{19}}{k_2 k_3^2} \right] + f \left[-\frac{(k_1^2 + k_2^2)\beta_{12}\gamma_1}{k_1^2 k_2^3} - \gamma_1 \frac{F\beta_6}{k_2 k_3^2} \right. \\
& \quad \left. + G\gamma_1 \frac{-\beta_7 - 3\gamma_2}{k_2 k_3^2} + G\gamma_2 \frac{\beta_{19}}{k_2 k_3^2} - \frac{\mu}{k_1 k_2^2} (\gamma_1\beta_{11} + \gamma_2\beta_{15}) - \gamma_2 \left(\frac{\beta_{14}}{k_1^2 k_2} + \frac{\beta_{16}}{k_2^3} \right) \right] \\
& \quad + b_1 \left[f \frac{(\beta_4 - \beta_3 + E\beta_5)}{k_1^2 k_2} - \gamma_2 \frac{(k_1^2 + k_2^2)\beta_{18}}{k_1^2 k_2^3} - \gamma_1 \gamma_2 f \left(\frac{1}{k_2^3} + \frac{2}{k_1^2 k_2} \right) \right. \\
& \quad \left. - \gamma_1 E \frac{(k_1^2 + 2k_2^2)\beta_{10}}{k_1^2 k_2^3} - \gamma_1 \frac{(k_1^2 + 2k_2^2)\beta_9}{k_1^2 k_2^3} - \gamma_1 \left(\frac{\beta_8}{k_1^2 k_2} + \frac{\beta_{13}}{k_2^3} \right) \right] \\
\mathcal{K}_{23}^{(3)} &= -\gamma_1^2 \frac{\beta_{18}}{k_1^2 k_2} + f\gamma_1 \frac{[\beta_8 + 3\beta_9 + 3E\beta_{10} + \beta_{13}]}{k_1^2 k_2} + f\gamma_2 \frac{[\beta_{17} + \beta_{18}]}{k_1 k_2^2} \\
& \quad + f^2 \frac{[-\beta_4 + \beta_3 - E\beta_5 + 3\gamma_1\gamma_2]}{k_1^2 k_2} \\
\mathcal{K}_{30}^{(3)} &= -f\gamma_2 \left[\frac{k_1\beta_{14}}{k_2^4} + \frac{\beta_{15}\mu}{k_2^3} + \frac{\beta_{16}}{k_1 k_2^2} \right] + f\gamma_2 G \frac{k_1(\beta_{19} - \gamma_1)}{k_2^2 k_3^2} - b_1 \gamma_1 \left[\frac{\beta_9 + E\beta_{10} + \beta_{13}}{k_1 k_2^2} \right] \\
& \quad - b_1 \gamma_2 \frac{(k_1^2 + k_2^2)\beta_{17}}{k_1 k_2^4} + b_1 f \frac{(\beta_4 - \beta_3 + E\beta_5 - \gamma_1\gamma_2)}{k_1 k_2^2} \\
\mathcal{K}_{32}^{(3)} &= -\gamma_1^2 \frac{\beta_{18}}{k_1 k_2^2} + f\gamma_1 \frac{(\beta_8 + 3\beta_9 + 3E\beta_{10} + \beta_{13})}{k_1 k_2^2} + f\gamma_2 \frac{(\beta_{17} + \beta_{18})}{k_1 k_2^2} \\
& \quad - f^2 \frac{(\beta_4 - \beta_3 + E\beta_5 - 3\gamma_1\gamma_2)}{k_1 k_2^2} \\
\mathcal{K}_{41}^{(3)} &= -\gamma_1^2 \frac{\beta_{17}}{k_2^3} + f^2 \frac{\gamma_1\gamma_2}{k_2^3} + f\gamma_1 \frac{(\beta_9 + E\beta_{10} + \beta_{13})}{k_2^3} + f\gamma_2 \frac{\beta_{18}}{k_2^3} \\
\mathcal{K}_{50}^{(3)} &= f\gamma_2 \frac{k_1\beta_{17}}{k_2^4}.
\end{aligned}$$

$$\mathcal{K}_{ab}^{(4)} = \begin{pmatrix} \bullet & \circ & \bullet & \circ & \bullet & \circ \\ \circ & \bullet & \circ & \bullet & \circ & \circ \\ \bullet & \circ & \bullet & \circ & \circ & \circ \\ \circ & \bullet & \circ & \circ & \circ & \circ \\ \bullet & \circ & \circ & \circ & \circ & \circ \\ \circ & \circ & \circ & \circ & \circ & \circ \end{pmatrix}, \quad (\text{D.3})$$

with coefficients,

D. Presentation of kernel coefficients

$$\begin{aligned}
\mathcal{K}_{00}^{(4)} &= \gamma_2^2 \frac{b_{s2} S}{k_1^2 k_2^2} + b_1 \gamma_2 \left[F \frac{(k_1^2 + k_2^2) \beta_6}{k_1^2 k_2^2 k_3^2} + G \frac{(k_1^2 + k_2^2) \beta_7}{k_1^2 k_2^2 k_3^2} + \frac{(k_1^2 + k_2^2) \beta_{11} \mu}{k_1^3 k_2^3} \right. \\
&\quad \left. + \frac{(k_1^2 + k_2^2)^2 \beta_{12}}{k_1^4 k_2^4} \right] + b_1 \gamma_2^2 \frac{(1 + F)}{k_1^2 k_2^2} + b_1^2 \frac{(\beta_1 + E \beta_2)}{k_1^2 k_2^2} \\
\mathcal{K}_{02}^{(4)} &= \gamma_1 \gamma_2 \left[\frac{\beta_{14}}{k_1^4} + \frac{\beta_{15} \mu}{k_1^3 k_2} + \frac{\beta_{16}}{k_1^2 k_2^2} - G \frac{\beta_{19}}{k_1^2 k_2^2} \right] - f \gamma_2 \left[F \frac{\beta_6}{k_1^2 k_3^2} + G \frac{\beta_7}{k_1^2 k_3^2} + \frac{\beta_{11} \mu}{k_1^3 k_2} \right. \\
&\quad \left. + \frac{(k_1^2 + k_2^2) \beta_{12}}{k_1^4 k_2^2} \right] - b_1 f \frac{(\beta_1 + E \beta_2 + \gamma_2^2)}{k_1^2 k_2^2} - b_1 \gamma_1 \frac{(\beta_4 - \beta_3 + E \beta_5)}{k_1^2 k_2^2} \\
&\quad - b_1 \gamma_2 \left[\frac{(k_1^2 + k_2^2) \beta_9}{k_1^4 k_2^2} + E \frac{(k_1^2 + k_2^2) \beta_{10}}{k_1^4 k_2^2} + \frac{\beta_{13}}{k_1^4} \right] \\
\mathcal{K}_{04}^{(4)} &= -\gamma_1 \gamma_2 \frac{\beta_{17}}{k_1^4} + f \gamma_2 \frac{(\beta_9 + E \beta_{10} + \beta_{13})}{k_1^4} \\
\mathcal{K}_{11}^{(4)} &= \gamma_1^2 \left[F \frac{\beta_6}{k_1 k_2 k_3^2} + G \frac{\beta_7}{k_1 k_2 k_3^2} + \frac{\beta_{11} \mu}{k_1^2 k_2^2} + \frac{(k_1^2 + k_2^2) \beta_{12}}{k_1^3 k_2^3} \right] - \gamma_2^2 f \frac{2G}{k_1 k_2 k_3^2} \\
&\quad + \gamma_1 \gamma_2 \left[\frac{(k_1^2 + k_2^2) \beta_{14}}{k_1^3 k_2^3} + 2 \frac{\beta_{15} \mu}{k_1^2 k_2^2} + \frac{(k_1^2 + k_2^2) \beta_{16}}{k_1^3 k_2^3} - 2G \frac{\beta_{19}}{k_1 k_2 k_3^2} \right] \\
&\quad - b_1 \gamma_1 \frac{(k_1^2 + k_2^2) (\beta_4 - \beta_3 + E \beta_5)}{k_1^3 k_2^3} - b_1 \gamma_2 \left[\frac{(k_1^2 + k_2^2) \beta_8}{k_1^3 k_2^3} \right. \\
&\quad \left. + 2 \frac{(k_1^2 + k_2^2) \beta_9}{k_1^3 k_2^3} + 2E \frac{(k_1^2 + k_2^2) \beta_{10}}{k_1^3 k_2^3} \right] - b_1 f \gamma_2^2 \frac{(k_1^2 + k_2^2)}{k_1^3 k_2^3} \\
\mathcal{K}_{13}^{(4)} &= f^2 \frac{\gamma_2^2}{k_1^3 k_2} + f \gamma_1 \frac{(\beta_4 - \beta_3 + E \beta_5)}{k_1^3 k_2} + f \gamma_2 \frac{(\beta_8 + 2\beta_9 + 2E\beta_{10})}{k_1^3 k_2} \\
&\quad - \gamma_1^2 \frac{(\beta_9 + E \beta_{10} + \beta_{13})}{k_1^3 k_2} - \gamma_1 \gamma_2 \frac{(\beta_{17} + \beta_{18})}{k_1^3 k_2} \\
\mathcal{K}_{20}^{(4)} &= \gamma_1 \gamma_2 \left[\frac{\beta_{14}}{k_2^4} + \frac{\beta_{15} \mu}{k_1 k_2^3} + \frac{\beta_{16}}{k_1^2 k_2^2} - G \frac{\beta_{19}}{k_2^2 k_3^2} \right] - f \gamma_2 \left[F \frac{\beta_6}{k_2^2 k_3^2} + G \frac{\beta_7}{k_2^2 k_3^2} + \frac{\beta_{11} \mu}{k_1 k_2^3} \right. \\
&\quad \left. + \frac{(k_1^2 + k_2^2) \beta_{12}}{k_1^2 k_2^4} \right] - f \gamma_2^2 \frac{G}{k_2^2 k_3^2} - b_1 \gamma_1 \frac{(\beta_4 - \beta_3 + E \beta_5)}{k_1^2 k_2^2} - b_1 \gamma_2 \left[\frac{(k_1^2 + k_2^2) \beta_9}{k_1^2 k_2^4} \right. \\
&\quad \left. + E \frac{(k_1^2 + k_2^2) \beta_{10}}{k_1^2 k_2^4} + \frac{(k_1^2 + k_2^2) \beta_{13}}{k_1^2 k_2^4} \right] + b_1 f \frac{(\beta_1 - E \beta_2 - \gamma_2^2)}{k_1^2 k_2^2} \\
\mathcal{K}_{22}^{(4)} &= -\gamma_1^2 \frac{(\beta_8 + 2\beta_9 + 2E\beta_{10})}{k_1^2 k_2^2} - \gamma_1 \gamma_2 \frac{2\beta_{18}}{k_1^2 k_2^2} + f \gamma_1 \frac{2(\beta_4 - \beta_3 + E \beta_5)}{k_1^2 k_2^2} \\
&\quad + f \gamma_2 \frac{2(\beta_9 + E \beta_{10} + \beta_{13})}{k_1^2 k_2^2} + f^2 \frac{(\beta_1 + E \beta_2 + 2\gamma_2^2)}{k_1^2 k_2^2} \\
\mathcal{K}_{31}^{(4)} &= f^2 \frac{\gamma_2^2}{k_1 k_2^3} + f \gamma_1 \frac{(\beta_4 - \beta_3 + E \beta_5)}{k_1 k_2^3} + f \gamma_2 \frac{(\beta_8 + 2\beta_9 + 2E\beta_{10})}{k_1 k_2^3} \\
&\quad - \gamma_1^2 \frac{(\beta_9 + E \beta_{10} + \beta_{13})}{k_1 k_2^3} - \gamma_1 \gamma_2 \frac{(\beta_{17} + \beta_{18})}{k_1 k_2^3}
\end{aligned}$$

D. Presentation of kernel coefficients

$$\mathcal{K}_{40}^{(4)} = -\gamma_1 \gamma_2 \frac{\beta_{17}}{k_2^4} + f \gamma_2 \frac{(\beta_9 + E\beta_{10} + \beta_{13})}{k_2^4}.$$

$$\mathcal{K}_{ab}^{(5)} = \begin{pmatrix} \circ & \bullet & \circ & \bullet & \circ & \circ \\ \bullet & \circ & \bullet & \circ & \circ & \circ \\ \circ & \bullet & \circ & \circ & \circ & \circ \\ \bullet & \circ & \circ & \circ & \circ & \circ \\ \circ & \circ & \circ & \circ & \circ & \circ \\ \circ & \circ & \circ & \circ & \circ & \circ \end{pmatrix}, \quad (\text{D.4})$$

with coefficients,

$$\begin{aligned} \mathcal{K}_{01}^{(5)} &= \gamma_1 \gamma_2 \left[\frac{(F\beta_6 + G\beta_7)}{k_1^2 k_2 k_3^2} + \frac{\beta_{11}\mu}{k_1^3 k_2^2} + \frac{(k_1^2 + k_2^2)\beta_{12}}{k_1^4 k_2^3} \right] + \gamma_2^2 \left[\frac{\beta_{14}}{k_1^4 k_2} + \frac{\beta_{15}\mu}{k_1^3 k_2^2} + \frac{\beta_{16}}{k_1^2 k_2^3} \right. \\ &\quad \left. - G \frac{\beta_{19}}{k_1^2 k_2 k_3^2} \right] + b_1 \gamma_1 \frac{(\beta_1 + E\beta_2)}{k_1^2 k_2^3} - b_1 \gamma_2 \frac{(k_1^2 + k_2^2)(\beta_4 - \beta_3 + E\beta_5)}{k_1^4 k_2^3} \\ \mathcal{K}_{03}^{(5)} &= -\gamma_1 \gamma_2 \frac{(\beta_9 + E\beta_{10} + \beta_{13})}{k_1^4 k_2} - \gamma_2^2 \frac{\beta_{17}}{k_1^4 k_2} + f \gamma_2 \frac{(\beta_4 - \beta_3 + E\beta_5)}{k_1^4 k_2} \\ \mathcal{K}_{10}^{(5)} &= \gamma_1 \gamma_2 \left[\frac{(F\beta_6 + G\beta_7)}{k_1 k_2^2 k_3^2} + \frac{\beta_{11}\mu}{k_1^2 k_2^3} + \frac{(k_1^2 + k_2^2)\beta_{12}}{k_1^3 k_2^4} \right] + \gamma_2^2 \left[\frac{\beta_{14}}{k_1 k_2^4} + \frac{\beta_{15}\mu}{k_1^2 k_2^3} + \frac{\beta_{16}}{k_1^3 k_2^2} \right. \\ &\quad \left. - G \frac{\beta_{19}}{k_1 k_2^2 k_3^2} \right] + b_1 \gamma_1 \frac{(\beta_1 + E\beta_2)}{k_1^3 k_2^2} - b_1 \gamma_2 \frac{(k_1^2 + k_2^2)(\beta_4 - \beta_3 + E\beta_5)}{k_1^3 k_2^4} \\ \mathcal{K}_{12}^{(5)} &= -\gamma_1^2 \frac{(\beta_4 - \beta_3 + E\beta_5)}{k_1^3 k_2^2} - \gamma_2^2 \frac{\beta_{18}}{k_1^3 k_2^2} - \gamma_1 \gamma_2 \frac{(\beta_8 + 3\beta_9 + 3E\beta_{10} + \beta_{13})}{k_1^3 k_2^2} \\ &\quad - f \gamma_1 \frac{(\beta_1 + E\beta_2)}{k_1^3 k_2^2} + f \gamma_2 \frac{(\beta_4 - \beta_3 + E\beta_5)}{k_1^3 k_2^2} \\ \mathcal{K}_{21}^{(5)} &= -\gamma_1^2 \frac{(\beta_4 - \beta_3 + E\beta_5)}{k_1^2 k_2^3} - \gamma_2^2 \frac{\beta_{18}}{k_1^2 k_2^3} - \gamma_1 \gamma_2 \frac{(\beta_8 + 3\beta_9 + 3E\beta_{10} + \beta_{13})}{k_1^2 k_2^3} \\ &\quad - f \gamma_1 \frac{(\beta_1 + E\beta_2)}{k_1^2 k_2^3} + f \gamma_2 \frac{[\beta_4 - \beta_3 + E\beta_5]}{k_1^2 k_2^3} \\ \mathcal{K}_{30}^{(5)} &= -\gamma_1 \gamma_2 \frac{(\beta_9 + E\beta_{10} + \beta_{13})}{k_1 k_2^4} - \gamma_2^2 \frac{\beta_{17}}{k_1 k_2^4} + f \gamma_2 \frac{(\beta_4 - \beta_3 + E\beta_5)}{k_1 k_2^4}. \end{aligned}$$

D. Presentation of kernel coefficients

$$\mathcal{K}_{ab}^{(6)} = \begin{pmatrix} \bullet & \circ & \bullet & \circ & \circ & \circ \\ \circ & \bullet & \circ & \circ & \circ & \circ \\ \bullet & \circ & \circ & \circ & \circ & \circ \\ \circ & \circ & \circ & \circ & \circ & \circ \\ \circ & \circ & \circ & \circ & \circ & \circ \\ \circ & \circ & \circ & \circ & \circ & \circ \end{pmatrix}, \quad (\text{D.5})$$

with coefficients,

$$\begin{aligned} \mathcal{K}_{00}^{(6)} &= \gamma_2^2 \left[\frac{(F\beta_6 + G\beta_7)}{k_1^2 k_2^2 k_3^2} + \frac{\beta_{11}\mu}{k_1^3 k_2^3} + \frac{(k_1^2 + k_2^2)\beta_{12}}{k_1^4 k_2^4} \right] + b_1 \gamma_2 \frac{(k_1^2 + k_2^2)(\beta_1 + E\beta_2)}{k_1^4 k_2^4} \\ \mathcal{K}_{02}^{(6)} &= -\gamma_1 \gamma_2 \frac{(\beta_4 - \beta_3 + E\beta_5)}{k_1^4 k_2^2} - \gamma_2^2 \frac{(\beta_9 + E\beta_{10} + \beta_{13})}{k_1^4 k_2^2} - f \gamma_2 \frac{(\beta_1 + E\beta_2)}{k_1^4 k_2^2} \\ \mathcal{K}_{11}^{(6)} &= \gamma_1^2 \frac{(\beta_1 + E\beta_2)}{k_1^3 k_2^3} - 2\gamma_1 \gamma_2 \frac{\beta_4 - \beta_3 + E\beta_5}{k_1^3 k_2^3} - \gamma_2^2 \frac{(\beta_8 + 2\beta_9 + 2E\beta_{10})}{k_1^3 k_2^3} \\ \mathcal{K}_{20}^{(6)} &= -\gamma_1 \gamma_2 \frac{(\beta_4 - \beta_3 + E\beta_5)}{k_1^2 k_2^4} - \gamma_2^2 \frac{(\beta_9 + E\beta_{10} + \beta_{13})}{k_1^2 k_2^4} - f \gamma_2 \frac{(\beta_1 + E\beta_2)}{k_1^2 k_2^4}. \end{aligned}$$

$$\mathcal{K}_{ab}^{(7)} = \begin{pmatrix} \circ & \bullet & \circ & \circ & \circ & \circ \\ \bullet & \circ & \circ & \circ & \circ & \circ \\ \circ & \circ & \circ & \circ & \circ & \circ \\ \circ & \circ & \circ & \circ & \circ & \circ \\ \circ & \circ & \circ & \circ & \circ & \circ \\ \circ & \circ & \circ & \circ & \circ & \circ \end{pmatrix}, \quad (\text{D.6})$$

with coefficients,

$$\begin{aligned} \mathcal{K}_{01}^{(7)} &= \gamma_1 \gamma_2 \frac{(\beta_1 + E\beta_2)}{k_1^4 k_2^3} - \gamma_2^2 \frac{(\beta_4 - \beta_3 + E\beta_5)}{k_1^4 k_2^3} \\ \mathcal{K}_{10}^{(7)} &= \gamma_1 \gamma_2 \frac{(\beta_1 + E\beta_2)}{k_1^3 k_2^4} - \gamma_2^2 \frac{(\beta_4 - \beta_3 + E\beta_5)}{k_1^3 k_2^4}. \end{aligned}$$

D. Presentation of kernel coefficients

$$\mathcal{K}_{ab}^{(8)} = \begin{pmatrix} \bullet & \circ & \circ & \circ & \circ & \circ \\ \circ & \circ & \circ & \circ & \circ & \circ \\ \circ & \circ & \circ & \circ & \circ & \circ \\ \circ & \circ & \circ & \circ & \circ & \circ \\ \circ & \circ & \circ & \circ & \circ & \circ \\ \circ & \circ & \circ & \circ & \circ & \circ \end{pmatrix}, \quad (\text{D.7})$$

with coefficient

$$\mathcal{K}_{00}^{(8)} = \gamma_2^2 \frac{(\beta_1 + E\beta_2)}{k_1^4 k_2^4}.$$

E. Squeezed limit of multipoles

These are the leading contributions to the squeezed limits for the multipoles – up to $O(\mathcal{H}/k)$ and $\ell = 3$.

$$B_{0,0} = -2\sqrt{\pi} \frac{P_L P_S}{105} \left[f^4 + \left(-3b_1 - \frac{15}{7} \right) f^3 + (-77b_1^2 - 33b_1 - 14b_2 + \frac{14}{3}b_{s^2}) f^2 - 105 \left(b_1^2 + \frac{31}{21}b_1 + \frac{4}{3}b_2 - \frac{4}{9}b_{s^2} \right) b_1 f - 195b_1^2 \left(b_1 + \frac{14b_2}{13} - \frac{14b_{s^2}}{39} \right) \right] \quad (\text{E.1})$$

$$B_{1,1} = \sqrt{6\pi} \frac{P_L P_S}{105 k_L} \left\{ \gamma_1 f^3 + \left(18b_1\gamma_1 - 9\beta_{14} + 6\beta_{16} - 5\beta_{17} + 2\beta_{18} + \frac{15}{7}\gamma_1 \right) f^2 + \left[49\gamma_1 b_1^2 + (-42\beta_{14} + 56\beta_{16} - 24\beta_{17} + 12\beta_{18} + 18\gamma_1) b_1 + 14\gamma_1 \left(b_2 - \frac{b_{s^2}}{3} \right) \right] f - 35 \left[\left(\beta_{14} - 2\beta_{16} + \frac{3\beta_{17}}{5} - \frac{2\beta_{18}}{5} - \frac{13\gamma_1}{7} \right) b_1 - 2\gamma_1 \left(b_2 - \frac{b_{s^2}}{3} \right) \right] b_1 \right\} \quad (\text{E.2})$$

$$B_{2,0} = -4\sqrt{5\pi} f \frac{P_L P_S}{1155} \left[f^3 + \left(-\frac{55}{14} - \frac{11b_1}{2} \right) f^2 + \left(-110b_1^2 - \frac{429}{7}b_1 - 11b_2 + \frac{11}{3}b_{s^2} \right) f - 231 \frac{b_1}{2} \left(b_1^2 + \frac{23}{21}b_1 + \frac{2}{3}b_2 - \frac{2}{9}b_{s^2} \right) \right] \quad (\text{E.3})$$

$$B_{2,2} = 2\sqrt{30\pi} f \frac{P_L P_S}{1155} \left[f^3 + \left(-\frac{11b_1}{6} - \frac{55}{42} \right) f^2 + \left(-44b_1^2 - \frac{99}{7}b_1 - 11b_2 + \frac{11}{3}b_{s^2} \right) f - 77 \frac{b_1}{2} \left(b_1^2 + \frac{13}{7}b_1 + 2b_2 - \frac{2}{3}b_{s^2} \right) \right] \quad (\text{E.4})$$

$$B_{3,1} = \sqrt{21\pi} \frac{P_L P_S}{165 k_L} \left\{ \gamma_1 f^3 + \left[\frac{418}{21}b_1\gamma_1 - \frac{33}{7}\beta_{14} + \frac{22}{7}\beta_{16} - 5\beta_{17} + 2\beta_{18} + \frac{440}{147}\gamma_1 \right] f^2 + \left[\frac{143\gamma_1 b_1^2}{7} + \left(-\frac{99\beta_{14}}{7} + \frac{22\beta_{16}}{7} - \frac{77\beta_{17}}{3} + \frac{242\beta_{18}}{21} + \frac{792\gamma_1}{49} \right) b_1 + \frac{88\gamma_1}{7} \left(b_2 - \frac{b_{s^2}}{3} \right) \right] f - b_1^2 \frac{132}{7} \left(\beta_{17} - \frac{2\beta_{18}}{3} \right) \right\} \quad (\text{E.5})$$

E. Squeezed limit of multipoles

$$B_{3,3} = -f\sqrt{35\pi}\frac{P_L P_S}{1155k_L} \left[\gamma_1 f^2 + \left(\frac{22b_1\gamma_1}{3} - 5\beta_{17} + 2\beta_{18} - 11\beta_{14} + \frac{22\beta_{16}}{3} \right) f \right. \\ \left. - 11 \left(-3b_1\gamma_1 + \beta_{17} - \frac{2\beta_{18}}{3} + 3\beta_{14} - 6\beta_{16} \right) b_1 \right] \quad (\text{E.6})$$

Bibliography

- [1] N. S. Team, *Matter and energy in the universe*, 2014.
- [2] ESA and C. Carreau, *Planck history of universe zoom*, 2013.
- [3] A. H. Guth, *The Inflationary Universe: A Possible Solution to the Horizon and Flatness Problems*, *Phys. Rev. D* **23** (1981) 347.
- [4] A. D. Linde, *A New Inflationary Universe Scenario: A Possible Solution of the Horizon, Flatness, Homogeneity, Isotropy and Primordial Monopole Problems*, *Phys. Lett. B* **108** (1982) 389.
- [5] A. Albrecht and P. J. Steinhardt, *Cosmology for Grand Unified Theories with Radiatively Induced Symmetry Breaking*, *Phys. Rev. Lett.* **48** (1982) 1220.
- [6] ESA and the Planck collaboration, *Planck cmb*, 2013.
- [7] V. Springel et al., *Simulating the joint evolution of quasars, galaxies and their large-scale distribution*, *Nature* **435** (2005) 629 [[astro-ph/0504097](#)].
- [8] PLANCK collaboration, N. Aghanim et al., *Planck 2018 results. VI. Cosmological parameters*, [1807.06209](#).
- [9] PLANCK collaboration, Y. Akrami et al., *Planck 2018 results. IX. Constraints on primordial non-Gaussianity*, *Astron. Astrophys.* **641** (2020) A9 [[1905.05697](#)].
- [10] C. L. Bennett, D. Larson, J. L. Weiland, N. Jarosik, G. Hinshaw, N. Odegard et al., *Nine-year wilkinson microwave anisotropy probe (wmap) observations: Final maps and results*, *The Astrophysical Journal Supplement Series* **208** (2013) 20.
- [11] S. Das et al., *The Atacama Cosmology Telescope: temperature and gravitational lensing power spectrum measurements from three seasons of data*, *JCAP* **04** (2014) 014 [[1301.1037](#)].
- [12] E. M. George et al., *A measurement of secondary cosmic microwave background anisotropies from the 2500-square-degree SPT-SZ survey*, *Astrophys. J.* **799** (2015) 177 [[1408.3161](#)].

Bibliography

- [13] BOSS collaboration, S. Alam et al., *The clustering of galaxies in the completed SDSS-III Baryon Oscillation Spectroscopic Survey: cosmological analysis of the DR12 galaxy sample*, *Mon. Not. Roy. Astron. Soc.* **470** (2017) 2617 [[1607.03155](#)].
- [14] A. J. Ross, L. Samushia, C. Howlett, W. J. Percival, A. Burden and M. Manera, *The clustering of the SDSS DR7 main Galaxy sample – I. A 4 per cent distance measure at $z = 0.15$* , *Mon. Not. Roy. Astron. Soc.* **449** (2015) 835 [[1409.3242](#)].
- [15] A. Oka, S. Saito, T. Nishimichi, A. Taruya and K. Yamamoto, *Simultaneous constraints on the growth of structure and cosmic expansion from the multipole power spectra of the SDSS DR7 LRG sample*, *Mon. Not. Roy. Astron. Soc.* **439** (2014) 2515 [[1310.2820](#)].
- [16] A. G. Sánchez, C. M. Baugh, W. J. Percival, J. A. Peacock, N. D. Padilla, S. Cole et al., *Cosmological parameters from cosmic microwave background measurements and the final 2dF Galaxy Redshift Survey power spectrum*, *MNRAS* **366** (2006) 189 [[astro-ph/0507583](#)].
- [17] F. Beutler, C. Blake, M. Colless, D. H. Jones, L. Staveley-Smith, L. Campbell et al., *The 6df galaxy survey: baryon acoustic oscillations and the local hubble constant*, *Monthly Notices of the Royal Astronomical Society* **416** (2011) 3017–3032.
- [18] E. A. Kazin et al., *The WiggleZ Dark Energy Survey: improved distance measurements to $z = 1$ with reconstruction of the baryonic acoustic feature*, *Mon. Not. Roy. Astron. Soc.* **441** (2014) 3524 [[1401.0358](#)].
- [19] SUPERNOVA SEARCH TEAM collaboration, A. G. Riess et al., *Observational evidence from supernovae for an accelerating universe and a cosmological constant*, *Astron. J.* **116** (1998) 1009 [[astro-ph/9805201](#)].
- [20] SUPERNOVA COSMOLOGY PROJECT collaboration, S. Perlmutter et al., *Measurements of Ω and Λ from 42 high redshift supernovae*, *Astrophys. J.* **517** (1999) 565 [[astro-ph/9812133](#)].
- [21] W. L. Freedman, B. F. Madore, V. Scowcroft, C. Burns, A. Monson, S. E. Persson et al., *Carnegie hubble program: A mid-infrared calibration of the hubble constant*, *The Astrophysical Journal* **758** (2012) 24.
- [22] A. G. Riess et al., *A 2.4% Determination of the Local Value of the Hubble Constant*, *Astrophys. J.* **826** (2016) 56 [[1604.01424](#)].
- [23] N. Suzuki, D. Rubin, C. Lidman, G. Aldering, R. Amanullah, K. Barbary et al., *The hubble space telescope cluster supernova survey. v. improving the dark-energy constraints above $z > 1$ and building an early-type-hosted supernova sample*, *The Astrophysical Journal* **746** (2012) 85.

Bibliography

- [24] SDSS collaboration, M. Betoule et al., *Improved cosmological constraints from a joint analysis of the SDSS-II and SNLS supernova samples*, *Astron. Astrophys.* **568** (2014) A22 [1401.4064].
- [25] DES collaboration, M. A. Troxel et al., *Dark Energy Survey Year 1 results: Cosmological constraints from cosmic shear*, *Phys. Rev. D* **98** (2018) 043528 [1708.01538].
- [26] C. Heymans et al., *CFHTLenS tomographic weak lensing cosmological parameter constraints: Mitigating the impact of intrinsic galaxy alignments*, *Mon. Not. Roy. Astron. Soc.* **432** (2013) 2433 [1303.1808].
- [27] BOSS collaboration, F. Beutler et al., *The clustering of galaxies in the completed SDSS-III Baryon Oscillation Spectroscopic Survey: Anisotropic galaxy clustering in Fourier-space*, *Mon. Not. Roy. Astron. Soc.* **466** (2017) 2242 [1607.03150].
- [28] BOSS collaboration, J. N. Grieb et al., *The clustering of galaxies in the completed SDSS-III Baryon Oscillation Spectroscopic Survey: Cosmological implications of the Fourier space wedges of the final sample*, *Mon. Not. Roy. Astron. Soc.* **467** (2017) 2085 [1607.03143].
- [29] E. P. Hubble, *Extragalactic nebulae.*, *Astrophysical Journal* **64** (1926) 321.
- [30] E. Hubble, *The Distribution of Extra-Galactic Nebulae*, *Astrophysical Journal* **79** (1934) 8.
- [31] C. Shane and C. Wirtanen, *The distribution of galaxies*. The University of California, 1967.
- [32] F. Zwicky, E. Herzog, P. Wild, M. Karpowicz and C. T. Kowal, *Catalogue of galaxies and of clusters of galaxies*, Vol. I. 1961.
- [33] P. J. E. Peebles, *Statistical Analysis of Catalogs of Extragalactic Objects. I. Theory*, *Astrophysical Journal* **185** (1973) 413.
- [34] Y. B. Zel'Dovich, *Reprint of 1970A&A.....5...84Z. Gravitational instability: an approximate theory for large density perturbations.*, *Astronomy and Astrophysics* **500** (1970) 13.
- [35] M. Davis, E. J. Groth and P. J. E. Peebles, *Study of galaxy correlations: evidence for the gravitational instability picture in a dense universe.*, *Astrophysical Journal, Part 2 - Letters to the Editor* **212** (1977) L107.
- [36] M. Davis and P. J. E. Peebles, *On the integration of the BBGKY equations for the development of strongly nonlinear clustering in an expanding universe.*, *Astrophysical Journal Supplement Series* **34** (1977) 425.
- [37] M. Davis and P. J. E. Peebles, *A survey of galaxy redshifts. V. The two-point position and velocity correlations.*, *Astrophysical Journal* **267** (1983) 465.

Bibliography

- [38] P. J. E. Peebles, *The large-scale structure of the universe*. 1980.
- [39] S. J. Maddox, G. Efstathiou, W. J. Sutherland and J. Loveday, *Galaxy correlations on large scales.*, *MNRAS* **242** (1990) 43.
- [40] D. J. Baumgart and J. N. Fry, *Fourier Spectra of Three-dimensional Data*, *Astrophysical Journal* **375** (1991) 25.
- [41] C. Park, I. Gott, J. R. and L. N. da Costa, *Large-Scale Structure in the Southern Sky Redshift Survey*, *Astrophysical Journal Letters* **392** (1992) L51.
- [42] M. Davis, G. Efstathiou, C. S. Frenk and S. D. M. White, *The evolution of large-scale structure in a universe dominated by cold dark matter*, *Astrophysical Journal* **292** (1985) 371.
- [43] M. J. Rees, *Mechanisms for biased galaxy formation*, *MNRAS* **213** (1985) 75P.
- [44] S. Cole and N. Kaiser, *Biased clustering in the cold dark matter cosmogony*, *Mon. Not. Roy. Astron. Soc.* **237** (1989) 1127.
- [45] N. Kaiser, *On the spatial correlations of Abell clusters.*, *Astrophysical Journal* **284** (1984) L9.
- [46] N. Kaiser, *Clustering in real space and in redshift space*, *Mon. Not. Roy. Astron. Soc.* **227** (1987) 1.
- [47] A. J. S. Hamilton, *Measuring Omega and the real correlation function from the redshift correlation function*, *Astrophys. J. Lett.* **385** (1992) L5.
- [48] S. Cole, K. B. Fisher and D. H. Weinberg, *Constraints on Omega from the IRAS redshift surveys*, *Mon. Not. Roy. Astron. Soc.* **275** (1995) 515 [[astro-ph/9412062](#)].
- [49] J. Loveday, G. Efstathiou, S. J. Maddox and B. A. Peterson, *The Stromlo - APM redshift survey. 3. Redshift space distortion, omega and bias*, *Astrophys. J.* **468** (1996) 1 [[astro-ph/9505099](#)].
- [50] H. Tadros et al., *Spherical harmonic analysis of the pscz galaxy catalogue: redshift distortions and the real-space power spectrum*, *Mon. Not. Roy. Astron. Soc.* **305** (1999) 527 [[astro-ph/9901351](#)].
- [51] S. collaboration, *Sdss cosmology*, 2018.
- [52] 2DFGRS collaboration, M. Colless et al., *The 2dF Galaxy Redshift Survey: Spectra and redshifts*, *Mon. Not. Roy. Astron. Soc.* **328** (2001) 1039 [[astro-ph/0106498](#)].
- [53] SDSS collaboration, D. G. York et al., *The Sloan Digital Sky Survey: Technical Summary*, *Astron. J.* **120** (2000) 1579 [[astro-ph/0006396](#)].

Bibliography

- [54] K. S. Dawson, D. J. Schlegel, C. P. Ahn, S. F. Anderson, E. Aubourg, S. Bailey et al., *The baryon oscillation spectroscopic survey of sdss-iii*, *The Astronomical Journal* **145** (2012) 10.
- [55] C. Blake, E. A. Kazin, F. Beutler, T. M. Davis, D. Parkinson, S. Brough et al., *The wigglez dark energy survey: mapping the distance-redshift relation with baryon acoustic oscillations*, *Monthly Notices of the Royal Astronomical Society* **418** (2011) 1707–1724.
- [56] C. Blake, S. Brough, M. Colless, C. Contreras, W. Couch, S. Croom et al., *The wigglez dark energy survey: the growth rate of cosmic structure since redshift $z=0.9$* , *Monthly Notices of the Royal Astronomical Society* **415** (2011) 2876–2891.
- [57] K. S. Dawson et al., *The SDSS-IV extended Baryon Oscillation Spectroscopic Survey: Overview and Early Data*, *Astron. J.* **151** (2016) 44 [[1508.04473](#)].
- [58] DES collaboration, H. T. Diehl et al., *The Dark Energy Survey and Operations: Year 1*, *Proc. SPIE Int. Soc. Opt. Eng.* **9149** (2014) 91490V.
- [59] G. J. Hill, K. Gebhardt, E. Komatsu, N. Drory, P. J. MacQueen, J. Adams et al., *The Hobby-Eberly Telescope Dark Energy Experiment (HETDEX): Description and Early Pilot Survey Results*, in *Panoramic Views of Galaxy Formation and Evolution* (T. Kodama, T. Yamada and K. Aoki, eds.), vol. 399 of *Astronomical Society of the Pacific Conference Series*, p. 115, Oct, 2008, 0806.0183.
- [60] J. Lesgourgues, *The cosmic linear anisotropy solving system (class) i: Overview*, 2011.
- [61] A. Lewis, A. Challinor and A. Lasenby, *Efficient computation of CMB anisotropies in closed FRW models*, *Astrophys. J.* **538** (2000) 473 [[astro-ph/9911177](#)].
- [62] F. Bernardeau, S. Colombi, E. Gaztañaga and R. Scoccimarro, *Large-scale structure of the universe and cosmological perturbation theory*, *Physics Reports* **367** (2002) 1–248.
- [63] M. H. Goroff, B. Grinstein, S. J. Rey and M. B. Wise, *Coupling of Modes of Cosmological Mass Density Fluctuations*, *Astrophys. J.* **311** (1986) 6.
- [64] B. Jain and E. Bertschinger, *Second order power spectrum and nonlinear evolution at high redshift*, *Astrophys. J.* **431** (1994) 495 [[astro-ph/9311070](#)].
- [65] A. Lewis, *The real shape of non-gaussianities*, *Journal of Cosmology and Astroparticle Physics* **2011** (2011) 026–026.
- [66] R. Scoccimarro, E. Sefusatti and M. Zaldarriaga, *Probing primordial non-Gaussianity with large - scale structure*, *Phys. Rev. D* **69** (2004) 103513 [[astro-ph/0312286](#)].

Bibliography

- [67] E. Sefusatti and E. Komatsu, *The Bispectrum of Galaxies from High-Redshift Galaxy Surveys: Primordial Non-Gaussianity and Non-Linear Galaxy Bias*, *Phys. Rev. D* **76** (2007) 083004 [[0705.0343](#)].
- [68] Y.-S. Song, A. Taruya and A. Oka, *Cosmology with anisotropic galaxy clustering from the combination of power spectrum and bispectrum*, *JCAP* **08** (2015) 007 [[1502.03099](#)].
- [69] M. Tellarini, A. J. Ross, G. Tasinato and D. Wands, *Galaxy bispectrum, primordial non-gaussianity and redshift space distortions*, *Journal of Cosmology and Astroparticle Physics* **2016** (2016) 014–014.
- [70] D. Yamauchi, S. Yokoyama and K. Takahashi, *Multitracer technique for galaxy bispectrum: An application to constraints on nonlocal primordial non-Gaussianities*, *Phys. Rev. D* **95** (2017) 063530 [[1611.03590](#)].
- [71] D. Karagiannis, A. Lazanu, M. Liguori, A. Raccanelli, N. Bartolo and L. Verde, *Constraining primordial non-gaussianity with bispectrum and power spectrum from upcoming optical and radio surveys*, *Monthly Notices of the Royal Astronomical Society* **478** (2018) 1341–1376.
- [72] D. Yamauchi, S. Yokoyama and H. Tashiro, *Constraining modified theories of gravity with the galaxy bispectrum*, *Phys. Rev. D* **96** (2017) 123516 [[1709.03243](#)].
- [73] R. Scoccimarro, H. A. Feldman, J. N. Fry and J. A. Frieman, *The Bispectrum of IRAS redshift catalogs*, *Astrophys. J.* **546** (2001) 652 [[astro-ph/0004087](#)].
- [74] H. A. Feldman, J. A. Frieman, J. N. Fry and R. Scoccimarro, *Constraints on galaxy bias, matter density, and primordial non-gaussianity from the PSCz galaxy redshift survey*, *Phys. Rev. Lett.* **86** (2001) 1434 [[astro-ph/0010205](#)].
- [75] WiggleZ collaboration, F. A. Marin et al., *The WiggleZ Dark Energy Survey: constraining galaxy bias and cosmic growth with 3-point correlation functions*, *Mon. Not. Roy. Astron. Soc.* **432** (2013) 2654 [[1303.6644](#)].
- [76] H. Gil-Marín, C. Wagner, J. Noreña, L. Verde and W. Percival, *Dark matter and halo bispectrum in redshift space: theory and applications*, *JCAP* **12** (2014) 029 [[1407.1836](#)].
- [77] H. Gil-Marín, W. J. Percival, L. Verde, J. R. Brownstein, C.-H. Chuang, F.-S. Kitaura et al., *The clustering of galaxies in the SDSS-III Baryon Oscillation Spectroscopic Survey: RSD measurement from the power spectrum and bispectrum of the DR12 BOSS galaxies*, *Mon. Not. Roy. Astron. Soc.* **465** (2017) 1757 [[1606.00439](#)].
- [78] L. Verde et al., *The 2dF Galaxy Redshift Survey: The Bias of galaxies and the density of the Universe*, *Mon. Not. Roy. Astron. Soc.* **335** (2002) 432 [[astro-ph/0112161](#)].

Bibliography

- [79] E. Sefusatti, M. Crocce, S. Pueblas and R. Scoccimarro, *Cosmology and the Bispectrum*, *Phys. Rev. D* **74** (2006) 023522 [[astro-ph/0604505](#)].
- [80] J. Byun, A. Eggemeier, D. Regan, D. Seery and R. E. Smith, *Towards optimal cosmological parameter recovery from compressed bispectrum statistics*, *Mon. Not. Roy. Astron. Soc.* **471** (2017) 1581 [[1705.04392](#)].
- [81] D. Gualdi, H. Gil-Marín, R. L. Schuhmann, M. Manera, B. Joachimi and O. Lahav, *Enhancing BOSS bispectrum cosmological constraints with maximal compression*, *Mon. Not. Roy. Astron. Soc.* **484** (2019) 3713 [[1806.02853](#)].
- [82] A. Moradinezhad Dizgah, H. Lee, J. B. Muñoz and C. Dvorkin, *Galaxy Bispectrum from Massive Spinning Particles*, *JCAP* **05** (2018) 013 [[1801.07265](#)].
- [83] V. Yankelevich and C. Porciani, *Cosmological information in the redshift-space bispectrum*, *Mon. Not. Roy. Astron. Soc.* **483** (2019) 2078 [[1807.07076](#)].
- [84] M. Liguori, E. Sefusatti, J. R. Fergusson and E. P. S. Shellard, *Primordial non-Gaussianity and Bispectrum Measurements in the Cosmic Microwave Background and Large-Scale Structure*, *Adv. Astron.* **2010** (2010) 980523 [[1001.4707](#)].
- [85] J. R. Fergusson and E. P. S. Shellard, *The shape of primordial non-Gaussianity and the CMB bispectrum*, *Phys. Rev. D* **80** (2009) 043510 [[0812.3413](#)].
- [86] V. Desjacques, D. Jeong and F. Schmidt, *Large-Scale Galaxy Bias*, *Phys. Rept.* **733** (2018) 1 [[1611.09787](#)].
- [87] T. Baldauf, U. Seljak, V. Desjacques and P. McDonald, *Evidence for quadratic tidal tensor bias from the halo bispectrum*, *Physical Review D* **86** (2012) .
- [88] C. Clarkson, E. M. de Weerd, S. Jolicoeur, R. Maartens and O. Umeh, *The dipole of the galaxy bispectrum*, *Monthly Notices of the Royal Astronomical Society* **486** (2019) L101 [[1812.09512](#)].
- [89] P. McDonald, *Gravitational redshift and other redshift-space distortions of the imaginary part of the power spectrum*, *JCAP* **11** (2009) 026 [[0907.5220](#)].
- [90] A. Challinor and A. Lewis, *The linear power spectrum of observed source number counts*, *Phys. Rev. D* **84** (2011) 043516 [[1105.5292](#)].
- [91] A. Raccanelli, D. Bertacca, D. Jeong, M. C. Neyrinck and A. S. Szalay, *Doppler term in the galaxy two-point correlation function: wide-angle, velocity, Doppler lensing and cosmic acceleration effects*, *Phys. Dark Univ.* **19** (2018) 109 [[1602.03186](#)].

Bibliography

- [92] A. Hall and C. Bonvin, *Measuring cosmic velocities with 21 cm intensity mapping and galaxy redshift survey cross-correlation dipoles*, *Phys. Rev. D* **95** (2017) 043530 [[1609.09252](#)].
- [93] L. R. Abramo and D. Bertacca, *Disentangling the effects of doppler velocity and primordial non-gaussianity in galaxy power spectra*, *Physical Review D* **96** (2017) .
- [94] C. Bonvin, *Isolating relativistic effects in large-scale structure*, *Class. Quant. Grav.* **31** (2014) 234002 [[1409.2224](#)].
- [95] E. Di Dio and U. Seljak, *The relativistic dipole and gravitational redshift on LSS*, *JCAP* **04** (2019) 050 [[1811.03054](#)].
- [96] R. Scoccimarro, H. M. P. Couchman and J. A. Frieman, *The bispectrum as a signature of gravitational instability in redshift space*, *The Astrophysical Journal* **517** (1999) 531–540.
- [97] Y. Nan, K. Yamamoto and C. Hikage, *Higher multipoles of the galaxy bispectrum in redshift space*, *JCAP* **07** (2018) 038 [[1706.03515](#)].
- [98] D. Bertacca, *Observed galaxy number counts on the light cone up to second order: III. Magnification bias*, *Class. Quant. Grav.* **32** (2015) 195011 [[1409.2024](#)].
- [99] D. Bertacca, R. Maartens and C. Clarkson, *Observed galaxy number counts on the lightcone up to second order: I. Main result*, *JCAP* **09** (2014) 037 [[1405.4403](#)].
- [100] J. Yoo and M. Zaldarriaga, *Beyond the Linear-Order Relativistic Effect in Galaxy Clustering: Second-Order Gauge-Invariant Formalism*, *Phys. Rev. D* **90** (2014) 023513 [[1406.4140](#)].
- [101] E. Di Dio, R. Durrer, G. Marozzi and F. Montanari, *Galaxy number counts to second order and their bispectrum*, *JCAP* **12** (2014) 017 [[1407.0376](#)].
- [102] S. Jolicoeur, O. Umeh, R. Maartens and C. Clarkson, *Imprints of local lightcone \ projection effects on the galaxy bispectrum. Part II*, *JCAP* **09** (2017) 040 [[1703.09630](#)].
- [103] E. Di Dio, R. Durrer, R. Maartens, F. Montanari and O. Umeh, *The Full-Sky Angular Bispectrum in Redshift Space*, *JCAP* **04** (2019) 053 [[1812.09297](#)].
- [104] V. Tansella, C. Bonvin, R. Durrer, B. Ghosh and E. Sellentin, *The full-sky relativistic correlation function and power spectrum of galaxy number counts. Part I: theoretical aspects*, *JCAP* **03** (2018) 019 [[1708.00492](#)].
- [105] L. Verde, A. F. Heavens, S. Matarrese and L. Moscardini, *Large-scale bias in the universe - ii. redshift-space bispectrum*, *Monthly Notices of the Royal Astronomical Society* **300** (1998) 747–756.

Bibliography

- [106] E. Villa and C. Rampf, *Relativistic perturbations in λ cdm: Eulerian & lagrangian approaches*, *JCAP* **1601** (2016) 030 [[1505.04782](#)].
- [107] S. Jolicoeur, O. Umeh, R. Maartens and C. Clarkson, *Imprints of local lightcone projection effects on the galaxy bispectrum. Part III. Relativistic corrections from nonlinear dynamical evolution on large-scales*, *JCAP* **03** (2018) 036 [[1711.01812](#)].
- [108] O. Umeh, S. Jolicoeur, R. Maartens and C. Clarkson, *A general relativistic signature in the galaxy bispectrum: the local effects of observing on the lightcone*, *JCAP* **03** (2017) 034 [[1610.03351](#)].
- [109] S. Jolicoeur, A. Allahyari, C. Clarkson, J. Larena, O. Umeh and R. Maartens, *Imprints of local lightcone projection effects on the galaxy bispectrum IV: Second-order vector and tensor contributions*, *JCAP* **03** (2019) 004 [[1811.05458](#)].
- [110] O. Umeh, R. Maartens and M. Santos, *Nonlinear modulation of the HI power spectrum on ultra-large scales. I*, *JCAP* **03** (2016) 061 [[1509.03786](#)].
- [111] J. Fonseca, R. Maartens and M. G. Santos, *Synergies between intensity maps of hydrogen lines*, *Mon. Not. Roy. Astron. Soc.* **479** (2018) 3490 [[1803.07077](#)].
- [112] S. Camera, J. Fonseca, R. Maartens and M. G. Santos, *Optimized angular power spectra for spectroscopic galaxy surveys*, *Mon. Not. Roy. Astron. Soc.* **481** (2018) 1251 [[1803.10773](#)].
- [113] S. Jolicoeur, R. Maartens, E. M. De Weerd, O. Umeh, C. Clarkson and S. Camera, *Detecting the relativistic bispectrum in 21cm intensity maps*, [2009.06197](#).
- [114] R. Maartens, S. Jolicoeur, O. Umeh, E. M. De Weerd, C. Clarkson and S. Camera, *Detecting the relativistic galaxy bispectrum*, *JCAP* **2020** (2020) 065–065.
- [115] D. Jeong and F. Schmidt, *Parity-odd galaxy bispectrum*, *Phys. Rev. D* **102** (2020) 023530 [[1906.05198](#)].
- [116] D. Jeong, F. Schmidt and C. M. Hirata, *Large-scale clustering of galaxies in general relativity*, *Physical Review D* **85** (2012) .
- [117] C. Bonvin and R. Durrer, *What galaxy surveys really measure*, *Phys. Rev. D* **84** (2011) 063505 [[1105.5280](#)].
- [118] D. Alonso, P. Bull, P. G. Ferreira, R. Maartens and M. Santos, *Ultra large-scale cosmology in next-generation experiments with single tracers*, *Astrophys. J.* **814** (2015) 145 [[1505.07596](#)].

Bibliography

- [119] C. Bonvin, *Effect of Peculiar Motion in Weak Lensing*, *Phys. Rev. D* **78** (2008) 123530 [[0810.0180](#)].
- [120] K. Bolejko, C. Clarkson, R. Maartens, D. Bacon, N. Meures and E. Beynon, *Antilensing: The Bright Side of Voids*, *Phys. Rev. Lett.* **110** (2013) 021302 [[1209.3142](#)].
- [121] L. Pozzetti, C. M. Hirata, J. E. Geach, A. Cimatti, C. Baugh, O. Cucciati et al., *Modelling the number density of H emitters for future spectroscopic near-IR space missions*, *Astron. Astrophys.* **590** (2016) A3 [[1603.01453](#)].
- [122] R. Maartens, J. Fonseca, S. Camera, S. Jolicoeur, J.-A. Viljoen and C. Clarkson, *Magnification and evolution biases in large-scale structure surveys*, [2107.13401](#).
- [123] K. C. Chan and L. Blot, *Assessment of the Information Content of the Power Spectrum and Bispectrum*, *Phys. Rev. D* **96** (2017) 023528 [[1610.06585](#)].
- [124] VIRGO CONSORTIUM collaboration, R. E. Smith, J. A. Peacock, A. Jenkins, S. D. M. White, C. S. Frenk, F. R. Pearce et al., *Stable clustering, the halo model and nonlinear cosmological power spectra*, *Mon. Not. Roy. Astron. Soc.* **341** (2003) 1311 [[astro-ph/0207664](#)].
- [125] A. Oddo, E. Sefusatti, C. Porciani, P. Monaco and A. G. Sánchez, *Toward a robust inference method for the galaxy bispectrum: likelihood function and model selection*, *JCAP* **03** (2020) 056 [[1908.01774](#)].
- [126] H. Pan, D. Obreschkow, C. Howlett, C. d. P. Lagos, P. J. Elahi, C. Baugh et al., *Multi-wavelength consensus of large-scale linear bias*, [1909.12069](#).
- [127] EUCLID collaboration, A. Blanchard et al., *Euclid preparation: VII. Forecast validation for Euclid cosmological probes*, *Astron. Astrophys.* **642** (2020) A191 [[1910.09273](#)].
- [128] C. Bonvin, L. Hui and E. Gaztanaga, *Asymmetric galaxy correlation functions*, *Phys. Rev. D* **89** (2014) 083535 [[1309.1321](#)].
- [129] C. Bonvin, L. Hui and E. Gaztanaga, *Optimising the measurement of relativistic distortions in large-scale structure*, *JCAP* **08** (2016) 021 [[1512.03566](#)].
- [130] E. Gaztanaga, C. Bonvin and L. Hui, *Measurement of the dipole in the cross-correlation function of galaxies*, *JCAP* **01** (2017) 032 [[1512.03918](#)].
- [131] V. Iršič, E. Di Dio and M. Viel, *Relativistic effects in Lyman- α forest*, *JCAP* **02** (2016) 051 [[1510.03436](#)].
- [132] F. Lepori, E. Di Dio, E. Villa and M. Viel, *Optimal galaxy survey for detecting the dipole in the cross-correlation with 21 cm Intensity Mapping*, *JCAP* **05** (2018) 043 [[1709.03523](#)].

Bibliography

- [133] C. Bonvin and P. Fleury, *Testing the equivalence principle on cosmological scales*, *JCAP* **05** (2018) 061 [[1803.02771](#)].
- [134] F. Lepori, V. Iršič, E. Di Dio and M. Viel, *The impact of relativistic effects on the 3D Quasar-Lyman- α cross-correlation*, *JCAP* **04** (2020) 006 [[1910.06305](#)].
- [135] C. Okoli, M. I. Scrimgeour, N. Afshordi and M. J. Hudson, *Dynamical friction in the primordial neutrino sea*, *Mon. Not. Roy. Astron. Soc.* **468** (2017) 2164 [[1611.04589](#)].
- [136] M. Vallisneri, *Use and abuse of the Fisher information matrix in the assessment of gravitational-wave parameter-estimation prospects*, *Phys. Rev. D* **77** (2008) 042001 [[gr-qc/0703086](#)].
- [137] F. Beutler, E. Castorina and P. Zhang, *Interpreting measurements of the anisotropic galaxy power spectrum*, *JCAP* **03** (2019) 040 [[1810.05051](#)].
- [138] E. Castorina and M. White, *Beyond the plane-parallel approximation for redshift surveys*, *Mon. Not. Roy. Astron. Soc.* **476** (2018) 4403 [[1709.09730](#)].
- [139] A. Kehagias, A. Moradinezhad Dizgah, J. Noreña, H. Perrier and A. Riotto, *A Consistency Relation for the Observed Galaxy Bispectrum and the Local non-Gaussianity from Relativistic Corrections*, *JCAP* **08** (2015) 018 [[1503.04467](#)].
- [140] E. Di Dio, R. Durrer, G. Marozzi and F. Montanari, *The bispectrum of relativistic galaxy number counts*, *JCAP* **01** (2016) 016 [[1510.04202](#)].
- [141] E. Di Dio, H. Perrier, R. Durrer, G. Marozzi, A. Moradinezhad Dizgah, J. Noreña et al., *Non-Gaussianities due to Relativistic Corrections to the Observed Galaxy Bispectrum*, *JCAP* **1703** (2017) 006 [[1611.03720](#)].
- [142] D. Bertacca, A. Raccanelli, N. Bartolo, M. Liguori, S. Matarrese and L. Verde, *Relativistic wide-angle galaxy bispectrum on the light-cone*, *Phys. Rev. D* **97** (2018) 023531 [[1705.09306](#)].
- [143] A. Hall, C. Bonvin and A. Challinor, *Testing General Relativity with 21-cm intensity mapping*, *Phys. Rev. D* **87** (2013) 064026 [[1212.0728](#)].
- [144] F. Villaescusa-Navarro et al., *Ingredients for 21 cm Intensity Mapping*, *Astrophys. J.* **866** (2018) 135 [[1804.09180](#)].
- [145] MEERKCLASS collaboration, M. G. Santos et al., *MeerKCLASS: MeerKAT Large Area Synoptic Survey*, in *MeerKAT Science: On the Pathway to the SKA*, 9, 2017, [1709.06099](#).
- [146] J. Fonseca, S. Camera, M. Santos and R. Maartens, *Hunting down horizon-scale effects with multi-wavelength surveys*, *Astrophys. J. Lett.* **812** (2015) L22 [[1507.04605](#)].

Bibliography

- [147] O. Umeh, *Imprint of non-linear effects on HI intensity mapping on large scales*, *JCAP* **06** (2017) 005 [[1611.04963](#)].
- [148] M. Jalilvand, E. Majorotto, R. Durrer and M. Kunz, *Intensity mapping of the 21 cm emission: lensing*, *JCAP* **01** (2019) 020 [[1807.01351](#)].
- [149] D. Bertacca, R. Maartens and C. Clarkson, *Observed galaxy number counts on the lightcone up to second order: II. Derivation*, *JCAP* **1411** (2014) 013 [[1406.0319](#)].
- [150] R. Durrer, M. Jalilvand, R. Kothari, R. Maartens and F. Montanari, *Full-sky bispectrum in redshift space for 21cm intensity maps*, *JCAP* **12** (2020) 003 [[2008.02266](#)].
- [151] C. J. Schmit, A. F. Heavens and J. R. Pritchard, *The gravitational and lensing-ISW bispectrum of 21 cm radiation*, *Mon. Not. Roy. Astron. Soc.* **483** (2019) 4259 [[1810.00973](#)].
- [152] D. Blas, J. Lesgourgues and T. Tram, *The Cosmic Linear Anisotropy Solving System (CLASS) II: Approximation schemes*, *JCAP* **07** (2011) 034 [[1104.2933](#)].
- [153] R. K. Sheth, H. J. Mo and G. Tormen, *Ellipsoidal collapse and an improved model for the number and spatial distribution of dark matter haloes*, *Mon. Not. Roy. Astron. Soc.* **323** (2001) 1 [[astro-ph/9907024](#)].
- [154] R. K. Sheth and G. Tormen, *An Excursion Set Model of Hierarchical Clustering : Ellipsoidal Collapse and the Moving Barrier*, *Mon. Not. Roy. Astron. Soc.* **329** (2002) 61 [[astro-ph/0105113](#)].
- [155] R. K. Sheth and G. Tormen, *Large scale bias and the peak background split*, *Mon. Not. Roy. Astron. Soc.* **308** (1999) 119 [[astro-ph/9901122](#)].
- [156] T. Kitayama and Y. Suto, *Semianalytical predictions for statistical properties of x-ray clusters of galaxies in cold dark matter universes*, *Astrophys. J.* **469** (1996) 480 [[astro-ph/9604141](#)].
- [157] P. Bull, P. G. Ferreira, P. Patel and M. G. Santos, *Late-time cosmology with 21cm intensity mapping experiments*, *Astrophys. J.* **803** (2015) 21 [[1405.1452](#)].
- [158] M. Tellarini, A. J. Ross, G. Tasinato and D. Wands, *Non-local bias in the halo bispectrum with primordial non-Gaussianity*, *JCAP* **07** (2015) 004 [[1504.00324](#)].
- [159] M. G. Santos et al., *Cosmology from a SKA HI intensity mapping survey*, *PoS AASKA14* (2015) 019 [[1501.03989](#)].
- [160] A. Liu and J. R. Shaw, *Data Analysis for Precision 21 cm Cosmology*, *Publ. Astron. Soc. Pac.* **132** (2020) 062001 [[1907.08211](#)].

Bibliography

- [161] J. C. Pober et al., *What Next-Generation 21 cm Power Spectrum Measurements Can Teach Us About the Epoch of Reionization*, *Astrophys. J.* **782** (2014) 66 [[1310.7031](#)].
- [162] D. Alonso, P. Bull, P. G. Ferreira and M. G. Santos, *Blind foreground subtraction for intensity mapping experiments*, *Mon. Not. Roy. Astron. Soc.* **447** (2015) 400 [[1409.8667](#)].
- [163] J. C. Pober, *The Impact of Foregrounds on Redshift Space Distortion Measurements With the Highly-Redshifted 21 cm Line*, *Mon. Not. Roy. Astron. Soc.* **447** (2015) 1705 [[1411.2050](#)].
- [164] L. Wolz, F. B. Abdalla, D. Alonso, C. Blake, P. Bull, T.-C. Chang et al., *Foreground Subtraction in Intensity Mapping with the SKA*, *PoS AASKA14* (2015) 035 [[1501.03823](#)].
- [165] J. R. Shaw, K. Sigurdson, M. Sitwell, A. Stebbins and U.-L. Pen, *Coaxing cosmic 21 cm fluctuations from the polarized sky using m-mode analysis*, *Phys. Rev. D* **91** (2015) 083514 [[1401.2095](#)].
- [166] A. Obuljen, E. Castorina, F. Villaescusa-Navarro and M. Viel, *High-redshift post-reionization cosmology with 21cm intensity mapping*, *JCAP* **05** (2018) 004 [[1709.07893](#)].
- [167] COSMIC VISIONS 21 CM collaboration, R. Ansari et al., *Inflation and Early Dark Energy with a Stage II Hydrogen Intensity Mapping experiment*, [1810.09572](#).
- [168] A. Witzemann, D. Alonso, J. Fonseca and M. G. Santos, *Simulated multitracer analyses with H i intensity mapping*, *Mon. Not. Roy. Astron. Soc.* **485** (2019) 5519 [[1808.03093](#)].
- [169] SKA collaboration, D. J. Bacon et al., *Cosmology with Phase 1 of the Square Kilometre Array: Red Book 2018: Technical specifications and performance forecasts*, *Publ. Astron. Soc. Austral.* **37** (2020) e007 [[1811.02743](#)].
- [170] J. Asorey, D. Parkinson, F. Shi, Y.-S. Song, K. Ahn, J. Kim et al., *HIR4: cosmology from a simulated neutral hydrogen full sky using Horizon Run 4*, *Mon. Not. Roy. Astron. Soc.* **495** (2020) 1788 [[2001.00833](#)].
- [171] S. Cunningham, A. Pourtsidou, P. S. Soares, C. Blake and D. Bacon, *Multipole expansion for H i intensity mapping experiments: simulations and modelling*, *Mon. Not. Roy. Astron. Soc.* **496** (2020) 415 [[2002.05626](#)].
- [172] H.-M. Zhu, U.-L. Pen, Y. Yu and X. Chen, *Recovering lost 21 cm radial modes via cosmic tidal reconstruction*, *Phys. Rev. D* **98** (2018) 043511 [[1610.07062](#)].
- [173] C. Modi, M. White, A. Slosar and E. Castorina, *Reconstructing large-scale structure with neutral hydrogen surveys*, *JCAP* **11** (2019) 023 [[1907.02330](#)].

Bibliography

- [174] D. Alonso, P. G. Ferreira, M. J. Jarvis and K. Moodley, *Calibrating photometric redshifts with intensity mapping observations*, *Phys. Rev. D* **96** (2017) 043515 [[1704.01941](#)].
- [175] A. Ghosh, F. Mertens and L. V. E. Koopmans, *Deconvolving the wedge: maximum-likelihood power spectra via spherical-wave visibility modelling*, *Mon. Not. Roy. Astron. Soc.* **474** (2018) 4552 [[1709.06752](#)].
- [176] D. Karagiannis, A. Slosar and M. Liguori, *Forecasts on Primordial non-Gaussianity from 21 cm Intensity Mapping experiments*, *JCAP* **11** (2020) 052 [[1911.03964](#)].
- [177] S.-F. Chen, E. Castorina, M. White and A. Slosar, *Synergies between radio, optical and microwave observations at high redshift*, *JCAP* **07** (2019) 023 [[1810.00911](#)].
- [178] E. Castorina and F. Villaescusa-Navarro, *On the spatial distribution of neutral hydrogen in the Universe: bias and shot-noise of the HI power spectrum*, *Mon. Not. Roy. Astron. Soc.* **471** (2017) 1788 [[1609.05157](#)].
- [179] J. L. Bernal, P. C. Breysse, H. Gil-Marín and E. D. Kovetz, *User's guide to extracting cosmological information from line-intensity maps*, *Phys. Rev. D* **100** (2019) 123522 [[1907.10067](#)].
- [180] M. Jalilvand, E. Majerotto, C. Bonvin, F. Lacasa, M. Kunz, W. Naidoo et al., *New Estimator for Gravitational Lensing Using Galaxy and Intensity Mapping Surveys*, *Phys. Rev. Lett.* **124** (2020) 031101 [[1907.00071](#)].
- [181] PUMA collaboration, A. Slosar et al., *Packed Ultra-wideband Mapping Array (PUMA): A Radio Telescope for Cosmology and Transients*, [1907.12559](#).
- [182] E. Castorina et al., *Packed Ultra-wideband Mapping Array (PUMA): Astro2020 RFI Response*, [2002.05072](#).
- [183] J. Fonseca, J.-A. Viljoen and R. Maartens, *Constraints on the growth rate using the observed galaxy power spectrum*, *JCAP* **12** (2019) 028 [[1907.02975](#)].
- [184] T. Matsubara, *The Correlation function in redshift space: General formula with wide angle effects and cosmological distortions*, *Astrophys. J.* **535** (2000) 1 [[astro-ph/9908056](#)].
- [185] R. Scoccimarro, *Fast Estimators for Redshift-Space Clustering*, *Phys. Rev. D* **92** (2015) 083532 [[1506.02729](#)].
- [186] N. S. Sugiyama, S. Saito, F. Beutler and H.-J. Seo, *A complete fft-based decomposition formalism for the redshift-space bispectrum*, *Monthly Notices of the Royal Astronomical Society* **484** (2018) 364–384.

Bibliography

- [187] D. Sarkar and S. Bharadwaj, *Redshift-space distortions of the H i 21-cm intensity mapping signal due to the internal motions within galaxies*, *Mon. Not. Roy. Astron. Soc.* **487** (2019) 5666 [[1906.07032](#)].
- [188] S. Mollerach and S. Matarrese, *Cosmic microwave background anisotropies from second order gravitational perturbations*, *Phys. Rev. D* **56** (1997) 4494 [[astro-ph/9702234](#)].
- [189] S. Matarrese, S. Mollerach and M. Bruni, *Second order perturbations of the Einstein-de Sitter universe*, *Phys. Rev. D* **58** (1998) 043504 [[astro-ph/9707278](#)].
- [190] J. L. Fuentes, J. C. Hidalgo and K. A. Malik, *Galaxy number counts at second order: an independent approach*, *Class. Quant. Grav.* **38** (2021) 065014 [[1908.08400](#)].
- [191] J. L. Fuentes, J. C. Hidalgo and K. A. Malik, *Galaxy number counts at second order in perturbation theory: a leading-order term comparison*, [2012.15326](#).
- [192] L. Verde, L.-M. Wang, A. Heavens and M. Kamionkowski, *Large scale structure, the cosmic microwave background, and primordial non-gaussianity*, *Mon. Not. Roy. Astron. Soc.* **313** (2000) L141 [[astro-ph/9906301](#)].
- [193] K. Tomita, *Relativistic second-order perturbations of nonzero-lambda flat cosmological models and CMB anisotropies*, *Phys. Rev. D* **71** (2005) 083504 [[astro-ph/0501663](#)].
- [194] S. Mollerach, D. Harari and S. Matarrese, *CMB polarization from secondary vector and tensor modes*, *Phys. Rev. D* **69** (2004) 063002 [[astro-ph/0310711](#)].
- [195] K. N. Ananda, C. Clarkson and D. Wands, *The Cosmological gravitational wave background from primordial density perturbations*, *Phys. Rev. D* **75** (2007) 123518 [[gr-qc/0612013](#)].
- [196] T. H.-C. Lu, K. Ananda and C. Clarkson, *Vector modes generated by primordial density fluctuations*, *Phys. Rev. D* **77** (2008) 043523 [[0709.1619](#)].
- [197] D. Baumann, P. J. Steinhardt, K. Takahashi and K. Ichiki, *Gravitational Wave Spectrum Induced by Primordial Scalar Perturbations*, *Phys. Rev. D* **76** (2007) 084019 [[hep-th/0703290](#)].
- [198] J.-C. Hwang, D. Jeong and H. Noh, *Gauge dependence of gravitational waves generated from scalar perturbations*, *Astrophys. J.* **842** (2017) 46 [[1704.03500](#)].
- [199] T. H.-C. Lu, K. Ananda, C. Clarkson and R. Maartens, *The cosmological background of vector modes*, *JCAP* **02** (2009) 023 [[0812.1349](#)].

Bibliography

- [200] S. Saga, D. Yamauchi and K. Ichiki, *Weak lensing induced by second-order vector mode*, *Phys. Rev. D* **92** (2015) 063533 [[1505.02774](#)].
- [201] M. Bojowald and G. M. Hossain, *Cosmological vector modes and quantum gravity effects*, *Class. Quant. Grav.* **24** (2007) 4801 [[0709.0872](#)].
- [202] L. Dai, D. Jeong and M. Kamionkowski, *Anisotropic imprint of long-wavelength tensor perturbations on cosmic structure*, *Phys. Rev. D* **88** (2013) 043507 [[1306.3985](#)].
- [203] S. Andrianomena, C. Clarkson, P. Patel, O. Umeh and J.-P. Uzan, *Non-linear relativistic contributions to the cosmological weak-lensing convergence*, *JCAP* **06** (2014) 023 [[1402.4350](#)].
- [204] S. Matarrese, O. Pantano and D. Saez, *General relativistic dynamics of irrotational dust: Cosmological implications*, *Phys. Rev. Lett.* **72** (1994) 320 [[astro-ph/9310036](#)].
- [205] H. Noh and J.-c. Hwang, *Second-order perturbations of the Friedmann world model*, *Phys. Rev. D* **69** (2004) 104011.
- [206] K. A. Malik and D. Wands, *Cosmological perturbations*, *Phys. Rept.* **475** (2009) 1 [[0809.4944](#)].
- [207] J.-c. Hwang and H. Noh, *Fully nonlinear and exact perturbations of the Friedmann world model*, *Mon. Not. Roy. Astron. Soc.* **433** (2013) 3472 [[1207.0264](#)].
- [208] C. Rampf, *Frame dragging and Eulerian frames in General Relativity*, *Phys. Rev. D* **89** (2014) 063509 [[1307.1725](#)].
- [209] B. Osano, *Second Order perturbation Theory: A covariant approach involving a barotropic equation of state*, *Class. Quant. Grav.* **34** (2017) 125004 [[1504.01495](#)].
- [210] C. Rampf and A. Wiegand, *Relativistic Lagrangian displacement field and tensor perturbations*, *Phys. Rev. D* **90** (2014) 123503 [[1409.2688](#)].
- [211] E. M. de Weerd, C. Clarkson, S. Jolicoeur, R. Maartens and O. Umeh, *Multipoles of the relativistic galaxy bispectrum*, *JCAP* **05** (2020) 018 [[1912.11016](#)].
- [212] D. Jeong and E. Komatsu, *Primordial non-Gaussianity, scale-dependent bias, and the bispectrum of galaxies*, *Astrophys. J.* **703** (2009) 1230 [[0904.0497](#)].
- [213] T. Baldauf, U. Seljak and L. Senatore, *Primordial non-Gaussianity in the Bispectrum of the Halo Density Field*, *JCAP* **1104** (2011) 006 [[1011.1513](#)].
- [214] M. Celoria and S. Matarrese, *Primordial Non-Gaussianity*, *Proc. Int. Sch. Phys. Fermi* **200** (2020) 179 [[1812.08197](#)].

Bibliography

- [215] O. Umeh, K. Koyama, R. Maartens, F. Schmidt and C. Clarkson, *General relativistic effects in the galaxy bias at second order*, *JCAP* **1905** (2019) 020 [[1901.07460](#)].
- [216] R. Maartens, S. Jolicoeur, O. Umeh, E. M. De Weerd and C. Clarkson, *Local primordial non-Gaussianity in the relativistic galaxy bispectrum*, *JCAP* **04** (2021) 013 [[2011.13660](#)].
- [217] W. L. W. Sargent and E. L. Turner, *A statistical method for determining the cosmological density parameter from the redshifts of a complete sample of galaxies.*, *The Astrophysical Journal* **212** (1977) L3.
- [218] J. V. Villumsen, *Clustering of faint galaxies: omega (Theta), induced by weak gravitational lensing*, [astro-ph/9512001](#).
- [219] J. Yoo, A. L. Fitzpatrick and M. Zaldarriaga, *A New Perspective on Galaxy Clustering as a Cosmological Probe: General Relativistic Effects*, *Phys. Rev. D* **80** (2009) 083514 [[0907.0707](#)].
- [220] J. Yoo, *General Relativistic Description of the Observed Galaxy Power Spectrum: Do We Understand What We Measure?*, *Phys. Rev. D* **82** (2010) 083508 [[1009.3021](#)].
- [221] M. Bruni, R. Crittenden, K. Koyama, R. Maartens, C. Pitrou and D. Wands, *Disentangling non-Gaussianity, bias and GR effects in the galaxy distribution*, *Phys. Rev. D* **85** (2012) 041301 [[1106.3999](#)].
- [222] N. Dalal, O. Dore, D. Huterer and A. Shirokov, *The imprints of primordial non-gaussianities on large-scale structure: scale dependent bias and abundance of virialized objects*, *Phys. Rev. D* **77** (2008) 123514 [[0710.4560](#)].
- [223] S. Matarrese and L. Verde, *The effect of primordial non-Gaussianity on halo bias*, *Astrophys. J. Lett.* **677** (2008) L77 [[0801.4826](#)].
- [224] S. Camera, R. Maartens and M. G. Santos, *Einstein's legacy in galaxy surveys*, *Mon. Not. Roy. Astron. Soc.* **451** (2015) L80 [[1412.4781](#)].
- [225] L. Lopez-Honorez, O. Mena and S. Rigolin, *Biases on cosmological parameters by general relativity effects*, *Phys. Rev. D* **85** (2012) 023511 [[1109.5117](#)].
- [226] J. Yoo, N. Hamaus, U. Seljak and M. Zaldarriaga, *Going beyond the Kaiser redshift-space distortion formula: a full general relativistic account of the effects and their detectability in galaxy clustering*, *Phys. Rev. D* **86** (2012) 063514 [[1206.5809](#)].
- [227] A. Raccanelli, D. Bertacca, O. Doré and R. Maartens, *Large-scale 3D galaxy correlation function and non-Gaussianity*, *JCAP* **08** (2014) 022 [[1306.6646](#)].

Bibliography

- [228] S. Camera, M. G. Santos and R. Maartens, *Probing primordial non-Gaussianity with SKA galaxy redshift surveys: a fully relativistic analysis*, *Mon. Not. Roy. Astron. Soc.* **448** (2015) 1035 [[1409.8286](#)].
- [229] A. Raccanelli, F. Montanari, D. Bertacca, O. Doré and R. Durrer, *Cosmological Measurements with General Relativistic Galaxy Correlations*, *JCAP* **05** (2016) 009 [[1505.06179](#)].
- [230] D. Alonso and P. G. Ferreira, *Constraining ultralarge-scale cosmology with multiple tracers in optical and radio surveys*, *Phys. Rev. D* **92** (2015) 063525 [[1507.03550](#)].
- [231] J. Fonseca, R. Maartens and M. G. Santos, *Probing the primordial Universe with MeerKAT and DES*, *Mon. Not. Roy. Astron. Soc.* **466** (2017) 2780 [[1611.01322](#)].
- [232] C. S. Lorenz, D. Alonso and P. G. Ferreira, *Impact of relativistic effects on cosmological parameter estimation*, *Phys. Rev. D* **97** (2018) 023537 [[1710.02477](#)].
- [233] M. Ballardini, W. L. Matthewson and R. Maartens, *Constraining primordial non-Gaussianity using two galaxy surveys and CMB lensing*, *Mon. Not. Roy. Astron. Soc.* **489** (2019) 1950 [[1906.04730](#)].
- [234] N. Grimm, F. Scaccabarozzi, J. Yoo, S. G. Biern and J.-O. Gong, *Galaxy Power Spectrum in General Relativity*, *JCAP* **11** (2020) 064 [[2005.06484](#)].
- [235] J. L. Bernal, N. Bellomo, A. Raccanelli and L. Verde, *Beware of commonly used approximations. Part II. Estimating systematic biases in the best-fit parameters*, *JCAP* **10** (2020) 017 [[2005.09666](#)].
- [236] M. S. Wang, F. Beutler and D. Bacon, *Impact of Relativistic Effects on the Primordial Non-Gaussianity Signature in the Large-Scale Clustering of Quasars*, *Mon. Not. Roy. Astron. Soc.* **499** (2020) 2598 [[2007.01802](#)].
- [237] O. Umeh and K. Koyama, *The galaxy bias at second order in general relativity with Non-Gaussian initial conditions*, *JCAP* **12** (2019) 048 [[1907.08094](#)].
- [238] K. Koyama, O. Umeh, R. Maartens and D. Bertacca, *The observed galaxy bispectrum from single-field inflation in the squeezed limit*, *JCAP* **07** (2018) 050 [[1805.09189](#)].
- [239] T. Giannantonio and C. Porciani, *Structure formation from non-Gaussian initial conditions: multivariate biasing, statistics, and comparison with N-body simulations*, *Phys. Rev. D* **81** (2010) 063530 [[0911.0017](#)].

Bibliography

- [240] C. A. Watkinson, S. Majumdar, J. R. Pritchard and R. Mondal, *A fast estimator for the bispectrum and beyond – a practical method for measuring non-Gaussianity in 21-cm maps*, *Mon. Not. Roy. Astron. Soc.* **472** (2017) 2436 [[1705.06284](#)].
- [241] S. Majumdar, J. R. Pritchard, R. Mondal, C. A. Watkinson, S. Bharadwaj and G. Mellema, *Quantifying the non-Gaussianity in the EoR 21-cm signal through bispectrum*, *Mon. Not. Roy. Astron. Soc.* **476** (2018) 4007 [[1708.08458](#)].
- [242] D. Sarkar, S. Majumdar and S. Bharadwaj, *Modelling the post-reionization neutral hydrogen (HI) 21-cm bispectrum*, *Mon. Not. Roy. Astron. Soc.* **490** (2019) 2880 [[1907.01819](#)].
- [243] S. Bharadwaj, A. Mazumdar and D. Sarkar, *Quantifying the Redshift Space Distortion of the Bispectrum I: Primordial Non-Gaussianity*, *Mon. Not. Roy. Astron. Soc.* **493** (2020) 594 [[2001.10243](#)].
- [244] D. Karagiannis, J. Fonseca, R. Maartens and S. Camera, *Probing primordial non-Gaussianity with the bispectrum of future 21cm intensity maps*, [2010.07034](#).
- [245] A. Moradinezhad Dizgah, M. Biagetti, E. Sefusatti, V. Desjacques and J. Noreña, *Primordial Non-Gaussianity from Biased Tracers: Likelihood Analysis of Real-Space Power Spectrum and Bispectrum*, [2010.14523](#).
- [246] O. Umeh, K. Koyama and R. Crittenden, *Testing the equivalence principle on cosmological scales using the odd multipoles of galaxy cross-power spectrum and bispectrum*, [2011.05876](#).
- [247] T. Tram, C. Fidler, R. Crittenden, K. Koyama, G. W. Pettinari and D. Wands, *The Intrinsic Matter Bispectrum in Λ CDM*, *JCAP* **05** (2016) 058 [[1602.05933](#)].
- [248] N. Bartolo, D. Bertacca, M. Bruni, K. Koyama, R. Maartens, S. Matarrese et al., *A relativistic signature in large-scale structure*, *Phys. Dark Univ.* **13** (2016) 30 [[1506.00915](#)].
- [249] D. Bertacca, N. Bartolo, M. Bruni, K. Koyama, R. Maartens, S. Matarrese et al., *Galaxy bias and gauges at second order in General Relativity*, *Class. Quant. Grav.* **32** (2015) 175019 [[1501.03163](#)].
- [250] A. Barreira, G. Cabass, F. Schmidt, A. Pillepich and D. Nelson, *Galaxy bias and primordial non-Gaussianity: insights from galaxy formation simulations with IllustrisTNG*, *JCAP* **12** (2020) 013 [[2006.09368](#)].
- [251] A. Barreira, *On the impact of galaxy bias uncertainties on primordial non-Gaussianity constraints*, *JCAP* **12** (2020) 031 [[2009.06622](#)].

Bibliography

- [252] L. Dai, E. Pajer and F. Schmidt, *On Separate Universes*, *JCAP* **10** (2015) 059 [[1504.00351](#)].
- [253] R. de Putter, O. Doré and D. Green, *Is There Scale-Dependent Bias in Single-Field Inflation?*, *JCAP* **10** (2015) 024 [[1504.05935](#)].
- [254] S. Matarrese, L. Pilo and R. Rollo, *Resilience of long modes in cosmological observables*, *JCAP* **01** (2021) 062 [[2007.08877](#)].
- [255] M. Bruni, J. C. Hidalgo, N. Meures and D. Wands, *Non-Gaussian Initial Conditions in Λ CDM: Newtonian, Relativistic, and Primordial Contributions*, *Astrophys. J.* **785** (2014) 2 [[1307.1478](#)].
- [256] P. Gagrani and L. Samushia, *Information Content of the Angular Multipoles of Redshift-Space Galaxy Bispectrum*, *Mon. Not. Roy. Astron. Soc.* **467** (2017) 928 [[1610.03488](#)].
- [257] M. Shirasaki, N. S. Sugiyama, R. Takahashi and F.-S. Kitaura, *Constraining primordial non-Gaussianity with postreconstructed galaxy bispectrum in redshift space*, *Phys. Rev. D* **103** (2021) 023506 [[2010.04567](#)].

List of Figures

1.1.	An illustration of the modern-day dominant energy components in the universe, taken from [1].	11
1.2.	Illustration of the timeline of the universe, starting from the Big Bang (<i>left side</i>) and including inflation, matter formation, recombination, and the formation of stars, galaxies, and larger structures observed today (<i>right side</i>). Taken from [2].	12
1.3.	Mollweide projection of the CMB map as observed by the Planck satellite. The colours show tiny (order μK) fluctuations in temperature, which correspond to regions of slightly different density and are the seeds of the structure we observe today. Figure is taken from [6].	13
1.4.	Snapshot of Millennium simulations [7] showing non-linear LSS. There are dense filaments (lighter) surrounded by milder underdensities (darker).	14
1.5.	Example sky map of a redshift survey, with the cosmic web at increasing redshift. This figure is adapted from the SDSS Science Results [51].	17
1.6.	Example of a linear matter power spectrum as generated by CAMB, at redshift $z = 1$	20

List of Figures

- 1.7. An illustration of a Fourier-space triangle shape and the corresponding real space signature— in this case the equilateral bispectrum. The field (denoted T here) can be decomposed into plane waves, and the three components that form an equilateral triangle can have different signs relative to each other. This gives an overall sign to bispectrum b , to be interpreted as an average probability of which sign is more likely. A positive sign corresponds to the combination of wavevectors being more likely to produce concentrated overdensities surrounded by areas of milder underdensity. For a negative equilateral bispectrum, this is the other way round, and one would expect to see on average more concentrated underdensities surrounded by areas with mild overdensity. Please note that these are slices of 3D figures, which extend into the page— meaning that a positive sign on the bispectrum corresponds to filaments of overdensities surrounded by areas of mild underdensity. Note also that this concerns a statistical quantity only, so while on average one would expect to see more of one type of signature, the observed distribution does not uniformly look like a given real space structure. Figure taken from [65].

1.8. Bispectrum monopole measurements in the LOWZ galaxy sample of BOSS DR12. The sample contains 361,762 galaxies with an effective redshift of $z = 0.32$. The wavevectors of the triangles are contained by $0.03 \text{ } h\text{Mpc}^{-1} \leq k \leq 0.18 \text{ } h\text{Mpc}^{-1}$, in 160 bins. The colours represent different triangle shapes as indicated— equilateral (red), isosceles (blue), and scalene (green) triangles. The black solid line represents the best-fit model, and the middle and bottom panel show the deviation of the model from the data. The binned bispectrum is plotted such that the first value plotted is an equilateral triangle with sides $N_0\Delta k$, where Δk is the bin size used and N_0 is an integer corresponding to the first bin size used— the ‘triangle index’. The plotting then loops sequentially through all possible values of k_1, k_2, k_3 up to a truncation value set by the scale constraints. Taken from [77]— see the reference for a detailed discussion.

23

25

List of Figures

1.9.	Signal-to-noise ratio for measurements of the galaxy power spectrum and bispectrum in a Euclid-like galaxy survey as a function of redshift z , as computed by [83]. Displayed are the SNR for the power spectrum (dot-dashed), bispectrum (dashed). Solid line is the combined SNR, and the SNR computed by neglecting the cross-covariance between the power spectrum and bispectrum is denoted by a dotted line.	26
1.10.	The three triangular configurations generally discussed in literature on the bispectrum and primordial non-Gaussianity. <i>Left</i> : squeezed shapes, where one side $k_3 \ll k_1, k_2$, <i>middle</i> : equilateral shapes, where $k_1 = k_2 = k_3$, and <i>right</i> : co-linear shapes, where $k_1 = k_2 \approx k_3/2$. Figure taken from [84].	27
1.11.	Illustration of the LIMD model of galaxy bias. The red line indicates a long wavelength perturbation, and the blue line denotes the density field δ_R . The dashed horizontal magenta line shows the critical density δ_{cr} . Regions of overdensity δ_R that get pushed above this critical density threshold collapse to form haloes in which galaxies are formed.	29
2.1.	Overview of the relevant vectors and angles for the Fourier-space bispectrum.	38
2.2.	The absolute value of the bispectrum dipole at $z = 1$ as a function of triangle size, in the flattened (<i>Left</i> , $\theta = 2^\circ$, for intensity mapping bias) and squeezed (<i>Right</i> , $\theta = 178^\circ$, for <i>Euclid</i> -like bias) configurations, with k_3 as the horizontal axis. Red is the $m = 0$ part and blue is $m = \pm 1$. Dashed (and dotted) lines show up to the $\mathcal{O}(\mathcal{H}/k)$ terms considered analytically here, while solid lines indicate larger-scale contributions. For reference the monopole is in black, with the dotted line the Newtonian part. (The zero-crossing in the monopole for the squeezed case is a result of the tidal bias.)	41
2.3.	(<i>Left</i>) We show the dipoles as a function of θ with a bias appropriate for a <i>Euclid</i> -like survey, for $k_1 = k_2 = 0.01 \text{ Mpc}^{-1}$. The left of the plot corresponds to the flattened case where the $m = 0$ (red) dipole reaches 10% of the monopole. (<i>Right</i>) We show the IM signal with $k_1 = k_2 = 0.1 \text{ Mpc}^{-1}$ versus the long mode k_3 . Except for very long modes $\theta \approx \pi$, our $\mathcal{O}(\mathcal{H}/k)$ truncation is a very good approximation in these examples.	42

List of Figures

3.1.	Effect on total relativistic SNR of changing number of φ and μ_1 bins.	53
3.2.	Clustering bias parameters (<i>left</i>), comoving volume and number density (<i>middle</i>) and RSD damping parameter (<i>right</i>). Points are the data from Table 1 in [83].	54
3.3.	Magnification and evolution bias (3.46), (3.47). The sharp discontinuity in evolution bias at redshift $z = 1.3$ is due to the discontinuity in modelling of the comoving density of H α emitters as in equation 3.41.	55
3.4.	Relativistic SNR per z -bin (<i>top</i>) and cumulative (<i>bottom</i>) for a Stage IV H α survey.	59
3.5.	Effect of changing k_{\max} on SNR per bin (<i>top</i>) and cumulative SNR (<i>bottom</i>).	60
3.6.	Effect of changing Q and b_e on relativistic cumulative SNR.	61
3.7.	Effect of changing k_{\min} on total relativistic SNR.	62
3.8.	As in Figure 3.4, but showing the effect of omitting the second-order relativistic contribution (3.49) to the bispectrum (dot-dashed curves).	63
3.9.	Marginal errors (cumulative) on the relativistic contribution, growth index and clustering amplitude, using the full bispectrum. Bias parameters are held fixed at their theoretical values. Parameter A_D corresponds to the relativistic part of the bispectrum. The fact that $\sigma_{A_D} \lesssim 0.1$ indicates that the relativistic effects remain detectable when the two other parameters are marginalised over.	64
3.10.	The number density (<i>top</i>), magnification bias (<i>bottom left</i>), and evolution bias (<i>bottom right</i>) for a Euclid-like survey with the Model 3 luminosity function and flux cut $F_c = 2 \cdot 10^{-16}$ erg cm $^{-2}$ s $^{-1}$. Figure taken from [122].	67
3.11.	SNR per z -bin (<i>left</i>) and cumulative SNR (<i>right</i>) for a Euclid-like survey with a Model 3 luminosity function. We obtain a cumulative SNR of ~ 18 , which points towards potential detectability.	68
3.12.	HI clustering and evolution bias parameters (<i>left</i>) and background temperature (<i>right</i>).	72
3.13.	Schematic of important scales in the k_{\parallel}, k_{\perp} -plane at fixed z . Shading indicates the included region for SD mode (light) and IF mode (dark).	78
3.14.	T_{sys} for the different frequency bands of MeerKAT and SKA1 (from Table 3.4).	83
3.15.	Minimum wavenumbers for the surveys, where k is subject to (3.7) (SD) or (3.104) (IF).	84
3.16.	Physical baseline density models for HIRAX (<i>left</i>) and PUMA (<i>right</i>).	85

List of Figures

3.17. Noise power spectra of the SD-mode surveys (at $z = 0.4$ for low- z_{\max} bands and $z = 1$ for high- z_{\max} bands) and IF-mode surveys (HIRAX at $z = 1$, PUMA at $z = 2$)	85
3.18. SNR of the relativistic bispectrum per z -bin (<i>left</i>) and cumulative (<i>right</i>) for SD-mode surveys.	86
3.19. Cumulative SNR of the relativistic bispectrum for IF-mode surveys. .	87
4.1. Monopole of the bispectrum at $z = 1$, taken from [108]. The different colours denote the different triangle shapes considered— blue representing a squeezed shape (chosen such that $k_3 \approx k/16$), and red denotes the equilateral shape. The shape is held fixed, and the overall scale of the triangle is varied (k along the x -axis). Dashed lines denote the Newtonian approximation, and the solid lines include local GR effects.	105
4.2. Effective f_{NL} due to neglecting GR projection effects, from comparison to a Newtonian bispectrum analysis but ignoring scale-dependent bias. The red solid line corresponds to the equilateral shape, and the blue solid line denotes the squeezed shape, as in Figure 4.1. This figure is taken from [108].	106
4.3. The separated vector, tensor, and scalar contributions to the monopole of the galaxy bispectrum, with the full GR bispectrum in black for reference. The vector and tensor modes are subdominant at a factor of about 3 orders of magnitude smaller than the scalar contributions, except outside the Hubble radius (and where unobservable) where they grow due to their k -dependence and where the Newtonian contribution becomes negative as a result of the tidal bias. The tensor contributions (purple) oscillate at small scales as they pick up the BAO.	110
5.1. Recap of the overview of the relevant vectors and angles for the Fourier-space bispectrum.	119

List of Figures

<p>5.2. Overview of all non-zero multipoles for the bispectrum, which includes ℓ from 0 to 8, and m from $-\ell$ to ℓ; the pattern here is the same for $m < 0$, so only $m \geq 0$ are displayed. Denoted in the figure are whether components are Newtonian+GR or GR only, triangle shapes indicating whether given components are non-vanishing in flattened (co-linear) or equilateral limits. Note how the dipole is unique in having the equilateral case vanish for every value of m. Also given is which powers of \mathcal{H}/k appear in each of the multipoles.</p> <p>5.3. Normalised total power for squeezed configuration for <i>Euclid</i>-like (<i>left</i>) and SKA HI intensity mapping (<i>right</i>) surveys. Long mode k_3 is plotted along the x-axis.</p> <p>5.4. Total power for flattened configuration for <i>Euclid</i>-like (<i>left</i>) and SKA HI intensity mapping (<i>right</i>) surveys. Long mode k_3 is plotted along the x-axis.</p> <p>5.5. Total power for equilateral configuration for <i>Euclid</i>-like (<i>left</i>) and SKA HI intensity mapping (<i>right</i>) surveys. Since the dipole vanishes in this limit, the $\ell = 1$ line is absent.</p> <p>5.6. A selection of multipoles of the galaxy bispectrum, $B_{\ell m}$, with $\ell = 0 \dots 3$ and $m = 0 \dots \ell$ as indicated in the figure. Bias model used is that for an Hα/<i>Euclid</i>-like survey. k_1 is kept fixed, the value of which is given alongside the plot, and the x and y axes vary respectively k_3 and k_2 with respect to the fixed k_1. The upper left corner of the wedge shape is the squeezed limit, the upper right corner is the equilateral configuration, and the lower corner is the co-linear configuration. Note the difference in range of the colour bars.</p> <p>5.7. Selected multipoles of the galaxy bispectrum, similar to Figure 5.6, but with the bias model appropriate for intensity mapping. The value of fixed k_1 is indicated on the figures. The upper left corner of a wedge shape is the squeezed limit, the upper right corner is the equilateral configuration, and the lower corner is the co-linear configuration.</p> <p>5.8. Results for the reduced bispectrum $Q_{\ell m}$, where $\ell = 0 \dots 3$ and negative m not shown. The multipoles ℓ, m are indicated on the figure, as well as the value of k_1 which is kept fixed. The colourbar and different colours denote the ratio of k_2/k_1, where the slightly thicker purple line is the isosceles triangle, which diverges as $\theta \rightarrow \pi$ since there $k_3 \rightarrow 0$.</p>	<p>131</p> <p>137</p> <p>137</p> <p>137</p> <p>138</p> <p>138</p> <p>139</p> <p>140</p>
--	---

List of Figures

5.9.	Total power contained in the relativistic bispectrum normalised by the Newtonian monopole as a function of redshift z ranging from 0.1 to 2. The three panels are the equilateral configuration (<i>left</i> , with $\ell = 1$ vanishing), squeezed (<i>middle</i>) and co-linear flattened configuration (<i>right</i>). Solid lines for $k = 0.1 \text{ Mpc}^{-1}$, and dash-dotted for $k = 0.01 \text{ Mpc}^{-1}$	141
6.1.	$\mathcal{M}^{-1} = \varphi_{\text{P}}/\delta_{\text{C}}^{(1)}$ at $z = 1$	151
6.2.	Monopole of the reduced bispectrum for a Stage IV H α survey at $z = 1$, for various f_{NL} , with $k_1 = k_2 = 0.1 h/\text{Mpc}$. Shading indicates the 1σ uncertainty (neglecting shot noise) for the $f_{\text{NL}} = 0$ case (solid blue curve). <i>Left</i> : Comparing the full relativistic monopole to the Newtonian approximation (dash-dot curves). <i>Right</i> : Comparing the full relativistic monopole to the monopole without the GR correction to second-order galaxy bias, (6.32) (dashed curves).	165
6.3.	Monopole of reduced bispectrum for isosceles triangles, as in Figure 6.2. <i>Left</i> : As a function of f_{NL} , for various values of $\theta \equiv \theta_{12}$, where $\theta = \pi$ is the squeezed limit. Dashed curves indicate negative values. <i>Right</i> : 2D colour map as a function of f_{NL} and θ/π	166
6.4.	First few nonzero multipoles for fixed triangle shape as a function of k_3 , with $f_{\text{NL}} = 10$ (solid) and $f_{\text{NL}} = 0$ (dashed). <i>Left</i> : Equilateral configuration, $k_1 = k_2 = k_3$. <i>Middle</i> : Flattened configuration, $k_1 = k_2 \approx k_3/2$, with $\theta_{12} = 2^\circ$. <i>Right</i> : Squeezed configuration with $\theta_{12} = 178^\circ$ and $k_1 = k_2 = k_3/(2 \sin \theta_{12}) \approx 14 k_3$	167

List of Tables